

VOLUME 31

NOVEMBER 1953

NUMBER 7

*Canadian
Journal of Physics*

Editor: G. M. VOLKOFF

*Published by THE NATIONAL RESEARCH COUNCIL
OTTAWA CANADA*

CANADIAN JOURNAL OF PHYSICS

(Formerly Section A, Canadian Journal of Research)

The CANADIAN JOURNAL OF PHYSICS is published bimonthly by the National Research Council of Canada under the authority of the Chairman of the Committee of the Privy Council on Scientific and Industrial Research. Matters of general policy are the responsibility of a joint Editorial Board consisting of members of the National Research Council of Canada and the Royal Society of Canada.

The National Research Council of Canada publishes also: *Canadian Journal of Botany*, *Canadian Journal of Chemistry*, *Canadian Journal of Medical Sciences*, *Canadian Journal of Technology*, *Canadian Journal of Zoology*.

EDITORIAL BOARD

Representing

NATIONAL RESEARCH COUNCIL

DR. C. W. ARGUE (*Chairman*),
Dean of Science and Professor of Biology,
University of New Brunswick,
Fredericton, N.B.

DR. G. E. HALL,
President and Vice-Chancellor,
University of Western Ontario,
London, Ont.

DR. T. THORVALDSON,
Dean Emeritus of Graduate Studies,
University of Saskatchewan,
Saskatoon, Sask.

DR. W. H. WATSON,
Professor and Head of the Department
of Physics,
University of Toronto,
Toronto, Ont.

THE CANADIAN ASSOCIATION OF PHYSICISTS

DR. G. M. VOLKOFF,
Professor of Physics,
University of British Columbia,
Vancouver, B.C.

ROYAL SOCIETY OF CANADA

DR. G. M. VOLKOFF,
Professor of Physics,
University of British Columbia,
Vancouver, B.C.

DR. T. THORVALDSON,
Dean Emeritus of Graduate
Studies,
University of Saskatchewan,
Saskatoon, Sask.

DR. D. L. BAILEY,
Department of Botany,
University of Toronto,
Toronto, Ont.

DR. E. HORNE CRAIGIE,
Department of Zoology,
University of Toronto,
Toronto, Ont.

Section
III

Section
V

THE CHEMICAL INSTITUTE OF CANADA

DR. H. G. THODE,
Department of Chemistry,
McMaster University,
Hamilton, Ont.

Ex officio

DR. LÉO MARION (*Editor-in-Chief*),
Director, Division of Pure Chemistry,
National Research Laboratories,
Ottawa.

DR. H. H. SAUNDERSON,
Director, Division of Information Services,
National Research Council,
Ottawa.

Manuscripts should be addressed to:

DR. LÉO MARION,
Editor-in-Chief,
Canadian Journal of Physics,
National Research Council,
Ottawa, Canada.

Each manuscript should be typewritten, double-spaced, and the original and one extra copy submitted (see **Notice to Contributors** inside of back cover).

Subscriptions, renewals, and orders for back numbers should be addressed to:

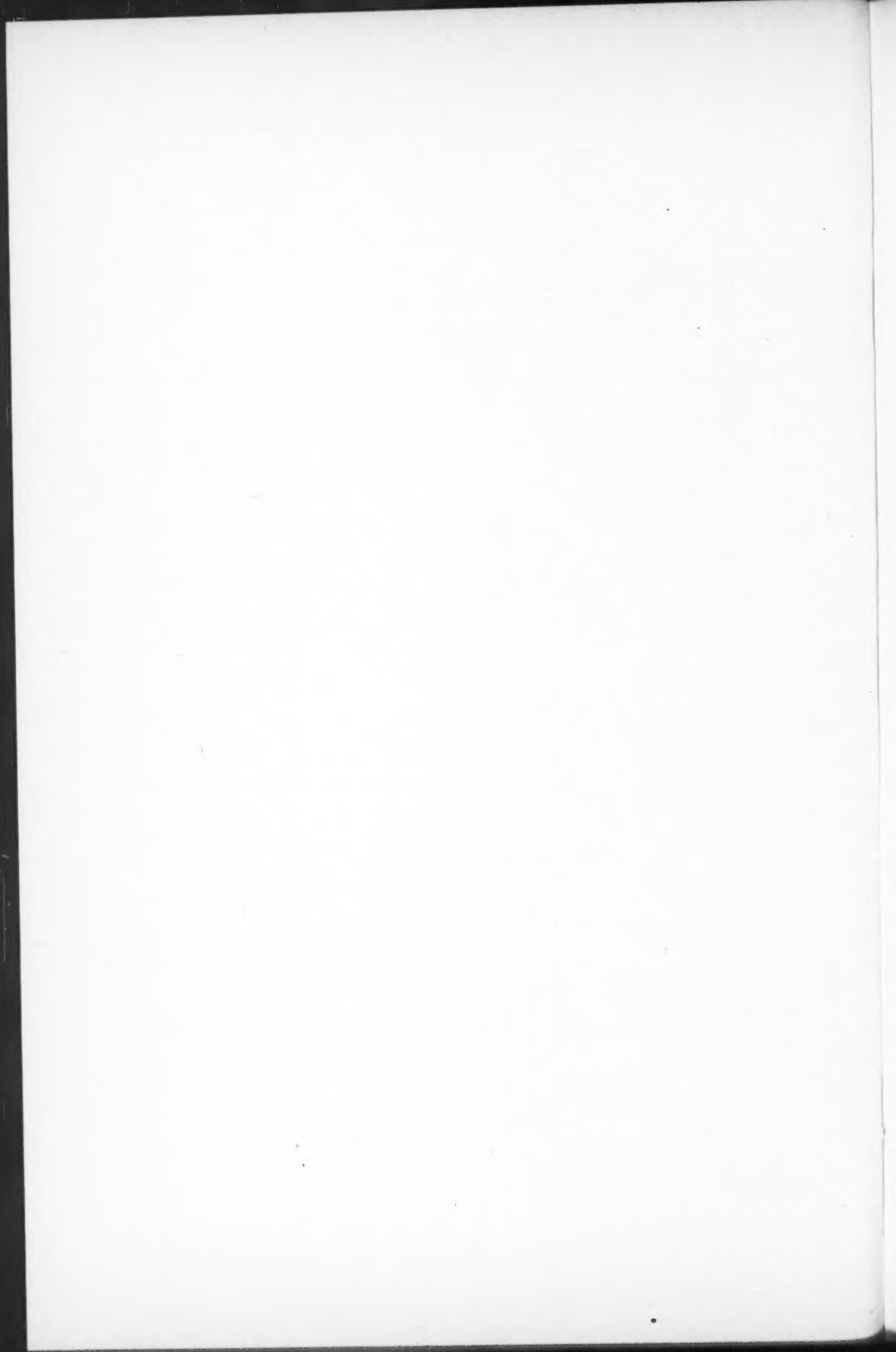
Administrative Services,
National Research Council,
Ottawa, Canada.

Subscription rate: \$3.00 a year; single numbers: 50 cents. Special rates can be obtained for subscriptions to more than one of the Journals published by the National Research Council.



NOTICE

Owing to the large increase in the number of papers submitted for publication in the *Canadian Journal of Physics*, this Journal will be published every month beginning in January 1954. This change should provide more prompt publication of papers submitted to the Journal. The subscription rate effective 1 January, 1954, will be \$4.00.



Canadian Journal of Physics

Issued by THE NATIONAL RESEARCH COUNCIL OF CANADA

VOLUME 31

NOVEMBER 1953

NUMBER 7

NEUTRON CAPTURE γ -RAYS FROM HEAVY ODD-CHARGE NUCLEI¹

By G. A. BARTHOLOMEW AND B. B. KINSEY

ABSTRACT

The neutron capture γ -ray spectra of arsenic, niobium, rhodium, silver, indium, antimony, praseodymium, tantalum, gold, and thallium are described. The energies and intensities of the strongest high energy γ -rays are given for each element.

INTRODUCTION

Pair spectrometer measurements of the neutron capture γ -rays emitted by the light elements up to zinc and by lead and bismuth have been described in earlier communications (2, 14, 17, 18, 19, 20). The capture γ -ray spectra of the odd-charge nuclei between zinc and lead which have been studied at this laboratory are described in the present paper.

The spectra of a number of these elements have been investigated by other methods with less resolution. The spectra of silver, indium, and gold were measured with the aid of D_2O -loaded plates by Hamermesh (10) and the spectra of rhodium, silver, indium, and antimony were measured with the aid of a crystal spectrometer by Hamermesh and Hummel (11). The maximum energies of the γ -rays of the spectra of silver and gold were investigated by Kubitschek and Dancoff (22).

Preliminary results for some of these elements were obtained in 1949 (3) with an early model of the pair spectrometer, hereafter called the "old apparatus". It was intended at the time that these measurements should be repeated as soon as possible with improved apparatus. Because of the ruptures in the N.R.X. pile at the end of 1952, this program has not been completed. The spectra of rhodium and silver and the high energy parts of the spectra of niobium and gold have been measured with the new apparatus. Since these measurements are more detailed they will be discussed first. The spectra of arsenic, indium, antimony, praseodymium, tantalum, and thallium, which have been investigated only with the old apparatus, will be described last.

In the old model of the spectrometer the magnetic field was stabilized by a conventional current regulator and the field was varied automatically through a number of predetermined values by a relay which changed the

¹ Manuscript received June 3, 1953.

Contribution from Atomic Energy of Canada Limited, Chalk River, Ont. Issued as A.E.C.L.
No. 51.

magnitude of the reference voltage supplied to the regulator. To avoid hysteresis effects, the field was cycled a number of times before each experiment and the strength of the field at selected points throughout the cycle was measured before and after each experiment with the aid of a proton resonance magnetometer. The field which obtained during the experiment was assumed to be the average of the two values at each point. Under these conditions, the energy of a γ -ray could seldom be measured more accurately than ± 20 kev, and the experimental points could not be placed conveniently at intervals smaller than about 20 kev. In the new apparatus (which is described in detail elsewhere (15)), the magnetic field control was changed to a system employing the proton resonance itself and, by changes in design, the counting efficiency was increased by a factor of 5, with the result that much more accurate and detailed measurements of capture γ -rays could be made.

In early experiments the sample material was enclosed in a container made entirely from Dural. The γ -rays produced by neutron capture in the Dural (mainly aluminum radiation) are superposed on the spectrum of the sample material and the true spectrum of the sample is obtained by subtracting the known Dural spectrum (19). In later experiments a sample container (4 in. diameter) with Bakelite ends was used. With this arrangement, the only unwanted γ -rays appearing in the spectrum are small amounts of lead and bismuth capture radiation produced in the bismuth plug and collimators (19) placed in the experimental hole of the pile and of incompletely absorbed aluminum radiation from the pile itself. In the coincidence spectra of samples enclosed in containers with Bakelite ends (shown in figures in the present paper and in the following paper) the contributions of these various types of background radiation are indicated by broken lines in those cases where their effect is not completely negligible.

In the absence of coincidences produced by unwanted γ -radiation there is still a small background of spurious counts above the chance coincidence rate. Scattering of electrons from the walls of the vacuum chamber and from the framework supporting the counter slits produces a high energy tail beyond each true coincidence peak. With the new apparatus, the scattering also gives rise to a weak ghost peak which is superposed on the tail (14, 15). An additional weak counting rate has been observed which probably results from coincidences between an electron in one counter and annihilation radiation in the other or between a positron in one counter and bremsstrahlung in the other. In both the latter cases one member of the electron pair is able to produce a count when it does not actually pass through the slit but merely stops in the neighborhood of it. The magnitude of this effect near 8 Mev. was estimated by measuring the coincidences produced by the prominent copper γ -rays (2) when the slit in front of one of the counters was completely closed and the other was left at its normal width. From these measurements it would appear that the spurious coincidences produce a broad peak of which the height is about 1% and the area is about 20% of the usual coincidence peak. The maximum of the broad peak coincides with that of the normal peak. This effect is of no importance in estimating γ -ray intensities from

peak counting rates in light elements where the γ -rays are well separated. In the spectra of heavy elements, however, a considerable background may be produced by the superposition of the contributions from a large number of γ -rays.

The method of obtaining the absolute intensities of capture γ -rays by comparing their coincidence counting rates with that of the 9.0 Mev. γ -ray of nickel is described elsewhere (15, 19). Nickel comparison measurements have been made only for niobium, silver, and gold.* Because of the interruption of pile operations, it is possible to make, for the remaining nuclei, only estimates of the absolute intensities using an approximate method. In this method we assume that samples of different elements which are of the same area and black to thermal neutrons undergo, in the same neutron flux, the same number of captures per second. For any γ -ray emitted by such a sample the absolute intensity in photons per capture is proportional to the counting rate divided by the relative counting efficiency of the spectrometer and by the transmission coefficients of the γ -ray in the sample material and in the neutron filters. If the absolute intensities of the γ -rays from one sample have been determined by the nickel comparison method, the proportionality constant can be determined and the absolute intensities of the γ -rays in the other samples, however, are not black to neutrons and it is necessary to allow for this. This we have done by plotting the ratio of the absolute intensities (when determined by the nickel method) at a fixed pile power to the counting rate (corrected as above) against the reciprocal of $N\sigma$, where N is the number of capturing atoms exposed to the view of the spectrometer and σ is the thermal capture cross section. The results for a number of γ -rays of different energies, derived from materials with very different capture cross sections, fall on a curve from which the unknown intensities of other γ -rays may be deduced. A check on the validity of this method of intensity calibration is occasionally afforded by the counting rate of the 7.72 Mev. aluminum γ -ray from those samples which were enclosed in the Dural container. The counting rate of this γ -ray gives a measure of the neutron flux at the sample. After calibration against γ -rays of known intensity from samples similarly enclosed, the counting rate in the aluminum peak can be used to measure the intensity of unknown gamma radiation in samples which are not black to thermal neutrons.

Absolute intensities determined by the nickel comparison method are probably not in error by more than 20% (15) over the spectra discussed in the present paper, while absolute intensities determined by the above approximate methods may be in error by as much as 50%. However, relative intensities for well-resolved γ -rays from the same sample are accurate to within about 15% for both methods.

The method of correcting the coincidence pair spectrum to find the γ -ray spectrum has been described in another communication (15). The result

*It has been shown (2) that the effect of epicadmium capture in intensity measurements in manganese is negligible and therefore we have ignored it in all cases except cadmium, samarium, and gadolinium (see following paper).

obtained, $\nu(E)$, is the number of γ -rays emitted per capture per unit energy range. For a homogeneous γ -ray the peak value of $\nu(E)$ depends on the resolution. When the width of the peak at half maximum (line width) is 100 kev. the peak value of $\nu(E)$ for a γ -ray of unit intensity is 7.2 γ -rays per capture per Mev. When the line width is 140 kev. the peak value is about 5.5 γ -rays per capture per Mev. It should be pointed out that the probable error of the ordinate in a corrected spectrum increases rapidly with decreasing energy. The probable error can always be deduced from an inspection of the statistical accuracy of the experimental points in the corresponding coincidence spectrum.

In general, only the γ -rays near the upper limit of the capture γ -ray spectra of heavy elements are well resolved with a line width of 100 to 140 kev. This energy region contains information of most immediate interest and it has been investigated in greatest detail. Measurements at lower energies, as a rule, reveal only the general energy distribution of the radiation. For convenience in investigating this region with the new apparatus, the number of experimental points per energy interval was reduced (20 or 40 per Mev.) and for simplicity when there is little useful detail, only the outline of the spectrum is shown (Figs. 1, 4, and 8) with an occasional experimental point to indicate the statistical accuracy of the measurements.

NIOBIUM

The niobium sample consisted of about 500 gm. of niobium pentoxide, Nb_2O_5 , enclosed in a Dural container with Bakelite ends. The coincidence spectrum was measured with a line width of 140 kev. from 2.5 to 7.7 Mev. with the old apparatus. The results are shown in Fig. 1. Owing to the obvious complexity of the niobium spectrum, it did not seem profitable to re-examine the whole of the spectrum with the new apparatus, and we have been content, therefore, to study only the upper end, which is shown in detail in Fig. 2 (line width 100 kev.). The niobium γ -rays are very weak, and at the upper end of the spectrum, they are superposed on the background produced by the lead and aluminum radiations. Only three γ -rays, A, B, and C, are clearly

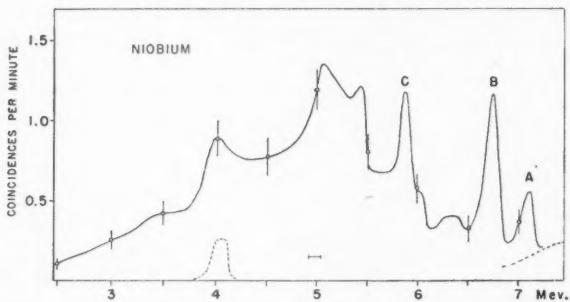


FIG. 1. Coincidence spectrum produced by niobium. Line width: 140 kev. Only occasional experimental points are shown to indicate statistical accuracy. The estimated contributions from bismuth and aluminum background radiations are shown by the broken curves.

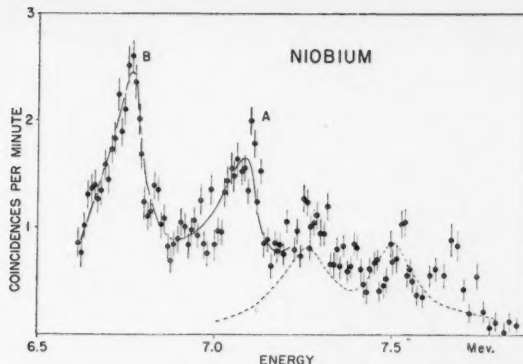


FIG. 2. High energy coincidence spectrum of niobium. Line width: 100 kev. The estimated contributions from lead and aluminum background radiations are indicated by the broken curve.

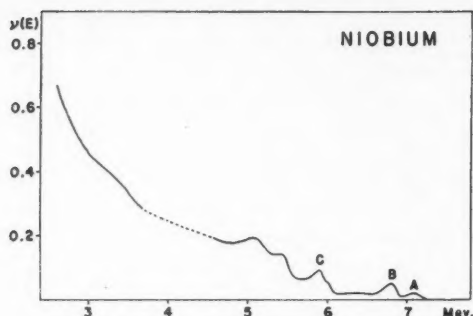
resolved. No γ -rays with energies above that of *A* can be reliably distinguished above the background.

The energies and intensities of the resolved γ -rays are listed in Table I. Use of nickel for direct intensity calibration of the niobium γ -rays is not convenient since nickel possesses a strong radiation, *H*, at 6.84 Mev. (14) which is almost coincident with the prominent niobium peak, *B*. As an alternative, intensities were measured by comparing the intensity of the γ -ray *B* with that of the 7.64 Mev. γ -ray from iron, in an intimate mixture of niobium oxide with iron carbide, the capture cross section of niobium being assumed to be 1.1 barns and that of iron, 2.43 barns. The corrected γ -ray spectrum is shown in Fig. 3.

TABLE I
ENERGIES AND INTENSITIES OF NIOBIUM γ -RAYS

γ -Ray	Energy in Mev.	Intensity in photons per 100 captures
<i>A</i>	7.19 ± 0.03	0.4
<i>B</i>	6.85 ± 0.03	0.8
<i>C</i>	5.90 ± 0.08	0.8

Niobium has only one stable isotope, Nb⁹³, and the spectrum obtained is caused, therefore, entirely by the excitation of Nb⁹⁴. According to Harvey (12) the neutron binding energy of Nb⁹⁴ is 7.26 ± 0.10 Mev. This result is in agreement with the energy of the γ -ray *A*, which may be identified, therefore, with the ground state γ -ray in this nucleus. This identification, however, is not certain, for Nb⁹⁴ is known to have an isomeric state (5) with an energy of 41 kev. The spin of Nb⁹³ is 9/2 and according to the shell model (21) the odd proton in this nucleus is in a $g_{9/2}$ orbit. Accordingly the compound state produced by neutron capture has a spin of 4 or 5 and even parity. From

FIG. 3. Corrected γ -ray spectrum of niobium.

data on the decay of the isomeric state and of the ground state of Nb^{94} , as summarized by Goldhaber and Hill (8), it may be surmised that the isomeric state has odd parity and spin 3 or 4 and that the ground state has even parity and spin 6 or 7. Because of the large number of spin alternatives presented by this data, it is not possible to deduce the multipole character of the direct transitions to either the isomeric state or to the ground state.

RHODIUM

The rhodium sample consisted of 60 gm. of the pure metal, in powder form, enclosed in a Bakelite container. The capture γ -ray spectrum was measured from 3 to 7.3 Mev. with the new apparatus (resolution 100 kev.). The results are shown in Figs. 4 and 5. The energies and intensities of the well-resolved γ -rays are given in Table II. The intensities were estimated from the peak counting rates by the approximate method described above, assuming that the thermal capture cross section of rhodium is 150 barns. The corrected spectrum is shown in Fig. 6.

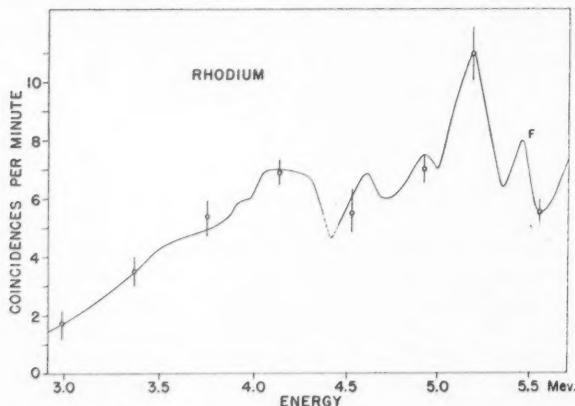


FIG. 4. Coincidence spectrum produced by rhodium, 3.0-5.7 Mev. Line width: 100 kev. Only occasional experimental points are shown to indicate statistical accuracy.

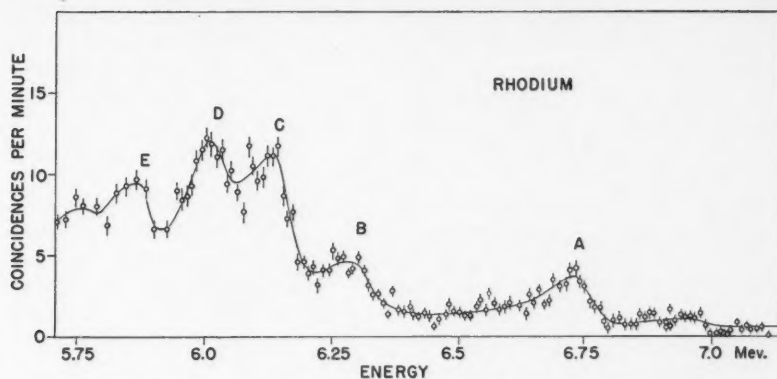
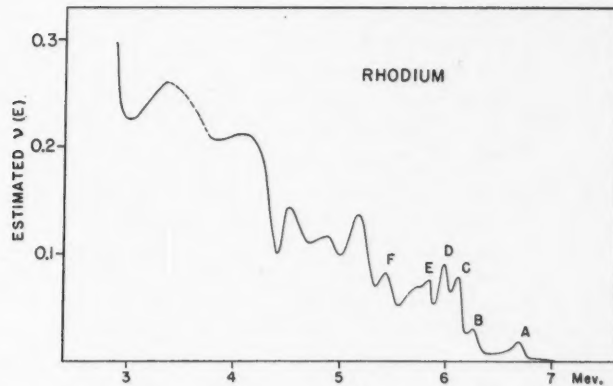


FIG. 5. Coincidence spectrum produced by rhodium, 5.7-7.2 Mev. Line width: 100 kev.

FIG. 6. Corrected γ -ray spectrum of rhodium.TABLE II
ENERGIES AND INTENSITIES OF RHODIUM γ -RAYS

γ -Ray	Energy in Mev.	Estimated intensity in photons per 100 captures
A	6.792 ± 0.014	0.2
B	6.355 ± 0.014	0.2
C	6.20 ± 0.02	0.7
D	6.06 ± 0.02	0.6
E	5.91 ± 0.02	0.5
F	5.55 ± 0.02	0.5

Harvey (12) obtained the value 6.81 ± 0.2 Mev. for the neutron binding energy of Rh¹⁰⁴ from a measurement of the Q -value of the Rh¹⁰³(d, p)Rh¹⁰⁴ reaction. The energy of the γ -ray A , 6.792 ± 0.014 Mev., is in good agreement with Harvey's value. There is a suggestion in Fig. 5 of another γ -ray near 7.0 Mev. though the evidence is not sufficient to establish its presence with certainty. We conclude tentatively that the γ -ray A is emitted in the ground state transition in Rh¹⁰⁴.

The spin of Rh¹⁰³ is $1/2$ and it is probable (8, 21) that the odd proton in this nucleus is in a $p_{1/2}$ -state. Therefore, the parity of Rh¹⁰³ and of the state in Rh¹⁰⁴ formed by neutron capture is odd. The spin of the 1.3 ev. resonance in rhodium is known to be unity (4) and it is probable that this level is the one largely responsible for thermal neutron capture. From β -decay evidence, the ground state of Rh¹⁰⁴ is almost certainly an even state with spin 1 (8). It follows therefore that the ground state γ -ray in Rh¹⁰⁴ is of the $E1$ type.*

Only one excited state, the 0.052 Mev. isomeric state, is known in Rh¹⁰⁴. There is no evidence of a γ -ray of energy 0.052 Mev. less than that of the γ -ray A nor should one be expected for if the isomeric state is odd with spin 4, the γ -ray emitted in the transition from the capturing state to this state is of the $E3$ type. It is plausible to assume that the γ -rays B and C and probably also D , E , and F are emitted in transitions from the capturing state to low lying excited states in Rh¹⁰⁴. If the γ -ray A is correctly identified as the ground state γ -ray, these excited states have energies of 0.44 ± 0.02 , 0.59 ± 0.02 , 0.73 ± 0.02 , 0.88 ± 0.02 , and 1.24 ± 0.02 Mev.

SILVER

The silver sample consisted of 83 gm. of the pure metal enclosed in a Bakelite container. The capture γ -ray spectrum was studied between 3 and 7.5 Mev. with the new apparatus. Above 6 Mev. the spectrum was studied in detail with a resolution of 100 kev. (Fig. 7). In the more complex region of the spectrum below 6 Mev. only the general energy distribution of the spectrum was investigated with a resolution of about 120 kev. (Fig. 8).

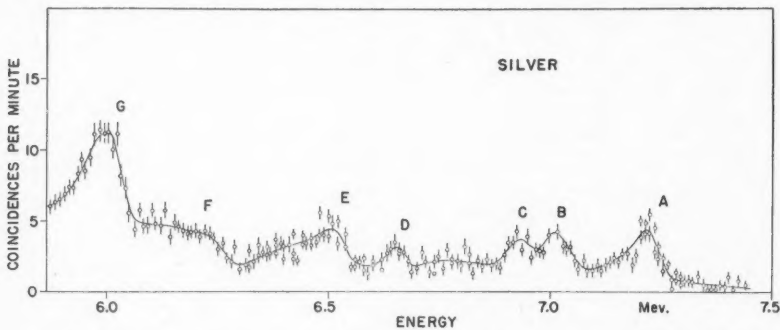


FIG. 7. Coincidence spectrum produced by silver, 5.8-7.5 Mev. Line width: 100 kev.

*We use the nomenclature of Goldhaber and Sunyar (9).

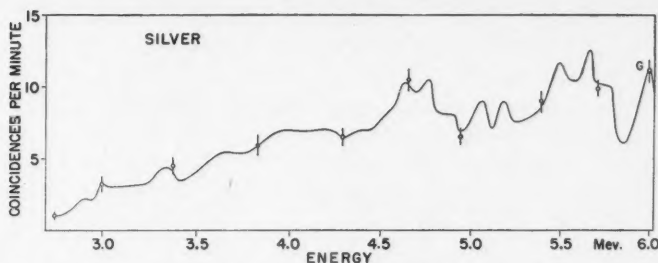


FIG. 8. Coincidence spectrum produced by silver, 2.7-6.0 Mev. Line width: 100 kev. Only occasional experimental points are shown to indicate statistical accuracy.

The energies and intensities of the prominent γ -rays are listed in Table III. The absolute intensities were obtained by comparing the peak counting rate of γ -ray G with that of the 9 Mev. γ -ray from nickel produced by a source consisting of alternate layers of silver and nickel sheets sandwiched together. The capture cross section for silver was assumed to be 60 barns. The corrected γ -ray spectrum is shown in Fig. 9.

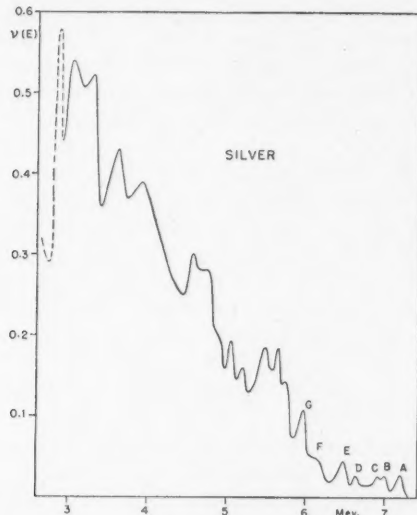


FIG. 9. Corrected γ -ray spectrum of silver.

Silver has two isotopes Ag^{107} and Ag^{109} which contribute 28% and 72% respectively to the total thermal neutron capture cross section. The end point of the γ -ray spectrum produced by neutron capture in silver has been found to be 6.5 ± 0.7 Mev. by Kubitschek and Dancoff (22). The neutron binding energy of Ag^{108} was found by Harvey (12) to be 7.01 ± 0.2 Mev. from a measurement of the Q of the $\text{Ag}^{107}(d,p)\text{Ag}^{108}$ reaction. No direct

TABLE III
ENERGIES AND INTENSITIES OF SILVER γ -RAYS

γ -Ray	Energy in Mev.	Intensity in photons per 100 captures
A	7.27 \pm 0.02	0.4
B	7.06 \pm 0.02	0.3
C	6.95 \pm 0.02	0.1
D	6.67 \pm 0.02	0.2
E	6.55 \pm 0.02	0.4
F	6.27 \pm 0.02	0.4
G	6.057 \pm 0.012	1.1

measurement of the neutron binding energy of Ag^{110} is available in the literature. However, an approximate value for this quantity may be obtained if it is assumed that the difference between the actual neutron binding energy and that calculated using the mass formula is close to the difference obtained for Ag^{108} . This difference is given by Harvey (12) to be -0.5 Mev. Using the mass tables of Metropolis and Reitwiesner* (23) we calculate a neutron binding energy of 7.0 Mev. for Ag^{110} whence the actual value should be close to 6.5 Mev.

The energy of the γ -ray A in Table III, viz. 7.27 ± 0.02 Mev., is close to the neutron binding energy of Ag^{108} obtained by Harvey and we conclude therefore that this γ -ray represents the ground state transition in that nucleus. It is not possible to identify the ground state transition in Ag^{110} with certainty. On the basis of the neutron binding energy estimate given above it seems probable that it is one of the γ -rays D or E. Since the energies of the γ -rays B and C exceed the neutron binding energy of Ag^{110} these radiations must correspond to transitions in Ag^{108} . It is probable, moreover, that they are emitted in transitions from the capturing state to low lying states at 0.21 ± 0.03 and 0.32 ± 0.03 Mev. These assignments cannot, at present, be confirmed since no other information is available concerning the level structure of Ag^{108} . The level structure of Ag^{110} is also unknown above the isomeric level at 0.116 Mev., and nothing further can be deduced from the present measurements since the radiations produced by Ag^{110} cannot be distinguished from those produced by Ag^{108} .

The spin of the ground states of both Ag^{107} and Ag^{109} is $1/2$ and, on the basis of the shell model, the parity is odd in both cases, i.e., the odd proton is in a $p_{1/2}$ orbit (8, 21). It follows that a neutron is captured into states of spin 0 or 1 and odd parity in both Ag^{108} and Ag^{110} . In Ag^{110} , the spin of the 5 ev. neutron resonance has been shown (24) to be 1, and it is probable that this resonance is largely responsible for thermal capture in this isotope. The β -spectra of both Ag^{108} and Ag^{110} are of the allowed type; it follows that their ground states have a spin of 1 and even parity. If these spin and parity assignments are correct, the ground state neutron capture γ -rays are of $E1$ type in both product nuclei.

*The mass formulae used by Harvey and by Metropolis and Reitwiesner are equivalent.

GOLD

The gold sample consisted of a disk of the pure metal, about 200 gm. in weight, mounted in a Dural cylinder with open ends. In an earlier experiment with the old apparatus the spectrum was investigated between 2.5 and 9.0 Mev. In a later experiment with the new apparatus the spectrum was measured between 3.5 and 7.8 Mev. The latter results are shown in Figs. 10 and 11. It will be seen that the high energy part of the spectrum contains a

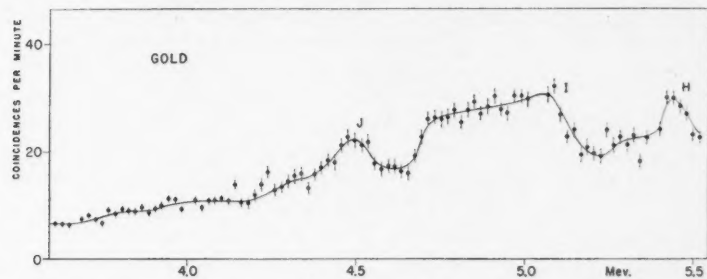


FIG. 10. Coincidence spectrum produced by gold, 3.5-5.5 Mev. Line width: 100 kev.

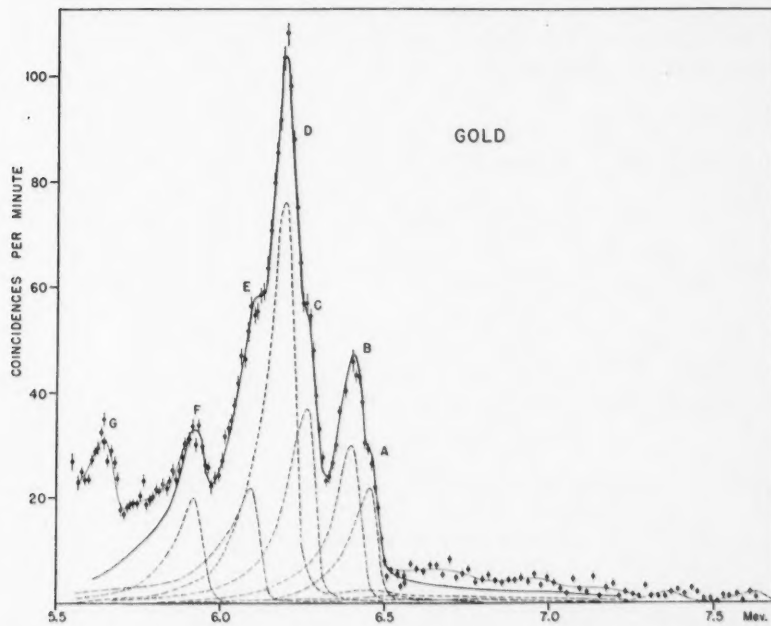


FIG. 11. Coincidence spectrum produced by gold, 5.5-7.6 Mev. Line width: 100 kev. The broken curves illustrate an analysis of the complex curve into component peaks (see text).

large number of γ -rays, few of which are clearly resolved, and also a prominent tail extending from 6.5 to 7.5 Mev. The energies and intensities of the prominent gold γ -rays are listed in Table IV. For the γ -rays *H*, *I*, and *J* the energy

TABLE IV
ENERGIES AND INTENSITIES OF GOLD γ -RAYS

γ -Ray	Energy in Mev.	Intensity in photons per 100 captures
<i>A</i>	6.494 ± 0.008	1.5
<i>B</i>	6.453 ± 0.011	2.1
<i>C</i>	6.310 ± 0.008	2.8
<i>D</i>	6.249 ± 0.009	6
<i>E</i>	6.146 ± 0.013	1.8
<i>F</i>	5.976 ± 0.011	1.8
<i>G</i>	5.702 ± 0.016	1.6
<i>H</i>	5.52 ± 0.03	1.3
<i>I</i>	5.20 ± 0.03	1.7
<i>J</i>	4.59 ± 0.04	3

given is that of the γ -ray of highest energy in an unresolved group. The absolute intensities were obtained by the nickel comparison method using the prominent peak *D* in Fig. 11. In this determination the capture cross section of gold was assumed to be 94 barns. The corrected spectrum given in Fig. 12 was constructed by combining the old results below 4.0 Mev. with the new results above that energy.

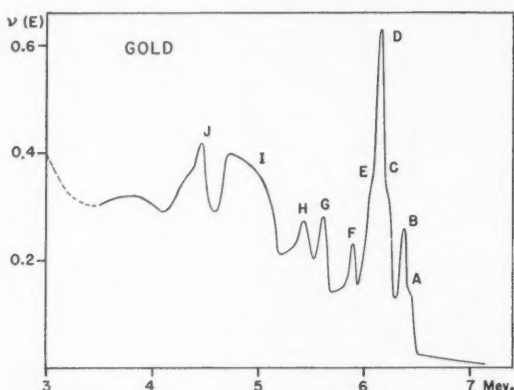


FIG. 12. Corrected γ -ray spectrum of gold.

The neutron binding energy of Au^{198} as measured by Harvey (12) is 6.35 ± 0.15 Mev. This value is in good agreement with the energy of the γ -ray *A*, 6.494 ± 0.008 Mev. However, after consideration of the multipole order of the ground state transition, it would seem probable that *A* is not, in fact, the ground state γ -ray.

The spin of Au¹⁹⁷ is known to be 3/2. According to the shell model the odd proton is in a $d_{3/2}$ orbit and therefore the parity of this nucleus and that of the compound state produced by neutron capture is even. Tittman and Sheer (27) have found that the spin of the 4.9 ev. resonance responsible for thermal capture is 1 unit and it has been shown by Elliott *et al.* (6) that the ground state of Au¹⁹⁸ has a spin of 3 and odd parity. Therefore, it follows that the γ -ray emitted in the direct transition to the ground state is of the $M2$ type. It is unlikely that the highest energy γ -ray (*A*) is to be identified with this ground state γ -ray for, as will be shown elsewhere (16), the absolute intensity of *A* is not inconsistent with *E1* radiation for a nucleus in this part of the periodic table. We conclude that the ground state γ -ray is too weak to be detected in the presence of the strong tail above 6.5 Mev.

In order to determine the magnitude of the various components contributing to the tail, an attempt was made to analyze the spectrum between 6 and 7.5 Mev. into separate radiations (Fig. 11). The coincidence peaks corresponding to the γ -rays assumed to be responsible for the observed spectrum are shown by broken lines. These curves include the estimated contributions from the second order effects (scattering, bremsstrahlung, and annihilation radiation) described earlier. The background produced by lead and aluminum radiations from the experimental hole is shown by the broken curves at 7.38 and 7.7 Mev. The heavy full curve is the sum of the curves representing the separate γ -rays and is in agreement with the experimental points everywhere except in the region between 6.5 and 7.3 Mev. Though this discrepancy suggests the presence of weak capture radiation from Au¹⁹⁸, there is no clear evidence for a coincidence peak just above peak *A* and, moreover, since the poor fit extends to much higher energies, it would seem probable that the contributions from the second order coincidence effects (which are not well known) have been underestimated.

An alternative possibility was investigated: that part of this tail might be due to γ -rays from Au¹⁹⁹ produced by double neutron capture in Au¹⁹⁷. The rate of neutron capture in Au¹⁹⁸ as a function of time is given by the expression:

$$\frac{C\eta}{\lambda + \eta} (1 - e^{-(\lambda + \eta)t})$$

where *C* is the rate of neutron capture in Au¹⁹⁷ and λ and η are the disintegration and neutron capture probabilities per atom per unit time for Au¹⁹⁸. Assuming a neutron flux of 5×10^{12} neutrons per sq. cm. per sec. and 38,000 barns (25) for the thermal neutron capture cross section of Au¹⁹⁸, we find that when equilibrium is established for the production of Au¹⁹⁸, the capture rate in Au¹⁹⁸ should be about 6% of that in Au¹⁹⁷. Now the calculated neutron binding energy (23) of Au¹⁹⁹ is about 1 Mev. greater than that of Au¹⁹⁸ and therefore if the ground state γ -ray or other high energy γ -rays in the Au¹⁹⁹ spectrum should happen to have high absolute intensities, they might be detected above 6.5 Mev. after sufficient time has elapsed to allow the build-up of Au¹⁹⁸.

To check this possibility the region between 6.4 and 7.5 Mev. was measured in two experiments, the first starting immediately after the gold sample was

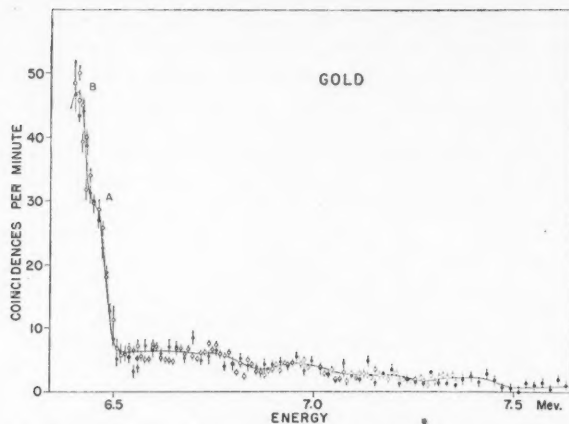


FIG. 13. High energy coincidence spectrum of gold. Full circles: measurements made at beginning of neutron irradiation. Open circles: measurements made after 72 hr. of continuous irradiation.

placed in the pile and the second starting after 72 hr. of continuous irradiation. The time taken to cover this energy region was 12 hr. in each experiment. The results obtained are given in Fig. 13 and show no apparent difference between the two sets of data. This indicates that no part of the tail is due to capture γ -rays from Au^{199} . However, it should be pointed out that such a result would also be obtained if the capture cross section of Au^{198} were extremely high. For example, the coincidence rate at 7.0 Mev. was measured at 6 hr. and again at 78 hr. after the beginning of the irradiation. If the capture cross section of Au^{198} were so large that the growth of this isotope in the sample reached saturation before the first six hours, there would be no difference between the two sets of measurements at 7 Mev. Indeed recently a value of 9×10^5 barns has been reported for the Au^{198} cross section (7). However, it is easy to show that if this cross section were correct, the capture rate after 6 hr. would only be about one sixth that after 78 hr. and that an even greater Au^{198} cross section is required in order that no difference between the capture rates at the two times should be obtained. Since a larger cross section is most unlikely it must be concluded that the counting rate in the tail is produced largely by spurious coincidences.

ARSENIC

The arsenic sample consisted of 2 kgm. of chemically pure As_2O_3 enclosed in a Dural container. The spectrum, which was studied with the old apparatus only, is shown in Fig. 14. The energies and intensities are given in Table V. The intensities were estimated by the approximate method, assuming a thermal capture cross section of 4.1 barns. The corrected spectrum is shown in Fig. 15.

The neutron binding energy of As^{76} has not been measured. The value for this quantity obtained from the mass tables of Metropolis and Reitwiesner

TABLE V
ENERGIES AND INTENSITIES OF ARSENIC γ -RAYS

γ -Ray	Energy in Mev.	Estimated intensity in photons per 100 captures
A	7.30 ± 0.04	0.5
B	7.05 ± 0.04	2
C	6.85 ± 0.04	2
D	6.38 ± 0.06	2
E	6.08 ± 0.04	1
F	5.41 ± 0.06	1
G	5.17 ± 0.06	2
H	4.97 ± 0.06	1
I	4.77 ± 0.06	1
J	4.53 ± 0.03	2

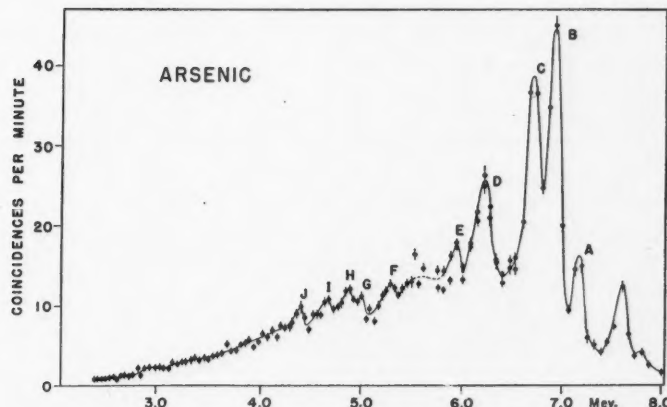
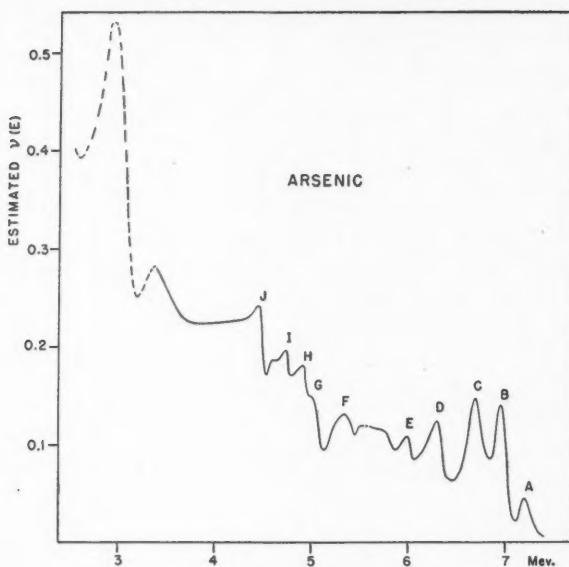


FIG. 14. Coincidence spectrum produced by arsenic. Line width: 140 kev. The peaks above peak A are ascribed to γ -rays from Dural.

(23) is 6.8 Mev. According to the binding energy compilation of Harvey (12), values computed from the mass formula are likely to be too low by about 0.5 Mev. near the neutron number 43. Hence the neutron binding energy of As⁷⁶ may be expected to be nearer to 7.3 Mev. than 6.8 Mev. Though the end point of the spectrum in Fig. 14 is not clear because of the presence of the aluminum radiation, the γ -ray of highest energy which is resolved is the γ -ray A at 7.30 ± 0.04 Mev. In view of the agreement with the estimated neutron binding energy of As⁷⁶ it is probable, though not certain, that the γ -ray A is emitted in the ground state transition in that nucleus. The energy of 7.30 Mev. at least represents a lower limit for the neutron binding energy.

The spin of As⁷⁶ is 3/2 and the shell assignment (21) for the proton configuration in that nucleus is $p_{3/2}$. It follows that the state produced by thermal neutron capture has a spin of 1 or 2 and odd parity. The spin of the ground state of As⁷⁶ has not been measured. However, it is fairly well established that

FIG. 15. Corrected γ -ray spectrum of arsenic.

it decays to the ground state of Se^{76} and the β -ray transition has a $\log ft$ of about 8, which suggests that the spin of As^{76} in its ground state is either 1 or 2 units. If this deduction is correct it follows that the ground state capture γ -ray is either $E1$ or $M1$ depending on the parity of the As^{76} ground state and regardless of the spin of the capturing state.

Assuming, then, that the γ -ray A is the ground state γ -ray and that it is either of the $E1$ or $M1$ type we may guess that the γ -rays B and C are also first order radiations and that they are emitted in transitions to low lying excited states at 0.25 ± 0.06 and 0.45 ± 0.06 Mev. The same conclusion does not apply to the γ -ray D since the width of this peak indicates that several radiations may contribute to it. Nothing is known about the excited states of As^{76} and therefore the existence of the above-mentioned states cannot be confirmed.

INDIUM

The indium sample consisted of a pure metal disk, weighing about 150 gm., mounted inside a Dural container. The spectrum was measured from 3 to 8.5 Mev. with the old apparatus. The results are shown in Fig. 16. The absolute intensities have been obtained by the approximate method described above, assuming that the thermal cross section of indium is 190 barns. The energies and intensities of the prominent γ -rays are given in Table VI. The corrected spectrum is shown in Fig. 17.

Indium possesses two naturally occurring isotopes, In^{113} and In^{115} . The capture γ -ray spectrum is almost entirely produced by capture in In^{115} since

TABLE VI
ENERGIES AND INTENSITIES OF INDIUM γ -RAYS

γ -Ray	Energy in Mev.	Estimated intensity in photons per 100 captures
A	5.86 ± 0.03	0.7
B	5.73 ± 0.05	0.3
C	5.55 ± 0.04	0.4
D	5.34 ± 0.04	0.8
E	5.17 ± 0.04	1.0
F	4.97 ± 0.04	1.1

the contribution of In¹¹³ to the total thermal neutron capture cross section is only about 1%. The binding energy of In¹¹⁶ has been measured by Harvey (12) who obtained the value 6.59 ± 0.2 Mev. No value for the neutron binding energy of In¹¹⁴ has been reported. However, Harvey's compilation of neutron binding energies indicates that values calculated from the mass formula should be in good agreement with experimental values at neutron numbers near 65. We therefore take the value 7.2 Mev. obtained from the mass tables of Metropolis and Reitwiesner (23) to be the neutron binding energy of In¹¹⁴.

The spin of In¹¹⁵ is 9/2 and according to shell theories the odd proton in this nucleus is in a g_{9/2} orbit. The parity of In¹¹⁵ and that of the state produced by neutron capture is therefore even. The resonance at 1.5 ev. which is largely responsible for thermal capture has been shown to have a spin of 4 units (4). Since the β -decay between the ground states of In¹¹⁶ and Sn¹¹⁶ has a log ft of about 4.3, we may conclude that the ground state of In¹¹⁶ has a spin of 1 and even parity. It follows, that the capture γ -ray emitted in the direct transition to the ground state in In¹¹⁶ is of the M3 type, and, therefore, will probably be too weak to be detected. In¹¹⁶ possesses an isomeric state whose decay to the ground state has not been observed. Släts, du Toit, and Siegbahn (26) have estimated the energy of the isomer to be 410 ± 150 kev. and have

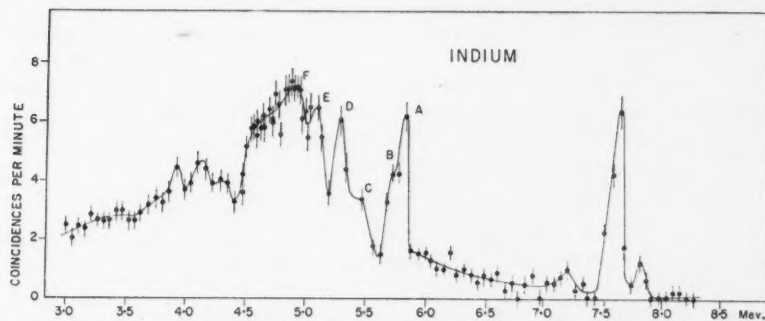
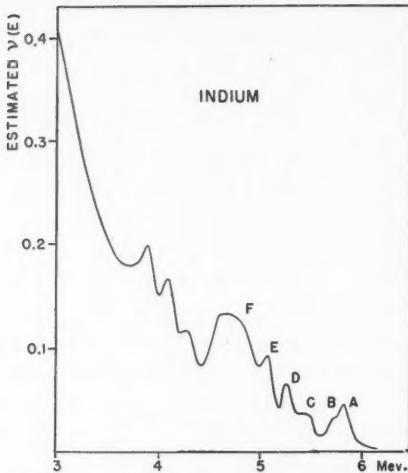


FIG. 16. Coincidence spectrum produced by indium. Line width: 140 kev. The peaks between 7 and 8 Mev. are ascribed to γ -rays from Dural.

FIG. 17. Corrected γ -ray spectrum of indium.

shown that its spin cannot be less than 3. When the failure of these authors to detect the isomeric transition is considered in the light of the recent analyses of isomeric transitions made by Goldhaber and Sunyar (9), it seems likely that the spin of this state cannot be less than 5. We may expect, therefore, that a γ -ray (either $M1$ or $E1$) with an energy 410 kev. less than the binding energy, i.e. 6.18 ± 0.3 Mev., might be present in the capture γ -ray spectrum of In^{116} .

The high energy end of the indium spectrum in Fig. 16 is obscure because of poor counting statistics and because of the presence of aluminum radiation. The γ -ray of highest energy which is most clearly resolved is peak A at 5.86 ± 0.03 Mev. which is in rather poor agreement with the energy expected for the γ -ray emitted in the transition to the isomeric state. The spectrum possesses an unresolved tail extending above 5.85 Mev. all of which cannot be accounted for by aluminum radiation. This tail may include the γ -ray emitted in the transition to the isomeric state or if this γ -ray is correctly identified with A the tail could be produced by weak radiations due to capture in In^{113} . Since nothing is known about other excited states in In^{116} none of the other γ -rays in the spectrum can be identified. From the present results we can only conclude that the neutron binding energy of In^{116} is not less than 6.27 ± 0.16 Mev. (i.e. $5.86 + 0.41$ Mev.).

ANTIMONY

The antimony source consisted of 1 kgm. of the oxide, Sb_2O_3 , enclosed in a Dural container. The spectrum was measured with the old apparatus from 2.5 to 10 Mev. The coincidence spectrum is shown in Fig. 18. No significant counting rate was observed above 8.2 Mev. It will be seen that the peak at 7.8 Mev. is about twice normal width. The size of the aluminum

peak which should be present at this energy can be crudely estimated from its size in the spectra of other elements where the sample used had similar neutron and γ -ray absorption properties as the present sample. We estimate in this way that the aluminum radiation should produce a peak whose height is about 70% of the broad peak at 7.8 Mev. This peak is shown by the broken

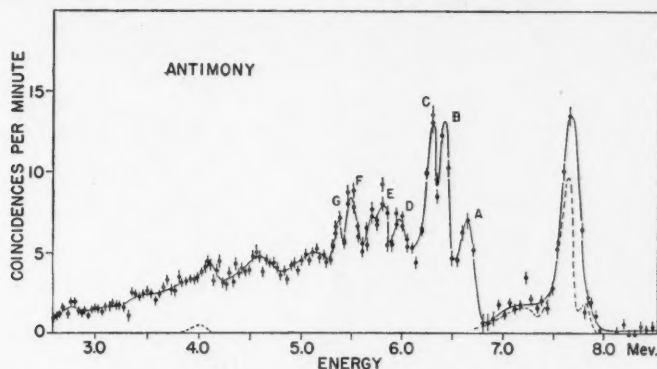


FIG. 18. Coincidence spectrum produced by antimony. Line width: 140 kev. The peaks above peak *A* are ascribed to γ -rays from Dural (See text).

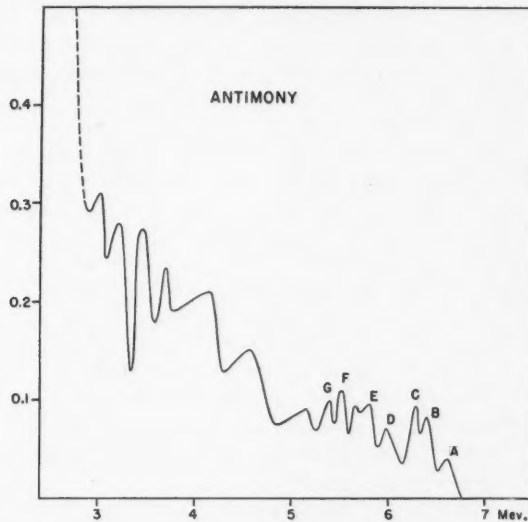


FIG. 19. Corrected γ -ray spectrum of antimony.

curve in Fig. 18. When this contribution is subtracted, a peak remains for which the height is also about 70% of the observed peak and the energy is 7.76 ± 0.06 Mev. However it would seem unwise to conclude definitely that

such a γ -ray is actually emitted by antimony for as will be shown below, its energy is much greater than the neutron binding energy of Sb¹²² as measured by Harvey (12). Also, there is good reason to doubt the experimental reliability of the single point which defines the width of the peak. The energies and intensities of the well-resolved high-energy antimony γ -rays are given in Table VII. The absolute intensities were obtained from the peak counting rates by the approximate method, assuming that the thermal capture cross section of antimony is 6.4 barns. The corrected spectrum is shown in Fig. 19.

TABLE VII
ENERGIES AND INTENSITIES OF ANTIMONY γ -RAYS

γ -Ray	Energy in Mev.	Estimated intensity in photons per 100 captures
A	6.80 \pm 0.04	0.7
B	6.50 \pm 0.03	1.6
C	6.33 \pm 0.04	1.1
D	6.11 \pm 0.06	1
E	5.89 \pm 0.04	1
F	5.61 \pm 0.03	1
G	5.43 \pm 0.03	0.5

Antimony has two stable isotopes, Sb¹²¹ and Sb¹²³, whose contributions to the total thermal neutron capture cross section are about 77% and 23% respectively. The capture γ -ray spectrum is therefore composed of the radiations emitted by both Sb¹²² and Sb¹²⁴. The neutron binding energy of Sb¹²² obtained by Harvey (12) from a study of the Sb¹²¹(d,p)Sb¹²² reaction is 6.64 \pm 0.2 Mev. The neutron binding energy of Sb¹²⁴ has not been measured. According to calculations based on the mass tables of Metropolis and Reitwiesner (23), it should be about 400 kev. less than the neutron binding energy of Sb¹²². The energy of the peak A, 6.80 \pm 0.04 Mev., is in agreement with Harvey's value of the neutron binding energy of Sb¹²². This suggests that the peak at 7.7 Mev. is entirely due to Dural. Because of the confusion of the spectra from Sb¹²² and Sb¹²⁴ and because of the poor knowledge of the neutron binding energies, it is impossible to interpret any of the other γ -rays in Fig. 18.

The shell structure assignment for the ground state of Sb¹²¹ is a $d_{5/2}$ -state. The ground state of Sb¹²² appears to be odd with a spin of 2 units (8); the ground state transition therefore should be E1 regardless of the spin of the compound state produced by neutron capture. The intensity of the γ -ray A appears to be consistent with the assumption that it is E1 and that it is the ground state γ -ray in Sb¹²².

PRASEODYMIUM

The praseodymium sample consisted of 95 gm. of praseodymium oxide* (as Pr₆O₁₁) enclosed in small Bakelite capsules which were mounted centrally in the experimental hole. The capture γ -ray spectrum which was measured

*We are indebted to Dr. F. H. Spedding, Iowa State College, Ames, Iowa, for providing this material.

with the old apparatus is shown in Fig. 20. The energies and intensities of the prominent γ -rays are given in Table VIII. The absolute intensities were obtained from the peak coincidence counting rates by the approximate method, assuming that the thermal capture cross section of praseodymium is 11.2 barns. The corrected spectrum is shown in Fig. 21.

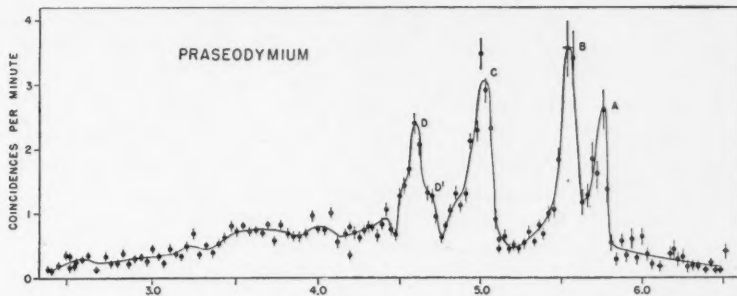


FIG. 20. Coincidence spectrum produced by praseodymium. Line width: 140 kev.

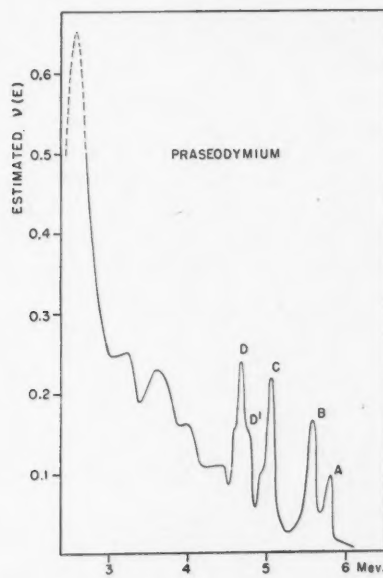


FIG. 21. Corrected γ -ray spectrum of praseodymium.

The neutron binding energy of Pr^{142} has not been measured. The calculated neutron binding energy obtained from the tables of Metropolis and Reitwiesner (23) is 6.58 Mev. However, Pr^{142} contains one neutron beyond the closed

TABLE VIII
ENERGIES AND INTENSITIES OF PRASEODYMIUM γ -RAYS

γ -Rays	Energy in Mev.	Estimated intensity in photons per 100 captures
A	5.83 ± 0.03	2
B	5.67 ± 0.03	3
C	5.16 ± 0.03	3
D'	4.79 ± 0.04	2
D	4.69 ± 0.04	3

shell at 82 and it is reasonable to expect that the neutron binding energy will be lower than that calculated by at least 0.5 Mev. (12), i.e. about 6.0 Mev. The γ -ray of highest energy which is clearly resolved is the γ -ray A at 5.83 ± 0.03 Mev. There is some evidence in Fig. 20 for the presence of weak coincidence peaks up to 6.23 Mev. though the statistics are too poor to establish their presence with certainty. Some of the counting rate in this energy region must be produced by spurious second order coincidences. It is possible to conclude only that the neutron binding energy of Pr^{142} is not less than 5.83 ± 0.03 Mev. Nothing is known about the excited states of Pr^{142} and, in view of the uncertainty in the neutron binding energy, a prediction of the positions of some of them on the basis of the γ -ray energies in Table VIII would be unjustified.

The spin of Pr^{141} is known to be $5/2$ and the shell model assignment (21) for the proton orbit is $d_{5/2}$. If this assignment is correct the compound state in Pr^{142} produced by neutron capture has a spin of 2 or 3 and even parity. It appears to be established from the β -decay of Pr^{142} that the spin of this nucleus is 2 and its parity odd (13). From this it follows that the ground state γ -ray in Pr^{142} is of the E1 type. This argument supports the assignment of the prominent γ -ray A to the ground state transition (16).

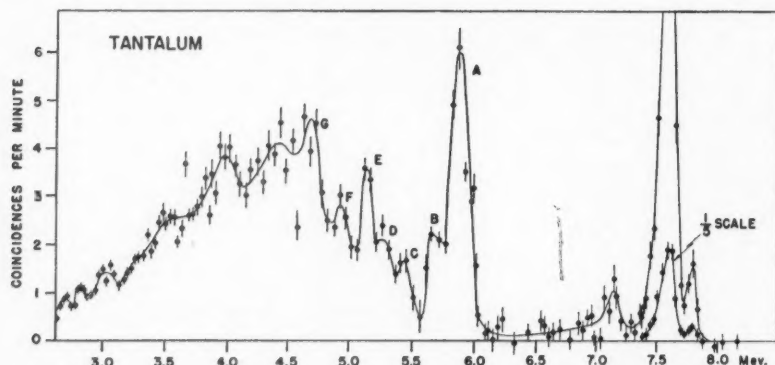


FIG. 22. Coincidence spectrum produced by tantalum. Line width: 140 kev. The peaks above peak A are ascribed to γ -rays from Dural.

TANTALUM

The tantalum sample consisted of a disk of the pure metal, weighing 600 gm., mounted in a Dural container. The spectrum was investigated from 2.5 to 8.0 Mev. with the old apparatus. The coincidence spectrum is shown in Fig. 22. The energies and intensities of the prominent capture γ -rays are given in Table IX. The absolute intensities were determined by the approximate method, assuming a thermal neutron capture cross section of 21.3 barns. The corrected spectrum is shown in Fig. 23.

TABLE IX
ENERGIES AND INTENSITIES OF TANTALUM γ -RAYS

γ -Ray	Energy in Mev.	Estimated intensity in photons per 100 captures
A	6.07 \pm 0.03	0.7
B	5.78 \pm 0.05	0.3
C	5.57 \pm 0.03	0.3
D	5.38 \pm 0.03	0.3
E	5.21 \pm 0.03	0.5
F	5.05 \pm 0.03	0.5
G	4.84 \pm 0.03	1

The large peaks between 7.0 and 8.0 Mev. in Fig. 22 are produced by neutron capture in the Dural of the sample container. There is no clear

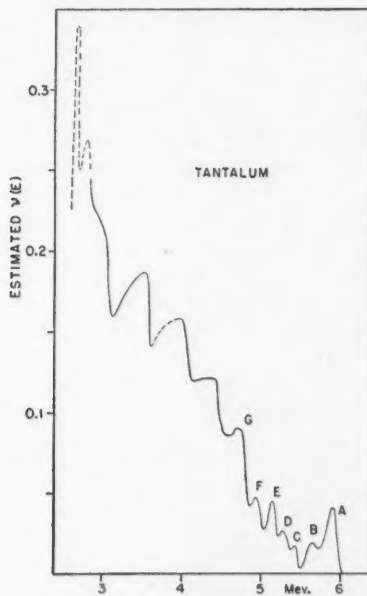


FIG. 23. Corrected γ -ray spectrum of tantalum.

evidence for radiations produced by tantalum above the strong peak *A* at 6.07 ± 0.03 Mev. The binding energy of Ta¹⁸² has been found by Harvey (12) to be 6.03 ± 0.15 Mev. In view of the agreement between this value and the energy of the γ -ray *A* we conclude that γ -ray *A* represents the ground state transition in Ta¹⁸² and that the neutron binding energy of that nucleus is 6.07 Mev. Only one excited state, the isomer at 0.18 Mev., is known in Ta¹⁸². Though the width of peak *A* is larger than that produced by a homogeneous radiation it cannot be concluded from the present data that the γ -ray produced in the transition from the capturing state to the isomeric state contributes appreciably to the counting rate. In the absence of further information on the excited states of Ta¹⁸² it is not possible to identify any of the γ -rays in the spectrum below the γ -ray *A*.

The spin of Ta¹⁸¹ is 7/2 and the shell model assignment (21) for the odd proton in this nucleus is $g_{7/2}$. It follows therefore, that the compound state produced by neutron capture has a spin of 3 or 4 and even parity. The spin of the ground state of Ta¹⁸² has not been measured, nor as yet is it possible to deduce it from its β -decay (8). However, a reasonable guess of the spin and parity can be made on the basis of the shell model. It is plausible to assume that the proton configuration in Ta¹⁸² is the same as that in Ta¹⁸¹, viz. $g_{7/2}$. The neutron configuration is very likely the same as that in W¹⁸³ which has the same number of neutrons. The shell model assignment for this nucleus is $p_{1/2}$ (21). If these assumptions are correct the ground state of Ta¹⁸² has a spin of either 3 or 4 and odd parity. The ground state capture γ -ray in Ta¹⁸² is therefore of the *E1* type regardless of the spin of the capturing state or of the ground state. This deduction is certainly not inconsistent with the high intensity observed for the γ -ray *A* (16).

THALLIUM

The thallium source consisted of about 1 kgm. of the pure oxide (Tl₂O₃) enclosed in a Dural container. The spectrum was investigated with the old apparatus from 2.5 to 10 Mev. The coincidence spectrum is shown in Fig. 24. The strong γ -rays between 7.0 and 8.0 Mev. are produced by neutron capture in the Dural of the sample container. Although the counting rate near 6.7 Mev. is high, there is no clear evidence for γ -radiation produced by thallium beyond the γ -ray *A* at 6.54 ± 0.03 Mev. The energies and intensities of the prominent γ -rays are given in Table X. The absolute intensities were obtained

TABLE X
ENERGIES AND INTENSITIES OF THALLIUM γ -RAYS

γ -Ray	Energy in Mev.	Estimated intensity in photons per 100 captures
<i>A</i>	6.54 ± 0.03	4
<i>B</i>	6.20 ± 0.03	8
<i>C</i>	5.90 ± 0.04	4
<i>D</i>	5.63 ± 0.03	17
<i>E</i>	5.25 ± 0.03	7
<i>F</i>	4.91 ± 0.04	4
<i>G</i>	4.72 ± 0.04	7

by the approximate method, assuming a thermal capture cross section of 3.3 barns. The corrected spectrum is shown in Fig. 25.

There are two stable isotopes of thallium, Tl^{203} (29.5%) and Tl^{205} (70.5%). The greater part, 86%, of the total thermal neutron capture cross section of

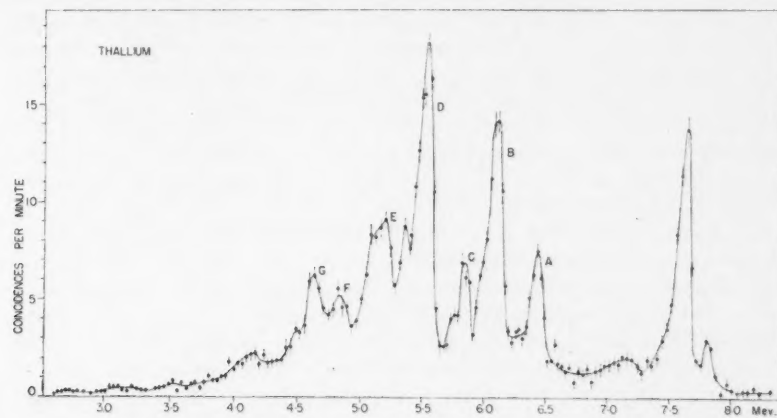


FIG. 24. Coincidence spectrum produced by thallium. Line width: 140 kev. The peaks above peak *A* are ascribed to γ -rays from Dural.

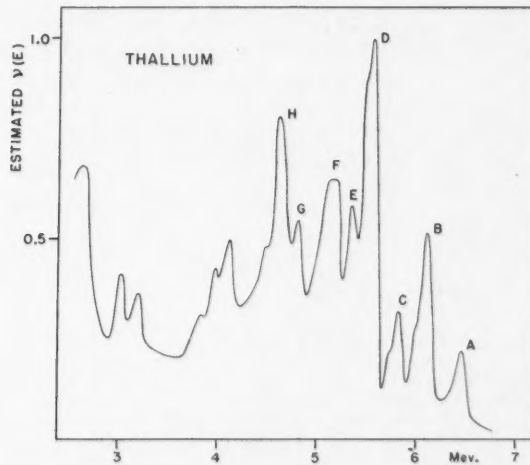


FIG. 25. Corrected γ -ray spectrum of thallium.

thallium is due to Tl^{203} and consequently most of the stronger γ -rays in Fig. 24 are emitted by Tl^{204} . The neutron binding energy of Tl^{204} has been found by Harvey (12) to be 6.52 ± 0.15 Mev. In view of the good agreement between this value and the energy of the γ -ray *A* (6.54 ± 0.03 Mev.) we conclude that

the latter is emitted in the ground state transition of Tl^{204} . For Tl^{206} , Harvey found the neutron binding energy of 6.16 ± 0.15 Mev. This energy is in good agreement with the energy of the γ -ray B , viz. 6.20 ± 0.03 Mev., and on this basis we have previously (18) assigned the γ -ray B to the ground state transition in Tl^{206} . Close inspection of Fig. 24 reveals a slight bulge on the low energy slope of peak B which, if real, could equally well be identified as the ground state γ -ray. Apart from considerations of multipolarity, the ground state transition in Tl^{206} would be expected to be weaker than that in Tl^{204} because of the relatively low capture rate in Tl^{206} . It must be concluded therefore, that though the assignment of the γ -ray A seems reasonable enough, that of the γ -ray B must be considered tentative. Since nothing is known about the excited states of either Tl^{204} or Tl^{206} it is not possible to interpret any of the other γ -rays in the spectrum.

The spin of both Tl^{203} and Tl^{205} is $1/2$ and the shell model assignment (21) for the odd proton in both nuclei is $s_{1/2}$. Therefore in both Tl^{204} and Tl^{206} the compound state produced by neutron capture is even and has a spin of either 0 or 1. The ground state of Tl^{204} is believed (8) to have a spin of 2 and odd parity. The ground state γ -ray, therefore, will be $E1$ if a capturing state of spin 1 is produced and $M2$ for a capturing state of spin 0. The value of $\log ft$ for the β -decay of Tl^{206} is 5.5 (1) and this indicates that the spin of that nucleus is probably 1. According to the shell model its parity can only be odd. It follows, therefore, that the ground state capture γ -ray in Tl^{206} will be of the $E1$ type.

The able assistance of Miss Katherine McLean who drew the figures appearing in this and the following paper is gratefully acknowledged.

REFERENCES

1. ALBURGER, D. E. and FRIEDLANDER, G. Phys. Rev. 82: 977. 1951.
2. BARTHOLOMEW, G. A. and KINSEY, B. B. Phys. Rev. 89: 386. 1953.
3. BARTHOLOMEW, G. A., KINSEY, B. B., and WALKER, W. H. Phys. Rev. 79: 218. 1950.
4. BROCKHOUSE, B. N. Can. J. Phys. 31: 432. 1952.
5. CALDWELL, R. L. Phys. Rev. 78: 407. 1950.
6. ELLIOTT, L. G., PRESTON, M. A., and WOLFSON, J. L. To be published.
7. FAN, C. Y. Phys. Rev. 87: 252. 1952.
8. GOLDHABER, M. and HILL, R. D. Revs. Mod. Phys. 24: 179. 1952.
9. GOLDHABER, M. and SUNYAR, A. W. Phys. Rev. 83: 906. 1951.
10. HAMERMESH, B. Phys. Rev. 80: 415. 1950; 81: 487. 1951.
11. HAMERMESH, B. and HUMMEL, V. Phys. Rev. 88: 916. 1952.
12. HARVEY, J. A. Phys. Rev. 81: 353. 1951.
13. JENSEN, E. N., LASLETT, L. J., and ZAFFARANO, D. J. Phys. Rev. 80: 862. 1950.
14. KINSEY, B. B. and BARTHOLOMEW, G. A. Phys. Rev. 89: 375. 1953.
15. KINSEY, B. B. and BARTHOLOMEW, G. A. Can. J. Phys. 31: 537. 1953.
16. KINSEY, B. B. and BARTHOLOMEW, G. A. Phys. Rev. To be published.
17. KINSEY, B. B., BARTHOLOMEW, G. A., and WALKER, W. H. Can. J. Phys. 29: 1. 1951.
18. KINSEY, B. B., BARTHOLOMEW, G. A., and WALKER, W. H. Phys. Rev. 82: 380. 1951.
19. KINSEY, B. B., BARTHOLOMEW, G. A., and WALKER, W. H. Phys. Rev. 83: 519. 1951.
20. KINSEY, B. B., BARTHOLOMEW, G. A., and WALKER, W. H. Phys. Rev. 85: 1012. 1952.
21. KLINKENBERG, P. F. A. Revs. Mod. Phys. 24: 63. 1952.
22. KUBITSCHKE, H. and DANCOFF, S. M. Phys. Rev. 76: 531. 1949.
23. METROPOLIS, N. and REITWIESNER, G. Table of atomic masses N.P.-1980. 1950.
24. SELOVE, W. Phys. Rev. 84: 869. 1951.
25. SHERK, P. M. and HILL, R. D. Phys. Rev. 83: 1097. 1951.
26. SLÄTIS, H., DU TOIT, S. J., and SIEGBAHN, K. Phys. Rev. 78: 498. 1950.
27. TITTMAN, J. and SHEER, C. Phys. Rev. 83: 746. 1951.

NEUTRON CAPTURE γ -RAYS FROM HEAVY EVEN-CHARGE NUCLEI¹

BY B. B. KINSEY AND G. A. BARTHOLOMEW

ABSTRACT

The neutron capture γ -ray spectra of the elements selenium, strontium, zirconium, molybdenum, cadmium, tin, barium, samarium, gadolinium, wolfram, platinum, and mercury are described. The energies and intensities of the strongest high energy γ -rays are given for each element.

INTRODUCTION

The neutron capture γ -ray spectra described in this paper were investigated under conditions similar to those applying in the study of the odd-charge nuclei discussed in the preceding paper. In the figures representing the corrected γ -ray spectra we have used the procedure adopted in that paper.

We first describe the spectra of the neutron capture γ -rays of selenium, strontium, molybdenum, cadmium, samarium, wolfram, platinum, and mercury, which were measured with the new and more accurate pair spectrometer. In some instances the absolute intensities of the γ -rays were determined by the nickel comparison method; in others, where the untimely breakdown of the N.R.X. reactor prevented such measurements, the intensities were estimated, as described in the preceding paper, from the peak coincidence counting rates and the rate of neutron capture. Finally we present the earlier data obtained with the old instrument; these results are less accurate, and were obtained with lower resolution. The elements studied were zirconium, tin, barium, and gadolinium.

The spectra of some of these elements have been investigated by other methods with less resolution. The spectra of cadmium, wolfram, and mercury were measured by Hamermesh (17) using a D_2O loaded-plate technique and the spectra of cadmium, tin, and barium were measured by Hamermesh and Hummel (18) with the aid of a crystal spectrometer. The maximum γ -ray energies of the spectra of cadmium, samarium, gadolinium, wolfram, and mercury were investigated by Kubitschek and Dancoff (28).

SELENIUM

The selenium sample consisted of about 900 gm. of SeO_2 placed in a Dural container with Bakelite ends. The spectrum was measured from 3.5 to 11 Mev. with a line width of 100 kev. The high energy part of the coincidence spectrum is shown in Figs. 1 and 2, and the low energy part in Fig. 3. The energies and approximate absolute intensities of the γ -rays are given in Table I. The intensity values in Table I were obtained directly from the coincidence counting rates by the method described in the preceding paper. An absolute calibration by the nickel comparison method had not been done

¹ Manuscript received June 3, 1953.
Contribution from Atomic Energy of Canada Limited, Chalk River, Ont. Issued as A.E.C.L. No. 55.

when the reactor stopped working. The corrected γ -ray spectrum is shown in Fig. 4.

Selenium consists of six stable isotopes. The abundances, the contributions of the separate isotopes (44) to the total thermal neutron capture cross section (11.8 ± 0.4 barns, (41)), and the neutron binding energies of the

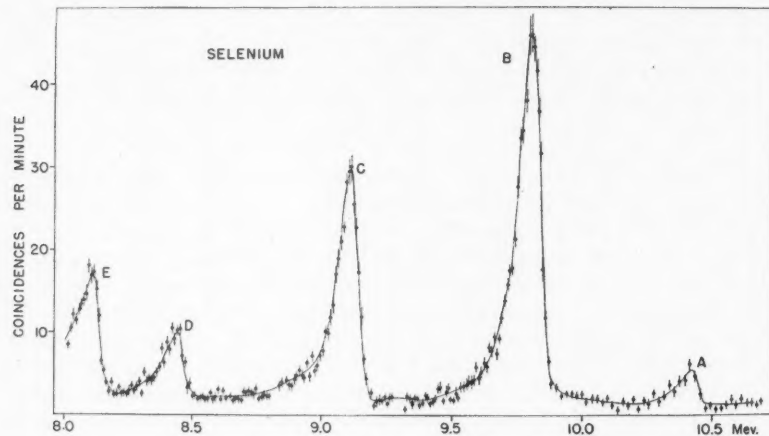


FIG. 1. Coincidence spectrum produced by selenium, 8.0–10.5 Mev. Line width 100 kev.

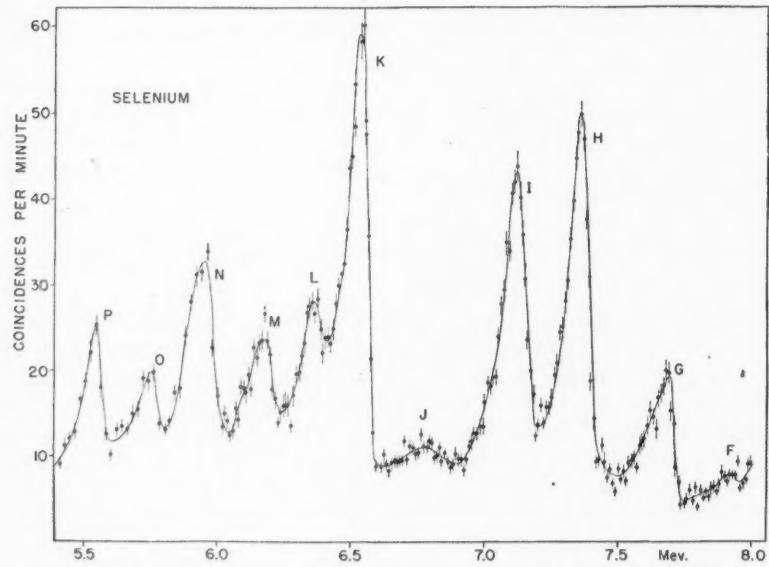


FIG. 2. Coincidence spectrum produced by selenium, 5.5–8.0 Mev. Line width 100 kev.

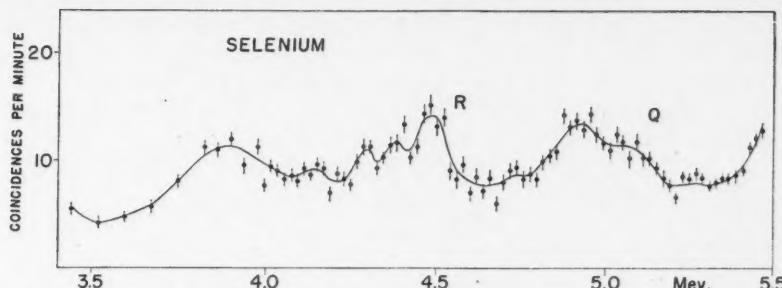


FIG. 3. Coincidence spectrum produced by selenium, 3.5-5.5 Mev. Line width 100 kev.

TABLE I
ENERGIES AND INTENSITIES OF SELENIUM γ -RAYS

γ -Ray	Energy in Mev.	Estimated intensity in photons per 100 captures	Probable origin
A	10.483 ± 0.014	0.08	Se^{78}
B	9.882 ± 0.009	1.0	Se^{78}
C	9.172 ± 0.009	0.7	Se^{78}
D	8.496 ± 0.014	0.2	Se^{78}
E	8.092 ± 0.009	0.5	Se^{78}
F	7.95 ± 0.02	0.1	Se^{78}
G	7.732 ± 0.011	0.7	Se^{78}
H	7.416 ± 0.009	2.2	Se^{77}
I	7.185 ± 0.009	1.8	Se^{77}
J	6.88 ± 0.02	0.3	$\text{Se}^{77} (?)$
K	6.586 ± 0.009	3.6	Se^{77}
L	6.41 ± 0.02	0.9	
M	6.228 ± 0.011	1.2	
N	6.023 ± 0.015	2.3	
O	5.80 ± 0.02	1.4	
P	5.59 ± 0.02	2.1	
Q	5.21 ± 0.03	0.7	
R	4.57 ± 0.03	2.0	

product nuclei are given in Table II. The neutron binding energy has not been determined by the (d,p) process for any of the selenium isotopes, but Sher, Halpern, and Mann (50) have found (γ,n) thresholds at 7.30 ± 0.20 and 9.35 ± 0.20 Mev. using a sample of natural selenium. The latter value probably refers to Se^{80} which is not produced in our experiment. In an earlier publication, Sher, Halpern, and Stephens (51) reported a threshold at 7.5 Mev. which they attributed to Se^{77} . If we assume that the γ -ray A gives the neutron binding energy of Se^{78} (see below), we can evaluate the neutron binding energy of Se^{77} from the mass data of Geschwind, Minden, and Townes (12). The value is 7.34 ± 0.4 Mev. which agrees with the (γ,n) threshold. In the absence of other data we give (in column 5 of Table II) the calculated neutron binding energies obtained from the mass tables of Metropolis and Reitwiesner (34). Harvey (20) has shown that the neutron binding energies calculated from the mass formula for nuclei with neutron numbers near 40 can be from 0.5 to 1 Mev. too low.

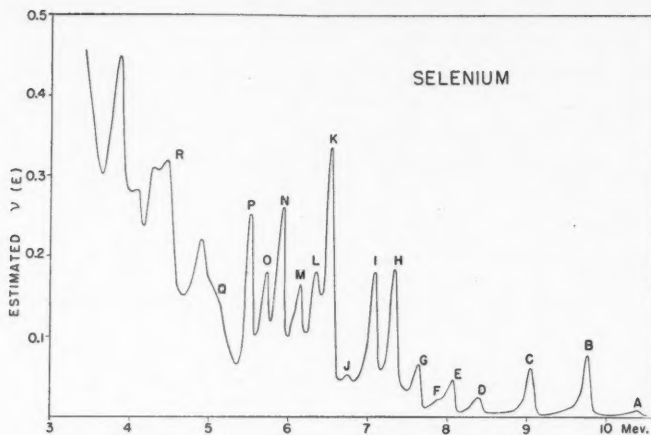
FIG. 4. Corrected γ -ray spectrum of selenium.

TABLE II
ABUNDANCES, CROSS SECTIONS, AND NEUTRON BINDING ENERGIES OF SELENIUM ISOTOPES

Target isotope	Abundance, %	Contribution to cross section, %	Neutron binding energy in product nucleus, Mev.	
			Observed	Calculated
Se ⁷⁴	0.87	3.6		8.2
Se ⁷⁶	9.0	63	7.3 ± 0.2 (?)	7.3
Se ⁷⁷	7.6	26		9.5
Se ⁷⁸	23.5	0.8		6.6
Se ⁸⁰	49.8	2.5		5.9
Se ⁸²	9.2	1.7		5.2

It is clear from an inspection of Table II, column 3, that most of the γ -rays in Figs. 1, 2, and 3 are produced by neutron capture in Se⁷⁶ and Se⁷⁷. The γ -ray of highest energy, *A*, (10.483 ± 0.014 Mev.) is undoubtedly produced by selenium for no γ -ray of this energy is known to be produced by any of the impurities which may be present in the sample. It is very probably caused by the direct transition to the ground state in Se⁷⁸ for its energy exceeds the calculated binding energy of that nucleus by 1.0 Mev., which is within the range predicted from Harvey's data. The parity of the ground state of Se⁷⁷ is probably odd (27) and its spin is 1/2 (10), and therefore the compound nucleus produced by neutron capture will have a spin of either 0 or 1 and odd parity. The ground state γ -ray in Se⁷⁸ will be absolutely forbidden for a capturing state of spin 0 and *E1* for a capturing state of spin 1. The relatively low intensity of the γ -ray *A* indicates that most captures occur in a state of spin 0.

The ground state γ -ray in Se⁷⁷ has an energy near 7.3 Mev. The positions of the excited states of Se⁷⁷ as determined by Canada and Mitchell (9) from

the decay of Br^{77} suggest that this transition is to be identified with the γ -ray H , and that the γ -rays I and K , and possibly J , are also derived from that nucleus.* The energies of these states according to these authors, and the differences between the energies of the capture γ -rays and that of the γ -ray H , are compared in Table III. The errors of the differences include only the statistical errors of counting.

TABLE III
EXCITED STATES OF Se^{77}

Energy of excited state, Mev.	Energy difference between γ -rays, Mev.
0.160 ± 0.001 (Isomeric state)	
0.237 ± 0.002	$H - I \quad 0.231 \pm 0.011$
0.520 ± 0.002	$H - J \quad 0.54 \pm 0.02$
0.813 ± 0.005	$H - K \quad 0.830 \pm 0.010$

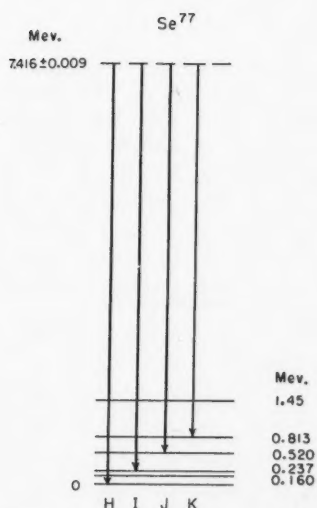


FIG. 5. Tentative decay scheme for the capture γ -rays from Se^{77} . The level energies on the right are the results of other authors (see text).

* Part of the counting rate in peak J , or possibly all of it, is caused by the ghost peak associated with peak K .

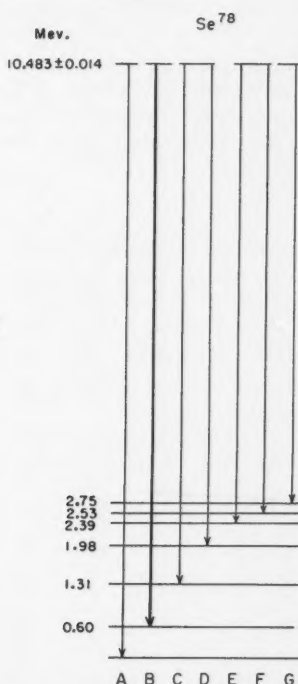


FIG. 6. Tentative decay scheme for the capture γ -rays from Se^{78} . The level energies on the left are obtained from the γ -ray measurements.

The agreement between the β -ray measurements and the energy differences for the γ -rays is good, and makes it very probable that the γ -ray H is indeed the ground state γ -ray in Se^{77} . A tentative decay scheme for Se^{77} is shown in Fig. 5. No γ -ray is observed corresponding to a transition to the 160 kev. isomeric state (1, 31) nor is its detection to be expected for such a transition should be highly forbidden. There is also no evidence for the existence of a γ -ray corresponding to the excited state at 1.45 Mev. found by Gideon, Miller, and Waldman (13).

Assuming then, that the γ -ray H is the ground state γ -ray in Se^{77} , it follows that all the γ -rays with higher energy are caused by Se^{75} or Se^{78} . Since the cross section of Se^{77} is some seven times greater than that of Se^{74} it is probable that most of these γ -rays are emitted by Se^{78} . The strong γ -ray B would appear to correspond to a transition to an excited state of Se^{78} at 600 kev. A possible decay scheme in which all of the γ -rays are assumed to be emitted by Se^{78} is shown in Fig. 6. There is no agreement between any of the levels in this figure and the excited states of Se^{78} indicated by the decay of As^{78} and Br^{78} . However, the positions of these states are not well known. In the decay of As^{78} , β -transitions of energy 1.4 and 4.1 Mev. were observed by Steinberg and Engelkemeir (53), and a γ -ray of 0.27 Mev. was detected by Sagane, Kojima, Miyamoto, and Ikawa (48). Two γ -rays with energies of 0.046 and 0.108 Mev. have been observed by Valley and McCreary (57) in the decay of Br^{78} .

STRONTIUM

The strontium sample consisted of about 800 gm. of SrCO_3 enclosed in a Dural container with Bakelite ends. In a preliminary experiment with the old apparatus, the spectrum was measured from 2.5 to 12 Mev. The counting rate was found to be negligible above 9.3 Mev. and therefore in the more detailed investigation with the improved spectrometer, measurements were limited to energies between 2.5 and 9.5 Mev. The high energy end of the coincidence spectrum obtained with the improved apparatus is shown in Figs. 7 and 8, and the low energy region in Fig. 9. The resolution was set at 100 kev. above 5.75 Mev. and 140 kev. below that energy. The energies and

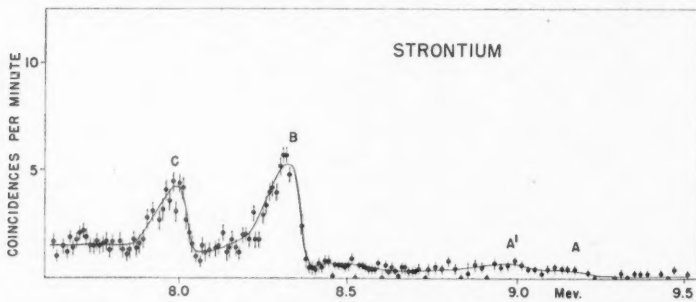


FIG. 7. Coincidence spectrum produced by strontium 7.6–9.5 Mev. Line width 100 kev.

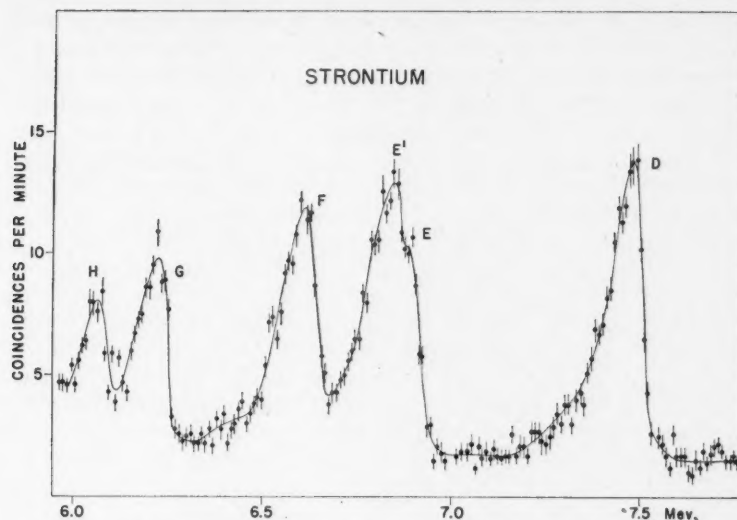


FIG. 8. Coincidence spectrum produced by strontium 6.0-7.6 Mev. Line width 100 kev.

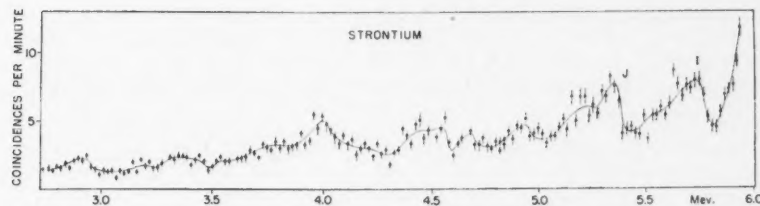


FIG. 9. Coincidence spectrum produced by strontium 2.7-6.0 Mev. Line width 140 kev.

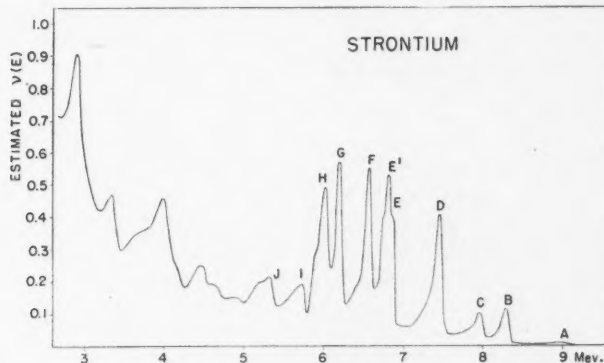


FIG. 10. Corrected γ -ray spectrum of strontium.

intensities of the prominent γ -rays are given in Table IV. No direct measurement of the absolute intensities has been made and the third column of this table contains the intensities estimated by the approximate method. The corrected spectrum is shown in Fig. 10.

TABLE IV
ENERGIES AND INTENSITIES OF STRONTIUM γ -RAYS

γ -Ray	Energy in Mev.	Estimated intensity in photons per 100 captures	Probable origin
A ?	9.22 \pm 0.06	0.06	Sr ⁸⁸
A' ?	9.06 \pm 0.04	0.1	Sr ⁸⁸
B	8.376 \pm 0.011	1.3	Sr ⁸⁸
C	8.045 \pm 0.014	1.1	Sr ⁸⁷
D	7.530 \pm 0.011	5	Sr ⁸⁷
E	6.95 \pm 0.02	5	
E'	6.87 \pm 0.02	6	
F	6.671 \pm 0.010	6	
G	6.268 \pm 0.012	5	
H	6.10 \pm 0.02	4	
I	5.82 \pm 0.02	2	
J	5.43 \pm 0.03	2	

Strontium consists of four stable isotopes. The abundances, the contributions to the thermal neutron capture cross section, and the neutron binding energies in the product nuclei are listed in Table V.

TABLE V
ABUNDANCES, CROSS SECTIONS, AND NEUTRON BINDING ENERGIES OF STRONTIUM ISOTOPES

Target isotope	Abundance, %	Contribution to total cross section, barns	Neutron binding energy of product nucleus, Mev.
Sr ⁸⁴	0.55		8.9 ^a
Sr ⁸⁶	9.8	0.13 ^b	8.46 \pm 0.2 ^c
Sr ⁸⁷	7.0		11.15 \pm 0.2 ^d
Sr ⁸⁸	82.7	0.004 ^e	6.55 \pm 0.2 ^f

^a Calculated binding energy plus 1 Mev. for neutron shell correction (see Reference 20).

^b Cross sections to form the 0.39 Mev. isomer of Sr⁸⁷.

^c Mean value; see References 20 and 50.

^d See Reference 50.

^e See Reference 49.

^f See Reference 20.

The contributions to the total capture cross section of 1.16 ± 0.06 barns (41) have been measured by activation methods (49) only for Sr⁸⁸ and for the production of the 0.390 Mev. isomer of Sr⁸⁷. It is probable that the cross section for the production of the ground state of Sr⁸⁷ will be smaller than that for the isomer, for following capture, four units of angular momentum must be radiated to produce the ground state while only one unit is required for the production of the isomeric state. (This rule holds for Rh¹⁰⁴ and Ag¹¹⁰ where the capture cross section for the production of the high spin isomer is respectively 10% and 2.5% of the cross section for the production of the low spin

ground state.) If this conclusion is valid, the large remainder of the total cross section must be due to Sr⁸⁷.

There is some evidence for a coincidence peak at *A* in Fig. 7. This peak is broad and may be due to two γ -rays at 9.22 and at 9.06 Mev. If these γ -rays exist, they are clearly caused by the excitation of Sr⁸⁸, for their energy is higher than the neutron binding energy of the other strontium isotopes (see Table V). The ground state γ -ray in this nucleus, which should have an energy near 11 Mev., was not detected in the earlier investigation and was not looked for with the newer apparatus. Its intensity is certainly less than 0.05 photons per 100 captures. This is to be expected for the ground state of Sr⁸⁷ probably has even parity (27) and its spin is 9/2; the ground state γ -ray of Sr⁸⁸ therefore must be *E4* or *M5*, and is highly forbidden. The γ -ray *B* (8.38 Mev.) has an energy very close to the neutron binding energy of Sr⁸⁷. However the ground state γ -ray in this nucleus is also of even type, and must be *E4*. It seems most improbable that a transition of such a high order would produce a γ -ray as strong as *B*, and we conclude that the coincidence peak at *B* is due to a γ -ray in Sr⁸⁸. In fact, its energy, as will be shown below, is close to that of the transition to the second excited state in that nucleus. The peak *B*, however, is about 20% broader than is to be expected of a homogeneous γ -ray and it is probable that more than one γ -ray contributes to it.

Two excited states are known in Sr⁸⁸ from studies of the decay of Rb⁸⁸ and Y⁸⁸. Bunker, Langer, and Moffat (8), using Rb⁸⁸, found that the energy of the first level was 1.86 Mev. in agreement with 1.853 Mev. found by Peacock and Jones (42) from the decay of Y⁸⁸. Measurements by the latter authors and by Metzger and Amacher (35) of the conversion coefficient of the γ -ray produced by this state are consistent with even parity for this state and a spin of one unit. For the second excited state, Bunker *et al.* obtained an energy of 2.8 Mev.; the value obtained by Peacock and Jones was 2.76 Mev. This second excited state probably has a spin of two units and odd parity, for this assignment is consistent with the value of the conversion coefficient of the γ -ray produced in a transition between the second and the first excited states (35, 42), with the presence of the relatively strong crossover γ -ray (2.76 Mev.) (42), and with the angular correlation of the successive γ -rays (6).

The γ -ray at *A*, if it exists, has an energy in rough agreement with the transition to the first excited state of Sr⁸⁸, for the energy of *A* plus 1.86 Mev. is 11.08 ± 0.06 Mev. The γ -ray *B* (8.376 Mev.) has an energy in agreement with that of the transition to the second excited state (in this case, *B* plus 2.76 Mev. is 11.14 ± 0.02 Mev.). The γ -ray *A* would then be *M3* or *E4* depending on the spin of the compound nucleus, and the γ -ray *B*, *M2* or *E3*.* This assignment, however, must be regarded as tentative, for it is not certain that the low coincidence peak at *A* is real, and, although the energy difference

* Note added in proof: Recently the angular correlation of the 0.90 Mev. and 1.86 Mev. γ -rays has been reinvestigated by R. M. Steffen, Phys. Rev. 90:321, 1953. It would appear from these results that the first excited state has a spin of 2 and even parity and the second state has a spin of 3 and odd parity whence the γ -ray *A* is *E2* or *M3* and the γ -ray *B* is *E1* or *M2* depending on the spin of the capturing state.

between *A* and *B* is in satisfactory agreement with the known energy difference between the two excited states of Sr⁸⁸, there is no independent evidence to show that the γ -ray *B* is, in fact, the transition to the second excited state. The abnormal width of the peak *B*, moreover, presents difficulties: a part of it could represent a transition to another state lying just above that at 2.76 Mev., and which is not excited in the β -decay; it could represent a transition to the ground state from a highly excited state in Sr⁸⁸ excited in its turn by a transition of low multipole order; or it could represent some γ -ray leading to a hitherto unknown low lying state in Sr⁸⁷, or to a state in Sr⁸⁶, for the contribution of Sr⁸⁴ to the total capture cross section of strontium is unknown.

The γ -rays *C* and *D* probably correspond to transitions to the first two excited states of Sr⁸⁷, both of which are produced in the decay of Y⁸⁷. As shown by Mann and Axel (30), these states are at 390 kev. and 875 kev. and their shell assignments are $p_{1/2}$ and $p_{3/2}$ respectively. The energy difference between the levels is 485 ± 3 kev. This is in rather poor agreement with the energy difference between the γ -rays *C* and *D*, viz., 0.515 ± 0.015 Mev. If 390 kev. is added to the energy of the γ -ray *C*, the value 8.435 ± 0.014 Mev. is obtained, in agreement with the neutron binding energy of Sr⁸⁷ (Table V). If *C* and *D* are thus identified, the small cross section contributed by Sr⁸⁶ makes them relatively more intense than any others in the spectrum of Sr⁸⁷. However, the discrepancy associated with the difference between their energies is large and difficult to explain, unless it is assumed that at least some part of the counting rates in the peaks *C* and *D* are due to radiations from Sr⁸⁸. The widths of these peaks, however, are normal. The high energy continuum above peak *D* breaks away from the linear edge of that peak at an unusually high value of the counting rate (Fig. 8); the statistics of counting however are too poor to establish the presence of a weak γ -ray in this position.

MOLYBDENUM

The molybdenum sample consisted of about 1 kgm. of molybdenum carbide, MoC, enclosed in a Dural cylinder with Bakelite ends. The coincidence spectrum was measured from 2.7 to 9.7 Mev. with a line width of 100 kev. The shape of the lower energy part of the spectrum is shown in Fig. 11. The coincidence counting rate was measured at points 20 kev. apart, only a few

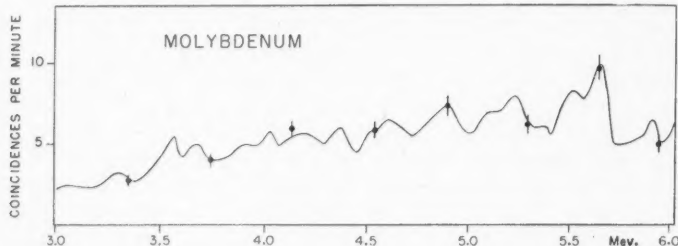


FIG. 11. Coincidence spectrum produced by molybdenum 3.0–6.0 Mev. Line width 100 kev. Only occasional experimental points are shown to indicate statistical accuracy.

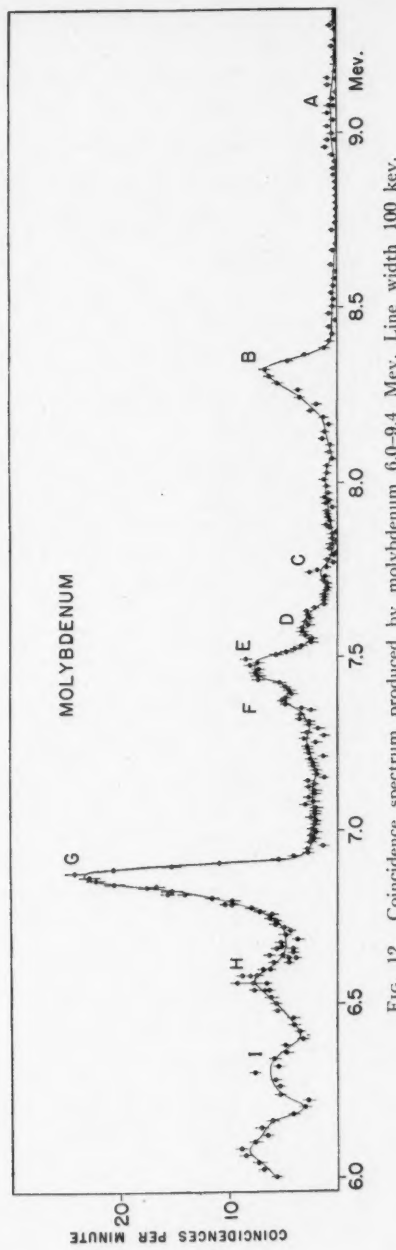


FIG. 12. Coincidence spectrum produced by molybdenum 6.0-9.4 Mev. Line width 100 kev.

of which are shown to indicate the statistical accuracy. The upper end of the spectrum is shown in detail in Fig. 12.

The energies and intensities of the γ -rays are listed in Table VI. The in-

TABLE VI
ENERGIES AND INTENSITIES OF MOLYBDENUM γ -RAYS

γ -Ray	Energy in Mev.	Estimated intensity in photons per 100 captures	Probable origin
A	9.15 \pm 0.05	0.03	Mo ⁹⁶
B	8.392 \pm 0.010	0.5	Mo ⁹⁶
C	7.79 \pm 0.03	0.1	
D	7.66 \pm 0.02	0.2	
E	7.54 \pm 0.02	0.7	Mo ⁹⁶
F	7.40 \pm 0.04	0.3	
G	6.916 \pm 0.010	3.1	Mo ⁹⁶
H	6.66 \pm 0.06	1.1	
I	6.39 \pm 0.03	0.7	

tensities were measured by comparing the peak G with that produced by the 7.64 Mev. iron γ -ray (26) from a mixture of iron and molybdenum carbides. The neutron absorption cross sections of both iron and molybdenum were assumed to be 2.4 barns. The corrected γ -ray spectrum is shown in Fig. 13.

The abundances, the cross section contributions, and the neutron binding energies of the product nuclei for the molybdenum isotopes are collected in Table VII. In the fourth column we list the measured neutron binding

TABLE VII
ABUNDANCES, CROSS SECTIONS, AND NEUTRON BINDING ENERGIES OF MOLYBDENUM ISOTOPES

Target isotope	Abundance, %	Contribution to cross section, %	Neutron binding energy in product nucleus, Mev.	
			Observed	Calculated ^a
Mo ⁹²	15.7	0.04 ^b	8.31 \pm 0.2 ^c	8.4
Mo ⁹⁴	9.3		7.95 \pm 0.25(?) ^e	7.8
Mo ⁹⁵	15.7	80 ^d		9.7
Mo ⁹⁶	16.5	7.5 ^d	7.1 \pm 0.3 ^f	7.2
Mo ⁹⁷	9.5	7.5 ^d	6.75 \pm 0.25(?) ^e	9.0
Mo ⁹⁸	23.9	3.4 ^d		6.6
Mo ¹⁰⁰	9.5	2 ^d		6.0

^a See Reference 34.

^b See Reference 49.

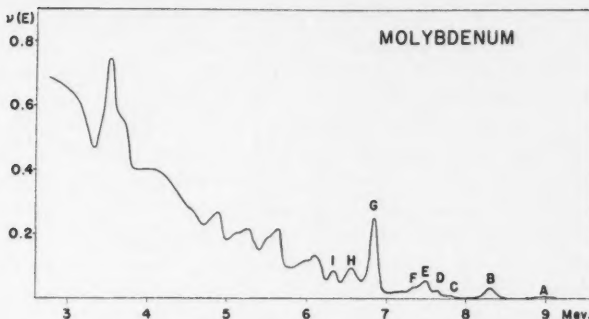
^c See Reference 20.

^d See Reference 44.

^e See Reference 44.

^f See Reference 19.

energies. The values for Mo⁹⁴ and Mo⁹⁶ are obtained from observed (γ, n) thresholds (19, 50) and the identification of the isotopes responsible is not certain. In the fifth column we list the neutron binding energies calculated from the tables of Metropolis and Reitwiesner (34).

FIG. 13. Corrected γ -ray spectrum of molybdenum.

It will be seen from Table VII that some 80% of the neutron capture cross section of natural molybdenum is due to capture by Mo⁹⁵. The greater part of the γ -ray spectrum, and the most intense γ -rays, therefore, are probably due to Mo⁹⁶. The cross section of the closed shell nucleus, Mo⁹², is very small and makes no appreciable contribution to the total cross section. The cross section of Mo⁹⁴ is not quoted by Pomerance (44) and, presumably, is also small. That part, therefore, of the γ -ray spectrum not produced by capture in Mo⁹⁵ is due, in the main, to capture by Mo⁹⁶ and Mo⁹⁷, with smaller contributions from Mo⁹⁸ and Mo¹⁰⁰.

There is some evidence in Fig. 12 for the existence of a γ -ray *A* near 9 Mev. A coincidence peak in this position was confirmed in subsequent measurements. From Table VII it is not clear whether this γ -ray is due to the excitation of Mo⁹⁶ or Mo⁹⁸. However, the greater part of the γ -ray spectrum is caused by Mo⁹⁶ and if *A* is assumed to be the ground state γ -ray in that nucleus, then it is also possible to ascribe some other γ -rays in the capture spectrum to the same nucleus. The positions of some of the excited states of Mo⁹⁶ have been determined (5, 32) from the decay of Tc⁹⁶ and of (45) Nb⁹⁶. If the energy of the first excited state (770 ± 2 kev.) is subtracted from that of *A*, we obtain 8.38 Mev., which is in very good agreement with the energy of the γ -ray *B*. Similarly, subtracting the energy (1610 ± 4 kev.) of the second excited state from that of *A* we obtain 7.54 Mev. in agreement with that of the γ -ray *E*. This suggests very strongly that the γ -ray *A* is indeed the ground state γ -ray in Mo⁹⁶. Its weakness is to be expected, for the spin of Mo⁹⁶ is $5/2$ ($d_{5/2}$ orbit, (27)), and therefore the γ -ray *A* is *E2* or *M3* according to the spin of the compound state. A tentative decay scheme for Mo⁹⁶ is shown in Fig. 14 in which the energies of the excited states observed in the decay of Tc⁹⁶ and Nb⁹⁶ (45) are shown on the right. A different level arrangement has been suggested by Easterday and Medicus (11) but their scheme does not agree as well with our results.

On account of its intensity, the peak *G*, which is of normal width (100 kev.), may also be ascribed to Mo⁹⁶. It probably represents a transition to a state not excited in the decay of Nb⁹⁶ and Tc⁹⁶. The position of this state can best

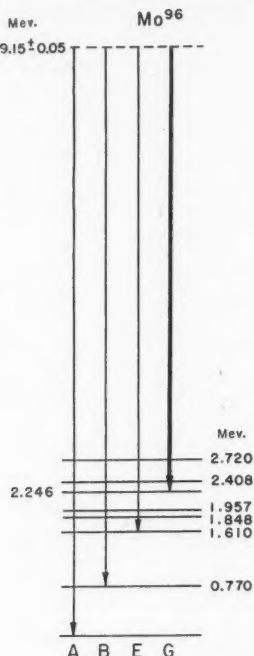


FIG. 14. Tentative decay scheme for the capture γ -rays from Mo⁹⁶. The level energies on the left are obtained from the γ -ray measurements, those on the right from the results of other authors (see text).

be obtained by adding the difference between the energies of the γ -rays *B* and *G*, 1.476 ± 0.010 Mev., to 770 kev. This is 2.246 ± 0.010 Mev. If the γ -ray *G* is of *E1* type, as is probable, this state must be odd, and the spin must lie between one and four units. This state therefore would not be excited directly by electron capture in Tc⁹⁶ or its isomeric state (11, 14). If it is assumed that the first excited state in Mo⁹⁶ is even with spin 2 and the second state is even with spin 3 or 4 (11, 14) then the γ -ray *B* is *M1* and the γ -ray *E* is *M1* or *E2*.

The γ -rays at *C*, *D*, and *F* are only partially resolved and cannot be accounted for by the term scheme constructed for the decay of Tc⁹⁶; if not produced by Mo⁹⁶, they must be derived from Mo⁹⁸. The ground state γ -ray in this nucleus does not appear if its energy is near the calculated value, 9.0 Mev. (see Table VII). This is not surprising for the cross section due to Mo⁹⁷ is only 10% of that due to Mo⁹⁸, and the multipole order of this γ -ray should be *E2* like that of the ground state γ -ray in Mo⁹⁶.

Below the γ -ray *G*, there are a few peaks which stand out above the continuous background of unresolved radiations. It is not possible to identify any of the γ -rays which must be emitted by Mo⁹⁹ and Mo¹⁰¹.

CADMIUM

It is well known that by far the greater part of the thermal neutron capture cross section in cadmium is due to the isotope Cd¹¹³. The capture γ -rays, therefore, are derived from the even-even isotope Cd¹¹⁴. Preliminary measurements were made in 1949 and more recent work has also been reported (2). Some of our older results have been used for comparison purposes by Pringle, Taylor, and Roulston (47), who have measured the cadmium γ -rays with the aid of a single crystal scintillation spectrometer. A number of authors (17, 18, 28, 36, 37, 59) have studied the energy distribution of the cadmium capture γ -ray spectrum and some of the low energy γ -rays have been measured by Thornton *et al.* (54), by Hibdon and Muehlhause (22), and by Motz (38).

The high energy coincidence spectrum obtained using a sample consisting of a sheet of cadmium mounted in a Dural cylinder with Bakelite ends is shown in Figs. 15 and 16. No γ -rays were observed with energies above that of the γ -ray *A* at 9.046 ± 0.008 Mev., a result which is in general agreement with the results of other authors. The residual coincidence rate near 9.2 Mev. and between peaks *A* and *B* is probably produced by unwanted coincidence from the annihilation and bremsstrahlung radiations discussed in the preceding paper. The spectrum near 7.6 Mev. is obviously complex. The

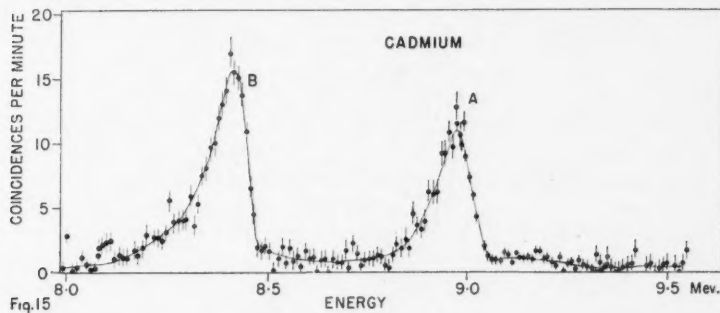


Fig. 15

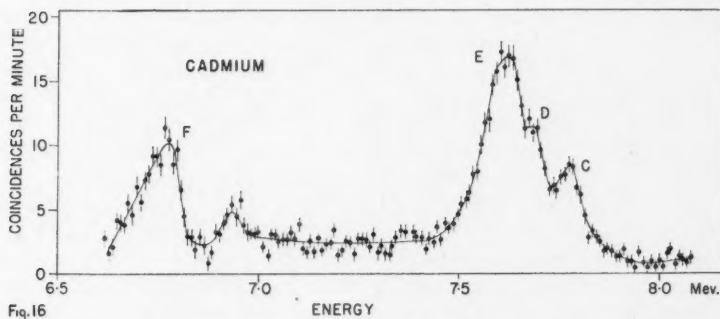


FIG. 15. Coincidence spectrum produced by cadmium 8.0-9.5 Mev. Line width 100 kev.
FIG. 16. Coincidence spectrum produced by cadmium 6.6-8.0 Mev. Line width 100 kev.

simplest interpretation of the curve is that it is composed of the peaks produced by three γ -rays, *C*, *D*, and *E*.

The preliminary measurements showed that below 6.6 Mev. the capture γ -ray spectrum cannot be resolved with the present instrument, and, though coincidence peaks are found to be superposed on the unresolved background, many of these peaks have widths greater than expected for homogeneous γ -rays. For this reason, in the present experiment, no attempt was made to study the spectrum in this region in detail and only the general intensity distribution was investigated between 2.75 and 6.6 Mev. The measurements in this energy region were made with a line width of 140 kev. The results are shown in Fig. 17 where the peak *F* is included for continuity.

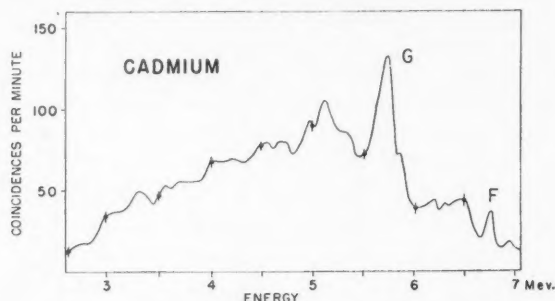


FIG. 17. Coincidence spectrum produced by cadmium 2.5-7.0 Mev. The line width is 140 kev. below 6.6 Mev. and 100 kev. above that energy.

The energies and intensities of the measurable γ -rays are given in Table VIII. The very strong γ -ray *G*, superposed on the continuous region of the spectrum below 6.6 Mev., is included in this list although it is probably complex. The absolute intensities were obtained by comparing the counting

TABLE VIII
ENERGIES AND INTENSITIES OF CADMIUM γ -RAYS

γ -Ray	Energy in Mev.	Intensity in photons per 100 captures
<i>A</i>	9.046 ± 0.008	0.14
<i>B</i>	8.483 ± 0.008	0.23
<i>C</i>	7.841 ± 0.014	0.12
<i>D</i>	7.726 ± 0.010	0.16
<i>E</i>	7.665 ± 0.010	0.21
<i>F</i>	6.820 ± 0.013	0.36
<i>G</i>	5.94 ± 0.01	2.2

rate of the 8.48 Mev. γ -ray *B* with that of the 7.64 Mev. γ -ray (26) of iron, in a sample consisting of an intimate mixture of weighed amounts of finely powdered Fe_2O_3 and CdO . The iron and cadmium cross sections were assumed to be 2.4 and 3500 barns (43) respectively. The latter value is an average over the spectrum of slow neutrons emitted by the pile and is more appropriate

for the present comparison than the lower cross section (2400 barns, see Reference 41) determined for neutrons of 2200 meters per second. The iron γ -ray was selected because the 9.0 Mev. nickel capture γ -ray which is normally used for comparison would be superposed on the γ -ray *A* produced by cadmium. The corrected γ -ray spectrum is shown in Fig. 18.

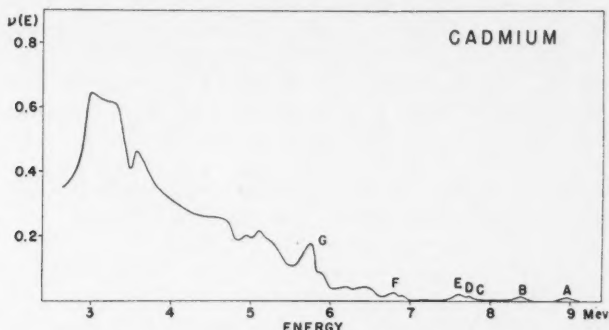


FIG. 18. Corrected γ -ray spectrum of cadmium.

Excited states in Cd^{114} have been observed (3, 33) at 0.55 Mev. and at 1.27 Mev. in a study of the disintegration of In^{114} . The energies of these states have recently been measured with great accuracy by Johns, Cox, Donnelly, and McMullen (25) who obtain the values: 0.556 ± 0.001 and 1.278 ± 0.002 Mev. These authors also found evidence for a third level at 1.856 ± 0.004 Mev. A γ -ray of 0.555 ± 0.005 Mev. was observed in the neutron capture γ -ray spectrum by Thornton *et al.* (54) and by Motz (38) and the internal conversion electrons corresponding to a γ -ray of 0.5619 Mev. were observed by Hibdon and Muehlhause (22). There is little doubt that the capture radiation studied in these experiments was emitted in the de-excitation of the first excited state in Cd^{114} . Hibdon and Muehlhause also observed conversion electrons corresponding to a γ -ray of 97 kev. It is probable that this radiation is emitted in a transition between low lying excited states, for as these authors point out, internal conversion is not likely to compete favorably with γ -emission in the decay of high energy excited states.

An unambiguous interpretation of the capture γ -rays measured in the present investigation seems possible only in the cases of the γ -rays *A* and *B*. The γ -ray *A* is certainly the ground state γ -ray, for its energy is in agreement with that deduced from mass measurements (16), viz., 8.95 ± 0.11 Mev. The difference between the energies of the γ -rays *A* and *B* is 0.563 ± 0.008 Mev. which is in good agreement with the known energy of the first excited state in Cd^{114} . The γ -ray *B*, therefore, represents the transition to the first excited state. Since the thermal capture in cadmium produces a compound state of unit spin and even parity, both γ -rays *A* and *B* are *M1*.

The interpretation of the γ -rays *C*, *D*, and *E* is more difficult for none of them corresponds to the transition to the excited state at 1.278 Mev. Such

a transition would have an energy of 7.768 Mev. and its coincidence peak would fall just in the valley between peaks *C* and *D* in Fig. 16. It is not improbable that a γ -ray of this energy is emitted for if its intensity were several times less than that of the γ -rays *C* and *D*, it might not be detected in the presence of the complex peak. If the γ -rays *C*, *D*, and *E* were emitted by the capturing state, they would produce excited states at 1.205 ± 0.014 , 1.320 ± 0.011 , and 1.381 ± 0.011 Mev. The existence of a state at 1.381 Mev. would appear to account for the 97 kev. transition observed by Hibdon and Muehlhause, for the energy of the transition between this state and that at 1.278 Mev. is 0.103 ± 0.011 Mev. It is curious that no excited states at 1.205, 1.320, and 1.381 Mev. have been observed in the decay of In¹¹⁴. An alternative explanation which might account for the γ -rays *C*, *D*, and *E* is that they may be emitted in transitions from high energy excited states to the ground state. A similar difficulty is encountered in the interpretation of the γ -rays *F* and *G*.

No γ -ray was found corresponding to a transition from the capturing state to the state at 1.856 Mev. found by Johns and co-workers. Such a γ -ray would have an energy of 7.190 Mev. and, if it is present, its intensity must be less than 0.02 photon per 100 captures. There is evidence in Fig. 16 for a weak

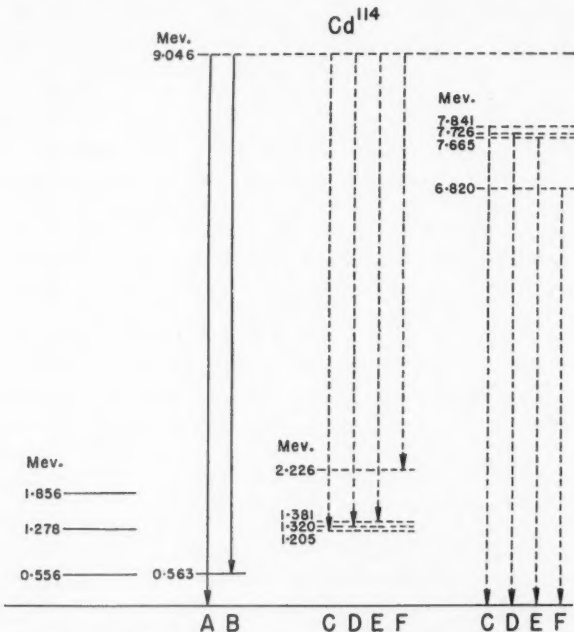


FIG. 19. Decay scheme for Cd^{114} . The level energies on the extreme left are those of other authors (see text), those in the remainder of the diagram are obtained from the γ -ray measurements. Alternative interpretations of the γ -rays *C*, *D*, *E*, and *F* are shown.

peak at 7.0 Mev. but the energy discrepancy, about 200 kev., is too large for this to be associated with the transition in question. The available information concerning the Cd¹¹⁴ levels and the possible interpretations of the high energy γ -rays are summarized in Fig. 19.

SAMARIUM

The samarium sample consisted of two small Bakelite capsules each containing 0.75 gm. of Sm₂O₃ mixed with Glyptal cement, and spread over an area of about 25 sq. cm. The Bakelite capsules were centrally mounted in a Dural cylinder with Bakelite ends. The samarium spectrum was studied with both the new and the old apparatus. In the experiments with the old apparatus the nickel comparison measurement was made at the same time. For this purpose, nickel sheets (0.111 gm. per sq. cm.) were placed on both sides of each capsule. This method of intensity calibration is unsatisfactory in that the nickel foils do not emit a radiation strictly proportional to the average neutron flux to which the samarium samples are exposed, for, on account of the very high thermal capture cross section of this element, the samples capture about half of the neutrons incident on them. The results obtained, however, are in good agreement with the intensity estimated by the approximate method described in the preceding paper. The cross section for samarium was assumed to be 10,600 barns (43). This cross section is an average over the

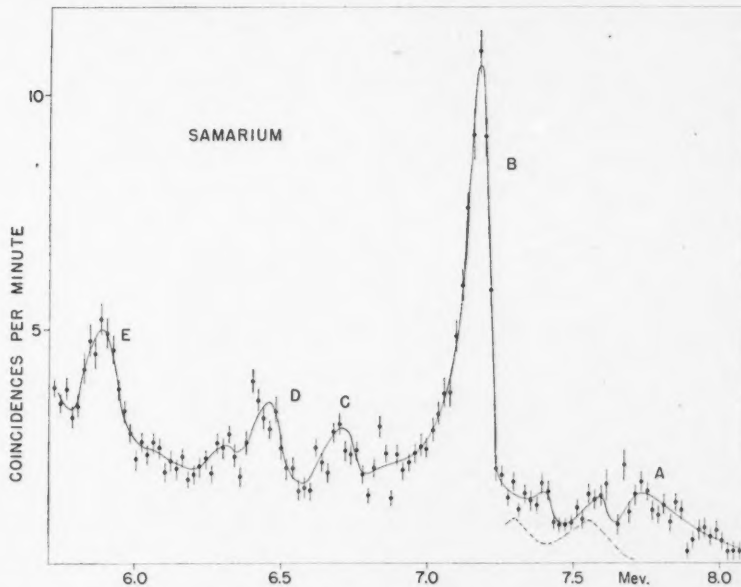


FIG. 20. Coincidence spectrum produced by samarium 5.7-8 Mev. Line width 100 kev. The estimated contributions from lead and aluminum background radiations are shown by the broken curve near 7.5 Mev.

spectrum of the slow neutrons emitted by the pile, and is more appropriate for the present comparison than the lower value (6500 barns, see Reference 41) determined for neutrons of 2200 meters per second. The spectrum was measured from 2.5 to 9.0 Mev. In the region between 7.4 and 9.0 Mev. no coincidence peaks were observed which could not be attributed to nickel. In later measurements made with the new apparatus, the nickel sheets were omitted and the spectrum was measured between 5.7 and 8.0 Mev. with the results shown in Fig. 20. The part of the spectrum below 5.7 Mev. was not remeasured with the new apparatus. It consists of a continuum on which few peaks can be discerned. The full corrected γ -ray spectrum is shown in Fig. 21. The energies and intensities of the high energy γ -rays are given in Table IX.

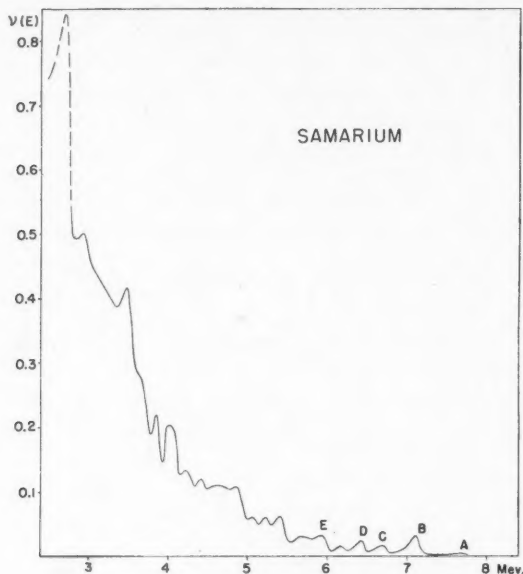


FIG. 21. Corrected γ -ray spectrum of samarium.

TABLE IX
ENERGIES AND INTENSITIES OF SAMARIUM γ -RAYS

γ -Ray	Energy in Mev.	Intensity in photons per 100 captures
A	7.89 ± 0.06	0.03
B	7.24 ± 0.02	0.3
C	6.79 ± 0.03	0.04
D	6.54 ± 0.03	0.06
E	5.99 ± 0.03	0.07

Almost all of the thermal neutron capture cross section of samarium is caused by Sm^{149} and therefore the γ -rays in Fig. 20 are emitted by Sm^{160} .

Kubitschek and Dancoff (28) obtained 6.6 ± 0.3 Mev. for the neutron binding energy of Sm^{150} . The value calculated from the tables of Metropolis and Reitwiesner (34) is 8.1 Mev. and the scant information (20) on neutron binding energies in this region (88 neutrons) suggests that this value is probably correct to within 400 kev.

Since the counting rates above 7.4 Mev. were extremely low, the shape of the spectrum above the peak *B* was difficult to determine. The contributions of the lead and aluminum background radiations are shown by the dotted lines in Fig. 20. It is probable that part of the counting rate at *A* is genuine; if this is true, the present results show that the neutron binding energy of Sm^{150} is not less than 7.89 ± 0.06 Mev. It is most improbable that the γ -ray *A*, if it exists, is emitted in the ground state transition of Sm^{150} since this radiation is expected to be highly forbidden. The spin *J* of Sm^{149} is either (4, 39) $5/2$ or $7/2$ and it has been shown by Brockhouse (7) that the spin of the samarium resonance responsible for thermal capture is $J + 1/2$. The spin of the capturing state is therefore three or four units, and the ground state transition should be highly forbidden.

In the absence of a good value for the neutron binding energy and of any data on the positions of the excited states of Sm^{150} , it is not possible to interpret any of the capture γ -rays shown in Fig. 20. However, it is obvious from the complexity of the spectrum (Fig. 21) that the level scheme for this nucleus is very complicated.

WOLFRAM

The wolfram sample consisted of 600 gm. of the pure metal enclosed in a Dural container with Bakelite ends. The spectrum was studied from 3 Mev. to 9 Mev. with a line width of 100 kev. above 4.2 Mev. and 140 kev. below that energy. The coincidence spectrum is shown in Fig. 22. The energies and intensities of the γ -rays are given in Table X. The absolute intensity of the γ -ray *D*

TABLE X
ENERGIES AND INTENSITIES OF WOLFRAM γ -RAYS

γ -Ray	Energy in Mev.	Intensity in photons per 100 captures	Probable origin
<i>A</i>	7.42 ± 0.02	0.3	W^{181}
<i>B</i>	6.73 ± 0.03	0.1	W^{181}
<i>C</i>	6.40 ± 0.05	0.3	W^{181}
<i>D</i>	6.182 ± 0.008	3.8	W^{181}
<i>D'</i> ?	6.02 ± 0.01	0.3	
<i>E</i>	5.77 ± 0.02	0.3	
<i>F</i>	5.304 ± 0.009	2.4	
<i>F'</i>	5.245 ± 0.009	3.4	
<i>F''</i>	5.14 ± 0.02	2.3	
<i>G</i>	4.94 ± 0.02	0.6	
<i>H</i>	4.67 ± 0.03	2.4	

was obtained by comparing its counting rate with that of the 9.0 Mev. γ -ray of nickel emitted from a sample consisting of a homogeneous mixture of weighed amounts of WO_3 and Ni_2O_3 . The thermal neutron capture cross section of

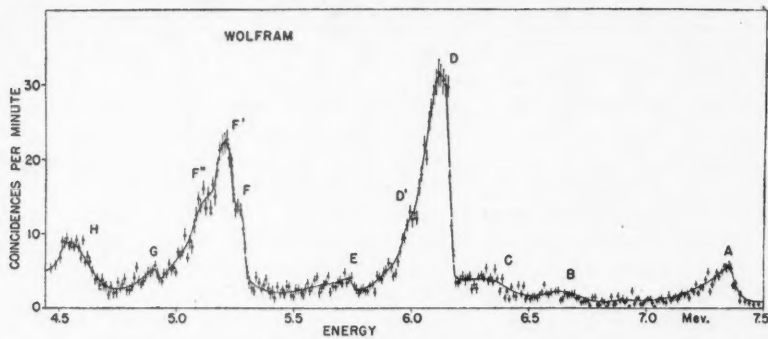


FIG. 22. Coincidence spectrum produced by wolfram 4.5-7.5 Mev. Line width 100 kev.

wolfram was assumed to be 19.2 barns. The corrected γ -ray spectrum is shown in Fig. 23.

Wolfram consists of five isotopes. The abundances, the contribution to the total thermal capture cross section (44), and the estimated neutron binding energies in the product nuclei are given in Table XI.

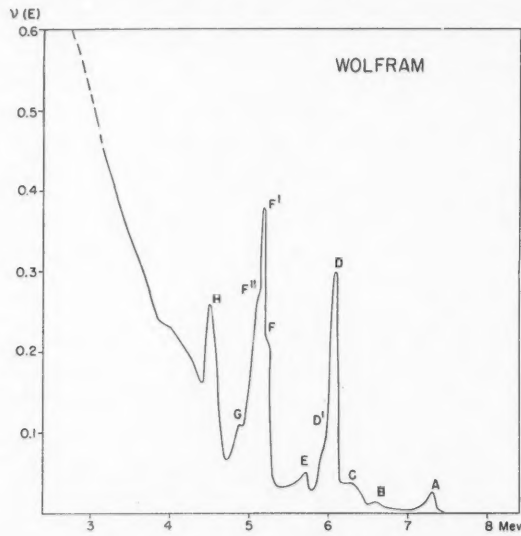


FIG. 23. Corrected γ -ray spectrum of wolfram.

The calculated neutron binding energies were obtained from the tables of Metropolis and Reitwiesner (34). According to the results of Harvey (20) the calculated binding energies may be too high by about 0.1 Mev. at the neutron number 110. Two (γ, n) thresholds at 6.25 and 7.15 Mev. were observed by Sher, Halpern, and Mann (50); we have assigned these to W^{183} and W^{184} .

TABLE XI
ABUNDANCES, CROSS SECTIONS, AND NEUTRON BINDING ENERGIES OF THE WOLFRAM ISOTOPES

Target isotope	Abundance, %	Contribution to total cross section, %	Neutron binding energy of product nucleus, Mev.	
			Observed ^a	Calculated ^b
W ¹⁸⁰	0.14	0.2		6.5
W ¹⁸²	26.2	29	6.25 \pm 0.3?	6.3
W ¹⁸³	14.3	9	7.15 \pm 0.3?	7.5
W ¹⁸⁴	30.7	3.5		6.0
W ¹⁸⁶	28.7	58		5.7

^a See Reference 50.

^b See Reference 34.

in Table XI. There is no doubt that the higher of these binding energies refers to W¹⁸⁴, but the lower is less certain.

The energy of the most energetic γ -ray, A , 7.42 ± 0.02 Mev., agrees with the binding energy of W¹⁸⁴ given in Table XI and may therefore represent the ground state transition in that nucleus. Since the shell model assignment of W¹⁸³ is $p_{1/2}$, the compound nucleus formed in W¹⁸⁴ has a spin of 0 or 1 and odd parity. It follows that the ground state γ -ray for a capturing state of spin 1 is of the $E1$ type. The W¹⁸⁴ binding energy is considerably greater than the binding energies of any of the other isotopes, and it is probably safe to assume that A , B , and C are derived from W¹⁸⁴.

If the γ -rays B and C are emitted by the capturing state, they must produce excited states in W¹⁸⁴ at 0.69 ± 0.04 and 1.02 ± 0.05 Mev. A number of γ -rays have been observed (56, 58) to follow the β -decay of Re¹⁸⁴ and among these a γ -ray with an energy near 1.0 Mev. seems to be well established. This suggests that an excited state near 1 Mev. exists, but it is clear that more information is required before the γ -ray C can be assigned with certainty.

The strong γ -ray D has an energy very close to the estimated binding energy of W¹⁸³ and may be emitted in the ground state transition in that nucleus. Since the shell assignment of the ground state of W¹⁸³ is a $p_{1/2}$ -state, this transition is $E1$. However, the peak D in Fig. 22 is complex and the presence of another unresolved γ -ray is indicated at D' . Some information concerning the excited states of W¹⁸³ is available from measurements of the decay of Re¹⁸³, in which a γ -ray with an energy near 1.07 Mev. was observed (56, 58). If, then, the γ -ray D is indeed the ground state transition in W¹⁸³, a γ -ray with an energy near 5.11 Mev. may be expected to be observed. Such a transition may account for one of γ -rays F , F' , F'' , and G .

Some 60% of the capture γ -rays are derived from the nucleus W¹⁸⁷. It is probable that at least a part of the peak F is due to the ground state γ -ray in this nucleus. At the present time, it is not possible to identify this γ -ray with any certainty.

PLATINUM

The platinum sample consisted of four 2-in. diameter disks of very pure platinum metal with a total weight of about 110 gm. enclosed in a Dural

cylinder with Bakelite ends. The upper end of the coincidence spectrum is shown in Fig. 24. The energies and intensities of the platinum γ -rays are listed in Table XII, the intensities being estimated by the approximate method

TABLE XII
ENERGIES AND ESTIMATED INTENSITIES OF PLATINUM γ -RAYS

γ -Ray	Energy in Mev.	Estimated intensity in photons per 100 captures	Probable origin
A	7.920 ± 0.012	0.3	Pt ¹⁹⁶
B	7.26 ± 0.03	0.2	Pt ¹⁹⁶
C	6.07 ± 0.04	1.1	
D	5.24 ± 0.03	1.8	

described in the preceding paper. The thermal cross section was assumed to be 8.1 barns. The corrected γ -ray spectrum is shown in Fig. 25.

Platinum consists of six stable isotopes; the contributions to the thermal neutron capture cross section of only three of these are known. The abundances, the contributions to the cross section, and the neutron binding energies are listed in Table XIII.

TABLE XIII
ABUNDANCES, CROSS SECTIONS, AND NEUTRON BINDING ENERGIES OF PLATINUM ISOTOPES

Target nucleus	Abundance, %	Contribution to cross section, % ^a	Neutron binding energy of product nucleus	
			Observed	Calculated ^d
Pt ¹⁹⁰	0.012			6.6
Pt ¹⁹²	0.78			6.3
Pt ¹⁹⁴	32.8	9	6.14 \pm 0.2 ^b 6.1 \pm 0.1 ^c	6.1
Pt ¹⁹⁵	33.7		8.0 \pm 0.2 ^b 8.2 \pm 0.2 ^c	7.2
Pt ¹⁹⁶	25.4	3.6		5.8
Pt ¹⁹⁸	7.2	3.5		5.6

^a See Reference 41.

^b See Reference 20.

^c See Reference 50.

^d See Reference 34.

Since the abundance of Pt¹⁹⁰ is very low, it is probable that the major contribution to the total capture cross section is caused by Pt¹⁹⁴ and Pt¹⁹⁵. The relative proportions in which this contribution is shared are not known.

It is clear from Tables XII and XIII that the γ -rays A and B must be emitted by Pt¹⁹⁶. Of these, the former probably represents the ground state transition in that nucleus, for its energy is in agreement with the measured neutron binding energy. The shell assignment of Pt¹⁹⁶ is $p_{1/2}$, and the states formed by thermal neutron capture are odd and have spins of 0 or 1. It follows that the transition from the latter state to the ground state of Pt¹⁹⁶ is E1. The γ -ray B probably represents the transition to an excited state. The positions

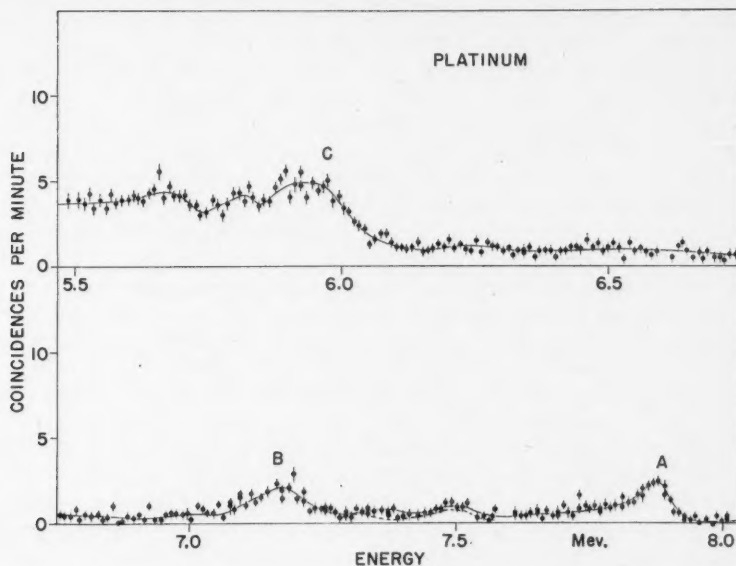


FIG. 24. Coincidence spectrum produced by platinum 5.5–8.0 Mev. Line width 100 kev. The estimated contributions from lead and aluminum background radiations are shown by the broken curve near 7.5 Mev.

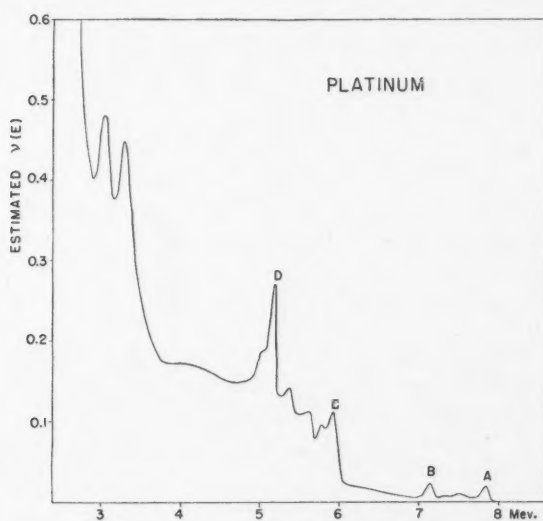


FIG. 25. Corrected γ -ray spectrum of platinum.

of two excited states in Pt¹⁹⁶ are known from the decay (52) of Au¹⁹⁶. The first of these, at 0.358 Mev., could be excited by a γ -ray with an energy of 7.57 Mev. There is no evidence for such a γ -ray in Fig. 24, for the low peaks near 7.5 Mev. and 7.3 Mev. can be ascribed to the background of aluminum and lead radiations (shown by the dotted line). The 7.57 Mev. γ -ray must be at least five times weaker than A, i.e., less than 0.06 photons per 100 captures. The second excited state, at 0.69 Mev., is probably excited by the γ -ray B, for the energy difference between A and B is 0.66 ± 0.03 Mev. in fair agreement with this value. Below B there is no clear evidence for the existence of any other radiation above the energy of the γ -ray C, at 6.07 Mev. The continuous coincidence counting rate observed between 6 and 7 Mev. may be due to a large number of weak γ -rays for it seems too strong to be attributed to the spurious coincidence effect described in the preceding paper. From the γ -ray C, downwards, there is a continuous distribution of γ -radiation on which only one peak (D) can be discerned (see Fig. 25). The upper edge of C is not well defined, and it is clear that this peak is produced by more than one γ -ray. These γ -rays could be due to the ground state transition in Pt¹⁹⁶, or to transitions to low lying excited states in that nucleus, or to Pt¹⁹⁶. The positions of low lying states in Pt¹⁹⁶ are known from the decay (52) of Au¹⁹⁶ but owing to the inadequate resolution of the present instrument, they are of no value in the interpretation of these results.

MERCURY

The mercury sample consisted of about 1 kgm. of mercuric fluoride enclosed in a Dural cylinder with Bakelite ends. The capture γ -ray spectrum was measured in detail with the new apparatus from 4.5 to 8 Mev. The coincidence

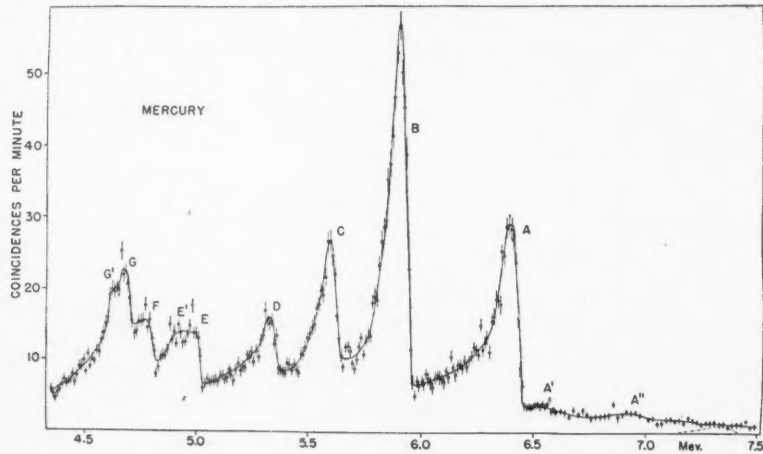
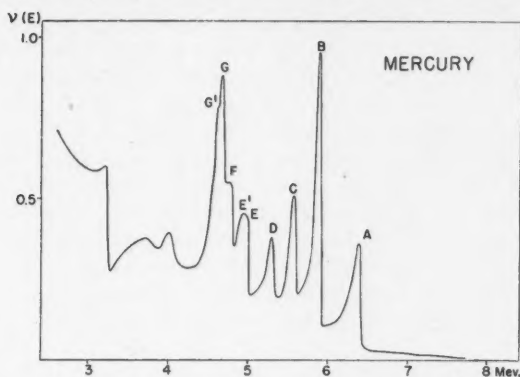


FIG. 26. Coincidence spectrum produced by mercury 4.4-7.5 Mev. Line width 100 kev. The estimated contribution from lead background radiation is shown by the broken curve at 7.3 Mev.

FIG. 27. Corrected γ -ray spectrum of mercury.

spectrum of this region is shown in Fig. 26. Between 4.5 and 2.5 Mev. the spectrum was investigated with the old apparatus and these measurements were not repeated in detail. These results were used in the construction of the corrected spectrum shown in Fig. 27. The energies and absolute intensities of the prominent γ -rays are given in Table XIV. The absolute intensities

TABLE XIV
ENERGIES AND INTENSITIES OF MERCURY γ -RAYS

γ -Ray	Energy in Mev.	Intensity in photons per 100 captures
A	6.446 ± 0.008	5
B	5.959 ± 0.008	12
C	5.647 ± 0.010	5
D	5.39 ± 0.02	3
E	5.07 ± 0.02	3
E'	4.95 ± 0.05	1
F	4.83 ± 0.01	3
G	4.73 ± 0.02	4
G'	4.66 ± 0.03	2

were obtained by the nickel comparison method using the prominent mercury γ -ray B, and another sample consisting of a mixture of mercuric fluoride and nickel oxide. The thermal capture cross section of mercury was assumed to be 380 ± 20 barns.

Mercury possesses seven stable isotopes, but only one of these, Hg^{199} , makes an appreciable contribution (at least 89%) to the total thermal capture cross section (24). The upper limit of the capture γ -ray spectrum has been measured by Kubitschek and Dancoff (28) who obtained 7.1 ± 0.4 Mev. The value calculated from the tables of Metropolis and Reitwiesner (34) is 7.4 Mev. Harvey has shown that calculated neutron binding energies for nuclei just below the closed shell of 126 neutrons may be too low by about 0.5 Mev.; a better estimate therefore of the neutron binding energy of Hg^{200}

is 7.9 Mev. No capture γ -ray of this energy was detected with either the new apparatus (up to 8 Mev.) or with the old apparatus (up to 9.3 Mev.). It is clear from these results that if this γ -ray is present its intensity is less than one photon per 1000 captures.

Since the shell structure indicates that the ground state of Hg^{199} should be a $p_{1/2}$ -state, an $E1$ ground state γ -ray is expected if the neutron capture produces a compound state with a spin of one unit. The capture and scattering properties of mercury at thermal neutron energies correspond to a resonance at negative energy (21); if this state has zero spin, the ground state transition is completely forbidden and the γ -ray would not be detected. This explanation, however, does not seem to be consistent with measurements of the scattering of slow neutrons in mercury, which, on the contrary, suggest that the spin is unity (23).

Above the strong peak A , there is a gently sloping tail extending to 8 Mev., the upper limit of measurement. We estimate that the counting rate contributed by the various background effects is not enough to account for all of this tail. There is some evidence for two weak radiations, A' at 6.6 Mev. and A'' at 7.1 Mev. If these γ -rays exist, their intensity is of the order of 0.3 photon per 100 captures. They may be caused by Hg^{200} or they may be due to other isotopes.

The strong γ -rays listed in Table XIV are probably all produced in Hg^{200} . While two γ -rays have been detected in the decay (40) of Tl^{200} , at about 0.35 and at 1.6 Mev., much more precise evidence is required before it becomes possible to identify the capture γ -rays with certainty.

ZIRCONIUM

The zirconium sample was a metal cylinder, 3 in. in diameter and 1 in. thick, of very pure material said to be entirely free of the hafnium impurity which usually contributes the greater part of the thermal capture cross section of this metal. The sample was enclosed in a Dural cylinder with Bakelite ends. The thermal capture cross section of pure zirconium is low, 0.18 barns (41); the counting rates obtained are low and the spectrum therefore is difficult to measure. The spectrum was explored between 2.5 and 10 Mev.; the results (obtained with the old apparatus) are shown in Fig. 28. The energies and estimated intensities of the more important γ -rays are given in Table XV. The corrected γ -ray spectrum is shown in Fig. 29.

TABLE XV
ENERGIES AND INTENSITIES OF ZIRCONIUM γ -RAYS

γ -Ray	Energy in Mev.	Estimated intensity in photons per 100 captures	Probable origin
A	8.66 ± 0.04	1	Zr^{92}
B	7.71 ± 0.04	1	Zr^{92}
C	7.38 ± 0.06	0.5	
D	6.30 ± 0.03	16	$Zr^{92}(?)$

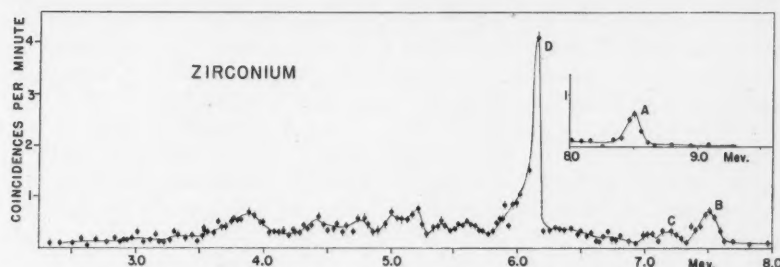
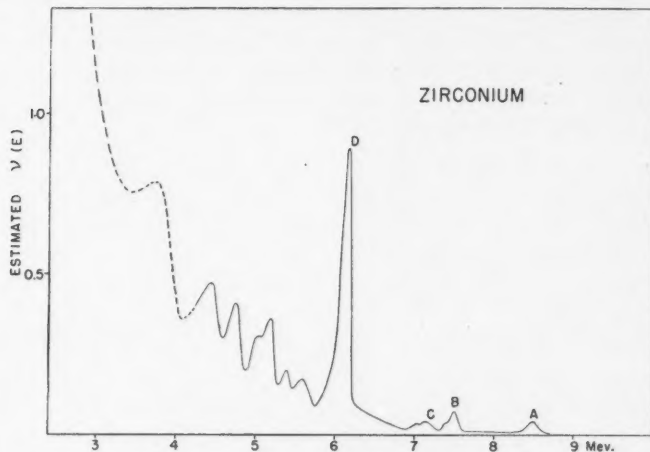


FIG. 28. Coincidence spectrum produced by zirconium. Line width 140 kev.

FIG. 29. Corrected γ -ray spectrum of zirconium.

The contributions of the various zirconium isotopes to the total cross section have been measured by Pomerance (44); his results, together with the observed neutron binding energies of the product nuclei, are listed in Table XVI.

TABLE XVI
ABUNDANCES, CROSS SECTIONS, AND NEUTRON BINDING ENERGIES OF ZIRCONIUM ISOTOPES

Target nucleus	Abundance, %	Contributions to cross sections, %	Neutron binding energies of product nucleus in Mev.
Zr ⁹⁰	52	21	7.16 ± 0.05^a 7.2 ± 0.4^b
Zr ⁹¹	11	60	8.73 ± 0.10^a
Zr ⁹²	17	14	6.56 ± 0.10^a
Zr ⁹⁴	17	4	
Zr ⁹⁶	3	1	

^a See Reference 20.^b See Reference 19.

It will be seen that most thermal captures produce Zr^{92} . This nucleus is probably responsible for the very strong γ -ray D , although, since the intensities given in Table XV are only estimates, Zr^{91} is not ruled out. The energies of the γ -rays A and B are such that they must also be emitted from Zr^{92} .

It is very probable that the γ -rays A and B respectively produce the ground state and the first excited state of Zr^{92} , for the difference in their energies, 0.95 ± 0.06 Mev., is in good agreement with the energy of the γ -ray emitted in the decay of Nb^{92} (0.93 Mev. (45, 55)). If this is true it is perhaps surprising that the γ -ray A is as strong as it appears, for the ground state of Zr^{91} is even and has a spin of $5/2$, whence it follows that this γ -ray must be $E2$ or $M3$.

Apart from a γ -ray of 0.6 Mev. produced by Y^{92} (15) there are no other data on the positions of the levels of Zr^{92} and the identity of the γ -ray D , if it belongs to Zr^{92} , cannot be determined. There is some reason to believe that an excited state in Zr^{91} may exist (29) near 1 Mev.; it is not impossible that C may represent the ground state transition in this nucleus and D the transition to the first excited state.

TIN

The tin sample consisted of a disk* of very pure tin weighing 2.6 kgm. placed inside a Dural container with Dural ends. The spectrum (obtained with the old apparatus) is very complex; the high energy end, unfortunately, is obscured by the radiation from the Dural. Below this point, few γ -rays can be resolved above the continuous background; above, only one γ -ray can be distinguished. The energy of this γ -ray is 9.35 ± 0.08 Mev., and its

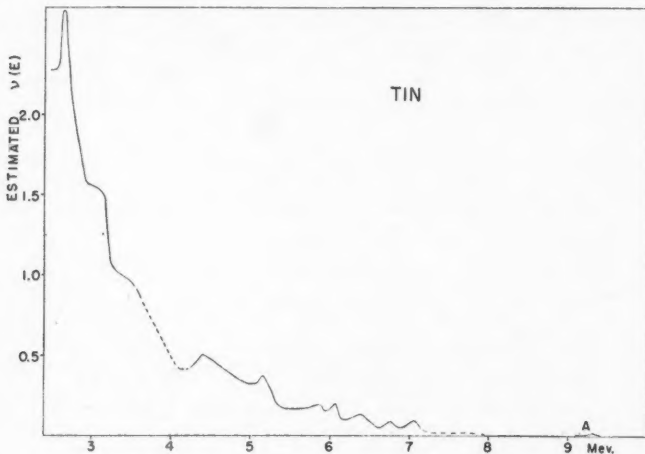


FIG. 30. Corrected γ -ray spectrum of tin.

* We are indebted to the Division of Physical Metallurgy, Department of Mines and Technical Surveys, Ottawa, for the provision of this sample.

estimated intensity is 0.4 photon per 100 captures. The corrected spectrum only is shown (Fig. 30). It has been calculated on the basis of the estimated intensities and a thermal capture cross section of 0.65 barn.

There are 10 isotopes of tin with mass numbers of 112, 114 to 120, 122, and 124. The isotope responsible for the 9 Mev. γ -ray cannot be identified with certainty for nothing is known about the relative contributions of the tin isotopes to the total thermal capture cross section. Harvey (20) has shown that the energy of this γ -ray is in good agreement with his value for the neutron binding energy of Sn^{118} (9.37 ± 0.2 Mev.), but this agreement may be fortuitous, for the observed neutron binding energies of the three even-even tin isotopes, Sn^{116} , Sn^{118} , and Sn^{120} , which could, in principle, be created by neutron capture, are very similar (9.1 ± 0.2 , 9.0 ± 0.2 , and 8.9 ± 0.2 Mev.). (See Reference 16.)

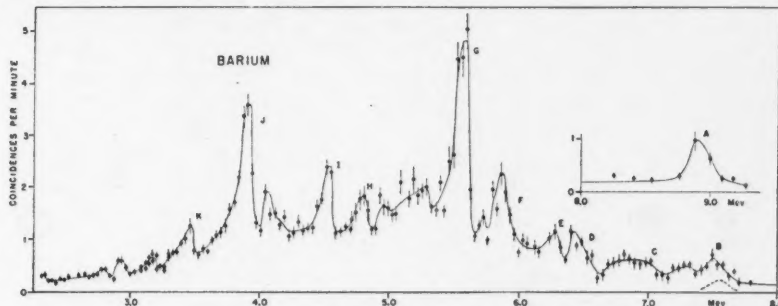


FIG. 31. Coincidence spectrum produced by barium. Line width 140 kev. The estimated contribution from aluminum background radiation is shown near 7.7 Mev.

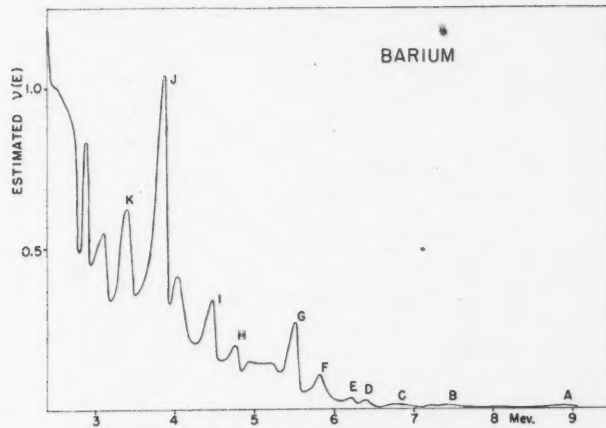


FIG. 32. Corrected γ -ray spectrum of barium.

BARIUM

The barium source consisted of some 2 kgm. of barium oxide. Preliminary measurements were made with a container of Dural; later measurements (with the old apparatus) were made with a Dural container with Bakelite ends, and the spectrum therefore is free from all but a trace of aluminum radiation. The later measurements extended from 2.4 to 8 Mev. and the results, together with the preliminary results above 8 Mev., are shown in Fig. 31. The energies and estimated intensities of the barium γ -rays are listed in Table XVII. The thermal capture cross section was assumed to be 1.17 barn. The corrected γ -ray spectrum is shown in Fig. 32.

TABLE XVII
ENERGIES AND ESTIMATED INTENSITIES OF BARIUM γ -RAYS

γ -Ray	Energy in Mev.	Estimated intensity in photons per 100 captures	Probable origin
A	9.23 ± 0.07	0.1	
B	7.79 ± 0.08	0.1	
C	7.18 ± 0.06	0.1	
D	6.68 ± 0.06	0.4	
E	6.44 ± 0.05	0.4	
F	6.06 ± 0.05	1	
G	5.74 ± 0.03	3.7	
H	4.98 ± 0.05	1	
I	4.70 ± 0.03	3	
J	4.10 ± 0.03	13	
K	3.66 ± 0.04	5	

Only three of the seven stable isotopes of barium (Ba^{135} , Ba^{137} , and Ba^{138}) contribute appreciably to the total cross section. The abundances, the contributions to the cross sections, and the neutron binding energies of the product nuclei, so far as they are known, are listed in Table XVIII.

TABLE XVIII
ABUNDANCES, CROSS SECTIONS, AND NEUTRON BINDING ENERGIES OF BARIUM ISOTOPES

Target isotope	Abundance, %	Contribution to cross section, %	Neutron binding energy of product nucleus, Mev.	
			Observed	Calculated ^a
Ba^{130}	0.1	0.002 ^b		7.3
Ba^{132}	0.1	0.6 ^b		6.9
Ba^{134}	2.4	3 ^b		6.5
Ba^{135}	6.6	25 ^b		8.0
Ba^{136}	7.8	2 ^b	6.80 ± 0.20^c	6.1
Ba^{137}	11	37 ^b	8.55 ± 0.25^c	7.6
Ba^{138}	72	34 ^b	5.2 ± 0.3^d	5.7

^a See Reference 34.

^b See Reference 41.

^c See Reference 50 in which the isotopes responsible for these thresholds are not specified; the above assignment seems to us the most plausible.

^d See Reference 20.

The last column of this table contains the neutron binding energies calculated from the tables of Metropolis and Reitwiesner (34). The difference between the observed and calculated values for the neutron binding energy shows the change in the binding energy which occurs near the magic number of 82 neutrons (20).

Unfortunately so little is known about the positions of the excited states of the barium isotopes of interest here that it is impossible to identify with certainty any of the barium γ -rays except possibly the γ -ray *A*. The evidence for the existence of this γ -ray is not very good for it is substantiated by only a few points; if it exists, its high energy indicates that it must represent the ground state transition in the closed shell nucleus Ba¹³⁸, which, probably, has the highest binding energy of any of the barium isotopes. According to shell structure theory the ground state of Ba¹³⁷ is a $d_{5/2}$ -state. The ground state γ -ray therefore is *M1* or *E2*. An excited state in Ba¹³⁸ exists at 0.807 (or 0.535) Mev. and another at 1.39 ± 0.03 Mev. (46). The difference between the energies of the γ -rays *A* and *B* is 1.44 ± 0.11 Mev.; and γ -ray *B*, therefore, may represent a transition to the second of these states. No γ -ray was found corresponding to a transition to the first excited state; however, a γ -ray producing a counting rate of less than one third of that of the peaks *A* and *B* would probably have been missed. None of the remaining γ -rays with energies below that of *B* can be identified. The most interesting of these is the γ -ray *J* which is unusually intense.

GADOLINIUM

The gadolinium sample consisted of about 0.5 gm. of gadolinium oxide, mixed with Glyptal cement, to form two uniform thin disks each about 25 sq. cm. in area. Four thin nickel sheets, two sandwiched between and two outside the Bakelite capsules containing the oxide, served as a measure of the neutron flux and produced weak coincidence peaks at 9 Mev., without contributing appreciably to the remainder of the coincidence spectrum. This method, like that used with samarium, was chosen to avoid contamination of the gadolinium oxide with nickel oxide, and the intensity calculated from the nickel comparison is in agreement with that estimated by the approximate method.

The cross section of gadolinium used in the calculation of absolute intensities was 36,300 barns, an average of the three pile oscillator values quoted by

TABLE XIX
ENERGIES AND INTENSITIES OF GADOLINIUM γ -RAYS

γ -Ray	Energy in Mev.	Estimated intensity in photons per 100 captures
<i>A</i>	7.78 ± 0.05	0.03
<i>B</i>	7.36 ± 0.06	0.03
<i>C</i>	6.73 ± 0.03	0.5
<i>D</i>	6.41 ± 0.04	0.2
<i>E</i>	5.87 ± 0.04	0.2
<i>F</i>	5.61 ± 0.04	0.3

Pomerance (43). As in the other cases of resonance capture (cadmium and samarium), this cross section is better for our purposes than that obtaining at 2200 meters per second.

The coincidence spectrum of gadolinium is shown in Fig. 33. The energies and intensities of the more prominent γ -rays are listed in Table XIX. The corrected spectrum is shown in Fig. 34.

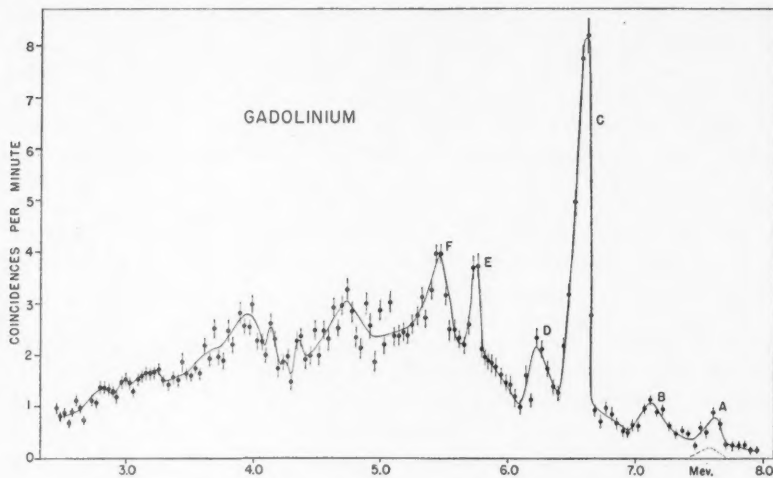


FIG. 33. Coincidence spectrum produced by gadolinium. Line width 140 kev. The estimated contribution from aluminum background radiation is shown near 7.7 Mev.

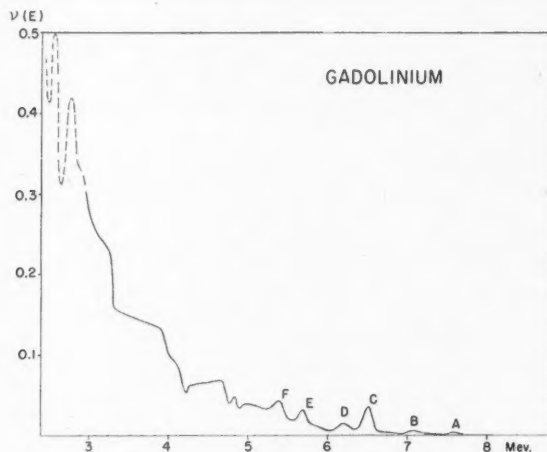


FIG. 34. Corrected γ -ray spectrum of gadolinium.

Two isotopes of gadolinium contribute (in the ratio of one to four) by far the greater part of the exceptionally high thermal capture cross section. They are Gd¹⁵⁵ and Gd¹⁵⁷ respectively. The highest energy γ -rays most probably are produced by the lighter isotope. Since the shell structure indicates very clearly that the ground states of the odd gadolinium isotopes are $f_{7/2}$ - or $f_{5/2}$ -states it follows that the ground state γ -rays in the product nuclei are M2 or E3; it is probable that they are too weak to be detected in the conditions in which the present measurements were made. There can be no certainty, therefore, that the γ -ray A is the ground state γ -ray in Gd¹⁵⁶. The calculated neutron binding energies of Gd¹⁵⁶ and Gd¹⁵⁸ are 7.9 and 7.6 respectively. Unfortunately, it is not possible to predict the actual neutron binding energies with any precision for the error in the calculated binding energies is not known in this part of the periodic table. Nor can any of the γ -rays observed be identified from the correspondence between their energies and the energies of excited states suggested by known γ -rays from radioactive nuclei which produce Gd¹⁵⁶.

REFERENCES

- ARNOLD, J. A. and SUGARMAN, N. J. Chem. Phys. 15: 703. 1947.
- BARTHOLOMEW, G. A. and KINSEY, B. B. Phys. Rev. 90: 355. 1953.
- BOEHM, F. and PREISWERK, P. Helv. Phys. Acta, 22: 331. 1949.
- BOGLE, G. S. and SCOVIL, H. E. D. Proc. Phys. Soc. (London), A, 65: 368. 1952.
- BOVD, G. E. and KETELLE, B. H. Phys. Rev. 83: 216. 1951.
- BRADY, E. L. and DEUTSCH, M. Phys. Rev. 78: 558. 1950.
- BROCKHOUSE, B. N. Can. J. Phys. 31: 432. 1953.
- BUNKER, M. E., LANGER, L. M., and MOFFAT, R. J. D. Phys. Rev. 81: 30. 1951.
- CANADA, R. and MITCHELL, A. C. G. Phys. Rev. 83: 955. 1951.
- DAVIS, S. P. and JENKINS, F. A. Phys. Rev. 83: 1269. 1951.
- EASTERDAY, H. T. and MEDICUS, H. A. Phys. Rev. 89: 752. 1953.
- GESCHWIND, S., MINDEN, H., and TOWNES, C. H. Phys. Rev. 78: 174. 1950.
- GIDEON, D. N., MILLER, W. C., and WALDMAN, B. Phys. Rev. 75: 329. 1949.
- GOLDHABER, M. and HILL, R. D. Revs. Mod. Phys. 24: 179. 1952.
- GÖTTE, H. Naturwiss. 29: 496. 1941.
- HALSTED, R. E. Phys. Rev. 88: 666. 1952.
- HAMERMESH, B. Phys. Rev. 76: 182. 1949; 80: 415. 1950; 81: 487. 1951.
- HAMERMESH, B. and HUMMEL, V. Phys. Rev. 88: 916. 1952.
- HANSON, A. O., DUFFIELD, R. B., KNIGHT, J. D., DIVEN, B. C., and PALEVSKY, H. Phys. Rev. 76: 578. 1949.
- HARVEY, J. A. Phys. Rev. 81: 353. 1951.
- HAVENS, W. W. and RAINWATER, J. Phys. Rev. 70: 154. 1946.
- HIBDON, C. T. and MUEHLHAUSE, C. O. Phys. Rev. 87: 222. 1952; 88: 943. 1952.
- HIBDON, C. T., MUEHLHAUSE, C. O., RINGO, G. R., and ROBILLARD, T. R. Phys. Rev. 82: 560. 1951.
- INGRAM, M. G., HESS, D. C., and HAYDEN, R. J. Phys. Rev. 71: 561. 1947.
- JOHNS, M. W., COX, C. D., DONNELLY, R. J., and McMULLEN, C. C. Phys. Rev. 87: 1134. 1952.
- KINSEY, B. B. and BARTHOLOMEW, G. A. Phys. Rev. 89: 375. 1953.
- KLINKENBERG, P. F. A. Revs. Mod. Phys. 24: 63. 1952.
- KUBITSCHKE, H. E. and DANCOFF, S. M. Phys. Rev. 76: 531. 1949.
- LANGER, L. M. and PRICE, H. C. Phys. Rev. 76: 641. 1949.
- MANN, L. G. and AXEL, P. Phys. Rev. 84: 221. 1951.
- MATEOSIAN, E. DER and GOLDHABER, M. Phys. Rev. 82: 115. 1951.
- MEDICUS, H. A., PREISWERK, P., and SCHERRER, P. Helv. Phys. Acta, 23: 299. 1950.
- MEI, J. Y., MITCHELL, A. C. G., and ZAFFARANO, D. J. Phys. Rev. 76: 1883. 1949.
- METROPOLIS, N. and REITWIESNER, G. NP-1980. 1950.
- METZGER, F. R. and AMACHER, H. C. Phys. Rev. 88: 147. 1952.
- MILLAR, C., CAMERON, A., and GLICKSMAN, M. Can. J. Research, A 28: 475. 1950.
- MOAK, C. D. and DABBS, J. W. T. Phys. Rev. 75: 1770. 1949.
- MOTZ, H. T. Phys. Rev. 90: 355. 1953.
- MURAKAWA, K. and ROSS, J. S. Phys. Rev. 82: 967. 1951.

40. NEUMANN, H. M. and PERLMAN, I. Phys. Rev. 78: 191. 1950.
41. NEUTRON CROSS SECTIONS. AECU-2040. 1952.
42. PEACOCK, W. C. and JONES, J. W. CNL-14. 1948.
43. POMERANCE, H. Phys. Rev. 83: 641. 1951.
44. POMERANCE, H. Phys. Rev. 88: 412. 1952.
45. PREISWERK, P. and STÅHÉLIN, P. Helv. Phys. Acta, 24: 300. 1951.
46. PRINGLE, R. W., STANDIL, S., TAYLOR, H. W., and FRYER, G. Phys. Rev. 84: 1066. 1951.
47. PRINGLE, R. W., TAYLOR, H. W., and ROULSTON, K. I. Phys. Rev. 87: 1016. 1952.
48. SAGANE, R., KOJIMA, S., MIYAMOTO, G., and IKAWA, M. Proc. Phys. Math. Soc. Japan, 21: 660. 1939.
49. SEREN, L., FRIEDLANDER, H. N., and TURKEL, S. H. Phys. Rev. 72: 888. 1947.
50. SHER, R., HALPERN, J., and MANN, A. K. Phys. Rev. 84: 387. 1951.
51. SHER, R., HALPERN, J., and STEPHENS, W. E. Phys. Rev. 81: 154. 1951.
52. STEFFEN, R. M., HUBER, O., and HUMBEL, F. Helv. Phys. Acta, 22: 167. 1949.
53. STEINBERG, E. P. and ENGELKEMEIR, D. W. National Nuclear Energy Series, 9: Paper 54. McGraw-Hill Book Company, Inc., New York and London. 1950.
54. THORNTON, W. A., DER MATEOSIAN, E., MOTZ, H. T., and GOLDHABER, M. Phys. Rev. 86: 604. 1952.
55. TICHO, H. K., GREEN, D., and RICHARDSON, J. R. Phys. Rev. 86: 422. 1952.
56. TURNER, S. E. and MORGAN, L. O. Phys. Rev. 81: 881. 1951.
57. VALLEY, G. E. and McCREARY, R. L. Phys. Rev. 56: 863. 1939.
58. WILKINSON, G. and HICKS, H. G. Phys. Rev. 77: 314. 1950.
59. WILSON, R. Phys. Rev. 80: 90. 1950.

A METHOD FOR THE EVALUATION OF SOME LATTICE SUMS OCCURRING IN CALCULATIONS OF PHYSICAL PROPERTIES OF CRYSTALS¹

BY B. M. E. VAN DER HOFF² AND G. C. BENSON

ABSTRACT

A method is described for the evaluation of sums of the inverse n^{th} power of the distances from a point P to all points of a lattice. The sums are expressed in sums of Bessel functions or e -powers that converge rather rapidly and Riemann ζ functions. The procedure can be used for any position of P with respect to the lattice.

INTRODUCTION

In calculations of physical properties of crystals by theories based on a point-lattice model of ions, one often requires numerical values for sums of the type

$$(A) \quad \sum'_{k l m} (k^2 + l^2 + m^2)^{-n}$$

or

$$(B) \quad \sum'_{k l m} (-1)^{k+l+m} (k^2 + l^2 + m^2)^{-n}$$

in which k , l , and m are integers and n is usually an integer or half integer. For type A the sum $k + l + m$ may be restricted to even or odd values. The limits of summation may be 1 to ∞ or $-\infty$ to $+\infty$; if the latter sum is required the case $k = l = m = 0$ is excluded as is indicated by the dash on the summation sign. The Coulomb energy of crystals, for example, involves a sum of type B with $n = 1/2$, the energy due to Van der Waals forces requires sums of type A with $n = 6/2$ and $n = 8/2$, and that due to Born repulsive forces involves sums with $n \geq 9/2$.

Formulae for the evaluation of type B with $n = 1/2$ have been worked out by Madelung (12), Ornstein and Zernike (13), Ewald ($n = 1/2, 3/2$) (5), Born (1), Kornfeld ($n = 3/2, 5/2$) (7), and Evjen (4). Formulae for the sums as a function of n have been derived by Emersleben (3) who generalized Ewald's method, but this work is unfortunately inaccessible. Later, Lennard-Jones and Ingham (9) computed sums with $n = 4/2$ to $30/2$ for face-centered and body-centered cubic lattices. However, their method involved rather tedious calculations. Topping (16) applied their procedure to the case $m = 0$, $n = 3/2$. Other authors, Lennard-Jones and Dent (8), Shuttleworth (15), Frank (6), Orr (14), and Young (20), followed a different method. They sum numerically for small values of k , l , and m representing a few hundred points that lie in a certain region and approximate to the contribution of the points outside that region, e.g. by integration. Recently a very powerful approach

¹ Manuscript received June 22, 1953.

Contribution from the Division of Pure Chemistry, National Research Council, Ottawa, Canada. Issued as N.R.C. No. 3062.

² National Research Council of Canada Postdoctorate Fellow, 1951-53. Present address: Research and Development Division, Polymer Corporation Limited, Sarnia, Ontario.

to the evaluation of these sums has been used by Mackenzie (10) in calculating the interaction energy between two hexagonal close-packed planes and later for (100) planes of a cubic lattice (11). The procedure transforms the lattice sums into sums of Bessel functions or e -powers that converge rather rapidly and Riemann ζ functions. The sums that can be computed in this way include those of the type

$$\sum'_{k \neq m} k(k^2 + l^2 + m^2)^{-n}$$

occurring in the calculations of surface properties. Here also $k + l + m$ may be restricted to even or odd values. An advantage of this method is its applicability to off-lattice points in which case $(k^2 + l^2 + m^2)^{-n}$ must be replaced by $\{(k+a)^2 + (l+b)^2 + (m+c)^2\}^{-n}$, where a, b , and c are the co-ordinates of the point under consideration with respect to a lattice point. It is not the purpose of the present paper to describe this method in full mathematical rigor, but rather to outline its use and to illustrate its utility by application to some specific examples of interest in chemical physics.

PROCEDURE

In this method, it is required that the limits of summation for l and m are $-\infty$ to $+\infty$. If those limits are 1 to ∞ , this sum can easily be expressed in sums with the required limits. For example:

$$\begin{aligned} \sum_{kl}^{\infty} (k^2 + l^2)^{-n} &= \frac{1}{2} \sum_k^{\infty} \sum_{l=-\infty}^{+\infty} (k^2 + l^2)^{-n} - \frac{1}{4} \sum_k^{\infty} \sum_{l=-\infty}^{+\infty} k^{-2n} \\ &= \frac{1}{2} \sum_k^{\infty} \sum_{l=-\infty}^{+\infty} (k^2 + l^2)^{-n} - \frac{1}{2} \zeta(2n). \end{aligned}$$

For the sums $\sum_{kl} (k^2 + l^2)^{-n}$ with $k + l$ = even or odd and for $\sum_{kl} (-1)^{k+l} (k^2 + l^2)^{-n}$, it is advantageous to rotate the co-ordinate axes through 45° . This leads to formulae which are more convenient for the purpose of calculation.

The procedure now consists of three steps.

I. The summand or part thereof is brought into an integral form, using

$$(k^2 + l^2 + m^2)^{-n} = \frac{1}{\Gamma(n)} \int_0^{\infty} t^{n-1} e^{-(k^2 + l^2 + m^2)t} dt,$$

which is Euler's expression for the Γ -function and is valid for $n > 0$.

II. Part of the resulting integrand along with its accompanying summation signs, namely

$$\sum_{l=-\infty}^{+\infty} e^{-l^2 t} \times \sum_{m=-\infty}^{+\infty} e^{-m^2 t},$$

is transformed using

$$\sum_{p=-\infty}^{+\infty} e^{-p^2 t} = \left(\frac{\pi}{t}\right)^{\frac{1}{2}} \sum_{q=-\infty}^{+\infty} e^{-q^2 \pi^2/t}, \quad (\text{Ref. 19}).$$

which holds for $t > 0$. This transformation is a special case of Jacobi's imaginary transformation for theta functions. If the sum $k + l + m$ is restricted to even or to odd values, then the required sum can be brought into a form

such that one or more of the variables k , l , and m become respectively $k + \frac{1}{2}$, $l + \frac{1}{2}$, and $m + \frac{1}{2}$. In that case a more general form of the transformation formula must be used, i.e.

$$(a) \quad \sum_{p=-\infty}^{+\infty} e^{-(p+a)^2 t} = \left(\frac{\pi}{t}\right)^{\frac{1}{2}} \sum_{q=-\infty}^{+\infty} e^{-q^2 \pi^2/t} \cos 2qa\pi \quad (\text{Ref. 19}).$$

which for the case of $a = \frac{1}{2}$ becomes

$$(b) \quad \sum_{p=-\infty}^{+\infty} e^{-(p+\frac{1}{2})^2 t} = \left(\frac{\pi}{t}\right)^{\frac{1}{2}} \sum_{q=-\infty}^{+\infty} (-1)^q e^{-q^2 \pi^2/t}.$$

Formulae (a) and (b) may be employed for sums over lattices with a symmetry lower than cubic or for off-lattice points.

III. The integral obtained in I now takes the form

$$\int_0^\infty t^{n-1} e^{-k^2 t - q^2 \pi^2/t} dt,$$

which is simply related to the modified Bessel functions of the second kind by

$$\int_0^\infty t^{n-1} e^{-k^2 t - q^2 \pi^2/t} dt = 2 \left(\frac{q\pi}{k}\right)^n K_n(2kq\pi) \quad (\text{Ref. 17, p. 183}).$$

This treatment is valid for any positive value of n . The function $K_n(z)$ takes a simple form when n is a half integer, since $K_{\nu+\frac{1}{2}}(z) = (\pi/2z)^{\frac{1}{2}} e^{-z} \times N$ where $N = 1$ for $\nu = 0$, $N = 1 + 1/z$ for $\nu = 1$, and in general

$$N = \sum_{r=0}^{\nu} \frac{(\nu+r)!}{r!(\nu-r)!(2z)^r} \quad (\text{Ref. 17, p. 80}).$$

The values for $K_n(z)$, if n is not a half integer and z is not too small, can conveniently be computed by means of the asymptotic expansion:

$$\begin{aligned} K_n(z) &= \left(\frac{\pi}{2z}\right)^{\frac{1}{2}} e^{-z} \left[1 + \frac{4n^2 - 1^2}{1! 8z} + \frac{(4n^2 - 1^2)(4n^2 - 3^2)}{2!(8z)^2} + \dots \right. \\ &\quad \left. + \frac{(4n^2 - 1^2)(4n^2 - 3^2) \dots \{4n^2 - (2p-1)^2\}}{p! (8z)^p} + O(z^{-p-1}) \right] \end{aligned} \quad (\text{Ref. 17, pp. 202, 198}).$$

Also tables of $K_n(z)$ exist for integral values of n (18).

EXAMPLES

I. As an example, the sum

$$S_a = \sum_{kl}^{l=\infty} (k^2 + l^2)^{-3/2}$$

will be evaluated. This sum occurs in the calculation of the mutual potential energy of a plane square network of dipoles and has been calculated by Topping (16, Case I).

$$\begin{aligned}
 S_a &= 2 \sum_{k=1}^{\infty} \sum_{l=-\infty}^{+\infty} \frac{1}{\Gamma(3/2)} \int_0^{\infty} t^{\frac{1}{2}} e^{-k^2 t - l^2 \pi^2/t} dt + 2 \sum_{k=1}^{\infty} l^{-3} \\
 &= 2 \sum_{k=1}^{\infty} \sum_{l=-\infty}^{+\infty} \frac{\pi^{\frac{1}{2}}}{\Gamma(3/2)} \int_0^{\infty} e^{-k^2 t - l^2 \pi^2/t} dt + 2\zeta(3) \\
 &= 8 \sum_{k=1}^{\infty} \sum_{l=1}^{\infty} \int_0^{\infty} e^{-k^2 t - l^2 \pi^2/t} dt + 4 \sum_{k=1}^{\infty} \int_0^{\infty} e^{-k^2 t} dt + 2\zeta(3) \\
 &= 16\pi \sum_{kl=1}^{\infty} \frac{l}{k} K_1(2\pi kl) + 4\zeta(2) + 2\zeta(3).
 \end{aligned}$$

It appears that only three values of $K_1(2\pi kl)$, namely $kl = 1, 2$, and 3 , are sufficient to give an accuracy of $1/10^8$. Using this method, S_a was found to be 9.0336217 , while Topping calculated 9.033629 .

II. The other lattice sum, computed by Topping (16, Case II), is worked out below as an illustration of the use of formula (a). The network of dipoles now has a hexagonal pattern (see Fig. 1). If we take the distance between

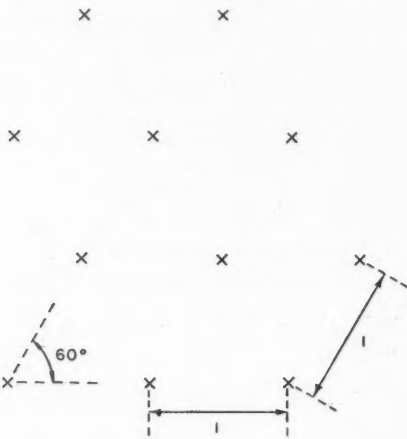


FIG. 1.

nearest neighbors as the unit length, the required sum over all lattice points can be written as the sum of two parts:

$$S_b = S_1 + S_2.$$

$$S_1 = \sum_{kl=-\infty}^{+\infty} (a^2 k^2 + l^2)^{-3/2} \text{ and}$$

$$S_2 = \sum_{kl=-\infty}^{+\infty} \{a^2(k + \frac{1}{2})^2 + (l + \frac{1}{2})^2\}^{-3/2} \text{ in which}$$

$$a = \tan 60^\circ = \sqrt{3}.$$

S_1 is worked out in the same way as before, leading to

$$\begin{aligned} S_1 &= \frac{16}{\sqrt{3}} \pi \sum_{k,l=1}^{\infty} \frac{l}{k} K_1(2\pi\sqrt{3}kl) + \frac{4}{3} \zeta(2) + 2\zeta(3), \\ S_2 &= 2 \sum_{k=0}^{\infty} \sum_{l=-\infty}^{+\infty} \frac{1}{\Gamma(3/2)} \int_0^{\infty} t^{\frac{1}{2}} e^{-a^2(k+\frac{1}{2})^2 t - (l+\frac{1}{2})^2 t} dt \\ &= 2 \sum_{k=0}^{\infty} \sum_{l=-\infty}^{+\infty} (-1)^l \frac{\pi^{\frac{1}{2}}}{\Gamma(3/2)} \int_0^{\infty} e^{-a^2(k+\frac{1}{2})^2 t - l^2\pi^2/t} dt \\ &= 8 \sum_{k=0}^{\infty} \sum_{l=1}^{\infty} (-1)^l \int_0^{\infty} e^{-a^2(k+\frac{1}{2})^2 t - l^2\pi^2/t} dt + 4 \sum_{k=0}^{\infty} \int_0^{\infty} e^{-a^2(k+\frac{1}{2})^2 t} dt \\ &= 16\pi \sum_{k=0}^{\infty} \sum_{l=1}^{\infty} (-1)^l \frac{l}{a(k+\frac{1}{2})} K_1(2\pi a(k+\frac{1}{2})l) + \frac{12}{a^2} \zeta(2) \\ &= \frac{32}{\sqrt{3}} \pi \sum_{\substack{k,l=1 \\ k \text{ odd}}}^{\infty} (-1)^l \frac{l}{k} K_1(\pi\sqrt{3}kl) + 4\zeta(2). \end{aligned}$$

Adding S_1 and S_2 yields

$$S_b = \frac{32}{\sqrt{3}} \pi \left[\sum_{k,l=1}^{\infty} -2 \sum_{\substack{k,l=1 \\ k \text{ odd} \\ l \text{ odd}}}^{\infty} \right] \frac{l}{k} K_1(\pi\sqrt{3}kl) + \frac{16}{3} \zeta(2) + 2\zeta(3).$$

Here also only three values of K_1 need to be evaluated. In this way S_b was found to be 11.0341754, while Topping calculated 11.0341⁸⁴₇₀.

III. A third example may demonstrate how to proceed for off-lattice points. Orr (14) evaluated sums of the inverse sixth power (Van der Waals forces) of the distances from a point P to all the lattice points of a semi-infinite cubic



FIG. 2.

lattice. P is considered to be situated in turn at a distance c normal to the (100) surface plane above:

1. the center of a lattice cell $a = b = \frac{1}{2}$,
2. the mid-point of a cell edge $a = 0, b = \frac{1}{2}$,
3. a lattice point $a = b = 0$ (see Fig. 2).

Recently, Young (20) calculated similar sums for the case in which the surface is formed by a (111) plane.

We derive now a general expression for the sum occurring in Orr's paper, in which a , b , and c are arbitrary parameters.

$$\begin{aligned}
 S_c &= \sum_{k,l=-\infty}^{+\infty} \sum_{m=0}^{\infty} \{(k+a)^2 + (l+b)^2 + (m+c)^2\}^{-3} \\
 &= \frac{1}{2} \sum_{k,l=-\infty}^{+\infty} \sum_{m=0}^{\infty} \int_0^{\infty} t^2 e^{-(k+a)^2 t - (l+b)^2 t - (m+c)^2 t} dt \\
 &= \frac{1}{2} \pi \sum_{k,l=-\infty}^{+\infty} \sum_{m=0}^{\infty} \cos 2ka\pi \times \cos 2lb\pi \int_0^{\infty} t e^{-(m+c)^2 t - (k^2 + l^2)\pi^2/t} dt \\
 (c) \quad &= 4\pi^3 \sum_{k,l=1}^{\infty} \sum_{m=0}^{\infty} \cos 2ka\pi \times \cos 2lb\pi \frac{k^2 + l^2}{(m+c)^2} K_2\{2\pi(m+c)\sqrt{k^2+l^2}\} \\
 &\quad + 2\pi^3 \sum_{k=1}^{\infty} \sum_{m=0}^{\infty} (\cos 2ka\pi + \cos 2kb\pi) \frac{k^2}{(m+c)^2} K_2\{2\pi k(m+c)\} \\
 &\quad + \frac{1}{2}\pi \sum_{m=0}^{\infty} (m+c)^{-4}.
 \end{aligned}$$

Sums of the type in the last term of equation (c) (generalized ξ functions) are simply related to polygamma functions for which tables are available (2). Equation (c) takes a simpler form if the point P is situated above a symmetrical position, as in 1, 2, and 3 of Fig. 2.

TABLE I
RESULTS OF CALCULATIONS FOR S_c

No.	Position of P			Values of S_c		
	a	b		$c = 1$	$c = 1\frac{1}{2}$	$c = 2$
1	$\frac{1}{2}$	$\frac{1}{2}$	This paper	1.56538	0.366776	0.129269
			Orr	1.5643	0.3658	0.1276
2	0	$\frac{1}{2}$	This paper	1.68320	0.368829	0.129313
			Orr	1.6825	0.3685	0.1286
3	0	0	This paper	1.87151	0.371165	0.129358
			Orr	1.8710	0.3700	0.1289

Table I lists some values of S_c calculated with formula (c); in total 10 values of $K_2(z)$ were computed. For comparison the corresponding values of Orr are given. The latter were obtained by summing numerically over at least 250 points and the contribution of the remaining part was determined by integration.

TABLE II
EXPRESSIONS FOR SUMS OVER SQUARE, PLANE AND CUBIC LATTICES

Sum	Restrictions on k, l , and m	Formula
$\sum_{k=0}^{+\infty} (k^2 + l^2)^{-n}$	None	$4 \sum_{k=1}^{+\infty} Y_1 + 2B\Gamma^{-(3n-1)}$
	$k = \text{even}$	$2^{1/2-n} \sum_{k=1}^{+\infty} X_1 + B\Gamma^{-(2n-1)}$
	$k = \text{odd}$	$2^{1/2-n} \sum_{k=1}^{+\infty} (-1)^k X_1 + B\Gamma^{-(2n-1)}$
$\sum_{k=0}^{+\infty} (-1)^k (k^2 + l^2)^{-n}$	None	$2^{1/2-n} \sum_{k=0}^{+\infty} X_1$
	None	$8 \sum_{k=1}^{+\infty} X_1 + 4B\Gamma(2n - 1) + 2Y(2n) = T$
	$k + l = \text{even}$	$2^{1/2-n} \left[\sum_{k=1}^{+\infty} -2 \sum_{l=0}^{+\infty} \right] X_1 + 2B\Gamma(2n - 1) + 2 \times 2^{-2n} Y(2n)$ or $2^{-n} T^*$
$\sum_{k=0}^{+\infty} (k^2 + l^2)^{-n}$	None	$2^{1/2-n} \left[\sum_{k=1}^{+\infty} -2 \sum_{l=0}^{+\infty} \right] X_1 + 2B\Gamma(2n - 1) + 2(1 - 2^{-2n}) Y(2n)$ or $(1 - 2^{-n}) T^*$
	$k + l = \text{odd}$	$2^{1/2-n} \sum_{k=0}^{+\infty} (-1)^k X_1 + 4(1 - 2^{-2n}) Y(2n)$ or $(-1 + 2^{-n+1}) T^*$
$\sum_{k=0}^{+\infty} (-1)^{k+l} (k^2 + l^2)^{-n}$	None	$8 \sum_{k=1}^{+\infty} \sum_{l=0}^{+\infty} Y_3 + 4A m^{-(2n-2)}$
	$k + l = \text{even}$	$2^{1-n} \sum_{k=1}^{+\infty} \sum_{l=0}^{+\infty} Y_1 + 2A m^{-(2n-2)}$
	$k + l = \text{odd}$	$2^{1-n} \sum_{k=1}^{+\infty} \sum_{l=0}^{+\infty} (-1)^k Y_1 + 2A m^{-(2n-2)}$
$\sum_{k=0}^{+\infty} (-1)^{k+l} (k^2 + l^2 + m^2)^{-n}$	None	$2^{1-n} \sum_{k=0}^{+\infty} Y_1$
	None	$16 \sum_{k=1}^{+\infty} \sum_{l=0}^{+\infty} Y_2 + 8 \sum_{k=1}^{+\infty} X_2 + 8A Y(2n - 2) + 4B\Gamma(2n - 1) + 2Y(2n)$
	$k + l + m = \text{even}$	$2^{1-n} \sum_{k=1}^{+\infty} \sum_{l=0}^{+\infty} \left[\sum_{m=0}^{+\infty} + (-1)^k \sum_{m=0}^{+\infty} \right] Y_1 + 2^{1/2-n} \left[\sum_{k=1}^{+\infty} - 2 \sum_{l=0}^{+\infty} \right] X_1 + 4A Y(2n - 2) + 2B\Gamma(2n - 1) + 2 \times 2^{-2n} Y(2n)$
	$k + l + m = \text{odd}$	$2^{1-n} \sum_{k=1}^{+\infty} \sum_{l=0}^{+\infty} \left[\sum_{m=0}^{+\infty} + (-1)^k \sum_{m=0}^{+\infty} \right] Y_1 + 2^{1/2-n} \left[\sum_{k=1}^{+\infty} - 2 \sum_{l=0}^{+\infty} \right] X_1 + 4A Y(2n - 2) + 2B\Gamma(2n - 1) + 2(1 - 2^{-2n}) Y(2n)$
$\sum_{k=0}^{+\infty} (-1)^{k+l+m} (k^2 + l^2 + m^2)^{-n}$	None	$2^{1-n} \sum_{k=0}^{+\infty} \sum_{l=0}^{+\infty} (-1)^k Y_1 + 2^{1/2-n} \sum_{k=0}^{+\infty} (-1)^k X_1 - 4(\frac{1}{2} - 2^{-2n}) Y(2n)$

* Obtained by rotating the co-ordinate axes through 45° .

IV. Finally in Table II we give expressions for sums over plane square and cubic lattices, derived with the procedure we have described. The following symbols are introduced:

$$A = \frac{\pi}{4\Gamma(n)} \int_0^\infty t^{n-2} e^{-t} dt, \text{ i.e. } A = \frac{\pi}{4(n-1)} \text{ for } n > 1, A = \infty \text{ for } n \leq 1,$$

$$B = \frac{\sqrt{\pi}}{2\Gamma(n)} \int_0^\infty t^{n-3/2} e^{-t} dt, \text{ i.e. } B = \frac{\sqrt{\pi}\Gamma(n-\frac{1}{2})}{2\Gamma(n)} \text{ for } n > \frac{1}{2}, B = \infty \text{ for } n \leq \frac{1}{2},$$

$$X_p = \frac{\pi^n}{\Gamma(n)} \left(\frac{k}{l}\right)^{n-\frac{1}{2}} K_{n-1}(p\pi kl),$$

$$Y_p = \frac{\pi^n}{\Gamma(n)} \left(\frac{\sqrt{k^2 + l^2}}{m}\right)^{n-1} K_{n-1}(p\pi m \sqrt{k^2 + l^2}).$$

ACKNOWLEDGMENT

One of the authors (v.d.H.) wishes to express his indebtedness to the National Research Council of Canada for the award of a Postdoctorate Fellowship.

REFERENCES

1. BORN, M. Z. Physik, 7: 124. 1921.
2. DAVIS, H. T. Tables of higher mathematical functions. Vol. II. The Principia Press, Bloomington, Ind. 1935. p. 11.
3. EMERSLEBEN, O. Dissertation. Göttingen. 1922. Physik. Z. 24: 73, 97. 1923.
4. EVJEN, H. M. Phys. Rev. 39: 675. 1932.
5. EWALD, P. P. Ann. Physik, 64: 253. 1921.
6. FRANK, F. C. Phil. Mag. 41: 1287. 1950.
7. KORNFELD, H. Z. Physik, 22: 27. 1924.
8. LENNARD-JONES, J. E. and DENT, B. M. Trans. Faraday Soc. 24: 92. 1928.
9. LENNARD-JONES, J. E. and INGHAM, A. E. Proc. Roy. Soc. (London), A, 107: 636. 1925.
10. MACKENZIE, J. K. Thesis, University of Bristol, Bristol. 1950.
11. MACKENZIE, J. K. Proc. Phys. Soc. (London), A, 63: 1370. 1950.
12. MADELUNG, E. Physik. Z. 19: 524. 1918.
13. ORNSTEIN, L. S. and ZERNIKE, F. Proc. Koninkl. Akad. Wetenschap. Amsterdam, 21: 911. 1918.
14. ORR, W. J. C. Trans. Faraday Soc. 35: 1247. 1939.
15. SHUTTLEWORTH, R. Proc. Phys. Soc. (London), A, 62: 167. 1949.
16. TOPPING, J. Proc. Roy. Soc. (London), A, 114: 67. 1927.
17. WATSON, G. N. A treatise on the theory of Bessel functions. 2nd ed. Cambridge University Press, London. 1948.
18. WATSON, G. N. A treatise on the theory of Bessel functions. 2nd ed. Cambridge University Press, London. 1948. pp. 698 and 737.
See also, British Association Mathematical Tables VI (1937) and X (1952). Cambridge University Press, London.
19. WHITTAKER, E. T. and WATSON, G. N. A course of modern analysis. 4th ed. Cambridge University Press, London. 1950. p. 124 (exercise 17 and 18).
20. YOUNG, D. M. Trans. Faraday Soc. 47: 1228. 1951.

THE EFFECT OF THERMAL RADIATION ON THE ELECTRICAL RESISTANCE OF HYDROPHILIC ORGANIC FILMS¹

By C. D. NIVEN

ABSTRACT

When thermal radiation falls on certain organic films it increases their electrical conductivity markedly; these films are all hydrophilic. Gelatin showed this effect in the most satisfactory manner but the noise in the film was quite large. In some cases the relative humidity of the air surrounding the film had a definite influence on the noise but there was apparently some other and more important factor involved which it has not been possible so far to identify and eliminate; consequently the hydrophilic film cannot compete with the inorganic detectors. The films were also found to be electrically sensitive to minute atmospheric pressure changes.

INTRODUCTION

In a previous communication (14), the use of cellophane as a means of detecting thermal radiation has been discussed. It was pointed out that the change in electrical resistance which cellophane undergoes when exposed to heat radiation was not to be accounted for by a process of driving off water molecules because the change noted was in the wrong direction for such an explanation to be valid. Cellophane appeared to respond to slight warming by heat radiation in a manner somewhat similar to that in which a normal semiconductor would respond—the electrical conductivity was improved.

The behavior of cellophane when used as a sensitive element in a bolometer opened up several interesting questions. In the first place, was cellophane the only organic film which would act as a heat detector or were there other organic films which would show a similar effect? In the second place, just exactly why should films of cellophane be so much more sensitive to heat radiation than films of materials like pliofilm if the change in resistance caused thereby was not due to a drying out process? In the third place, what caused the drift of the galvanometer needle of the detector and in fact its general instability which had given so much trouble? In the fourth place, was there any possibility of improving the amplifying device, so that the bolometer might detect far lower radiation densities even if it were impossible to completely overcome the instability?

For brevity the term "radiation effect" is used below to describe the decrease in resistance which a film like cellophane undergoes when thermal radiation falls on it. This effect is much larger than the change in resistance which any, so-called, insulator exhibits when heated.

For all practical purposes the effect can be considered to be a "total radiation" effect and not a "selective" effect caused by particular band widths of the spectrum. One would not expect selectivity because, generally speaking, organic films do not have low-lying energy levels. Furthermore, by employing

¹ Manuscript received March 19, 1953.
Contribution from the Division of Physics, National Research Council, Ottawa, Canada.
Issued as N.R.C. No. 3068.

for the incident radiation the beam from a wide slit in a Perkin-Elmer monochromator, it was shown that the effect was a maximum at the peak of the black body radiation curve and fell off sharply on each side of the peak. Any selective effect, if present at all, can therefore be considered of very secondary magnitude in comparison with the main effect.

CHOICE OF SAMPLES

In choosing samples likely to show the effect, special consideration was given to the outstanding quality which cellulose (1) possesses of adsorbing large numbers of water molecules on the surfaces of the micelles or macromolecules of which it is composed. These water molecules are believed to be held by means of the hydrogen (5, 9) or hydroxyl (6) bond. It seemed possible then that any organic film which possessed an abundance of hydrogen or hydroxyl bonds might also show the radiation effect. To test this idea, gelatin was tried with striking success, because it not only responded to thermal radiation but the drift and unsteadiness of the galvanometer were markedly cut down. Success with gelatin led to the testing of other hydrophilic films and the following showed the effect: potato starch, polyvinyl alcohol, casein, zein, gluten, and egg albumin. In sharp contrast ploofilm, polyethylene, and cellulose acetate which are not hydrophilic failed to show the radiation effect.

Films which are only slightly moisture absorbing will not necessarily show the effect and each of these marginal cases would have to be investigated individually. Only certain substances will form suitable films for testing; even of these only the most easily available have been qualitatively tested; therefore it is too early to state that all organic films which are decidedly hydrophilic are sensitive to thermal radiation; nonetheless it looks as if such a statement may be correct.

PREPARATION OF THE SAMPLES

Cellophane samples were taken from pieces of washed commercial sheets of cellophane 0.0008 in. thick which originally contained no other plasticizer than glycerin. The technique of coating small areas on each side with conducting paint so as to provide contact surfaces for measuring resistance *through* the film was much as described in the previous communication (11) except that conducting neoprene paint was used instead of aquadag. The size of the small areas coated on either side was about 3 sq. mm. The incident radiation had to pass through a rock salt window in a cap which covered the mounting for the film. The film was mounted on brass electrodes screwed into polystyrene; it was found as a rule convenient to attach the film to the electrodes by means of the conducting neoprene paint. Using this technique it was best to coat the ends of the electrodes with the paint after the film had been painted and the paint was dry; then after waiting until the coating on the electrodes was nearly but not quite dry, the film was placed on them in the position desired and pressed down with the finger on each electrode; where it was suspected that contact was poor the spot was touched with some of the paint. This method of mounting the films for the measurements was used with all of the samples where possible; but in some cases where the

sample was not flat or was brittle and thick a small screw screwed into the end of the electrode was needed to help get a firm contact.

The films of gelatin and potato starch were prepared by weighing out 0.1 gm. of substance and dissolving it in 25 cc. of boiling water and then pouring the solution on to a surface of mercury in a petri dish (about 9 cm. in diameter). In the case of the polyvinyl alcohol about 0.5 gm. of the completely hydrolyzed substance was needed. The film of casein had to be pressed out thin in a hydraulic press. The films of zein and gluten were prepared in much the same way as the films of gelatin except that in the case of zein, ethyl alcohol had to be used in place of water and in the case of gluten a solution had to be prepared by one of the biochemical laboratories by a special agitation process. The film of egg albumin was prepared by spreading the white of an egg over the mercury and letting it dry; it formed a thick brittle film which was difficult to handle, but a suitable piece for testing was obtained.

Of the various films gelatin showed the effect in the most satisfactory manner. It could be tanned by pouring a tanning solution over the film before it was removed from the petri dish and some of the most satisfactory results were obtained with tanned films. For tanning solutions either 1 gm. of tannic acid in 25 cc. water or 5 cc. of formaldehyde in 25 cc. water was used.

The thickness of the films of gelatin was around five ten thousandths of an inch.

APPARATUS USED FOR MEASURING THE RADIATION EFFECT

In Fig. 1 is shown the circuit diagram for a d-c. amplifier used in discriminating between films which would show the radiation effect and films which would not.

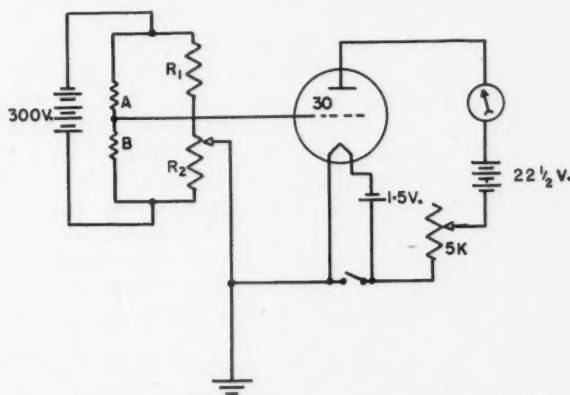


FIG. 1. Circuit diagram of d-c. amplifier of apparatus used for qualitative tests.

In order to get much more amplification it was necessary to use some sort of a-c. amplifier. Since the amount of amplification permissible depended on the magnitude of the signal to noise ratio, the investigation developed into

a study of signal to noise ratios for the tanned and untanned gelatin films. In Fig. 2 is shown the circuit diagram of the a-c. amplifier used for this purpose; it is after a design used by T. M. Dauphinee for another purpose and has the specific quality that it cuts out low frequencies but amplifies frequencies

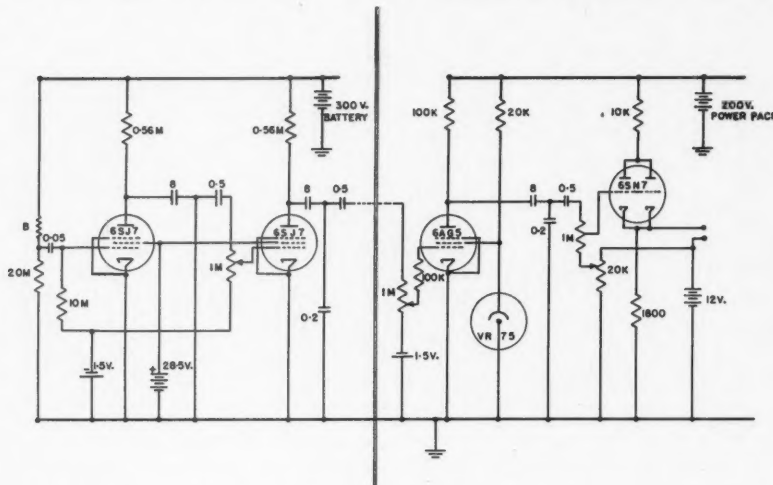


FIG. 2. Circuit diagram of a-c. amplifier used for signal to noise ratio measurements.

of the order of 15 cycles per minute. Instead of using a chopper the signal was flashed on by closing a knife switch and the resulting output from the amplifier was indicated on a chart by the throw of the needle of an Esterline-Angus graphic ammeter. In Fig. 2 the bolometer resistance is indicated by the letter *B*.

The signal which was used in testing bolometers on this amplifier was the radiation from a 25 watt lamp at a distance of 200 cm. The gain controls were adjusted until this signal gave a throw of the needle of about 20 divisions when the switch was closed. The noise was then observed as the width of the trace. If according to the usual convention, the limit of detection be taken as the signal which equals the noise, then a trace of width 1 division indicates a minimum detectable energy density of $25/4\pi(200)^2 \times 20$ watts per sq. cm. In round figures four-fifths of a division indicates a limit of about two microwatts per square centimeter.

Charts showing some special signal to noise records are reproduced in Figs. 3 and 4. The chart paper was marked with curved lines across the line of travel, spaced so that on the slow speed it took 15 min. for the pen to go from one line to the next and on the fast speed 15 sec. In order to be able to compare different films the gain was adjusted before each test so that the 25 watt lamp at 200 cm. gave a swing of the needle equal to about 20 divisions on the chart, measured from peak to peak. It was difficult to hit

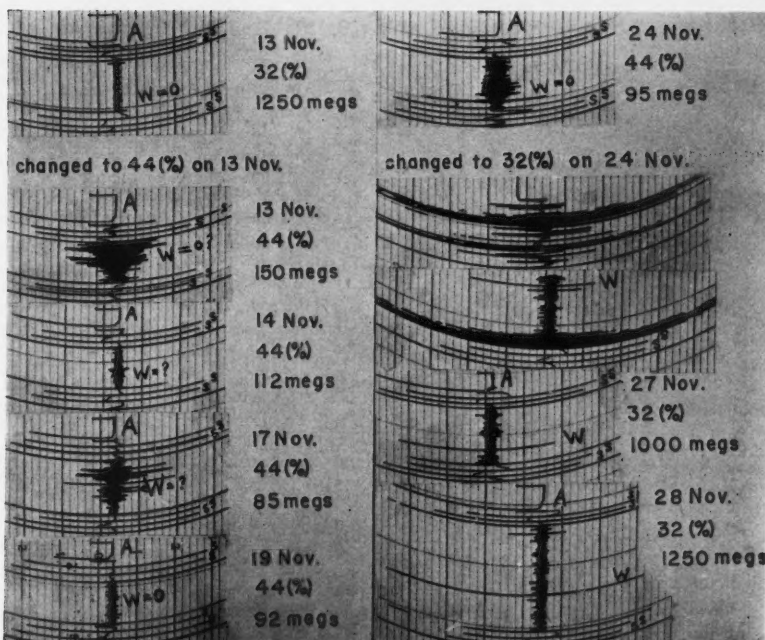


FIG. 3. Signal to noise ratio charts for a film of gelatin tanned in formaldehyde. Note that although the resistance of the film is the same at the beginning and at the end, its character has changed by being exposed to a higher relative humidity and then again to the lower one.

this figure exactly and in many of the records the swing is about 25 divisions because it was preferable to have the signal too large rather than too small since the test of good performance was the smallness of the corresponding noise. After the adjustment of the gain controls had been completed the following procedure was adopted. The first, that is to say the lowest line, was put on by passing the warm hand in front of the bolometer to mark the start of the record. The recording galvanometer was then put on the high speed and the switch to the 25 watt lamp was closed to give the galvanometer needle a throw; after the needle had returned to zero, the switch was opened again which caused another throw. These are marked SS on the chart. The speed of the recorder was then changed to slow, a metal cap was placed over the front of the bolometer to prevent stray heat radiation from entering the window, and the instrument was left to record for about 15 min. Once during that period a pressure change in the atmosphere of the room was made in order to get a qualitative indication of the bolometer's pressure sensitivity. This is marked on the chart with the letter W. After the noise had been recorded the bolometer was taken out of its socket in the amplifier and the terminals thus exposed were covered with the metal cap to shield them from electrical effects. The amplifier noise was then recorded. The width of the trace at A

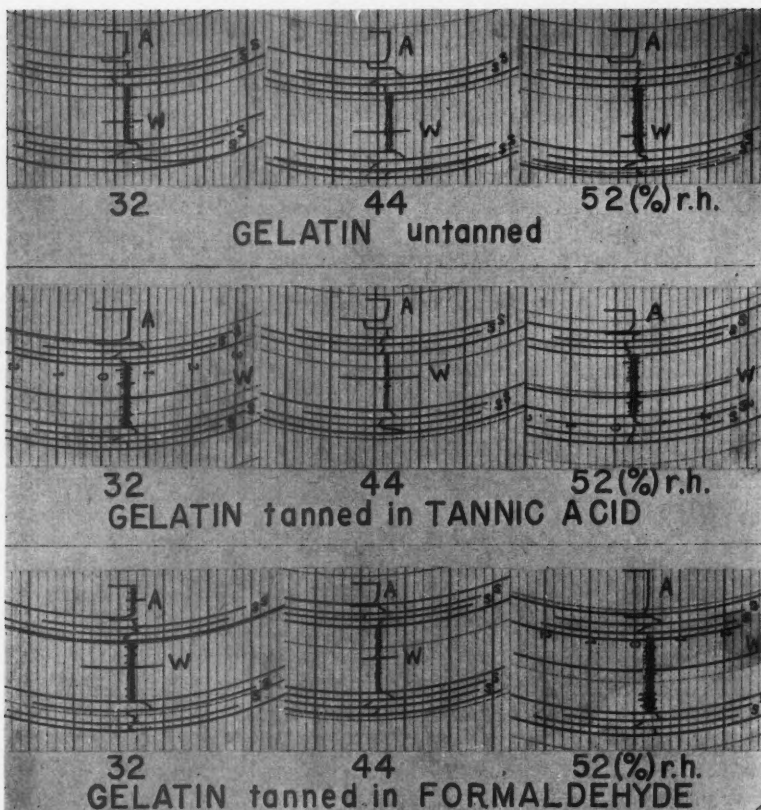


FIG. 4. Signal to noise ratio charts for selected untanned and tanned gelatin films exposed to air at three different relative humidities. The signal is indicated by \bar{S} , the noise by the width of the trace in the central part of each chart.

gives a measure of this and it was found to be as a rule negligible; only when the resistance of the film was large so that the gain was turned up high did the amplifier noise become important. Throughout this procedure the gain control was not touched.

SIGNAL-TO-NOISE RATIO MEASUREMENTS

Using the a-c. amplifier just mentioned, extensive work was done on the signal to noise ratios of films of gelatin and gelatin tanned in tannic acid or in formaldehyde. The reason why the study was confined to these films is that they were the ones which gave the largest ratio in the early work. It must not, however, be assumed that the performance of some other films might not be good too but in order to cut out one of the variables in the confusion of data, the work was narrowed down to the type of film which showed up

best in the preliminary trials. Even when the effort was thus focused on one substance the task of explaining and coordinating the results was very difficult because they defied generalizations.

The resistance of these films changes enormously with changes in the lower range of the relative humidity of the air surrounding them. A film of gelatin measuring around 100 megohms at 52% will probably measure around 1500 megohms at 32%. It was therefore not unreasonable to suppose that moisture changes might affect the performance of the films as radiation detectors; indeed early experiments had shown that when the air was evacuated from a bolometer the sensitivity of a film was ruined altogether.

Bolometers were accordingly designed so that the tube containing a saturated salt solution could be changed easily. The three salts calcium chloride, potassium carbonate, and sodium dichromate were used to give respectively 32%, 44%, and 52%. With this technique it was possible to keep a film for long periods at a particular humidity without having to monopolize some elaborate humidity control equipment during that time. The question of how long a film has to be left at a particular humidity to reach equilibrium is an important point. The main change in noise probably comes about in 24 hr. but the resistance has certainly not always completely changed in that time; furthermore the noise may change later too. Forty hours was considered to be sufficiently long to wait for the purpose of deciding whether noise had increased or decreased or was unchanged.

The following observations were made:—

1. Some films repeat their noise values fairly well after having had the humidity changed to one of the other two humidities and then back to the original humidity: others do not. If the noise happens to be exceptionally low to start with, repetition of the exceptionally low value rarely, if ever, occurs.
2. All the gelatin films investigated, which had normal resistance values, showed less noise at 32% than at 52% relative humidity. In some cases this difference was slight but in others it was much more marked.
3. When the humidity is changed from 32% to 52% and back to 32% and then back to 52%, the noise at 52% may vary considerably even if the noise at 32% repeats well. One record indicated a variation of seven times.
4. Noise may suddenly change. This does not necessarily indicate that the film is bad permanently but rather that a change is happening inside which is manifested as spontaneous electrical disturbance. The best instance of this is shown in Fig. 3 where a film clearly underwent a change of character by being changed from 32 to 44% and then back again to 32%. The change in character is indicated by the appearance of pressure sensitivity as well as by the noise record; the resistance, however, repeated well.
5. Occasionally a film which has been acting well will give full scale noise signals which will not disappear with time. Films of untanned gelatin appear more likely to do this than those which are tanned. It has not been observed with the quietest films of either tanned or untanned gelatin provided the humidity is kept constant; it is most likely to happen with a film of unusually high resistance.

It is quite evident that to try and find general laws which apply even in the small range of humidity under discussion is out of the question. The nearest approach to a general law is that lowering the humidity reduces the noise, but this is certainly not true in every case. The fact that it does occur is, however, of importance because lowering the humidity increases the resistance. This, then, means that increase of resistance can be accompanied by reduction in noise—an observation which suggests a different type of noise to that with which radio engineers commonly deal. Merely lowering the humidity will not always make a noisy bolometer quiet, nor will it necessarily elevate the quiet bolometer into the exceptionally quiet class. This implies that there must be something more than the amount of vapor that determines the noise. To extend the range of humidities would therefore not help at all in the search for quiet films.

Just to demonstrate the fact that comparatively quiet bolometers can be found at all of the three humidities under discussion an array of nine charts is shown in Fig. 4. Each of these indicates a signal to noise ratio of about 20 or better. The records at the three relative humidities do not refer to the same film but merely to the same type of film. Taken by itself Fig. 4 would suggest that relative humidity has little to do with the noise but this would be a very superficial and erroneous conclusion because Fig. 3 on the other hand suggests that humidity can entirely change the character of the film. Taking these two pieces of evidence together one is simply forced to the conclusion that while the relative humidity of the air surrounding the film plays some tremendously important part in the creation and elimination of noise in these films, there is some other factor, which is still more important, to take into account in explaining why some films are exceptionally quiet and others are not.

COMPARISON OF FILM BOLOMETER WITH OTHER DETECTORS

Fig. 4 suggests that if peak to peak values of signal and noise be employed, the 25 watt lamp at 2 meters swings the needle at best about 25 times as much as the width of the trace caused by the noise. From the calculation explained in an earlier paragraph this means that the minimum energy density which the film can detect is 2 microwatts per sq. cm. Since the area of the bolometer is about 0.03 sq. cm. this implies that the minimum signal it will detect is $2 \times 0.03 \times 10^{-6}$ watts. An unbacked thermistor bolometer (4) with a receiving area of 0.6 sq. mm. has a limiting signal of 1×10^{-10} watts; therefore it is not difficult to see that the film cannot compete with the inorganic materials as a sensitive element.

It is nonetheless of interest to give to the gelatin film an approximate rating in comparison with other detectors. Jones, in three papers (10, 11, 12) referred to by their author as Papers I, II, and III, has specified an over-all figure or factor of merit for detectors of infrared radiation. Unfortunately the calculation of this factor of merit requires very many more data than are readily available.

Jones's factor of merit M_2 is given by the equation

$$M_2 = 3.0 \times 10^{-12} A^{\frac{1}{2}} / P_m \tau$$

where A = area of detecting surface in sq. mm.,

τ = time constant in seconds,

P_m = noise equivalent power (in watts) in "reference condition A", as specified by Jones in Paper II.

The values τ and P_m are therefore required. Neither of these is available in the form that is specified by Jones, but values can be assigned to them which will give to M_2 an approximate value and thus determine its order of magnitude.

Instead of the special reference time constant which Jones specifies it is proposed to take the ordinary time constant which turns up in the differential equation for a body being heated, namely the time it takes to reach $(1 - 1/e)$ of its final value. By means of the d-c. amplifier referred to above this time constant was shown to be about one second.

P_m is given by Jones as equal to

$$P \times \frac{R_s}{R_0} \times \left(\frac{1/4\tau}{\Delta f} \right)^{\frac{1}{2}} \left(\frac{N(f_s)}{N_{\max}} \right)^{\frac{1}{2}}$$

where P = noise equivalent power measured under conditions which are different from "reference condition A" of Jones's Paper II,

R_s = ratio of responsivity to noise at signal frequency,

R_0 = ratio of responsivity to noise at zero frequency,

Δf = noise band width of the amplifier,

$N(f)$ is power spectrum of noise,

f_s is frequency of a sinusoidal radiation signal.

None of these factors are readily available. However, with some approximations a value of the right order of magnitude can be obtained. If peak to peak values are taken, P can be evaluated from Fig. 4 and as explained above it is under these circumstances equal to 6×10^{-8} watts. R_s/R_0 is a fraction because the ratio of responsivity to noise is greatest at zero frequency according to Fig. 1 in Jones's Paper II. $N(f_s)/N_{\max}$ is also a fraction by definition of N_{\max} . Therefore by ignoring $R_s/R_0 \times (N(f_s)/N_{\max})^{\frac{1}{2}}$ in the expression for P_m one virtually increases the value of P_m .

To give to Δf an approximate value, the band width of the amplifier has been taken: this was equal to 0.6 c.p.s. P_m therefore is smaller than $6 \times 10^{-8} \times (\frac{1}{4}/0.6)^{\frac{1}{2}}$. This expression equals 3.88×10^{-8} . Substituting in the formula $M_2 = 3.0 \times 10^{-12} A^{\frac{1}{2}}/P_m \tau$, $A = 3$ sq. mm., $\tau = 1$ sec., and for P_m a value less than 3.88×10^{-8} watts, M_2 works out to have a value greater than 1.34×10^{-4} . The poorest figure listed in Jones's Paper III is 4.29×10^{-3} , while figures greater than 2×10^{-1} are listed for many bolometers. On the whole then the results suggest that the film's response to heat radiation may help to explain something about the internal electrical behavior of the film but is unlikely to add anything important to the technique of heat detection. The best that can be said is that if the factor of merit had taken into account ease of amplification, the film bolometer might have shown up to much better advantage because the early work with single stage amplification was encouraging.

SENSITIVITY OF GELATIN FILMS TO PRESSURE CHANGES

It was observed that these films were highly sensitive to sudden pressure changes in the atmosphere of the room, caused for instance when a door was suddenly drawn inwards. As the pressure change had to pass through the cap of the bolometer, it was not possible to compare pressure effects for different bolometers.

By means of a manometer and levelling bulb connected to a special bolometer cap it was found that by increasing the pressure suddenly from 17 cm. Hg below atmospheric pressure to 13 cm. Hg above atmospheric pressure a decrease of about 25% in the resistance value for gelatin occurred. It was observed, however, that the change was not permanent and at the higher pressure or at the lower pressure the resistance drifted back after a few seconds to the value registered at atmospheric pressure.

Cellophane was found to behave in a similar manner. One must therefore regard this temporary change of conductivity with sudden change of pressure as something which any adequate theory on the hydrophilic substances will have to explain.

THE QUESTION OF THE ELECTRICAL INSTABILITY OF THE FILM

While this was listed as one of the four questions that had to be answered in connection with cellophane, the results of the present investigation only warrant the very general answer that it is because the film is hydrophilic that it is unstable. To go farther by way of explanation leads into some very debatable points on which the best authorities in the field differ—concerning for instance (1) the internal structure of a hydrophilic organic substance (1, 7, 3), (2) whether the adsorbed water is a monomolecular layer or a poly-molecular layer (2), (3) the mechanism whereby these substances conduct electricity at all (13, 15, 16, 8). It is desirable nonetheless to have some sort of mental picture, however inadequately proved; the one which the writer favors is a basic structure of insulating micelles with interstices in which water molecules are held either directly to the micelles as the original Langmuir hypothesis demands or indirectly by one or more other molecules as the Brunauer, Emmett, and Teller hypothesis permits, the water molecules forming thereby an incomplete and probably distorted water structure (17) inside the interstices, bridging across from micelle to micelle.

The incompleteness of the water lattice might permit of alternative arrangements of the atoms, thus giving a highly unstable structure electrically which might turn up as noise on a high gain amplifier. Warming of the film by radiation appears to increase the "activity" of the adsorbed water which in turn increases the conductivity.

SUMMARY OF CONCLUSIONS

1. Cellophane is not unique in being electrically sensitive to thermal radiation; gelatin and several other strongly hydrophilic organic films are also sensitive.
2. The effect is not a "selective" effect connected with some band in the infrared spectrum but a total radiation effect.

3. Gelatin, either tanned or untanned, shows the effect in a more satisfactory manner than any of the other films tried. For this reason its signal to noise ratio has been investigated. Results indicate that noise remains at such a high level that even with selected films the limiting detectable radiation energy density is around 2 microwatts per sq. cm.

4. The effect of changing the relative humidity in the air surrounding the film usually has marked effects on the behavior of the film as a heat detector.

5. Films of gelatin and of cellophane have been found to be electrically sensitive to very small changes of pressure. Sudden increase of pressure causes a temporary decrease in resistance.

ACKNOWLEDGMENTS

The writer would like to express grateful acknowledgment to Dr. T. M. Dauphinee for the design of a suitable electronic device without which this investigation could not have been undertaken; to Dr. I. E. Puddington, Director of the Division of Applied Chemistry, for much helpful advice in the selection of films; to Dr. A. E. Douglas for demonstrating by means of the Perkin-Elmer Infrared Monochromator that the radiation effect discussed above was a total radiation effect; and to Mr. A. S. Runciman of the Shawinigan Power Company for an electronic circuit design.

REFERENCES

1. ARGUE, G. H. and MAASS, O. Can. J. Research, A, 24: 93. 1946.
2. BABBITT, J. D., Can. J. Research, A, 20: 143. 1942.
3. BANGA, I. and SZENT-GYÖRGYI, A. Science, 92: 514. 1940.
4. BECKER, J. A. and MOORE, H. R. J. Opt. Soc. Amer. 36: 354. 1946.
5. BERNAL, J. D. and FOWLER, R. H. J. Chem. Phys. 1: 515. 1933.
6. BERNAL, J. D. and MEGAW, H. D. Proc. Roy. Soc. (London), A, 151: 384. 1935.
7. ELLIS, J. W. and BATH, J. J. Am. Chem. Soc. 62: 2859. 1940.
8. EVANS, M. G. and GERGELY, J. Biochim et Biophys. Acta, 3: 188. 1949.
9. HUGGINS, M. L. J. Org. Chem. 1: 407. 1936.
10. JONES, R. C. J. Opt. Soc. Amer. 37: 879. 1947.
11. JONES, R. C. J. Opt. Soc. Amer. 39: 327. 1949.
12. JONES, R. C. J. Opt. Soc. Amer. 39: 344. 1949.
13. MURPHY, E. J. and LOWRY, H. H. J. Phys. Chem. 34: 598. 1930.
14. NIVEN, C. D. Can. J. Research, A, 24: 93. 1946.
15. SMEKAL, A. Z. Physik, 45: 869. 1927.
16. SZENT-GYÖRGYI, A. Science, 93: 609. 1941.
17. WEYL, W. A. J. Colloid Sci. 6: 389. 1951.

THE EMISSION SPECTRUM OF ALUMINUM MONOFLUORIDE I¹

By S. M. NAUDÉ AND T. J. HUGO

ABSTRACT

Two band systems of the emission spectrum of AlF are described, viz. the far ultraviolet $A^1\Pi - X^1\Sigma$ system discovered by Rochester in absorption, and a new system due to a $^1\Sigma - A^1\Pi$ transition in the region 8175 Å–6670 Å. A revised vibrational analysis of the $A^1\Pi - X^1\Sigma$ system is given as well as the vibrational and rotational analyses of the new system, which is the $C^1\Sigma - A^1\Pi$ system of AlF.

(A) INTRODUCTION

The spectrum of AlF has been studied by Rochester (2), Yuasa (4), Rowlinson and Barrow (3), and the authors (1). Rochester studied the spectrum in absorption and found a very symmetrical and strong system of bands in the region 2360 Å–2200 Å. These bands were identified by him as the expected $A^1\Pi - X^1\Sigma$ system of AlF, and he gave the following equation for the vibrational structure:

$$\nu = 43,935 + 822.9(v' + \frac{1}{2}) - 8.5(v' + \frac{1}{2})^2 - 0.187(v' + \frac{1}{2})^3 - 814.5(v'' + \frac{1}{2}) + 8.1(v'' + \frac{1}{2})^2.$$

Yuasa, Rowlinson, and Barrow and the authors studied the emission spectrum. Yuasa, using a heated discharge tube, observed a number of bands in the violet and near ultraviolet which he ascribed to the AlF molecule, but which were later identified by Rowlinson and Barrow (3) as belonging to the sulphur molecule. Rowlinson and Barrow observed the $A^1\Pi - X^1\Sigma$ system in emission, as well as a complex system in the near ultraviolet, another complex system in the yellow-green, and some double-headed bands above 6600 Å. The first two systems were analyzed by these authors, who gave the following equation for the vibrational structure of the $A^1\Pi - X^1\Sigma$ system:

$$\nu = 43,947.6 + [803.95(v' + \frac{1}{2}) - 6.14_1(v' + \frac{1}{2})^2 - 0.0039_1(v' + \frac{1}{2})^4] - [801.5_2(v'' + \frac{1}{2}) - 4.7_0(v'' + \frac{1}{2})^2 + 0.01_0(v'' + \frac{1}{2})^3].$$

The present authors made new exposures of the AlF bands on a 21-ft. concave grating. A specially designed hollow cathode discharge tube was used and several new band systems were discovered. A preliminary report (1) of this work has already been published, and the present paper gives further details of two of the strongest singlet systems, viz. the far ultraviolet $A^1\Pi - X^1\Sigma$ system and the new $C^1\Sigma - A^1\Pi$ system in the red and near infrared region.

Manuscript received July 8, 1953.

Contribution from the National Physical Laboratory, Council for Scientific and Industrial Research, Pretoria, Union of South Africa.

The work described in the present paper was carried out by one of us (T. J. H.) in part fulfillment of the requirements for the D. Sc. degree of the University of Stellenbosch.

(B) EXPERIMENTAL

The hollow cathode was constructed from a 2 cm. diameter stainless steel cylinder. The cavity was 5 cm. long and had a diameter of 1.4 cm. The open end could be closed by means of a snug-fitting stainless steel diaphragm having a 2 mm. aperture in its center. The other end of the hollow cathode was rigidly connected to a water-cooled invar-steel cone which fitted into a standard B-29 socket. This socket formed the one end of the 2.4 cm. diameter quartz discharge tube. The other end of the tube was closed by means of a water-cooled quartz window. The anode was a hollow nickel-iron cylinder of 2.2 cm. outer diameter.

The hollow cathode discharge tube, which was used horizontally, formed part of a small vacuum system in which a single stage mercury diffusion pump circulated highly purified helium at a pressure of about 4 mm. Helium gas served as carrier of the discharge.

The AlF bands were excited in the discharge when an intimate mixture of high purity aluminum powder and dehydrated aluminum fluoride powder was placed inside the hollow cathode. It was found convenient to compress these chemicals into small pellets before they were placed in the hollow cathode.

A 3 kva. transformer giving 1500 volts in the secondary circuit and an appropriate rectifying unit were used to pass the discharge through the tube. A secondary current of 0.6 amp. was used. The discharge usually stabilized in about ten minutes. At this stage the hollow cathode was at a bright red heat and the AlF bands were emitted with great intensity and remarkable purity.

Preliminary exposures of the AlF bands were made on medium and low dispersion instruments. The final plates were taken on the 21-ft. concave grating of the University of Stellenbosch. The grating has 15,000 lines per inch and is mounted according to Paschen.

(C) THE ULTRAVIOLET $A^{\prime}\Pi - X^{\prime}\Sigma$ SYSTEM(1) *Vibrational Analysis*

This system was photographed in the first and second orders of the grating. The exposure times varied from one minute for the strongest bands in the (0,0) sequence to one hour for the weak bands of the (1,0) sequence. On these plates the band heads were sufficiently resolved to permit a vibrational analysis.

The appearance of this system in emission was described by Rowlinson and Barrow (3), who also gave the frequencies, estimated intensities, and directions of degradation of the different bands. The frequencies of the band heads, as determined from the grating spectrograms, are almost identical to the frequencies as determined by Rowlinson and Barrow and will not be given in this paper. The same vibrational quantum numbers were also assigned to the different bands, but the authors obtained the following, slightly different, equation for the vibrational structure:

$$\nu_Q = 43,947.0 + [804.6_3(v' + \frac{1}{2}) - 6.3_5(v' + \frac{1}{2})^2 - 0.0028_6(v' + \frac{1}{2})^4] \\ - [801.0_3(v'' + \frac{1}{2}) - 4.7_5(v'' + \frac{1}{2})^2 + 0.01_8(v'' + \frac{1}{2})^3].$$

A summary of the vibrational constants is given in Table III, together with the constants of the infrared system which has its lower state in common with the upper state of this system.

(2) Rotational Analysis

The strongest bands of the (0,0) and (0,1) sequences were photographed in the seventh and ninth orders of the grating respectively. The rotational structure was, however, still unresolved owing to the strong overlapping of successive bands in these sequences. The other bands were too weak to photograph in the high orders and consequently a rotational analysis could not be made.

(D) THE RED AND INFRARED $C^1\Sigma - A^1\Pi$ SYSTEM

(1) Vibrational Analysis

These bands were photographed in the first and second orders of the concave grating. In the second order the rotational structure was well resolved. In Plate I a second order spectrogram of the (0,0) band is reproduced.

This system consists of four obvious sequences of violet degraded double-headed bands. Accordingly the bands could be arranged into a Deslandres scheme without difficulty. Details of the band heads, formed by the P branches, are given in Table I.

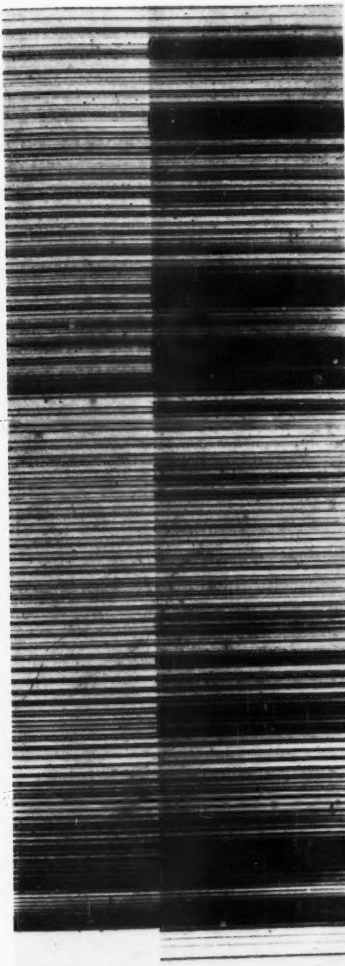
TABLE I
BAND HEAD DATA OF THE $C^1\Sigma - A^1\Pi$ SYSTEM

Wave length (Å)	Wave number (cm. ⁻¹)	Intensity	Assignment ($v'v''$)
8175.4	12,228.4	4	0, 2
8068.8	12,390.0	2	1, 3
7963.2	12,554.3	0	2, 4
7858.6	12,721.4	0	3, 5
7686.2	13,006.8	6	0, 1
7600.5	13,153.5	3	1, 2
7512.8	13,307.0	0	2, 3
7245.9	13,797.1	10	0, 0
7174.7	13,933.7	3	1, 1
6789.9	14,723.7	6	1, 0
6732.1	14,850.1	4	2, 1
6674.9	14,978.3	1	3, 2

Since the rotational analyses of all the bands were available, the various band origins were determined graphically, using the Q branch data and the equation $Q(J) = \nu_0 + (B'_0 - B''_0)J(J+1)$. The band origins were arranged in the Deslandres scheme given in Table II. The following equation gives the frequencies of the band origins of the $C^1\Sigma - A^1\Pi$ system:

$$\nu = 13,739.55 + [938.39(v' + \frac{1}{2}) - 5.18(v' + \frac{1}{2})^2] \\ - [804.63(v'' + \frac{1}{2}) - 6.34(v'' + \frac{1}{2})^2].$$

PLATE I



The (0,0) band of the $C^{\prime}\Sigma - A^{\prime\prime}\Pi$ system.

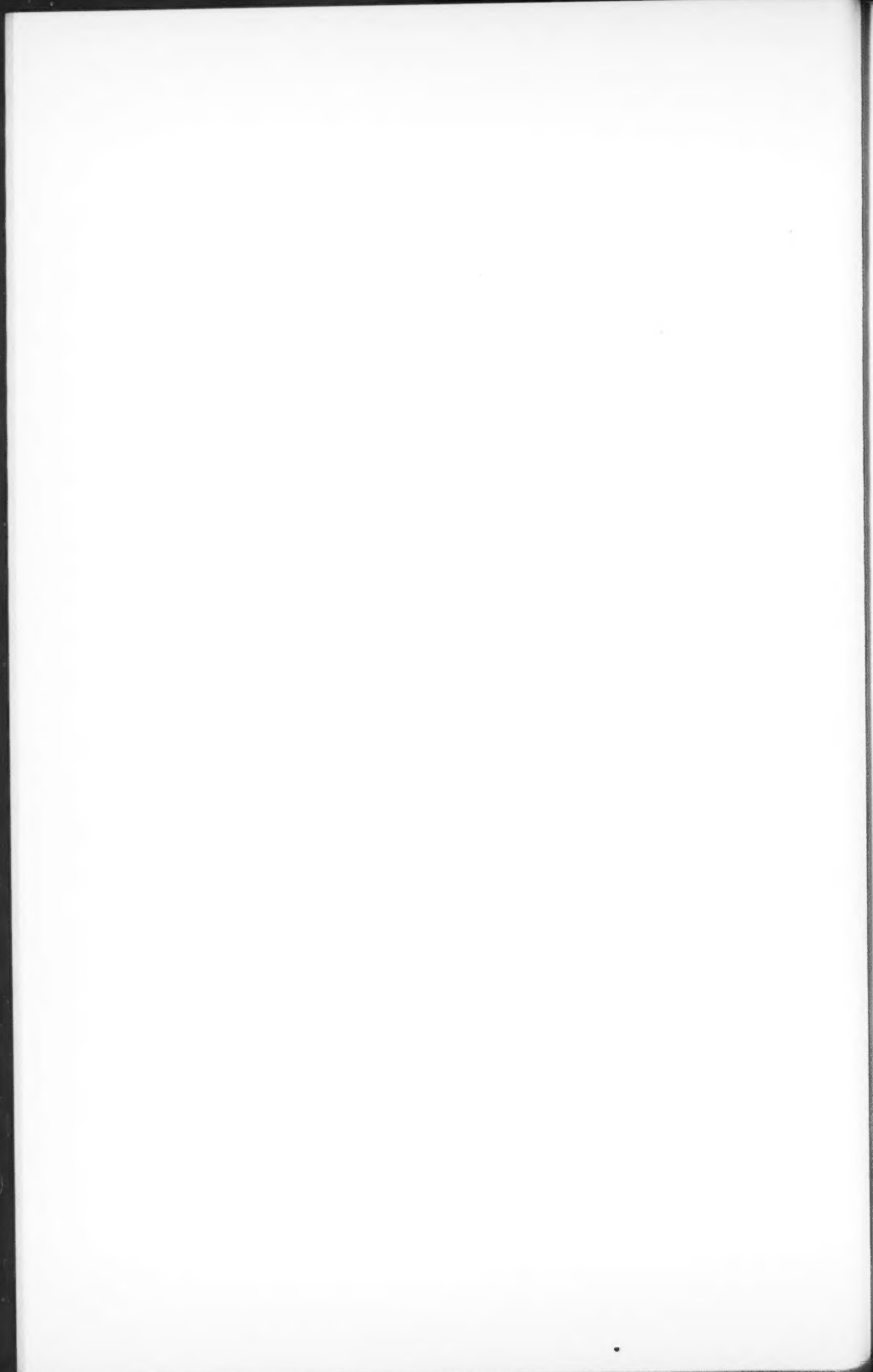


TABLE II
DESLANDRES SCHEME FOR THE $C^1\Sigma - A^1\Pi$ SYSTEM

v''	0	1	2	3	4
v'					
0	13,806.70	13,014.78	12,235.52		
1	14,734.78	13,942.80	13,163.52	12,396.85	
2		14,860.48		13,314.51	12,560.83
3			14,988.34		

TABLE III
VIBRATIONAL AND FORCE CONSTANTS* OF THE $X^1\Sigma$, $A^1\Pi$, AND $C^1\Sigma$ STATES OF AlF

Constant	$X^1\Sigma$	$A^1\Pi$	$C^1\Sigma$
ν_0	—	43,947.0	13,739.55
ν_{00}	—	43,948.4	+ 43,947.0
ω_e	801.03	804.63	938.39
ω_0	796.2 ₈	798.29	933.21
ω_{ex_e}	4.75	6.34	5.18
k_e	4.212×10^6	4.250×10^6	5.781×10^6

* Conversion factors were obtained from "Spectra of diatomic molecules", Second Edition (D. Van Nostrand Company, Inc., New York, 1950) by Gerhard Herzberg.

In Table III a summary of the vibrational constants of the two systems discussed is given. Because the $A^1\Pi$ state is common to both systems, only the more accurate values, obtained from the near infrared system, are given in Table III.

(2) Rotational Analysis

The second order spectrograms revealed the presence of three branches, viz. single P , Q , and R branches, with the Q branch the most intense.

The intensities of the lines of the (0,0) band were measured on a recording photometer. According to these measurements the P branch is more intense than the R branch for low values of the rotational quantum number, thus indicating a $^1\Sigma - A^1\Pi$ transition. Furthermore, the $P(1)$ line could be identified on the photometer record, thereby verifying the above conclusion about the type of transition. A number of other singlet systems were also observed and it was established that this $^1\Sigma$ state is probably the $C^1\Sigma^+$ state of AlF. In Table IV the wave numbers of the lines of some bands are given.

In Table V the combination differences $\Delta_2 F'(J)$, $\Delta_2 F_c''(J)$, and $\Delta_2 F_d''(J)$ are given.

The rotational constants were determined from the combination differences $\Delta_2 F'(J)$ and $\Delta_2 F''(J)$, which are given by the following relations:

$$\Delta_2 F'(J) = R(J) - P(J),$$

$$\Delta_2 F_c''(J) = R(J-1) - P(J+1),$$

$$\Delta_2 F_d''(J) = [R(J) - P(J)] - [Q(J+1) - Q(J-1)].$$

TABLE IV

WAVE NUMBERS IN CM.⁻¹ OF THE LINES OF THE (0,0), (0,1), (0,2), (1,0), (1,1), AND (1,2) BANDS
OF THE C¹ Σ - A⁴ Π SYSTEM OF AlF

J	(0,0) Band λ head = 7245.9 Å			(0,1) Band λ head = 7686.2 Å			(0,2) Band λ head = 8175.4 Å		
	R	Q	P	R	Q	P	R	Q	P
2		13806.95	13804.55						
3		07.13	03.61						
4	13813.32	07.47*	02.70						
5	14.85*	07.74	01.87						
6	16.37	08.15	01.08						
7	18.01	08.68*	00.39						
8	19.60*	09.17	13799.76						
9	21.52	09.77	99.26						
10	23.40	10.46	98.70						
11	25.44*	11.21	98.27						
12	27.29	12.02	97.89						
13	29.38	12.88*		13021.00					
14	31.48	13.83			22.08*				
15	33.69	14.85*			23.12				
16	35.90	15.95*			24.31				
17	38.30*	17.11		13045.51	25.53*				
18	40.67	18.30			48.05	26.91			
19	43.18*	19.60*			50.64	28.30	13007.22*	73.23*	
20	45.66	20.94			53.31	29.82	07.53*	76.07	
21	48.26	22.41	97.77		58.89	33.05*	08.45*	82.08	
22	50.92	23.88	98.10		61.81	34.77	09.02	85.24	58.20
23	53.65	25.36*	98.50		64.80	36.58	09.70	88.50	60.00
24	56.47	27.08*	98.97		67.85	38.47	10.44	91.82	62.46
25	59.31	28.81	99.41		70.91	40.45	11.25	95.49	64.68
26	62.27	30.57	13800.12		74.22	42.50	12.12	98.82	66.94
27	65.36*	32.41	00.79		77.55	44.64	13.10		36.61*
28	68.34*	34.30	01.54		80.94	46.85*	14.14	12306.05	72.00
29	71.51	36.28	02.35		84.40	49.12	15.29	09.87	37.95
30	74.72	38.38*	03.24		87.96	51.51	16.50	13.73	40.70
31	78.00	40.42	04.20		91.59	53.97	17.76	17.71	42.25
32	81.35	42.61	05.23		95.30	56.50	19.18	21.79*	50.10
33	84.76	44.87	06.32		99.06	59.11	20.62	25.90	43.87*
34	88.25	47.19	07.47*	13102.95	61.81	22.08*	30.16	89.05	49.24*
35	91.81	49.60	08.68*	06.91	64.60	23.76	34.49	92.23	51.34
36	95.43	52.03	10.03	10.92	67.44	25.53*	38.93	95.46*	53.40*
37	99.14	54.57	11.41	15.04	70.39*	27.22	43.41	98.82	55.63
38	13902.91	57.13*	12.88*	19.23	73.41*	29.03	48.04		57.95
39	60.75	59.83*	14.36	23.49	76.51	31.05	52.72	12305.81	60.30
40	10.65	62.57	15.95*	27.83	79.70	33.05*	57.51	09.44	62.79
41	14.64	65.36	17.63	32.25	82.97	35.18*	62.39*	13.16	65.35
42	18.70	68.34*	19.36	36.77	86.32	37.38	67.38	16.97*	68.03
43	22.80	71.25	21.17	41.38	89.74	39.65	72.46	20.88	70.78
44	26.99	74.25	23.06	46.03	93.27	42.01	77.57	24.86	73.65
45	31.25	77.35	25.01	50.78	96.87	44.47	82.86	28.95	76.58*
46	35.50	80.49	27.08*		13100.51	46.85*	88.19	33.16	79.63
47	39.98	83.75	29.14	60.49	04.28	49.58	93.62	37.41	82.77
48	44.44	87.04	31.32		08.10	52.30	99.16	41.36	85.98
49	48.99	90.43	33.54		12.04	55.07	12404.79	46.25	89.32
50	53.58	93.89	35.90		16.05	57.95	10.56	50.82	92.77
51	58.26	97.40	38.30*	13901.00	20.14	60.89	16.45		
52	63.92	101.00	40.47		24.29	63.93		60.1	
53	67.84	04.67	43.18*		28.57	67.05		65.05	
54	72.73	08.41	45.83		32.89	70.39		70.00	
55	77.69	12.22	48.51		37.32	73.41		75.03	
56	82.74	16.12	51.27		41.85	76.93*		80.17	
57	87.84*	19.79	54.10		46.40	80.41		85.39	
58	93.02*	24.12	57.13		51.08			90.73	
59	98.27	28.23	59.83*		55.83	87.59		96.16	
60	14003.60	32.41	63.03		91.30			12401.67	
61	09.01	36.65	66.17						
62	14.47	40.99	69.39						
63	20.01	45.38	72.65						
64	25.60	49.87	76.01						
65	31.37	54.43	79.45						
66	37.09	59.04*	82.96						
67		63.74	86.56						
68		68.53	90.21						
69		73.38	93.89						
70		78.31	97.76						
71		83.31	13901.66						
72		88.40	05.73						
73		93.58							
74		98.78							
75		14004.12							
76		09.50							
77		14.99							
78		20.52							
79		26.19							
80		31.88							
81		37.64							
82		43.51							
83		49.43							

* Lines marked with an asterisk could not be measured accurately.

TABLE IV (concluded)

J	(1,0) Band λ head = 6789.9 Å			(1,1) Band λ head = 7174.9 Å			(1,2) Band λ head = 7600.5 Å		
	R	Q	P	R	Q	P	R	Q	P
8	14736.77						13166.41		
9	37.35			13945.99			67.13		
10	37.99			46.69			67.94		
11	38.57			47.46			68.84		
12	39.32			48.31			69.79		
13	40.04			49.07			70.82		
14	40.84			50.17			71.96		
15	41.73			51.21			73.16		
16	14762.50	42.67		13972.21*	52.30		74.44	13155.83	
17	64.68	43.69*		74.50	53.58		75.75*	56.04	
18	66.88	44.73		76.90	54.73		77.28	56.34	
19	69.17	45.83		79.42	56.07	13934.01	78.80	56.70	
20	71.52	47.03		82.00*	57.47	34.26*	80.42	57.15	
21	73.88	48.25		84.59	59.00*	34.57*	82.12	57.68	
22	76.34	49.54		87.30	60.44	34.98*	83.88	58.28	
23	78.85	50.86		92.08	62.05	35.45	85.78	59.01	
24	81.43	52.20		93.00*	63.75	35.84*	86.69	59.81	
25	84.08	53.76	14724.76	95.81	65.50	36.46	89.70	60.67	
26	86.78	55.30	25.10	98.83	67.31	37.10	91.81	61.62	
27	89.51	56.88	25.53	14001.86	69.17	37.84	96.64	93.99	62.63
28	92.33	58.50	26.03	94.98	71.14	38.64	90.13	96.27	63.74
29	95.18	60.25	26.59	98.19	73.15	39.52	93.61*	98.60	64.97
30	98.10	62.01	27.22	11.44	75.25	40.40*	37.18*	13201.03	66.25
31	14801.12	63.83	27.87	14.75*	77.42	41.47	40.87	03.57	67.61
32	04.17	65.71	28.63	18.17	79.68	42.56	44.61	06.14	69.03
33	07.15*	67.68	29.41	21.63	82.00	43.74	48.48	08.81	70.59
34	10.44	69.68	30.27	25.25*	84.35	44.99*	52.37	11.57	72.17
35	13.66	71.75	31.19	28.78	86.83	46.27	56.37	14.41	73.88
36	16.91	73.88	32.19	32.44	89.34	47.65	60.47*	17.31	75.75
37	20.31	76.07	33.24	36.20	91.96	49.07	64.58*	20.34	77.50
38	23.71*	78.31	34.34	40.02	94.61	50.62	68.86	23.44	79.46
39	27.20	80.63	35.54*	43.90	97.35	52.30	26.64	81.48	
40	30.70	82.97	36.77	47.89	14000.18	53.90	77.58	29.89	83.62
41	34.32	85.41	37.99	51.91	03.06	55.63	82.11	33.24	85.78
42	37.96	87.92	39.32		06.04	57.47	86.69	36.65	88.09
43	41.66	90.47	40.84	60.20	09.07	59.32	91.32	40.14	90.47
44	45.42	93.11	42.30	64.44	12.16	61.32	96.11	43.76	92.92
45	49.27	95.75		68.77	15.32	63.39	13300.89	47.45	95.48
46	53.16	98.50	45.45	73.22	18.58	65.50	05.81	51.21	98.09
47	57.13	14801.29		77.64	21.90	67.66		55.05	
48	61.13	04.17		82.17	25.25	69.88		58.99	
49	65.20	07.15	50.65	86.80	28.78	72.21		62.99	
50	69.35	10.07	52.52	91.48	32.30	74.64		67.08	
51	73.51	13.14	54.43	94.23	35.92	77.42		71.55	
52	77.80	16.26	56.11	14101.08	39.60	79.68		75.51	
53	82.16*	19.45	58.50	06.01	43.36	82.34		79.87	
54	86.52	22.70	60.57	10.99	47.19			84.32	
55	90.97	25.99	62.75	16.03	51.09			88.73	
56		29.36	65.02	21.20*	55.08	90.73		93.47	
57		32.79	67.34	26.34*	59.14	93.60		98.17	
58		36.29	69.68	31.59*	63.26	96.68			
59		39.86	72.14	37.03	67.48	99.81			
60		43.49	74.66	42.44	71.76				
61		47.15	77.23	47.92	76.14	14006.21			
62			79.88	53.50*	80.55				
63			82.60	59.14	85.09	12.96			
64				64.87	89.69				
65				70.62	94.35				
66					99.14	23.66			
67				14103.93					
68					08.84				
69					13.86				
70					18.90*				
71					24.05				
72					29.24				
73					34.54				
74					39.94				
75					45.39				
76					50.92				

* Lines marked with an asterisk could not be measured accurately.

The average values for the various rotational levels were determined wherever possible. In order to obtain the highest possible accuracy in the determination of the rotational constants, the graphical procedure described by Herzberg (*Spectra of diatomic molecules*, Second Edition, p. 181) was adopted. In Table VI a summary of the various rotational constants is given.

TABLE V
COMBINATION DIFFERENCES $\Delta_2 F'(J)$, $\Delta_2 F_c''(J)$, AND $\Delta_2 F_d''(J)$ FOR THE $v = 0$ VIBRATIONAL STATES OF THE $C^1\Sigma$ AND $A^1\Pi$ STATES OF AlF

J	$\Delta_2 F'(J)$			$\Delta_2 F_d''(J)$		$\Delta_2 F_c''(J)$	
	(0,0)	(0,1)	(0,2)	(0,0)	(1,0)	(0,0)	(1,0)
4	10.62	10.01
5	12.98	12.30	...	12.24	...
6	15.29	14.35	...	14.46	...
7	17.62	16.60	...	16.61	...
8	19.84	18.75	...	18.75	...
9	22.26	20.97	...	20.90	...
10	24.70	23.26	...	23.25	...
11	27.17	25.61	...	25.51	...
12	29.40	27.73
13
14
15
16
17	...	41.06
18	...	43.42	43.49
19	...	45.78	45.79
20	...	48.15	48.10	45.41	...
21	50.49	50.44	50.44	47.55	...	47.56	...
22	52.82	52.79	52.79	49.79	...	49.76	...
23	55.15	55.10	55.24	51.95	...	51.95	...
24	57.50	57.41	57.46	54.13	...	54.14	54.09
25	59.80	59.76	...	56.31	56.32	56.35	56.33
26	62.15	62.10	62.21	58.55	58.56	58.52	58.55
27	64.57	64.45	...	60.84	60.78	60.73	60.75
28	66.80	66.80	66.83	62.93	62.93	63.01	62.92
29	69.16	69.11	69.17	65.16	65.08	65.10	65.11
30	71.48	71.46	71.48	67.31	67.30	67.31	67.31
31	73.80	73.83	73.84	69.49	69.55	69.49	69.47
32	76.12	76.12	76.18	71.67	71.69	71.68	71.71
33	78.44	78.44	78.48	73.86	73.77	73.88	73.90
34	80.78*	80.87	80.92	76.05	76.10	76.08	75.96
35	83.13	83.15	83.15	78.29	78.27	78.22	78.25
36	85.40	85.39	85.53*	80.43	80.40	80.40	80.42
37	87.73	87.82	87.78	82.63	82.64	82.55	82.57
38	90.03	90.20*	90.09	84.77	84.81	84.78	84.77
39	92.39	92.44	92.42	86.95	87.00	86.96	86.94
40	94.70	94.78	94.72	89.17	89.16	89.12	89.21
41	97.01	97.07	97.04	91.24	91.38	91.29	91.38
42	99.34	99.39	99.35	93.45	93.58	93.47	93.48
43	101.63	101.73	101.68	95.72	95.63	95.64	95.66
44	103.93	104.02	103.92	98.83	97.84	97.79	97.79
45	106.34	106.31	106.28	100.00	99.91	99.91	99.97
46	108.48	...	108.56	102.08	102.17	102.11	...
47	110.84	110.91	110.85	104.29	...	104.24	...
48	113.12	...	113.18	106.44	...	106.44	106.48
49	115.45	...	115.47	108.60	108.65	108.54	108.61
50	117.68	110.71	110.84	110.69	110.77
51	119.96	112.85	112.89	112.91	112.94
52	122.35	115.08	115.10	115.08	115.01
53	124.66	117.25	117.22	117.21	117.23
54	126.92	119.37	119.41	119.33	119.41
55	129.18	121.47	121.56	121.46	121.50
56	131.47	123.90	...	123.59	123.63
57	133.74	125.74*	...	125.61*	...
58	135.89	127.45*	...	128.01*	...
59	138.44	130.15*	...	129.99*	...
60	140.57	132.15	...	132.10	...
61	142.84	134.26*	...	134.21	...
62	145.08	136.35	...	136.36*	...
63	147.36	138.48	...	138.46	...
64	149.59	140.54	...	140.56	...
65	151.92	142.75*	...	142.64*	...
66	154.13	144.82	...	144.81	...
67	146.88	...

*Combination differences marked with an asterisk were obtained from lines which could not be measured accurately.

From the data given in Table VI the equilibrium rotational constants given in Table VII were evaluated. The data were not sufficiently accurate to determine a reliable β_e value from the various D_s values. The following weighted average values $D' = 9.7 \times 10^{-7} \text{ cm.}^{-1}$ and $D'' = 1.1_0 \times 10^{-6} \text{ cm.}^{-1}$ were obtained for the rotational constant D in the upper $C^1\Sigma$ and lower $A^1\Pi$

TABLE VI
ROTATIONAL CONSTANTS OF THE NEAR INFRARED SYSTEM OF AlF

v	$^1\Sigma$ state		$^1\Pi_c$ state		$^1\Pi_d$ state		$^1\Pi$ state	
	B_v (cm. ⁻¹)	D_v (cm. ⁻¹)	B_v^e (cm. ⁻¹)	D_v^e (cm. ⁻¹)	B_v^d (cm. ⁻¹)	D_v^d (cm. ⁻¹)	B_v	D_v
0	0.5877 ₁	9.4×10^{-7}	0.5537 ₁	11.0×10^{-7}	0.5538 ₈	10.5×10^{-7}	0.5538 ₈	10.8×10^{-7}
1	0.5833 ₀	9.7×10^{-7}	0.5481 ₈	10.1×10^{-7}	0.5482 ₈	10.1×10^{-7}	0.5482 ₈	10.1×10^{-7}
2	0.5784 ₀	9.6×10^{-7}	0.5427 ₇	10.7×10^{-7}	0.5429 ₈	10.7×10^{-7}	0.5428 ₈	10.7×10^{-7}
3	0.5743 ₁	1.1×10^{-6}	0.5370 ₈	13.6×10^{-7}	0.5376 ₈	13.8×10^{-7}	0.5373 ₇	13.7×10^{-7}
4	0.5316 ₈	11.7×10^{-7}	0.5315 ₈	11.6×10^{-7}	0.5316 ₈	11.7×10^{-7}

TABLE VII
EQUILIBRIUM ROTATIONAL CONSTANTS FOR THE $C^1\Sigma - A^1\Pi$ BAND SYSTEM OF AlF

State	B_e (cm. ⁻¹)	α_e (cm. ⁻¹)	$r_e \times 10^{-8}$ (cm.)
$C^1\Sigma$	0.5900 ₈	0.0045 ₆	1.601
$A^1\Pi$	0.5566 ₀	0.0055 ₆	1.648

states of the near infrared system. These values are in agreement with the values $D_e' = 9.3 \times 10^{-7}$ and $D_e'' = 1.07 \times 10^{-6}$ calculated from the formula

$$D_e = 4B_e^3/\omega_e^2.$$

According to theory the Λ -doubling for a $^1\Sigma - ^1\Pi$ transition is given by

$$\frac{1}{2}\epsilon(J) = (B_v^d - B_v^e)J(J + 1).$$

In the present analysis the value $(B_v^d - B_v^e) = 0.0001_0$ was obtained from the B_v^e and B_v^d values listed in Table VII. Accordingly the Λ -type doubling of the Π -state is given by

$$\frac{1}{2}\epsilon(J) = 0.0001_0 J(J + 1).$$

The curve obtained from this equation fits the Λ -type doubling curve determined from the following combination relations:

$$R(J) - Q(J) = Q(J + 1) - P(J + 1) + \epsilon(J)$$

$$\text{and } R(J) - Q(J + 1) = Q(J) - P(J + 1) + \epsilon(J).$$

In addition to the two systems described in this paper the authors also observed and analyzed the following singlet systems:

$$E(?)^1\Pi - A^1\Pi, \quad D^1\Delta - A^1\Pi, \quad E(?)^1\Pi - B^1\Sigma.$$

The detailed analyses of these systems will be published shortly.

ACKNOWLEDGMENTS

The authors wish to thank Dr. P. B. Zeeman of the Merensky Institute for Physics for suggesting this problem, and Prof. P. de Vos for placing the facilities of his laboratory at our disposal, as well as Mr. S. Meier for his help during the experimental work.

This paper is published by permission of the South African Council for Scientific and Industrial Research.

REFERENCES

1. NAUDÉ, S. M. and HUGO, T. J. Phys. Rev. 90: 318. 1953.
2. ROCHESTER, G. D. Phys. Rev. 56: 305. 1939.
3. ROWLINSON, H. C. and BARROW, R. F. Proc. Phys. Soc. (London), A, 66: 437. 1953.
4. YUASA, T. Science Repts. Tokyo Bunrika Daigaku, 3: 239. 1938.

ON THE SHRINKAGE FACTOR OF NUCLEAR EMULSIONS¹

BY L. H. GREENBERG AND R. N. H. HASLAM

ABSTRACT

A simple and accurate method to determine the shrinkage factor of nuclear emulsions is presented. Its use shows that the shrinkage factor is not a function of the angle of inclination of the alpha particle tracks in the emulsion.

In the study of alpha particle tracks produced in nuclear emulsions irradiated in the beam of the 24 Mev. Saskatchewan betatron, it has been necessary to obtain accurate shrinkage factors for the emulsions used. A new method to measure shrinkage has been added to those reported in the literature and found to give a quick, accurate result.

The shrinkage of an emulsion may be obtained in several ways.

1. By measuring the thickness of the emulsion before and after development (2, 6, 8).
2. By weighing the emulsion before and after development and calculating the thickness on the basis of the density of the components before and after development (2, 6, 8).
3. By putting tracks of a known length into the undeveloped emulsion and obtaining a shrinkage factor which will make the tracks at all angles the same length (2, 6, 7).
4. By putting tracks in at a known angle and obtaining a shrinkage factor which will correct the measured angle in the developed emulsion to the known angle in the undeveloped emulsion (3, 5, 6).

To obtain the shrinkage from a series of tracks of known length, measurements are made of the lengths of the components of the tracks in the plane of the emulsion, l , and perpendicular to the plane of the emulsion, d , the "depth" of the track. If R is the known length of the tracks, then for each track $R^2 = l^2 + S^2d^2$, where S is the shrinkage factor. A plot of l^2 against d^2 for the series of tracks would be a straight line if S were constant. A straight line has in fact been obtained (2, 6, 7). The main difficulty with this method is in obtaining a series of tracks of constant length. Alphas from natural radioactive substances have a constant range but must be incorporated into the emulsion without changing it, or be put in from a thin source near the surface. Any absorption in the source will then produce scatter in the points. The stars produced by slight natural contamination with Ra, Rn, or Th could be used but there usually are too few to give good results. In our case anyway all such stars and background tracks are irradiated before irradiation by the betatron (7).

Method 4, using tracks at known angles, has been found to give the best results. Rather than a collimated beam as has been used previously (3, 5, 6)

¹ Manuscript received July 20, 1953.
Contribution from the Department of Physics, University of Saskatchewan, Saskatoon, Sask.

an effectively point source of alphas at a known distance from the emulsion is used. The position of the track with respect to the position of the source determines the angle of the tracks. The horizontal and vertical components of a track in the developed emulsion are measured in microscope scale divisions l , and d , and calibration constants c_1 and c_2 convert these divisions to microns. Referring to Fig. 1, the components of the track in the developed emulsion

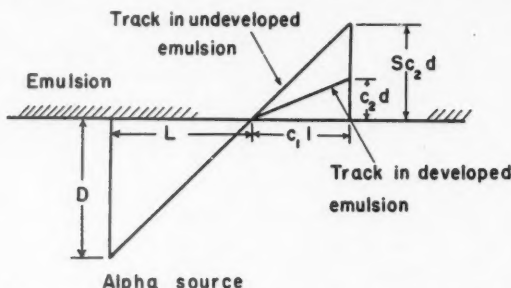


FIG. 1. Diagram showing track directions in original and processed emulsion.

are $c_1 l$ and $c_2 d$. The perpendicular distance D to the alpha source and L to the position of the track may easily be measured and then $L/D = c_1 l/Sc_2 d$ or, rearranging, $l/d = (Sc_2/c_1 D)L$.

A plot of l/d against L for several tracks would then be a straight line if S were constant. S is accurately determined from the slope of the line. The same result is obtained if the position P of the track measured from an arbitrary point is used in place of L .

It is most convenient to measure P on the stage of the microscope and measure only tracks which are in the direction of travel of the microscope. If the track deviates by an angle θ from this direction, $l \cos \theta$ must be used in place of l . If θ is limited to 5° this correction is less than 1%. The calibration constant c_2 involves the calibration of the vertical motion of the microscope and the index of refraction of the emulsion. In place of S the quantity Sc_2 may be determined and regarded as a correction factor which will give the proper angle to any measured track. It is then not necessary to obtain c_2 . If c_2 has been obtained but is in error, the evaluated S will correct the error.

As an illustration of this method of obtaining the shrinkage factor we present the results for a typical Ilford E₁ plate. The plate was exposed in a vacuum to alpha particles from polonium plated on a 0.25 mm. platinum wire. By means of a polystyrene holder, the wire was supported 0.95 cm. above the center of the plate and the α particles from only 1 mm. of the wire were allowed to strike the plate. The exposure time was chosen to give about 500 alpha tracks per square millimeter directly below the source. The plate was then developed in a modified form of Van der Grinten developer (8) and otherwise handled in a conventional manner.

The components l and d , and angle θ , of 87 tracks in the developed emulsion were measured. θ for most tracks chosen was less than 5° and no tracks having θ greater than 10° were measured. Fig. 2 shows a plot of $(l \cos\theta)/d$ against the

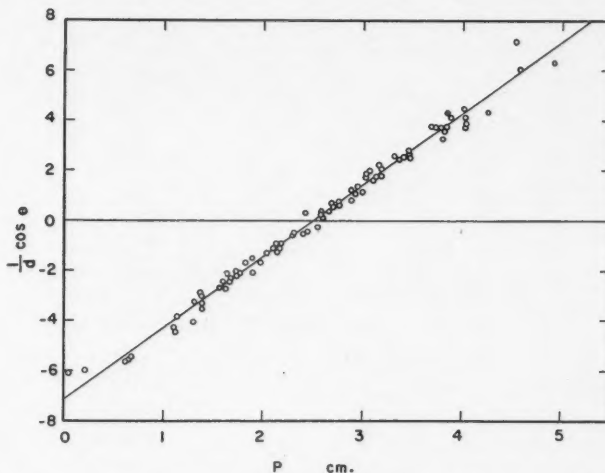


FIG. 2. Plot of $(l \cos\theta)/d$ vs. track position for an Ilford E₁ nuclear emulsion.

position of the track P . The points obviously form a straight line as expected for constant S . Using the calibration constants c_1 and c_2 as $1.41 \mu/\text{div.}$ and $1.72 \mu/\text{div.}$ respectively for our instrument, the shrinkage factor S obtained from the slope of the line was 2.22.

The source need not yield monoenergetic alpha particles; a small speck of glass from an old radon seed has given good results with the plate supported 1 cm. above the source in air. The exposure time has been as short as two minutes. It is possible to expose only a narrow strip and the remainder of the plate may then be used for other work. Therefore, the shrinkage factor may be measured on the plate on which other measurements are also made, eliminating the effect of variation of shrinkage between the plates on which the shrinkage factor and other events are measured. Checks may then be made to detect daily variation of shrinkage with humidity.

Using this method of measuring the shrinkage, an Ilford E₁ plate after irradiation of background tracks in hydrogen peroxide vapor and exposure in the betatron beam at 25 Mev. showed a shrinkage factor of 3.0. The axis of the beam was normal to the surface of the plate, but angles are measured either up or down from the plane of the emulsion. The actual angular distribution of 1111 alpha tracks produced by (γ, α) reactions in the emulsion is plotted as a histogram in Fig. 3. After correcting the tracks for escape from the 100μ emulsion the number of tracks was 1438. Each track was corrected

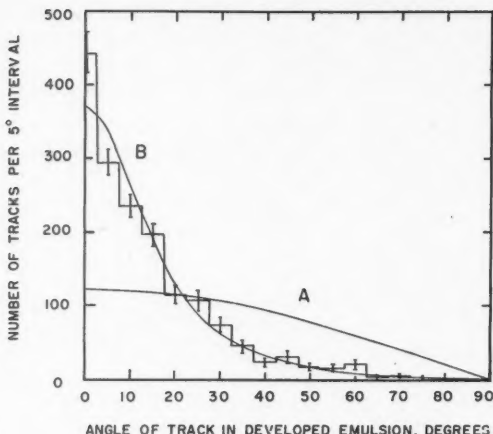


FIG. 3. Angular distribution of alpha particle tracks due to (γ, α) events in a nuclear emulsion. Curve *A* is for an isotropic distribution and no shrinkage. Curve *B* is for an initially isotropic distribution and a shrinkage factor of 3.0.

individually on the basis of the depth, *d*, of the track in relation to the emulsion thickness. Curve *A* is the expected distribution if the plate does not shrink and the tracks are isotropic. Curve *B* is calculated for an initially isotropic distribution of tracks and a shrinkage factor of 3.0. The excess of tracks at 0° and deficiency at 5° is not believed due to any change in shrinkage but because short tracks which are close to 0° appear flat in the emulsion. For instance a 15μ track at 5° dips only 0.44μ between the ends of the track and this may easily be classified as a flat, 0° track. The good fit of experimental data to the theoretical shows that there is no change of shrinkage with depth in the emulsion nor with the angle of inclination of the track.

These results are in good agreement with those of Jenny and Hurliman (2), Vigneron (6), and Wäffler and Younis (7), but are in marked contrast to those of Rotblat and Tai (4) and more recently of Horan (1), who have reported that the shrinkage is a strong function of the angle of inclination of the track in the emulsion. In each of these latter cases the shrinkage factor was based on the measurement of emulsion thickness. Using this factor, it was found that the calculated lengths of tracks of heavily ionizing particles increased with the angle of inclination of the track in the emulsion. If this were the case for our work, a straight line plot would not have been obtained in Fig. 2, nor would we have obtained the distribution of alpha particle tracks shown in Fig. 3. As a further test of the results of the above-named investigators Ilford E₁ plates and Kodak NTB plates were exposed to a plated polonium alpha source, and the shrinkage factor calculated by the method presented here. The lengths of the tracks were then calculated and plotted as a function of angle of inclination in the developed emulsion. The results for the NTB

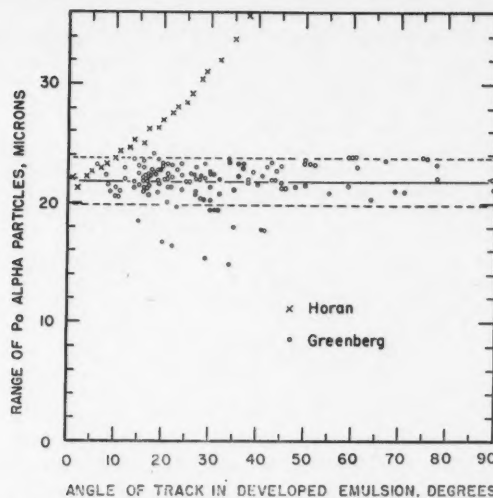


FIG. 4. Range of polonium alpha particles in a NTB emulsion.

plate are illustrated in Fig. 4, along with the results of Horan. It is not possible to present the results of Rotblat and Tai on the same graph because their results were given for emulsions loaded with lithium or extra gelatin.

It is clear that in our results there is no significant variation in track length with inclination, even at very large angles of inclination. The few short tracks obtained may be due to self-absorption in the alpha source. Our measurements gave a mean range for polonium alpha particles in NTB emulsions of $21.8 \pm 0.17 \mu$ and in Ilford E₁ emulsions, $21.76 \pm 0.26 \mu$.

Jenny and Hurliman (2) pointed out that the track lengths calculated by Rotblat and Tai (4) would have been constant if a shrinkage factor differing by 23% had been used. Similarly from the results of Horan (1) one may calculate for each angle of inclination a new shrinkage factor which would make all tracks 21.3μ long as Horan expected. Because of the large errors in the calculated lengths, tracks of inclinations of 18° or less do not give a significant result. However, for the tracks which are inclined at angles from 19° to his maximum of 38° the calculated shrinkage factor is 1.35 with a mean deviation of only ± 0.05 . Horan had used a shrinkage factor of 2.7 which is a more common value. Whether the factor of 2 between this calculated and his measured shrinkage factor is due to an increase in humidity causing a swelling of the emulsion, to microscope calibration, or to some other cause is not clear. The significant point, however, is that these results may be corrected by a new and constant shrinkage factor, showing that there is no dependence of shrinkage on angle but rather that an incorrect shrinkage factor had originally been used.

REFERENCES

1. HORAN, J. R. Phys. Rev. 90: 717. 1953.
2. JENNY, L. and HURLIMAN, T. Helv. Phys. Acta, 24: 235. 1951.
3. POWELL, C. F. and OCCHIALINI, G. P. S. J. Sci. Instr. 23: 102. 1946.
4. ROTBLAT, J. and TAI, C. T. Nature, 164: 835. 1949.
5. TELEGI, V. L. and ZUNTI, W. Helv. Phys. Acta, 23: 746. 1950.
6. VIGNERON, L. J. phys. radium, 10: 305. 1949.
7. WAFFLER, H. and YOUNIS, S. Helv. Phys. Acta, 24: 483. 1951.
8. YAGODA, H. Radioactive measurements in nuclear emulsions. John Wiley and Sons, Inc., New York. 1949.
9. YAGODA, H. and KAPLAN, N. Phys. Rev. 73: 634. 1948.

METEOR ECHO DURATION AND RADIO WAVE LENGTH¹

BY D. W. R. MCKINLEY

ABSTRACT

The durations of radar echoes from meteors have been observed simultaneously on 9.22 m. and 5.35 m., and also on 9.22 m. and 2.83 m. The ratio of durations on two wave lengths decreases with increasing duration by a factor of two over the observed range, deviating significantly from the accepted square law of wave length. Plotting the log of the ratio against the log of the duration yields two straight lines of different slopes, one in the short-duration range and the other applying to the longer echoes. General empirical formulae are developed to predict the echo duration on one radio equipment in terms of the duration of the same echo recorded by another apparatus of different sensitivity and wave length.

INTRODUCTION

In an earlier paper (7) it was shown from simultaneous observations of meteor echoes, using high and low power radar sets on nearly the same wave length, that the ratio of the echo duration decreases as the duration increases. A general empirical relationship was deduced as follows:

$$[1] \quad \log R = \log (T_1/T_2) = (1 - 0.83^{0.303x}) (2.88 - \log T_2)$$

where T_2 is the echo duration observed on one radar set and T_1 is the computed echo duration that should be observed on the other set. The two equipments differ in effective sensitivity by an amount $x = \log (G_1 P_1 \epsilon_2 / G_2 P_2 \epsilon_1)$ where G is the antenna gain, P the transmitter power, and ϵ the minimum detectable signal. In the original formula x was given in decibels, but the simple common logarithm will be used here because it will be combined later with the logarithm of the wave length ratio. It was remarked in the previous report that a preliminary investigation of echo durations on different radio wave lengths had indicated that there was an appreciable deviation from the commonly accepted square law relation. This paper will present experimental evidence to show that the ratio of echo durations on two wave lengths definitely decreases with duration, and that the relation is slightly different for the short and for the long duration echoes.

The radar records were made during 1950 primarily for the purpose of comparing echo rates on various wave lengths (6), and they have recently been re-examined to obtain information about the durations. Data are available on three wave lengths 9.22 m., 5.35 m., and 2.83 m. The radar parameters listed below in Table I are taken from Table VI of Ref. 6. The sensitivity of the high power 9.22 m. set is here defined as the reference and the sensitivities of the other two equipments are relative to the 9.22 m. set. Transmitter power, minimum detectable signal in the presence of internal and external noise, and antenna pattern are all included in the sensitivity factor, but the wave length has been excluded. The three equipments differed in peak transmitter power and receiver sensitivity, and, of course, in wave length, but were similar in other

¹ Manuscript received July 22, 1958.
Contribution from the Radio and Electrical Engineering Division, National Research Laboratories, Ottawa, Canada. Issued as N.R.C. No. 3081.

TABLE I
PARAMETERS OF THE RADAR EQUIPMENTS

Wave length, m.	Transmitter power, watts	Minimum signal, watts	x =sensitivity
9.22	2×10^8	2×10^{-14}	0
5.35	5×10^4	2×10^{-14}	0.60
2.83	3×10^4	2×10^{-13}	1.83

respects such as pulse width, recurrence frequency, and type of display and recording. Half-wave dipoles were employed, mounted one-quarter wave above ground and suitably scaled in wave length. Simultaneous echo records were obtained, using either the 9.22 m. and 5.35 m. equipments together, or the 9.22 m. and 2.83 m. sets.

OBSERVATIONS

The 9.22-2.83 m. combination was operated intermittently from February to April, 1950. In approximately 70 hr. of observation 134 echo pairs were measured; these are listed in Table II. The echo durations (T_9 referring to the 9.22 m. set and T_2 to the 2.83 m. set) were measured to 0.05 sec. for echoes less than 1 sec., with proportionally greater tolerances for the longer-duration echoes. The short wave length echoes were grouped in arbitrary time intervals, since the existence of a short wave length echo was the determining factor in the selection of echo pairs; no echo appeared on 2.83 m. that did not also show on 9.22 m. The common logarithms of the echo durations were averaged to give the mean values of $\log T_9$ and $\log T_2$ shown in Table II. $\log R = \log T_9 - \log T_2$

TABLE II
ECHO DURATIONS OBSERVED ON 9.22 AND 2.83 M.

$T_2 \rightarrow$	0.05-0.15	0.20-0.35	0.40-0.95	1.0-2.9	3.0→	Total
N	58	48	15	10	3	134
$\log T_9$	0.34	0.65	0.81	1.15	1.62	
$\log T_2$	-1.11	-0.63	-0.31	0.10	0.72	
$\log R$	1.45	1.28	1.12	1.05	0.90	

is the logarithm of the ratio of the durations, uncorrected for the difference in sensitivity between the two systems. Fig. 1 shows $\log R$ plotted against $\log T_2$, as circled points. The horizontal lines on the graph indicate the constant ratios that would be obtained if the ratio of echo durations were respectively proportional to the 1st, 2nd, and 3rd power of the wave length ratio. It is apparent that the ratio of echo durations decreases with increasing duration and that the square law applies only for a narrow range of T_2 .

The 9.22/2.83 observations were made and reduced before the 9.22/5.35 data were analyzed. In the absence of further information one would draw a straight line through the circled points of Fig. 1 to represent the observed relation. However, the 9.22/5.35 experiments yielded more accurate results, which have

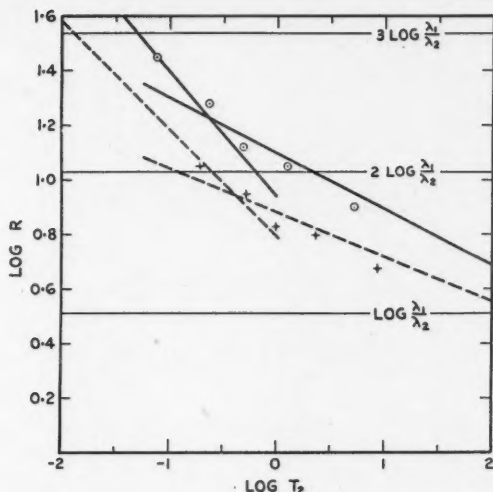


FIG. 1. Relation between the logarithm of the ratio of 9.22 m. and 2.83 m. durations and the logarithm of the 2.83 m. durations.

Circled points.—Observational data.

Solid lines.—Predicted relation obtained from general formulae based on 9.22/5.35 m. experiment.

Crossed points.—Observational data corrected for difference in equipment sensitivities.

Dashed lines.—Predicted relation corrected for sensitivity difference.

been used to predict the solid and dashed straight lines, and the crossed points of Fig. 1. This will be discussed later.

The 9.22/5.35 m. observations were carried out from Aug. 9 to Aug. 15, 1950. On the night of Aug. 10–11, a check of the film records of the previous night showed that the 9.22 m. echo rate was about half of the expected rate, and investigation revealed that the power output of the 9.22 m. set had fallen below 50 kw., owing to a defective transmitter tube. The tube was replaced and the output was maintained at 200 kw. for the balance of the observations. About 41 hr. of film records have been examined in detail, corresponding to the peak of the Perseid shower activity from Aug. 11 to Aug. 14. Three films, each running for about 280 min., were made in the interval 1630 hr. E.S.T. to 0700 hr. each day, so it has been convenient to divide the observing time into three periods to ascertain whether any effect could be found due to diurnal variation or to the changing altitude of the Perseid shower radiant. Table III contains the data for the first period, Table IV for the second, and Table V for the third. Data obtained prior to the detection of the transmitter fault are shown later in Table VII.

Individual graphs of $\log R$ versus $\log T_5$ have been plotted (but are not reproduced here) for each of the nine films listed in Tables III, IV, and V. Any appreciable trend from one film period to the next was masked by the scatter of the data. The sums of the logarithms of the individual durations are given

TABLE III
ECHO DURATIONS OBSERVED ON 9.55 M. AND 5.83 M. FIRST PERIOD, 1630-2110 E.S.T. APPROX.

$T_b \rightarrow$	0.05-	0.15-	0.30-	0.50-	1.0-	2.0-	4.0-	8.0-	16.0-	32.0-	64.0-	Total
Film No. 2 Aug. 11, 1950 1634-2110 E.S.T. (276 min.)	0.10 -29.00	0.25 -30.30	0.45 -7.31	0.95 -3.46	1.9 0.86	1.4 1.04	3.9 3.63	7.9 1.10	15.9 2.48	31.9 —	63.9 —	116
Film No. 5 Aug. 12, 1950 1630-2115 E.S.T. (285 min.)	N 52 -13.72 -58.30	$\Sigma \log T_b^9$ 48 -2.53 -34.86	N 49 4.49 -13.88	N 5.45 -2.91	N 7.61 1.84	N 3.42 1.76	N 4.83 2.84	N 3 3.18	N 1.79 1.42	N —	N —	168
Film No. 8 Aug. 13, 1950 1630-2110 E.S.T. (280 min.)	N 62 -23.20 -70.13	$\Sigma \log T_b^9$ 46 -3.43 -33.62	N 1.86 -2.96	N 3.89 0.53	N 6 2.27	N 5 2.27	N 3 2.55	N 3 1.00	N 1 1.48	N —	N —	152
Sum of No.'s 2, 5, 8 Total time 841 min.	N 140 -1.125 0.779	$\Sigma \log T_b^9$ 136 -0.726 0.666	N 61 -0.222 0.600	N 42 0.526	N 25 0.486	N 11 0.409	N 12 0.443	N 5 0.378	N 4 0.398	N —	N —	436

TABLE IV
ECHO DURATIONS OBSERVED ON 9.55 M. AND 5.88 M. SECOND PERIOD, 2120-0200 E.S.T. APPROX.

$T_b \rightarrow$	0.05-	0.15-	0.30-	0.50-	1.0-	2.0-	4.0-	8.0-	16.0-	32.0-	64.0-	Total
Film No. 3 Aug. 11/12, 1950 2118-0200 E.S.T. (282 min.)	65 -23.04 -71.60	79 -5.65 -57.14	41 5.10 -18.70	31 9.97 -6.24	13 7.91 1.90	17 14.26 6.97	19 22.21 14.21	9 12.63 9.15	6 10.45 8.13	3 5.89 4.79	2 4.63 3.96	285
Film No. 6 Aug. 12/13, 1950 2122-0200 E.S.T. (278 min.)	119 -40.60 -132.24	84 -6.82 -61.18	34 3.35 -15.83	27 8.86 -6.06	16 10.35 2.22	14 12.35 5.40	15 16.45 10.50	8 11.31 8.31	3 5.28 4.10	2 3.77 3.18	— —	322
Film No. 9 Aug. 13/14, 1950 2120-0211 E.S.T. (291 min.)	90 -32.97 -101.14	68 -3.68 -51.22	28 3.40 -13.12	15 5.28 -3.24	11 6.93 1.38	12 11.10 4.88	14 15.94 9.78	7 9.96 7.91	2 3.62 2.86	1 2.07 1.73	— —	248
Sum of No.'s 3, 6, 9 Total time 851 min.	-274 -1.113 0.760	231 -0.734 0.664	103 -0.463 0.578	73 -0.213 0.543	40 0.138 0.492	43 0.401 0.464	48 0.719 0.419	24 1.020 0.393	11 1.372 0.387	6 1.617 0.338	2 1.98 0.335	855

TABLE V
ECHO DURATIONS OBSERVED ON 9.55 M. AND 5.83 M. THIRD PERIOD, 0210-0650 E.S.T. APPROX.

$T_b \rightarrow$	0.05-	0.15-	0.30-	0.50-	1.0-	2.0-	4.0-	8.0-	16.0-	32.0-	64.0-	Total
Film No. 1 Aug. 11, 1950 0211-0600 E.S.T. (229 min.)	N $\Sigma \log T_b$ $\Sigma \log T_s$	59 - 22.36 - 64.17	46 - 3.44 - 34.35	25 3.51 - 11.85	7 2.82 - 0.82	10 7.01 1.87	6 6.05 2.65	9 10.86 6.60	8 12.45 8.31	5 9.20 6.77	3 6.05 4.93	178
Film No. 4 Aug. 12, 1950 0207-0657 E.S.T. (290 min.)	N $\Sigma \log T_b$ $\Sigma \log T_s$	91 - 34.28 - 103.94	71 - 8.28 - 51.64	31 2.79 - 14.63	16 5.31 - 3.65	11 7.57 1.49	16 13.81 6.91	11 13.73 8.21	15 21.60 15.54	16 28.37 21.86	14 27.30 22.68	299
Film No. 7 Aug. 13, 1950 0207-0649 E.S.T. (282 min.)	N $\Sigma \log T_b$ $\Sigma \log T_s$	126 - 39.22 - 138.94	77 - 4.31 - 57.22	33 4.11 - 15.78	16 5.72 - 3.44	8 5.21 1.27	13 11.43 5.29	19 22.70 13.72	16 23.31 16.44	12 21.24 16.88	10 20.04 16.19	331
Sum of No.'s 1, 4, 7 Total time 801 min.	N $\log T_b$ $\log R$	276 - 1.113 0.765	194 - 0.738 0.656	89 - 0.475 0.592	39 - 0.203 0.558	29 0.160 0.523	35 0.424 0.470	39 0.732 0.481	39 1.033 0.437	33 1.379 0.403	27 1.622 0.355	808

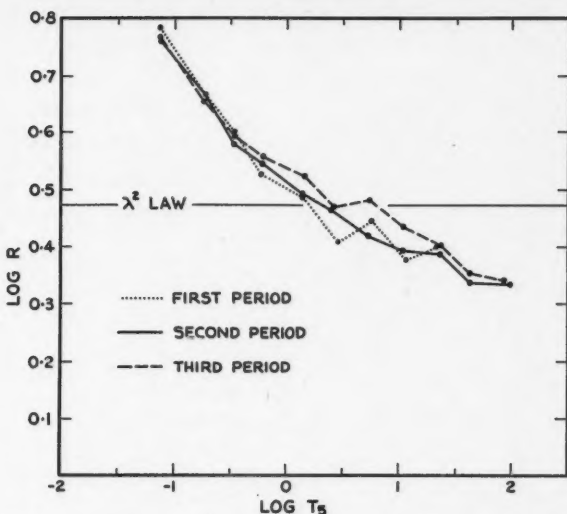


FIG. 2. Relation between the logarithm of the ratios of 9.22 m. and 5.35 m. durations and the logarithm of the 5.35 m. duration.

Dotted graph.—First period. All echoes of Table III.

Solid graph.—Second period. All echoes of Table IV.

Dashed graph.—Third period. All echoes of Table V.

for each film record to enable this plotting to be done, if desired. The tables also summarize the average values of $\log T_5$ and $\log R$ for all three films in each period, and these data are plotted in Fig. 2; the dotted line being the first period, the solid line the second period, and the dashed line the third period. No significant difference in the three periods is observable, except that $\log R$ for the third period is slightly greater than for the other two periods for the larger values of T_5 . The horizontal line corresponding to the square law of wave length is shown on Fig. 2. The data have not yet been corrected for the difference in sensitivity between the systems but it is quite obvious that the square law relation can only be a first approximation to the observations.

While not particularly relevant to the subject of this paper, data in Tables III, IV, and V show an increase in the percentage of long enduring echoes from 1630 hr. to 0700 hr. In Fig. 3, the percentage of echoes in each of the selected intervals of T_5 has been plotted against $\log T_5$, for each of the three periods. The percentages of echoes of duration 1 sec. and longer, observed during the first, second, and third periods, are respectively 13, 20, and 26%. The respective percentages for echoes over 8 sec. duration are 2, 5, and 13%. Two factors are contributing to this increase in the proportion of long enduring echoes, first, the normal diurnal variation in duration of the background meteor echoes, and second, the fact that the Perseid radiant is low in the sky during the first period and very high during the third period. The probability function for the Ottawa radar set (5) shows that few of the smaller Perseid meteors should be detected

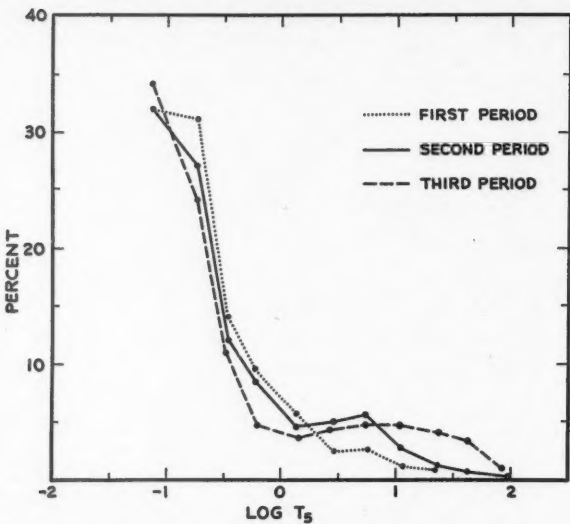


FIG. 3. Percentages of echoes in the selected intervals of durations observed on 5.35 m.
Dotted graph.—First period; Table III.
Solid graph.—Second period; Table IV.
Dashed graph.—Third period; Table V.

in the third period. However, the radar probability function for the very bright meteors, which usually yield long-duration echoes, is more like the visual probability function, that is, it is roughly proportional to the cosine of the zenith angle of the radiant because the long-duration meteor echoes tend to lose all aspect sensitivity. The hourly rates for the three periods, respectively 31, 60, and 61 echoes per hour, indicate that the over-all contribution of the Perseids has fallen off considerably in the third period, and the over-all rate for that period is sustained only by the increasing numbers of background meteors.

No further attempt will be made here to use these data to analyze the Perseid shower because the selection process has restricted the information to observations made on the 5.35 m. set. During the Perseid shower of 1950, the combined meteor program of the National Research Council and the Dominion Observatory included echo records made with the two Ottawa radars, with radars at Arnprior and Carleton Place for the triangulation of heights, and with the doppler equipment at South Gloucester for the measurement of velocities, coupled closely with visual observations and photographic and spectrographic records. Regrettably, it may be some time before all these records can be fully analyzed.

A GENERAL RELATION BETWEEN ECHO DURATION AND SYSTEM PARAMETERS

The data for all three periods listed in Tables III, IV, and V have been totalled for convenience in Table VI, which shows the average values of $\log R$ and $\log T_s$ in the selected intervals of T_s . This information has been plotted in

TABLE VI
ECCHO DURATIONS OBSERVED ON 9.22 M. AND 5.35 M. ALL PERIODS, 1630-0650 E.S.T. APPROX., AUG. 11-14TH, 1950

$T_b \rightarrow$	0.05-	0.15-	0.30-	0.50-	1.0-	2.0-	4.0-	8.0-	16.0-	32.0-	64.0-	Total
0.10	0.25	0.45	0.95	0.95	1.9	3.9	7.9	15.9	31.9	63.9	127.9	
561	253	154	94	89	99	68	48	33	10	1.639	2099	
-0.734 0.662	-0.468 0.588	-0.213 0.542	0.142 0.500	0.418 0.465	0.728 0.446	1.030 0.418	1.375 0.399	1.621 0.352	0.352 0.323	0.323		

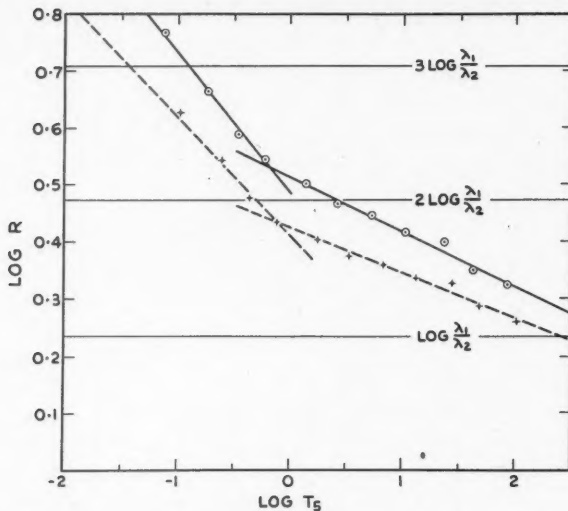


FIG. 4. Relation between the logarithm of the ratios of 9.22 m. and 5.35 m. durations and the logarithm of the 5.35 m. durations. All periods; Table VI, Aug. 11-14, 1950.

Circled points.—Observational data.

Solid lines.—Drawn to fit the observational data.

Crossed points.—Observational data corrected for difference in equipment sensitivities.

Dashed lines.—Solid lines after correcting for sensitivity difference.

Fig. 4, as the circled points. The variation of $\log R$ with $\log T_5$ can be represented by two straight lines, rather than one, as there is a definite change in slope near $\log T_5 = 0$. The equations of these lines drawn through the observed points are:

$$[2] \quad \log R = (1 - 0.757) (2.0 - \log T_5), \quad T_5 < 1 \text{ sec. approx.}$$

$$[3] \quad \log R = (1 - 0.905) (5.4 - \log T_5), \quad T_5 > 1 \text{ sec. approx.}$$

In the previous paper (7) a general relation between echo duration and system sensitivity was deduced. Through similar reasoning we can establish a general equation for the variation of $\log R$ with $\log T$ in terms of both the sensitivity ratio and the wave length ratio, as follows:

$$[4] \quad \log R = (1 - M^p) (K - \log T),$$

where

$$[5] \quad p = a \log (\lambda_1/\lambda_2) + bx.$$

The two wave lengths involved are λ_1 and λ_2 , a and b are constants to be determined, and M and K are constants which will have two values corresponding to the observational Equations [2] and [3].

After considering Fig. 4, which shows that $\log R$ versus $\log T$ is a bilinear function beyond any experimental error, it is not unreasonable to return to the high-low power data and to replace Equation [1] by two straight lines, one

drawn through the short-duration points of Fig. 1 of Ref. (7) and the point, $\log R = 0, \log T_l = 2.0$, and the other through the longer duration points and the point, $\log R = 0, \log T_l = 5.4$. The first line fits quite well, but most of the observed points are somewhat below the second line. However, there are few observations in the long-duration brackets of the high-low power experiment, and the total number of observations was only one-tenth of the present number of comparisons between 9.22 m. and 5.35 m. More data might well reveal a definite bilinear relationship in the former case. In any event the arbitrary substitution of two lines of different slopes for Equation [1] makes only a second-order change in the computed duration ratios, and has little effect on the remainder of the conclusions of the previous paper. The substitution does enable one to incorporate the sensitivity as well as the wave length in the present discussion. The equations of the adopted lines of $\log R$ versus $\log T_l$ (high-low power experiment) are

$$[6] \quad \log R = [1 - (0.775)^{0.303x}][2.0 - \log T_l],$$

$$[7] \quad \log R = [1 - (0.912)^{0.303x}][5.4 - \log T_l].$$

In the present case, if there were no sensitivity difference between the 9.22 m. and 5.35 m. equipments, we would have in equation [4] $M = 0.757$, or 0.905, and $p = 1$. Hence $a = 1/\log(9.22/5.35) = 4.23$. As there is a sensitivity difference we have to solve simultaneously for M and b . Since $x = 0.60$ from Table I, we have,

$$[8] \quad M_1^{1+0.60b} = 0.757 \text{ and } M_1^b = 0.775^{0.303}, \text{ for } T < 1,$$

$$[9] \quad M_2^{1+0.60b} = 0.905 \text{ and } M_2^b = 0.912^{0.303}, \text{ for } T > 1,$$

whence $M_1 = 0.796$, $M_2 = 0.921$; and $b = 0.333$. The desired general equations are

$$[10] \quad \log R = (1 - 0.796^p)(2.0 - \log T_{\lambda_s}), \quad T_{\lambda_s} < 3 \text{ sec. approx.},$$

$$[11] \quad \log R = (1 - 0.921^p)(5.4 - \log T_{\lambda_s}), \quad T_{\lambda_s} > 3 \text{ sec. approx.}$$

where $p = 4.23 \log(\lambda_1/\lambda_2) + 0.333x$. For convenience we have assumed the parameters of our 9.22 m. set as a standard, for which the change-over occurs at $T \approx 3$ sec. Equations [10] and [11] reduce to Equations [2] and [3] when $p = 1 + (0.333)(0.60) = 1.200$.

The expression for p shows that the duration depends much more on the wave length than on the sensitivity. For example, a wave length ratio of 2 has the same effect as a sensitivity ratio of 6500.

The observed data (circled points of Fig. 4) may be corrected for the sensitivity difference of the radars in the following manner. Compute the corrected durations, T_b' , that would have been seen on 5.35 m. if both sets had had equal sensitivities, from $\log(T_b'/T_b) = (1 - 0.796^{0.200})(2.0 - \log T_b)$ and $\log(T_b'/T_b) = (1 - 0.921^{0.200})(5.4 - \log T_b)$ respectively. Subtracting $\log T_b'$ from $\log T_b$ yields $\log R'$ which has been plotted against the T_b' values as the crossed points in Fig. 4. The equations of the corrected straight lines, shown in Fig. 4 as dashed lines, can be found immediately by putting $p = 1$ in Equations [10] and [11].

In the earlier high-low power experiments no correction was made for the slight difference in wave lengths of the high-power set on 9.22 m. and the low-power set on 9.55 m. Inserting the particular parameters of these equipments in Equations [10] and [11] it is found that the slopes of the adopted lines, Equations [6] and [7], should be reduced by about 4%, to a first approximation. This would change the values of M_1 and M_2 slightly. However, the original data of the high-low power experiment were scarcely good enough to determine a slope to this order of accuracy, and moreover the adopted lines, Equations [6] and [7], were fitted somewhat forcibly and arbitrarily to these data and could easily have been chosen with slightly different slopes. Therefore, this small correction has not been inserted in Equations [10] and [11].

Returning to the 9.22/2.83 data and Fig. 1, we shall now use Equations [10] and [11] to compute the predicted variation of $\log R$ with $\log T_2$. Here $\log(\lambda_1/\lambda_2) = 0.513$ and $x = 1.83$, so that $p = 2.17 + 0.60 = 2.77$. The calculated lines are drawn on Fig. 1 as solid lines. The agreement with the observations is good, and certainly is within the limits of error of the observations. An analyst, presented with the observational points only, would probably have drawn a single straight line, which is all that would be warranted by the accuracy of these data alone. Were many more data to be available from the 9.22/2.83 m. trials it is suggested that a definite bilinear relation would have been obtained. The circled points have been corrected for the difference in power sensitivities of the two radars, in the manner described above, to give the crossed points. The dashed straight lines have been obtained by putting $p = 2.17$ in Equations [10] and [11].

It was remarked earlier that the observations made from 1630 E.S.T. Aug. 9 to about 0200 E.S.T. Aug. 11, 1950, were not included in the above analysis of 9.22/5.35 m. durations because the transmitter power of the 9.22 m. set was well below normal. Only one power measurement of the 9.22 m. set was recorded prior to the detection of the transmitter fault. This was 40 kw. (Needless to say, after rectifying the fault the power was more carefully monitored.) However, confirmation of this low power is available from spot checks of 9.22 m. echo counts for Aug. 9-10, 1950, compared to the corresponding period of the Perseid shower during the previous year when the power was known to be 200 kw. The echo rates averaged about one-half of the expected rates. Echo rates have been shown to depend on the square root of the transmitter power (6), hence the power must have been about one-quarter of the normal output of 200 kw.

The observational data for the period 2230 E.S.T. Aug. 9 to 0650 E.S.T. Aug. 10 are summarized in Table VII, and are plotted as circled points in Fig. 5. For a power of 40 kw. on 9.22 m. the relative sensitivity factor for the 9.22 m. and 5.35 m. sets becomes $x = -0.1$. The solid straight lines have been computed by putting $p = 1 + 0.333(-0.1)$ in Equations [10] and [11]. These lines differ very little, of course, from the dashed straight lines of Fig. 4. The long-duration points are scattered, as might be expected from the few observations available, but the short-duration points follow the predicted trend fairly well.*

*Inclusion in this paper of the observations made when the 9.22 m. system sensitivity was slightly less than the 5.35 m. system sensitivity was suggested by correspondence with Dr. Von R. Eshleman, of Stanford University, who was kind enough to offer helpful criticism of an earlier draft of the manuscript.

TABLE VII
ECHO DURATIONS OBSERVED ON 9.22 M. AND 5.35 M., 2230-0650 E.S.T., AUG. 9-10TH, 1950

T_s	0.05- 0.10	0.15- 0.25	0.30- 0.45	0.50- 0.95	1.0- 1.9	2.0- 3.9	4.0- 7.9	8.0- 15.9	16.0- 31.9	32.0- 63.9	64.0- 127.9	Total
$N \log T_s$ $\log R$	124 -1.134 0.658	65 -0.732 0.559	22 -0.455 0.487	12 -0.188 0.429	10 0.127 0.420	12 0.416 0.375	6 0.742 0.333	1 1.08 0.28	7 1.442 0.359	1 1.80 0.34	-	260

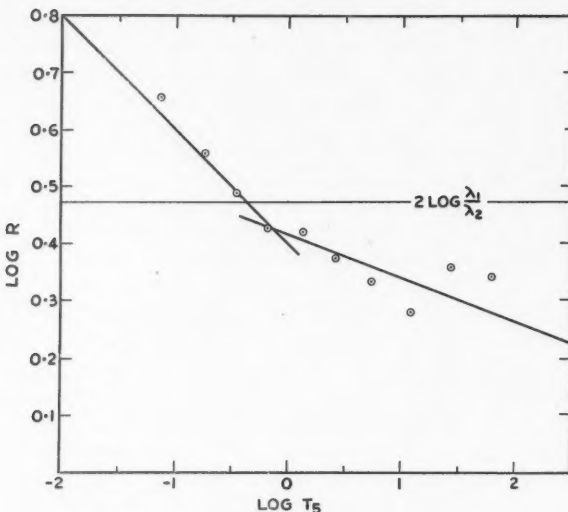


FIG. 5. Relation between the logarithm of the ratios of 9.22 m. and 5.35 m. durations and the logarithm of the 5.35 m. durations. Table VII, Aug. 9-10, 1950.

Circled points.—Observational data.
Solid lines.—Predicted relation.

Returning to Fig. 1, it is seen that the dashed straight line crosses the horizontal line, $\log R = 2 \log (\lambda_1/\lambda_2)$, at $\log T_2 = -0.60$ and the corresponding T_9 is 2.5 sec. In Fig. 4 the intersection occurs at $\log T_5 = -0.29$, with $T_9 = 1.5$ sec. If we regard the 9.22 system as a standard it would appear that, on the average, an echo observed on 9.22 m. with a duration between 1 and 3 sec. will have a duration on another equipment, of equal sensitivity but different wave length, that obeys the square law. Shorter-duration echoes will approach the cube law, and the longer-duration echoes will be closer to the linear law. The observed variation in the duration ratio is more than 2:1, which is by no means negligible. In Fig. 1, over the range of the corrected observational data the ratio changes from 4.7:1 for the long echoes to 11:1 for the short echoes, and in Fig. 4, the ratio changes from 1.8:1 to 4.2:1. Earlier work by Pineo and Gautier (8) on the comparison of meteor echo durations on 27.2 Mc. and 41.0 Mc. did not show any significant change of the ratio with echo duration, but it is possible that their recording systems had inadequate resolution. Greenhow (2) does show a graph in which the observed ratio decreases with increasing duration, though there are insufficient data to indicate any discontinuity in the relation.

In Fig. 1, the point of discontinuity in the slope of the corrected $\log R$ versus $\log T_2$ relation (the intersection of the dashed lines) occurs at $\log T_2 = -0.37$ where $T_9 \doteq 5$ sec. In Fig. 4 the point of discontinuity is at $\log T_5 = -0.12$, and $T_9 \doteq 2$ sec. This suggests that one model of meteoric ionization may apply to echoes of less than approximately three seconds' duration on the 9.22 m. radar,

and another model to longer echoes. Such theoretical models have already been developed (1, 2, 3, 4) and lead to the following quoted relations:

$$[12] \quad T = \lambda^2 / 16\pi^2 D \text{ for short-duration echoes,}$$

and

$$[13] \quad T = \alpha / 4\pi DN_c \text{ for long-duration echoes,}$$

where D is the diffusion coefficient, α is the electron line density, and N_c is the critical density for the wave length employed. Since $N_c \sim 1/\lambda^2$, Equation [13] becomes

$$[14] \quad T \sim \alpha \lambda^2 / D,$$

for long-duration echoes. Hence, at first glance, both models predict a simple λ^2 relation.

However, Greenhow (2) presents arguments based on considerations of turbulence in the meteor trail to indicate that the echo duration will be less than that predicted by Equation [13] for large T 's, and that this effect will be more pronounced for longer wave lengths, hence the ratio of durations will decrease. On the other hand, from Equation [12], one might expect in Figs. 1, 4, and 5, that the slopes of the lines to the left of the discontinuities should have decreased to approach the line $\log R = 2 \log (\lambda_1 / \lambda_2)$ more closely, rather than increasing sharply. A more careful inspection of the theory applying to short-duration echoes suggests that the discrepancy between theory and experiment may not be as great as is implied by Equation [12]. In the revised expression for the short echo durations, proposed by Eshleman (1), T is proportional to λ^2 multiplied by a factor that also includes the wave length. Thus, while theory and observation have yet to be reconciled in detail, they are in agreement in demonstrating that the commonly-accepted square law relation, Equation [12], holds only as a first approximation. The second approximation might be regarded as the general decrease in $\log R$ with $\log T$, and arguments have been put forward to account for this effect in general terms for both short and long duration echoes. The third approximation, i.e., the observed change in slope of the $\log R$ versus $\log T$ graph, yet remains to be explained quantitatively for either short or long duration echoes.

REFERENCES

1. ESHLEMAN, VON R. Electronics Research Lab., Stanford Univ. Tech. Rept. No. 59. Feb. 1, 1953.
2. GREENHOW, J. S. Proc. Phys. Soc. (London), B, 65: 169. 1952.
3. HERLOFSON, N. Repts. Progr. in Phys. 11: 444. 1948.
4. KAISER, T. R. and CLOSS, R. L. Phil. Mag. 43: 1. 1952.
5. MCKINLEY, D. W. R. Astrophys. J. 113: 225. 1951.
6. MCKINLEY, D. W. R. Can. J. Phys. 29: 403. 1951.
7. MCKINLEY, D. W. R. Can. J. Phys. 31: 758. 1953.
8. PINEO, V. C. and GAUTIER, T. N. Science, 114: 460. 1951.

THE DECAY OF Cd¹⁰⁵¹

By F. A. JOHNSON²

ABSTRACT

The isotope Cd¹⁰⁵ (55 min.) has been produced by the Ag¹⁰⁷ ($p, 3n$) reaction in the McGill University synchrocyclotron and has been investigated by means of a 180° spectrograph of high resolution, a lens spectrometer, and a scintillation spectrometer.

The positron end point was found to be 1.691 ± 0.005 Mev. and the Fermi plot of the spectrum was straight down to about 800 kev. where a slight upward curvature began. Internal conversion lines found in the 180° spectrograph indicated γ -rays of energies 25.50, 27.69, 263.0, 292.5, 308.0, 312.1, 317.1, 320.5, 324.9, 336.3, 340.7, 347.0, 433.1, and 606.7 kev. High energy internal conversion lines found in the lens spectrometer beyond the end point of the positron spectrum were assigned to γ -rays of energies 1.908, 1.957, 1.995, 2.045, 2.277, and 2.318 Mev.

In addition lines assigned to Ag¹⁰⁵ have been recorded. These correspond to γ -rays of energies 64.0, 280.8, 319.4, 331.5, 344.9, 392.6, and 443.2 kev., of which that of 331.5 kev. has not been reported previously.

1. INTRODUCTION

The radiations from the neutron deficient isotope Cd¹⁰⁵ have been investigated by means of a 180° permanent magnet spectrograph of high resolution, a lens spectrometer, and a scintillation spectrometer. In the course of the investigation additional information was obtained concerning the radiations from Ag^{109m}, Ag^{107m}, and Ag¹⁰⁵.

The active cadmium was produced by proton bombardment of silver in the McGill University synchrocyclotron. All silver used in these experiments was supplied by Johnson, Matthey and Mallory Co. Ltd. and was claimed to be 99.9% pure. Spectrographic analysis indicated the presence of very slight traces of iron, cadmium, and tin. Surface contamination was removed prior to bombardment by means of dilute nitric acid. All bombardments were carried out at a nominal proton energy of 30 Mev., where it was found that the Cd¹⁰⁵ activity was produced in high yield and free from the complicating activities of lower mass isotopes. The threshold for the production of Cd¹⁰⁵ was found to be about 20 Mev., while above 30 Mev. the production of Cd¹⁰⁴ was initiated (12). Cd¹⁰⁷ (6.7 hr.) was present at all bombardment energies, but, having a longer half-life than Cd¹⁰⁵ and a very much lower positron end point, it did not seriously complicate the investigation.

Cd¹⁰⁵ has previously been produced by Cd($n, 2n$) and Pd(α, n) reactions, but no reference has been found concerning its production by the Ag¹⁰⁷($p, 3n$) reaction. Gum and Pool (8), in the most recent investigation, report a half-life of 57 min., and by aluminum absorption have determined the positron end point to be 1.5 Mev. They also report the presence of an X-ray and a γ -ray, but make no mention of the approximate energy of the latter.

2. SOURCE PREPARATION

The separation of the active cadmium from the irradiated silver target was effected by means of an evaporation process *in vacuo*, this being considered the

¹ Manuscript received June 19, 1953.

Contribution from the Radiation Laboratory, McGill University, Montreal, Que.

² Present address: Canadian Aviation Electronics Ltd., Winnipeg, Man.

most feasible way of preparing thin carrier-free sources of high specific activity. Consideration of the melting and boiling points of the two elements:

Ag	Cd
M.p. 960	320°C.
B.p. 1950	767

indicated that it was reasonable to expect that if the silver could be melted, the cadmium would then boil off and could be collected on a cold surface. The process was found to work satisfactorily provided a little aluminum foil (m.p. 659) was added; this melted first and made good thermal contact between the silver and the quartz evaporation apparatus.

Two types of quartz evaporation apparatus were used, one for the preparation of lens spectrometer sources, the other for 180° spectrograph sources. The essential feature was that as the cadmium boiled off it streamed through a narrow opening in the quartz apparatus and was caught respectively on a cooled $\frac{1}{8}$ in. diameter aluminum disk (1.7 mgm./cm.²) or on a fine tungsten wire $\frac{3}{4}$ in. long and 2 to 10 mils in diameter. Activities obtained were of the order of 10-20 roentgens per hour on the aluminum disk, 2-3 roentgens per hour on a 2 mil wire, and 10 or more on a 10 mil wire. All activities were measured on a Beckman radiation meter with the source about one inch from the sensitive volume of the meter, and the values given are those obtained from a cyclotron run of one and a half hours. Autoradiographs showed the sources to be completely uniform.

This method of separating the cadmium had the advantage of speed. It was possible to start counting in the lens spectrometer, or to start an exposure in the 180° spectrograph, within 20 min. of the end of a cyclotron bombardment.

3. MEASUREMENTS WITH THE 180° SPECTROGRAPH

The $H\rho$ values and energies of the conversion lines detected in the 180° spectrograph are listed in Table I, together with their assignments. The added binding energies are obtained from the most recent values of the X-ray level energies (11).

Since the Auger lines have been listed and discussed in a previous paper (13), they are not included in the table. No shift in energy could be detected between the Auger lines of Ag¹⁰⁷ and those of Ag¹⁰⁵, nor were the relative intensities measurably different in the two cases.

The conversion lines of the 25.5 kev. γ -ray of Cd¹⁰⁵ are of special interest since they lie within the region of the Auger lines from the silver X-rays, and it is important to verify that they are not Auger lines. Fig. 1 shows spectrograph plates of the Auger region, 1(a) taken with a source produced at 20 Mev. (Cd¹⁰⁷), and 1(b) taken with a source produced at 30 Mev. (Cd¹⁰⁷ + Cd¹⁰⁵). The presence of new lines at 30 Mev. is very apparent, and measurement shows that none of these lines coincide with known Auger lines. The line designated as L_{111} is higher in energy than the $K \rightarrow L_{111} N_{11,111}$ Auger line by 85 ± 10 volts, and L_{11} is higher than the $K \rightarrow L_{11} N_{11,111}$ line by 68 ± 10 volts. A line that could have been called L_1 was not seen; such a line if present would have been about 37 volts lower in energy than the $K \rightarrow L_{111} M_{IV,V}$

TABLE I
INTERNAL CONVERSION LINES OF Cd¹⁰⁵ DETECTED IN 180° SPECTROGRAPH

$H\rho$, gauss-cm.	E , kev.	Assignment	γ -Energy, kev.
504.5	21.91 ± 0.06	L_{II}	25.46
506.6	22.09	L_{III}	25.47
527.0	23.87	L_I	27.70
538.3	24.88	M_{II}	25.51
538.8	24.92	M_{III}	25.51
541.2	25.14	$M_{IV,V}$	25.53
544.0	25.36	N_I	25.48
560.7	26.94	M_I	27.68
1824.3	237.5 ± 0.3	K	263.0
1957.0	267.0	K	292.5
2024.7	282.5	K	308.0
2042.9	286.6	K	312.1
2064.3	291.6	K	317.1
		L_I	295.4
2079.1	295.0	K	320.5
		$M_{IV,V}$	295.4
2098.1	299.4	K	324.9
2116.4	303.7 ± 0.4	K	329.2
		L_I	307.5
2146.9	310.8	K	336.3
2165.7	315.2	K	340.7
2192.3	321.5	K	347.0
2282.9	343.1	L_I	346.9
2546.3	407.6 ± 0.5	K	433.1
2634.2	429.6	L_{II}	433.1
3219.8	581.2 ± 0.6	K	606.7

Auger line and could have been just resolved from it, as evidenced by the resolution of the M lines of this γ -ray. Such a line was not seen, nor was the $K \rightarrow L_{III}M_{IV,V}$ line increased in intensity. Thus L_I must be extremely weak. Similarly the M and N conversion lines of this γ -ray did not coincide with the position of known Auger lines.

It has been assumed that this 25.5 kev. γ -ray, which shows the same half-life as the Cd¹⁰⁵ positron spectrum considered later, is converted in silver and thus follows positron emission or K -capture in Cd¹⁰⁵. The main basis for this statement rests on the separation of the L_{II} and L_{III} conversion lines. Although the absolute energy values of these lines are subject to some uncertainty, the energy differences may be measured with considerable accuracy. The $L_{II}-L_{III}$ energy difference for cadmium, silver, and palladium is 0.190, 0.172, and 0.157 kev. respectively. The measured separation of the L_{II} and L_{III} conversion lines is 0.179 kev., which would indicate that conversion takes place in silver.

The relative $L_{II} + L_{III}/M + N$ conversion coefficient of this γ -ray was determined in the lens spectrometer, and by planimetric measurement of the areas under the lines, a value of 4 ± 1 was obtained.

The lines of energy 23.87 and 26.94 kev. were likewise not seen at 20 Mev. bombardment energy, and also did not coincide with known Auger lines. The former line was approximately twice as intense as the latter, as determined by visual observation of the plate. On this basis and in view of their separation it might be assumed that the 23.87 kev. line was the L_I line and the 26.94 kev. line the M_I line of a 27.69 kev. γ -ray.

PLATE I

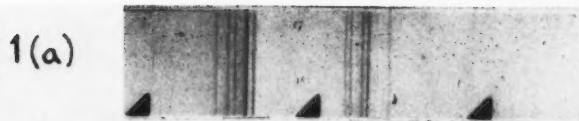
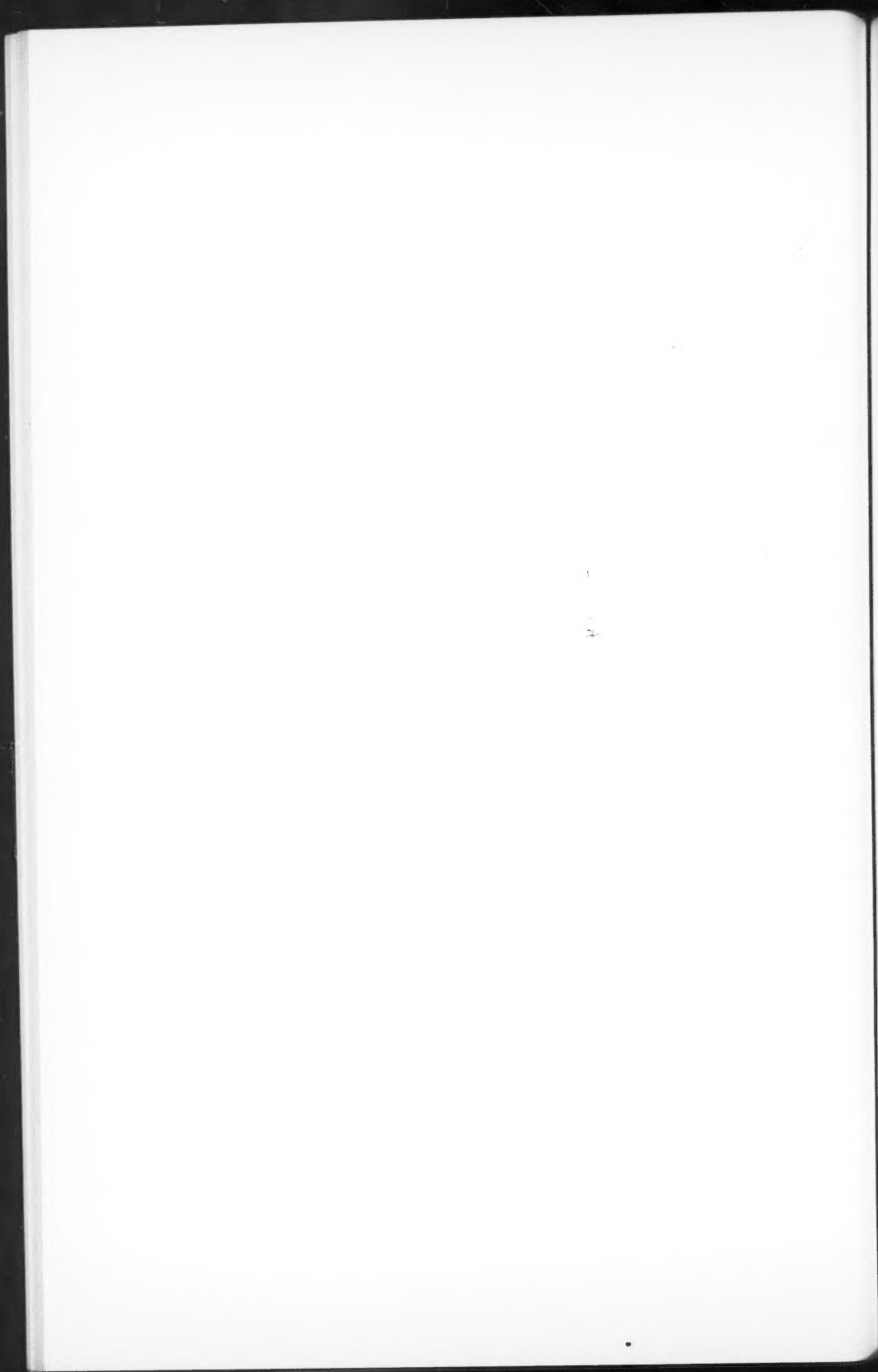


FIG. 1. Spectrograph plates of Auger region, (a) taken with source produced at 20 Mev. (Cd^{107}), (b) taken with source produced at 30 Mev. (Cd^{107} and Cd^{105}) (upper set of labels refer to 25.5 kev. γ -ray, lower set to 27.69 kev. γ -ray).

FIG. 2. L_{I} , L_{II} , L_{III} , and M_{III} lines of the 93.0 kev. γ -ray of Ag^{107m} .



Of the other conversion lines measured, $H\rho$ 2192.3 was the strongest with $H\rho$ 2024.7 and 2546.3 each about half as intense. The $H\rho$ values quoted for these three strongest lines are the averages of at least six determinations, using three different magnetic field settings in the spectrograph. The maximum variation did not exceed ± 3 gauss-cm. The lines of $H\rho$ 2079.1 and 2282.9 were about half as weak again as the $H\rho$ 2024.7 and 2546.3 lines.

All other conversion lines were very faint and some were found only by superimposing a number of very intense sources on the same plate. In only two cases was an unambiguous $K-L$ difference found, that of the 433.1 kev. γ -ray where both the K and L_{11} lines could be identified, and that of the 347.0 kev. γ -ray where the K and L_1 lines were visible; in the former case the L assignment could possibly be L_{111} , but in the latter L_1 is fairly certain. In both cases $K/L \sim 4$. All other lines were assumed to be K conversion lines.

The interpretation of the two lines of $H\rho$ 2024.7 and 2116.4 is rather uncertain: if they are assigned as K and L_1 , the energy of the γ -ray comes out to be 308.0 and 307.5 kev. respectively, and the internal discrepancy is rather large. Alternatively the $H\rho$ 2116.4 line could be assigned as the K line of a 329.2 kev. γ -ray. Also the case of the two lines of $H\rho$ 2064.3 and 2079.1 is puzzling. They seem to be related as the L_1 and $M_{IV,V}$ of a 295.4 kev. γ -ray, but the K conversion line of such a γ -ray was not seen. If this alternative assignment is correct, then the $M_{IV,V}$ conversion is much stronger than the L_1 , which in turn is very much stronger than the K . Both assignments are listed in the table, but on the basis of intensities it is felt that it is more probable that both lines are K lines.

In all sources produced at 30 Mev. there was an indication of a long-lived activity, and a half-life measurement over a period of 50 days indicated a half-life of 40–50 days. This indicated the possible growth of Ag¹⁰⁵ from Cd¹⁰⁵. A spectrograph source which had been allowed to stand for a period of more than a day, thus enabling the shorter period Cd¹⁰⁵ to die out, was exposed in the spectrograph for 20 days. The lines observed on the plate are listed in Table II, together with their assignments.

TABLE II
INTERNAL CONVERSION LINES OF Ag¹⁰⁵

$H\rho$ gauss-cm.	E_γ kev.	Assignment	γ -Energy, kev.
1909.9	256.4 \pm 0.5	K	280.8
2001.7	277.2	L_1	280.8
2015.9	280.4	$M_{IV,V}$	280.8
2079.2	295.0	K	319.4
2131.2	307.1	K	331.5
2188.3	320.6 \pm 0.6	K	345.0
2274.9	341.2	L_1	344.8
2386.4	368.2 \pm 0.7	K	392.6
2591.2	418.8	K	443.2

In the momentum region investigated, the γ -ray energies confirm those of Ag¹⁰⁵ determined by Hayward (9) to within his stated limits of error. In addition a previously unreported γ -ray of 331.5 kev. is indicated on the basis of the

conversion line of $H\rho$ 2131.2. The K/L_I ratios of the 280.8 kev. and 344.9 kev. γ -rays were both $\geq 5:1$.

The difference of 64.1 kev. between the 344.9 and the 280.8 kev. γ -rays indicated that Hayward's value of 62 kev. for the lowest energy γ -ray he observed might be low. Accordingly a long exposure was made at a lower magnetic field setting. The lines observed are listed in Table III.

TABLE III
INTERNAL CONVERSION LINES OF THE LOW-ENERGY γ -RAY OF Ag^{105} AND OF Ag^{109m}

$H\rho$, gauss-cm.	E , kev.	Assignment	γ -Energy, kev.
684.1	39.62 ± 0.1	K	63.98
852.7	60.38	L_I	63.99
867.6	62.39	K Ag^{109m}	87.93
874.7	63.36	M_I	64.04
1019.6	84.45	L_{II}, L_{III} Ag^{109m} unresolved	88.00, 87.83

These results indicate a value of 64.0 kev. for this γ -ray and also give a more accurate value than previously reported for the γ -ray of Ag^{109m} . Conversion lines due to the weak 112, 154, and 180 kev. γ -rays reported by Hayward were not observed.

There is an interesting similarity between the 319.4 kev. γ -ray of Ag^{105} and the 320.5 kev. γ -ray of Cd^{105} . In both cases the K conversion lines have the same momentum value ($H\rho$ 2079) within the limits of experimental error. The two nuclei differ only by exchange of a neutron for a proton, but such regularities are not commonly found.

The isotope Cd^{107} (6.7 hr.) was present in all sources and the opportunity was taken to redetermine the energy of the γ -ray of the metastable Ag^{107} . The conversion lines measured are listed in Table IV, and the L conversion lines, clearly resolved, are shown in Fig. 2, along with the M_{III} (or M_{II}) line. The energy of this γ -ray is thus indicated to be 93.0 kev., which does not

TABLE IV
INTERNAL CONVERSION LINES OF THE γ -RAY OF Ag^{107m}

$H\rho$, gauss-cm.	E , kev.	Assignment	γ -Energy, kev.
904.4	67.48 ± 0.06	K	93.02
1050.3	89.22 ± 0.07	L_I	93.05
1052.1	89.51	L_{II}	93.06
1053.2	89.68	L_{III}	93.06
1070.8	92.47	M_{III} (or M_{II})	93.06
1073.9	92.97	$N_{II, III}$ (or N_I)	93.05

agree with the value of 93.9 ± 0.2 kev. published by Bradt *et al.* (1). The discrepancy, however, is thought to be merely one of calibration. Since the value of 93.0 kev. was determined using the most recent values of the thorium A and F lines (3, 14) it is probably the more accurate.

4. MEASUREMENTS WITH THE LENS SPECTROMETER

4.1 Conversion Lines

The decay of the $L_{II, III}$ and M, N conversion lines of the 25.5 kev. γ -ray was measured in the lens spectrometer and values of 56.9 and 57.1 min. respectively were obtained for the half-life. In the initial measurement of the decay of these lines, a Geiger counter detector was used, and the counting rates were so very high on the peaks ($\sim 100,000$ c./50 sec.) that it was necessary to apply counting loss corrections for the initial part of the decay. These corrections were determined by following the decay of a sample of C¹¹ (20.25 min.) (2) of comparable initial activity, for a period of six half-lives. Owing to the large magnitude of the corrections in the early part of the Cd¹⁰⁵ decay, and the consequent uncertainty in their true value, it is felt that the half-lives so determined might be in error by ± 2 min. While an attempt was made to take account of the background, the fact that the 6.7 hr. Auger lines of the Cd¹⁰⁷ decay lay underneath these lines will account for the half-lives being slightly longer than those determined from the decay of the positron continuum.

The decay rates of the other lines detected in the 180° spectrograph were not measured in the lens spectrometer. These lines were very weak and could not be counted satisfactorily on top of the intense positron continuum. Qualitatively, in successive exposures in the 180° spectrograph, they disappeared at a rate consistent with a half-life of the order of an hour.

The region beyond the end point to the positron continuum was investigated carefully in order to obtain accurate energy values for higher energy γ -rays which had been found by means of a scintillation spectrometer (see below). By this time a scintillation detector (anthracene crystal + RCA 5819) had been adapted to the spectrometer and with the discrimination level set high in order to cut out noise background, a number of internal conversion peaks were found. These are shown in Fig. 3. Four definite peaks are apparent with energies of 1.882, 2.020, 2.252 (± 0.006 Mev.), and 2.295 Mev. (± 0.01 Mev.), and there are indications of two other peaks not clearly resolved of energies 1.932 and 1.970 Mev. (± 0.015 Mev.). On the assumption that these peaks are all due to internal conversion in the K shell, the energies of the γ -rays are 1.908, 1.957, 1.995, 2.045, 2.277, and 2.318 Mev. There seems to be a rather extended distribution of particles under the peaks below 2.05 Mev., and it is possible that this distribution may be made up in part by Compton electrons produced in the source from the two highest energy γ -rays as well as by a very small fraction of the positrons being scattered in the spectrometer.

These conversion lines were very weak, as is to be expected for such energies, and even with a very active source, the peak counting rate was never greater than 450 c./60 sec. In different runs, however, the peaks were always reproducible. With such low counting rates, an accurate determination of the decay rate was not feasible, but a rough estimate gave a value consistent with that determined from the positron spectrum. At times, when the silver target was heated for too long in the evaporation process, active silver was evaporated over along with the cadmium, and since this consisted mostly of Ag¹⁰⁶ (24.5 min.) from the Ag¹⁰⁷ (p, pn) reaction, the 2.0 Mev. positron spectrum of this

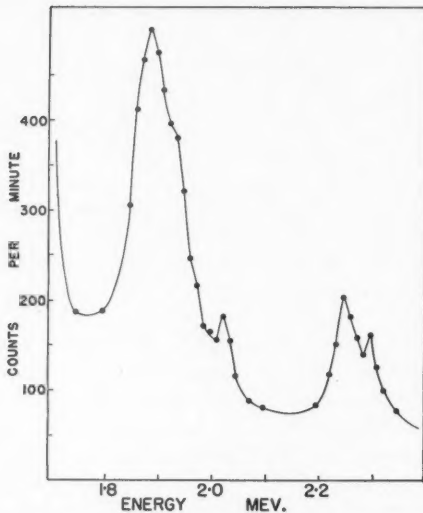


FIG. 3. High-energy internal conversion lines of Cd¹⁰⁵ found in lens spectrometer (successive points not corrected for half-life). The statistical accuracy of the plotted points is about ± 15 c./min.

isotope was detectable in the region where the high-energy conversion lines lay. The results from such contaminated sources were not used and it is possible to say that the decay rate of the recorded conversion lines was not as low as 25 min. Also the energies of these γ -rays do not correspond with any of those already assigned to Ag¹⁰⁶ (9).

A search was made for conversion lines from the other γ -rays found by means of the scintillation spectrometer, but no peaks could be detected on top of the positron continuum.

4.2 Positron Spectrum

The positron spectrum of Cd¹⁰⁵ was very intense and it was possible to obtain very high initial counting rates ($\sim 70,000$ c./50 sec.) at the maximum, with consequent good statistics. The lens spectrometer was operated at a resolution of 1.6% for these measurements, and the scintillation detector made it possible to count at these high counting rates without loss. The average source strength corresponded to 2 mc. in positrons alone.

A Fermi plot of the positron distribution is shown in Fig. 4, and an end point of 1.691 ± 0.005 Mev. is indicated. In order to make the plotted points as free from statistical errors as possible, all points of the spectrum were followed for a period of five hours. A decay curve was drawn for each point and from these curves the counting rates at a given instant of time were obtained, whence the Fermi plot was calculated. Values of the Fermi function were taken from the National Bureau of Standards publication AMS 13, and the screening correction was incorporated. All points above 350 kev. showed a simple decay of half-life 54.7 ± 0.8 min.

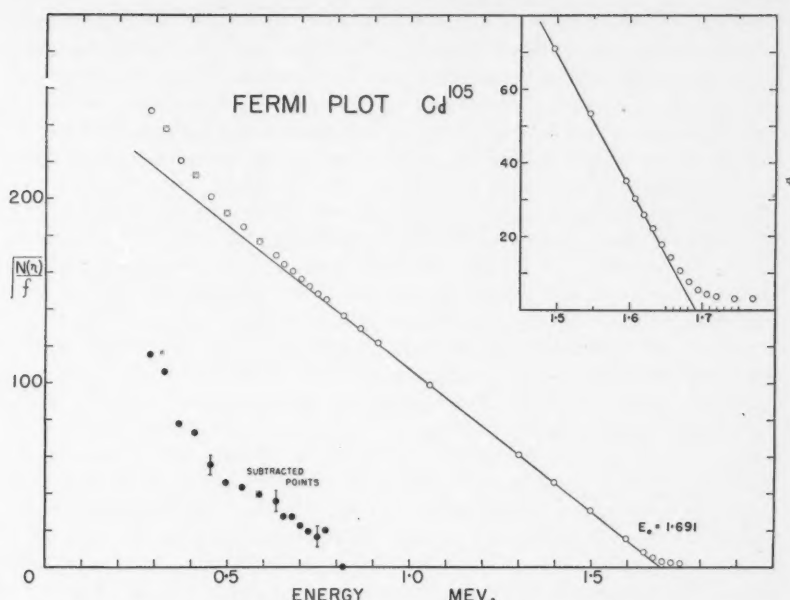


FIG. 4. Fermi plot of Cd¹⁰⁵ positron spectrum, with enlargement of end point region as an inset. The counting statistics for the high-energy component are no larger than the plotted points.

From Fig. 4 it will be seen that the Fermi plot is straight from about 800 kev. to about 75 kev. below the end point. Hence the spectrum may be assumed to have an allowed shape. Below 800 kev. (the maximum $N(\eta)$ of the spectrum is ~ 720 kev.) there is a slight upward curvature which was obtained in all runs with both weak and strong sources. Subtraction of the main group from the total yielded an approximately straight line, giving an end point of 800 ± 75 kev. There seemed to be a slight curvature of these points similar to that of an " α " type forbidden spectrum, but the statistics of this subtracted spectrum did not warrant a further analysis. Internal conversion lines from the 347, 433, and 607 kev. γ -rays are partly responsible for a few of the points being off a straight line, but even when these are neglected the curvature is still present. The fact that the γ -spectrum is so complex makes it quite probable that there are other positron spectra besides the main group. Below 325 kev. the Fermi plot curves upward very strongly, owing to the presence of the Cd¹⁰⁷ (6.7 hr.) spectrum.

The curvature near the end point of the main spectrum was obtained on every run but was so slight that it was impossible to say definitely that a higher energy spectrum was present. A more reasonable explanation for this deviation is the uncertainty in the background with the current on in the spectrometer, slight scattering in the spectrometer, and the presence of high-energy γ -rays which possibly produce in the source a Compton distribution of electrons. An enlargement of the Fermi plot near the end point is shown as an inset in Fig. 4.

5. MEASUREMENTS WITH THE SCINTILLATION SPECTROMETER

A scintillation spectrometer using a NaI (Tl) crystal, which had been built up by Henrikson (10) and Breckon (2), was employed in a search for high-energy γ -rays. A single channel analyzer was used to obtain a pulse height distribution, and calibration was made with the photoelectric and pair peaks of the 2.62 Mev. γ -ray of ThC'. During an actual count on the source the annihilation radiation peak was used as an additional calibration point.

In the high-energy region definite peaks were found of energies 0.94 ± 0.01 , 1.30 , 1.64 , 1.93 ± 0.02 , and 2.28 ± 0.03 Mev., with an indication of another peak of energy 1.03 ± 0.03 Mev. The underlying continuum was rather intense and there was a strong possibility that other unresolved peaks were present.

With the low resolution of the scintillation spectrometer as compared to that of the lens spectrometer it is not to be expected that as detailed information would be obtained from these data as from an examination of the internal conversion peaks. In addition the possible presence of three (or four) peaks (photoelectric, pair (single and/or double escape), and Compton) for each γ -ray makes analysis difficult. The peak of energy 2.28 Mev. is obviously the photo peak due to the γ -rays of 2.277 and 2.318 Mev., and the 1.30 Mev. peak can be assumed to be the pair peak, while the Compton peak of energy about 2.07 Mev. was not obvious from the data. The peak of energy 1.93 Mev. can be assumed to be the photo peak from the unresolved 1.908, 1.957, and 1.995 Mev. γ -rays, with the 0.94 Mev. peak being the associated pair peak. The peak of energy 1.64 Mev. is a little too low in energy to be definitely assigned as the Compton peak for this group and might therefore indicate the presence of a γ -ray of 1.64 Mev. The peak of energy 1.03 Mev. can be assigned as the pair peak due to the 2.045 Mev. γ -ray, but the Compton and photoelectric peaks have not been identified.

At lower energies photoelectric peaks were found corresponding to γ -rays of energies 600, 440, 350, and 270 kev. but there was no indication of any γ -ray which had not already been found in the 180° spectrograph and listed in Table I.

6. DISCUSSION OF RESULTS

The mass assignment of the activity discussed in this paper has been claimed by Gum and Pool (8) on the basis of its production from scarce isotopes by the $Pd(\alpha, n)$ and Cd (fast n) reactions and by their inability to produce it by the $Ag(d)$ and Cd (slow n) reactions.

Confirmation for the assignment to mass 105 may be obtained from the threshold energies for the $Ag^{107}(p, 3n)Cd^{105}$ and $Ag^{107}(p, 4n)Cd^{104}$ reactions. These may be calculated approximately from the data contained in the Table of Atomic Masses of Metropolis and Reitwiesner (16) as 22 Mev. and 32 Mev. respectively. Experimental results indicated that the activity which was assigned to Cd^{105} began to appear at a nominal proton bombardment energy of about 20 Mev., and the activity assigned to Cd^{104} began to appear just above 30 Mev.

From the graphs given by Feenberg and Trigg (4) it is seen that the K capture to positron ratio for allowed decays to a given level increases as the available energy decreases. For the 1.691 Mev. positron spectrum the theoretical K

capture to positron ratio is 1; transitions to more highly excited levels will proceed predominantly by K capture. Thus the great number of γ -rays which were found, especially those of high energy, can be assumed to follow K capture to excited levels in Ag¹⁰⁵, positron emission to these same levels being very much less probable. Apart from the observed nature of the positron spectrum, little can be said about the detailed relative probabilities of the transitions to the various levels. Analysis of the NaI scintillation spectrometer results, however, where the annihilation radiation was compared with the other radiations, indicates that the γ -radiations constitute the major portion (50 to 90%) of the decay.

The positron end point of 1.691 Mev., taken in conjunction with the experimentally determined half-life of 55 min., gives a $\log ft$ product of 5.0. Since this positron decay constitutes between 10 and 50% of the total decay, the partial $\log ft$ for this transition lies between 5.3 and 6.0. The f value used in this calculation was determined from the graphs given by Feenberg and Trigg and includes the theoretical correction for K capture. On the basis of the classification of $\log ft$ values of Mayer, Moszkowski, and Nordheim (15) a value of 5.3–6.0 indicates an allowed transition with spin change 0 or 1 and no parity change. On the basis of the shell model a $g_{7/2}$ configuration is indicated for the ground state of Cd¹⁰⁵ (the only other (unlikely) possibility is a partially filled $g_{7/2}$ shell with an odd neutron in a $d_{5/2}$ orbit). For the ground state of Ag¹⁰⁵ the configurations $g_{9/2}$, $p_{1/2}$, or $7/2+$ may be considered. Assuming $g_{7/2}$ for Cd¹⁰⁵, the $g_{9/2}$ or $7/2+$ states are consistent with the 1.691 Mev. spectrum being an allowed ground state transition. However, the level structure for Pd¹⁰⁵ given by Goldhaber and Hill (6) favors $p_{1/2}$ for the ground state of Ag¹⁰⁵. If this $p_{1/2}$ assignment is correct (implying a spin change of 3 units in the decay of Cd¹⁰⁵), then the 1.691 Mev. positron spectrum cannot be assumed to be a ground state transition. Attempts were made to find $\beta-\gamma$ coincidences by means of the scintillation spectrometer, but apparently only chance coincidences were observed. If the positrons are in coincidence with any γ -rays, then these γ -rays would appear to be in the energy region below 500 kev.

A determination of the multipole order of a γ -ray is useful if an attempt is to be made to construct a decay scheme. In this investigation the intensities of most of the conversion lines obtained in the 180° spectrograph were not sufficient to attempt a determination of the multipole order of the associated γ -rays on the basis of relative intensities of K and L lines. The rough value of 4 obtained for the K/L ratios of both the 347 and 433 kev. γ -rays would indicate a multipole order of 2 or 3, with an $E3$ transition being most probable from the empirical K/L ratios (7) (higher multipolarities can be excluded on the basis of lifetimes). $E1$, $M1$, and $E2$ can be ruled out for the 433 kev. transition on the experimental evidence that the L_1 conversion line was not seen (5). For the 347 kev. transition none of the possible multipolarities can be ruled out from the evidence that only the L_1 conversion line was observed. More definite information can be obtained about the 25.5 kev. γ -ray. Only the L_{11} and L_{111} lines of this γ -ray were observed, ($L_{11} < L_{111}$ in intensity), the L_1 line being too weak to be recorded on the photographic plate. Comparison with the theoretical L shell

ratios (5, 17) indicates that this γ -ray cannot be $E1$, $M1$, or $M2$, and is most probably $E2$ (higher multipolarities being excluded from lifetime considerations). The $L/M, N$ ratio was measured in the lens spectrometer as ~ 4 , but there are no theoretical values for comparison.

The complexity of the γ -ray spectrum and the apparent presence of one or more β -spectra below 800 kev. precludes any attempt at constructing at this time a complete decay scheme for Cd^{105} . On the basis of the energy values determined for the γ -rays it is possible to fit a number of these γ -rays into consistent groups, but with the data available it is impossible to fit these groups into an over-all scheme. The following γ -ray combinations may be noted: $340.7 + 320.5 = 324.9 + 336.3 = 661.2$; $661.2 + 292.5 = 606.7 + 347.0 = 953.7$, $317.1 + 312.1 + 324.9 = 954.1$, $317.1 + 329.2 + 308.0 = 954.3$; $1908 + 433 = 2341$, $1995 + 347 = 2342$; $1957 + 433 = 2390$; $2045 + 347 = 2392$; $1957 + 321 = 2278$, 2277 . An investigation of the radiations by γ - γ coincidence techniques would probably clarify the situation somewhat, although the large number of γ -rays would make some resolutions difficult.

The determination of accurate energy values for most of the γ -rays of Ag^{105} makes it possible to extend the decay scheme for this isotope as given by Goldhaber and Hill (6) (proposed by Hayward). A possible decay scheme, which includes all of the γ -rays listed by Hayward (9), is given in Fig. 5. It will be

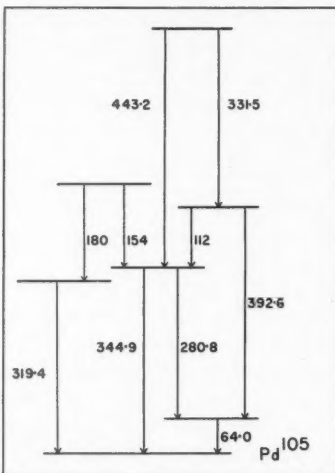


FIG. 5. Proposed energy levels in Pd^{105} based on energy measurements of the γ -rays following K -capture in Ag^{105} .

seen that the presence of the 331.5 kev. transition makes it possible to assign the 443.2 kev. transition unambiguously. It would appear that the 319.4 kev. transition is identical with the 320–322 kev. γ -ray found in the Rh^{105} decay.

The case of the 93.0 kev. γ -ray of Ag^{107m} is of interest since this has already been established as an $E3$ transition (1, 6). Thus the relative intensities of the

L_I , L_{II} , and L_{III} lines of this γ -ray, measured roughly as 0.2: 1: 1, can be taken as characteristic of an $E3$ transition at this energy.

ACKNOWLEDGMENTS

The author wishes to thank Dr. J. S. Foster, Director of the Radiation Laboratory, for his continued interest throughout the course of this investigation. Discussions of theory with Dr. J. D. Jackson were most appreciated and served to clarify somewhat the complexity of the experimental results. Thanks are due to Mr. R. H. Mills who operated the cyclotron during the many hours of bombardment, to Mr. R. Lorimer for his painstaking work with the quartz apparatus, and to the many other members of the Radiation Laboratory who contributed to this investigation.

REFERENCES

1. BRADT, H., GUGELOT, P. C., HUBER, O., MEDICUS, H., PREISWERK, P., SHERRER, P., and STEFFEN, R. Helv. Phys. Acta, 20: 153. 1947.
2. BRECKON, S. W. Thesis, McGill University, Montreal, Quebec. 1951.
3. CRAIG, H. Phys. Rev. 85: 688. 1952.
4. FEENBERG, E. and TRIGG, G. Revs. Mod. Phys. 22: 399. 1950.
5. GELLMAN, H., GRIFFITH, B. A., and STANLEY, J. P. Phys. Rev. 85: 944. 1952.
6. GOLDHABER, M. and HILL, R. D. Revs. Mod. Phys. 24: 179. 1952.
7. GOLDHABER, M. and SUNVAR, A. W. Phys. Rev. 83: 906. 1951.
8. GUM, J. R. and POOL, M. L. Phys. Rev. 80: 315. 1950.
9. HAYWARD, R. W. Phys. Rev. 85: 760. 1952.
10. HENRIKSON, A. Thesis, McGill University, Montreal, Quebec. 1953.
11. HILL, R. D., CHURCH, E. L., and MIHELICH, J. W. Rev. Sci. Instr. 23: 523. 1952.
12. JOHNSON, F. A. Abstract No. 76, Royal Society of Canada, June Meeting, Quebec. 1952.
13. JOHNSON, F. A. and FOSTER, J. S. Can. J. Phys. 31: 469. 1953.
14. LINDSTROM, G. Phys. Rev. 83: 465. 1951.
15. MAYER, M. G., MOSZKOWSKI, S. A., and NORDHEIM, L. W. Revs. Mod. Phys. 23: 315. 1951.
16. METROPOLIS, N. and REITWIESNER, G. Table of Atomic Masses. Argonne National Laboratory. 1950.
17. TRALLI, N. and LOWEN, I. S. Phys. Rev. 76: 1541. 1949.

ON SOME PHYSICAL ASPECTS OF THE THEORY OF THE ORIGIN OF MOUNTAIN BELTS AND ISLAND ARCS¹

BY ADRIAN E. SCHEIDECKER²

ABSTRACT

It is shown that a physical explanation can be given within the framework of the contraction hypothesis of orogenesis for the four types of junctions of island arcs and mountain belts observed by geologists.

1. INTRODUCTION

The problem of physical causes of orogenesis has puzzled geologists and geophysicists for a long time. A great number of theories have been postulated to solve the problem, and new ones are still being advanced. The writer has reviewed such theories on several occasions (Refs. 3, 4, 5) and he came to the conclusion that the contraction hypothesis, in connection with failure of the outer shells of the earth as set forth by Wilson (Refs. 6, 7), holds probably the best promise for being the correct explanation of such salient features of the earth's surface as mountain belts and island arcs.

A necessary requirement of any sensible theory of orogenesis is that it be based upon sound physical reasoning. It has been the quest of the author during the past few years to set the explanation of geological features upon such a physical basis. For any one theory of orogenesis, this is by necessity something that has to be accomplished piece by piece, since only a limited portion of the great wealth of geological data can be considered at any one time, and other portions have to be relegated to further investigations.

Thus, the author analyzed some physical aspects of the contraction hypothesis of orogenesis in Reference 3; the present paper is thought to add another chapter to that study.

As stated in Reference 3, the contraction hypothesis upon grounds of thermal and mechanical behavior divides the earth into three shells which may be termed (i) the interior (no strain, still hot), (ii) the orogenetic shell (cooling and therefore in a state of tension), and (iii) the surface (largely cooled and therefore in a state of compression). The situation is illustrated in Fig. 1. These shells are not dependent upon the earth's composition and hence should not be confused with such terms as core, mantle, and crust. Fig. 1 also exemplifies how the contraction hypothesis of orogenesis provides for an explanation of island and mountain arcs on the earth's surface. For more details about this theory the reader is referred to Reference 3.

It has been observed by Wilson (Ref. 6) that the arcs on the earth's surface occur in belts, the junction between arcs being one of four types illustrated in Fig. 2. It is proposed to give in this paper a rational explanation for those four types of junctions between arcs.

¹ Manuscript received April 27, 1953.
Private communication.

² Present address: 3023-36th Street S.W., Calgary, Alta.

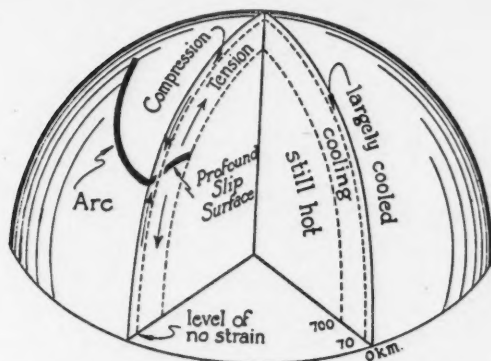


FIG. 1. Stresses in the earth according to the contraction hypothesis; fracture in the shell under tension is the cause of an arc. After Wilson.

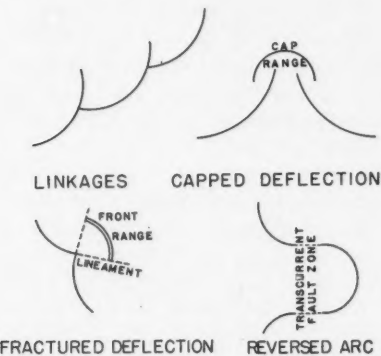


Fig. 2. The four types of junctions of arcs; after Wilson.

2. PRIMARY EFFECTS

According to the contraction hypothesis, the surface features of the earth are the expression of phenomena taking place in the orogenetic shell. If one is to investigate the cause of the different types of junctions between the arcs, one will therefore have to split the phenomenon into a "primary" effect taking place within the orogenetic shell, and another, "secondary" one, which is the surface expression of the first-mentioned primary effect.

We shall turn first to the primary effect. During the formation of an island or mountain arc, the phenomenon thought to occur in the orogenetic shell is a conical fracture with slippage taking place along the cone of fracture. (For a detailed description see Reference 5.) Within a cross section through the orogenetic shell parallel to the surface of the earth, the motion is therefore as illustrated in Fig. 3. Within the cross section, the surface of slippage is seen as a line which is, in the mathematical sense, singular. The displacements of the

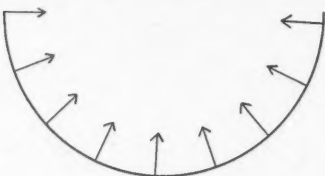


FIG. 3. Motion within a cross section parallel to the surface of the earth through the orogenetic shell during the formation of an arc.

material elements in the cross section of the orogenetic shell are everywhere continuous during the orogenetic diastrophism except on that singular line which is the trace of the surface of slippage on the cross section.

It is quite obvious that the displacements of material within the orogenetic shell of the earth during an orogenetic diastrophism must obey a continuity equation, since no material can be created or annihilated in the process. Whatever the displacements (denoted by ξ) may be, they must therefore be subject to the equation

$$[2.1] \quad \operatorname{div} \rho \xi = 0.$$

If the density ρ of the material is assumed as (more or less) constant, this means that the displacement field must be a divergence-free field. It is known that such a divergence-free field cannot satisfy arbitrarily singular boundary conditions.

This fact can be illustrated by elementary geometry which is directly applicable to the theory of island arcs and mountain belts.

Thus assume that two island arcs join, forming an angle α at the junction point. In a cross section of the orogenetic shell parallel to the surface of the earth, within the neighborhood of the junction, one will have a singular line, having a "kink" of angle α at the junction point of the arcs. If it be borne in mind that *ab hypothesi* the motion has to be at right angles to the singular line (see Fig. 3), it is immediately clear that, for continuity reasons, at least one other singular line must join the first one at the "kink". Furthermore, elementary geometry shows that this new singular line must lie within the sector formed by the two normals to the original singular line at the kink. Fig. 4 will clarify the situation, the permitted sector for the additional singular line being shaded; a possible position of the latter has been drawn in and the arrows signify the motion of every element in the cross section of the orogenetic shell which is under consideration. It is seen that this arrangement of singularities corresponds to the junction termed "linkage" by Wilson (see Fig. 2).

It has been stated above that there has to be *at least* one additional singular line joining the island arcs at their junction. There may be more. In every case, the additional lines must lie within the shaded area of Fig. 4; a possible position of *two* singular lines together with the displacement field has been drawn in Fig. 5. It must be expected that this is the case which gives rise to a junction of arcs with cap range and lineaments. However, those two latter occurrences are phenomena of the surface and not of the orogenetic layer, and will be treated later.

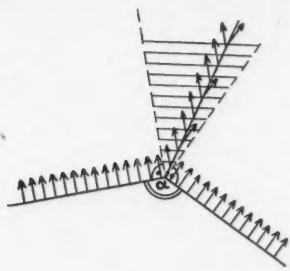


FIG. 4. Motion within a cross section parallel to the surface of the earth through the orogenetic shell in the neighborhood of the junction of two arcs if only *one* additional singular line is present. The permitted sector for the additional singular line is shaded.

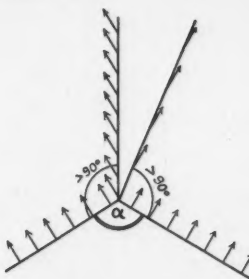


FIG. 5. Motion within a cross section parallel to the surface of the earth through the orogenetic shell in the neighborhood of the junction of two arcs, if *two* additional singular lines are present.

It is obviously not meaningful to have more than two additional singular lines joining the arcs at the junction, as the motion of the additional sector created would be entirely arbitrary and connected in no way with the formation of the arcs.

There is one additional possibility; that is when the junction of two arcs forms no kink at all. If the arcs are to be distinct, this suggests that they must be joined in reverse. It is anticipated that this arrangement will give rise to the "reversed arcs" as described by Wilson (see Fig. 2).

3. SECONDARY EFFECTS

The primary effects discussed in the last section are not immediately manifest on the surface of the earth. Owing to secondary effects occurring within the surface layer of the earth, features additional to those occurring in the orogenetic shell may be observed.

The surface shell of the earth overlies the orogenetic shell. Any movement of the orogenetic shell will therefore transmit itself to the surface shell because the two layers act upon each other. It must therefore be expected that fracture lines within the orogenetic shell will also be reflected as fracture lines on the surface. The types of fracture to be expected at the surface will depend on the relative motion of the fractured parts of the underlying (ogenetic) region. There will be two extreme cases: viz. if the motion of the orogenetic shell is at right angles to the singular line, a hiatus will be the result on the surface; contrariwise, if the relative motion of the orogenetic shell is parallel to the singular line, a simple shearing fracture or shift will be the surface result. The two types of surface fractures are illustrated in Fig. 6.

There will be some additional effects, however. It is a salient feature of the contraction hypothesis that it assumes that the earth as a whole is shrinking. The shrinkage essentially takes place within the orogenetic layer; the surface is therefore in a state of (planar) compression. Superimposed on the shear transmitted from the motion of the layers below, there is therefore a compression which will tend to cause the surface to buckle.

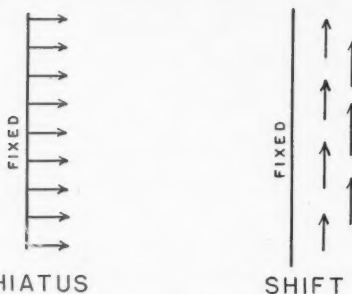


FIG. 6. The two types of surface fracture.

If we examine the phenomena occurring in the orogenetic shell with reference to their appearance on the surface, it is seen that the case illustrated in Fig. 4, where there is only *one* additional singular line at the junction, will give rise to essentially a hiatus. Were it not for the compression which is superimposed, the surface expression of this hiatus would always be a trench. Owing to the compression, however, this is not necessarily the case, as following the formation of the trench, the latter may play the rôle of a weak region in a shell about to fail, so that all that can be said is that the singular lines below are reflected as tectonic disturbances—upward or downward—on the surface. These disturbances are arrayed exactly like the singular lines below, i.e. they correspond to the first example in Fig. 2, called “linkage”. Wilson (Ref. 6) collected some cases where this type of junction of island arcs is found upon the earth.

More complex are the phenomena to be expected when there are *two* additional singular lines (in a cross section of the orogenetic shell) originating from the junction of two arcs. In this case, the relative motion of the orogenetic shell is essentially parallel to the singular lines (as seen from Fig. 5), such that a shearing fracture or shift would be expected to be the surface result. The fracture will be *exactly* a shear or shift if the angles between the additional singular lines and the arcs are right ones. Geologically, this would cause a lineament on the earth's surface. Such lineaments have actually been observed as stated by Wilson (Reference 6).

However, the superimposed compression may change the picture considerably. It must be assumed that the shearing occurs under any circumstances. The surface, therefore, will be cut up into a tooth-shaped triangular pattern which is pointed towards the junction point of the arcs. The size of the triangle depends on the plasticity of the crust; its utmost limits, however, are given by the size of the arcs as illustrated by Fig. 7. In the case of pure shear, the triangle cannot be bigger than that formed by the centers and the junction points of two adjoining arcs.

The triangle which is thus cut out of the surface of the earth will start to buckle owing to the superimposed pressure. The buckling of a triangle can be easily calculated. If we denote the angle at the vertex by β , the distance from the vertex of a line parallel to the base by x , and the deflection of that line from



FIG. 7. Maximum size of triangle (shaded) into which the surface may be cut owing to pure shearing motion of the orogenetic shell.

the original plane of the triangle by y , the condition of static equilibrium yields

$$[3.1] \quad -Fy(x) = Mx \tan \beta d^2y/dx^2.$$

The left-hand side of this equation is the moment of a force F parallel to the original plane of the triangle and normal to the base, applied at the vertex (that is the force causing buckling), and M is the resistance to bending provided by the material of the triangle. The solution of this differential equation is a Bessel function (see Ref. 2):

$$[3.2] \quad y = x^{\frac{1}{2}} J_1 [2x^{\frac{1}{2}} (M \tan \beta)^{-\frac{1}{2}} F^{\frac{1}{2}}]$$

whose zeros are at $X = 0, 3.83, \dots$, with

$$[3.3] \quad X = 2(M \tan \beta/F)^{-\frac{1}{2}} x^{\frac{1}{2}}.$$

The maxima of y are at those points where $dy/dx = 0$. Thus

$$[3.4] \quad dy/dx = \frac{1}{2}x^{-\frac{1}{2}} J_1(X) + (M \tan \beta/F)^{-\frac{1}{2}} J_1'(X).$$

However, one has (see Ref. 1)

$$[3.5] \quad J_1' = -\frac{1}{2}(M \tan \beta/F)^{\frac{1}{2}} x^{-\frac{1}{2}} J_1(X) + J_0(X),$$

so that it is seen that the zeros of $y' = dy/dx$ are the same as those of $J_0(X)$. The latter are $X = 2.40, 5.52, \dots$

In order for buckling to be possible, the buckling force F must have such a value that y is zero for $x = 0$ and $x = h$ (h being the height of the triangle); thus, one has for first-order buckling:

$$[3.6] \quad 3.83 = 2(M \tan \beta/F)^{-\frac{1}{2}} h^{\frac{1}{2}}.$$

The maximum deflection (the "ridge") is obtained for $X = 2.40$, thus

$$[3.7] \quad 2.40 = 2(M \tan \beta/F)^{-\frac{1}{2}} x_{\max}^{\frac{1}{2}}$$

whence

$$[3.8] \quad x_{\max} = 0.393 h.$$

It is thus seen that the distance of the buckling ridge from the vertex of the triangle depends only on the height of the triangle and not on the angle at the vertex.

If we apply these results to the buckling of the surface of the earth, the following may be seen.

In the case of pure shear, lineaments may be expected to start out from the junction of two arcs. Some distance away, a high ridge (the "buckling ridge")

will be formed facing the junction. The foregoing discussions pertain to buckling in a plane; naturally, on a sphere, the straight lines on the plane will be curved. It is therefore reasonable to expect that a situation as illustrated in Fig. 8 will be the result.

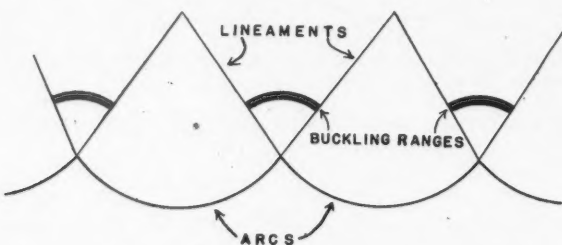


FIG. 8. Geographical expression of buckling ranges.

In the case of pure shear, the lineaments are at 90° to the arcs. The larger the angle α between the arcs, the smaller is the angle β of the triangle, and the larger the triangle may be. Therefore, the smaller the angle between arcs, the closer to the junction point the buckling range will be found. If it is very close, it could well be the "cap range" discovered by Wilson (see Fig. 2); if it is farther away, it could correspond to the "front range".

In this manner it is possible to explain three of the types of junctions observed by Wilson. It remains to explain the last possibility, the "reversed arc" in Fig. 2. This is easily done by recurring to the remark of Section 2. It was stated there that there is one possibility for which there may be no kink between two arcs, viz. when the arcs are joined in reverse. The surface features connected with reverse arcs may then be thought of as a direct manifestation of the arrangements in the orogenetic shell.

4. CONCLUSION

The foregoing discussion shows that it is possible to find a rational explanation of the types of junctions observed between island arcs and mountain belts, based upon the fracture theory for explaining the latter. This adds another remarkable fact to the arguments corroborating the fracture theory of orogenesis.

The arguments used in the present paper may be felt to be rather abstract, viz. the idealized plane and its buckling are somewhat of an abstraction compared to the actual earth. But only if such abstractions are introduced, can one hope to make the complex phenomena of geology amenable to an exact (as opposed to a descriptive) interpretation.

It is rather unfortunate that no estimate can be given of the height which the buckling range is expected to attain for any one given movement in the orogenetic shell. The reason for this is, of course, that the slippages within the orogenetic shell are only indirectly connected with the pressure in the surface layer of the earth which governs the buckling. True, they have a common cause in the cooling of the orogenetic layer, but they are not directly dependent upon

each other. The height of the mountain ranges can therefore only be estimated in a more general manner as was done in an earlier paper of the author (Ref. 3).

In conclusion, the writer wishes to acknowledge his indebtedness to Dr. J. Tuzo Wilson of the University of Toronto for the interest he has taken in this work and also for critically reading this manuscript.

REFERENCES

1. JAHNKE, E. and EMDE, F. Tables of functions with formulae and curves. 4th ed. Dover Publications, New York. 1945.
2. KAMKE, E. Differentialgleichungen, Lösungsmethoden und Lösungen. Chelsea Publishing Company, New York. 1948.
3. SCHEIDECKER, A. E. Can. J. Phys. 30: 14. 1952.
4. SCHEIDECKER, A. E. Trans. Am. Geophys. Union, 33: 585. 1952.
5. SCHEIDECKER, A. E. Bull. Geol. Soc. Amer. 64: 127. 1953.
6. WILSON, J. T. Proc. Geol. Assoc. Can. 3: 141. 1950.
7. WILSON, J. T. Papers & Proc. Roy. Soc. Tasmania, 1950: 85. 1951.

FIRST SOUND IN LIQUID HELIUM AT HIGH PRESSURES¹

By K. R. ATKINS AND R. A. STASIOR

ABSTRACT

The velocity of ordinary sound in liquid helium has been measured in the temperature range from 1.2°K. to 4.2°K. at pressures up to 69 atm. A pulse technique was used with a carrier frequency of 12 Mc.p.s. Curves are given for the variation of velocity with temperature at constant pressure and also at constant density. There is no detectable discontinuity along the λ -curve. The results are used to discuss the ratio of the specific heats, the coefficient of expansion below 0.6°K., and the specific heat above 3°K.

1. INTRODUCTION

There are two types of wave propagation in liquid helium II. Ordinary sound, consisting of pressure oscillations, is commonly called first sound in order to distinguish it clearly from second sound which consists of temperature oscillations. The velocity of first sound along the vapor pressure curve has already been measured by Findlay, Pitt, Grayson-Smith, and Wilhelm (3), Pellam and Squire (7), and by Atkins and Chase (1). Before the work described in this paper the only measurements at higher pressures were those of Findlay, Pitt, Grayson-Smith, and Wilhelm (4), but their highest pressure was 5.55 atm. and their lowest temperature was 2.0°K. The present work covers the temperature range from 1.2°K. to 4.2°K. and extends up to a pressure of 69 atm.

There are several reasons for wishing to extend the first sound velocity measurements. Firstly, the velocity is related to the adiabatic compressibility and is therefore helpful in deriving various thermodynamic quantities. Secondly, there is good reason to believe that, below about 0.6°K., the thermal excitations in liquid helium consist almost entirely of longitudinal Debye waves (phonons) and the thermodynamic nature of the liquid is then almost completely defined once the velocity of first sound is known as a function of pressure. In particular, the behavior of second sound near 0°K. is intimately related to the velocity of first sound. Thirdly, if the λ -transition is of the second order, there is a discontinuity in the isothermal compressibility along the λ -curve and this might imply a discontinuity in the velocity of first sound. No such discontinuity has been found at the vapor pressure (1, 3, 7) but the work of Findlay, Pitt, Grayson-Smith, and Wilhelm (4) suggested that there might be a discontinuity at higher pressures.

2. APPARATUS AND METHOD

2.1. Ultrasonics Technique

The technique was very similar to that used by Atkins and Chase (1). A pulse of length 10 μ sec. at a carrier frequency of 11.8 ± 0.3 Mc.p.s. was fed into the liquid helium by a quartz crystal transducer, reflected from a plane brass surface, and received by the same transducer. The crystal holder is shown in Fig. 1. The upper face of the crystal X was silvered and was in electrical

¹ Manuscript received August 4, 1953.

Contribution from the Department of Physics, University of Toronto, Toronto, Ont.

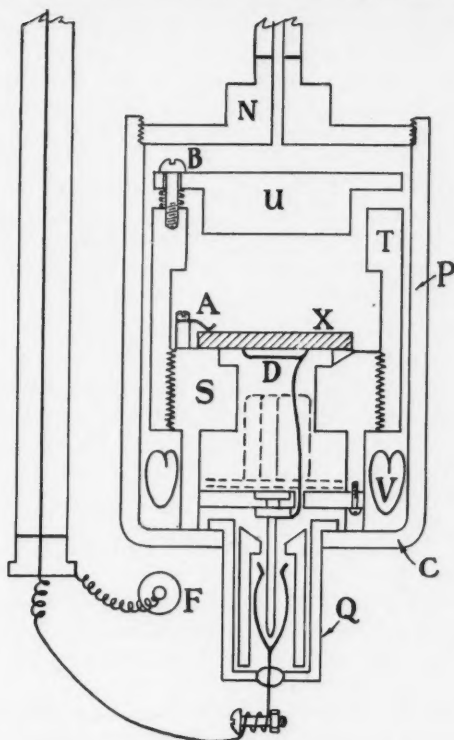


FIG. 1. The bomb and crystal holder.

contact with the brass holder via the springs *A*. The high frequency power was fed in through a fine copper wire embedded in a layer of silver paint *D* covering the central part of the lower face of the crystal. The space behind the crystal was packed with flint sanding cloth to eliminate echoes from this region. The brass reflector *U* was aligned parallel to the crystal by adjusting three levelling screws *B* while observing the echoes in liquid air.

2.2. High Pressure Equipment

The crystal holder was contained inside the copper bomb *C* which was immersed in a bath of liquid helium. The high pressure was applied via the monel capillary *N* and was kept constant either by introducing gas from a cylinder or by releasing gas to the atmosphere. The pressure was measured with an accuracy of 1% on three Bourdon gauges which had been calibrated against a pressure balance.

2.3. Temperature Measurement and Control

The vapor pressure of the bath was read on a mercury manometer at higher pressures and on a butyl phthalate manometer at lower pressures. The 1949 temperature scale was used (2). Whenever the bath liquid was above the λ -point

a correction was applied for the hydrostatic pressure head effect (1). The bomb was probably at a slightly higher temperature than the bath because of the heat flowing down into it and outwards through its wall. This effect depends upon the thermal resistance at the liquid-solid boundary (5, 8) and therefore varies in a complicated and unknown manner with pressure and temperature. The temperature difference was probably as great as 0.01°K . under some conditions and this limits the accuracy of the temperature measurement.

To maintain the temperature steady a carbon resistance thermometer was immersed in the bath near the bomb and formed one arm of a Wheatstone bridge. The power fed into a heater at the bottom of the bath was adjusted so that the galvanometer in the Wheatstone bridge maintained a steady reading, and the temperature was thereby kept constant to better than $2 \times 10^{-4}^{\circ}\text{K}$.

2.4. Accuracy

Possible sources of error in the velocity measurements have been discussed in detail by Atkins and Chase (1). We estimate that, in our case also, relative values of the velocity are in error by 0.3%, but that the absolute error might be as large as 1%. The pressure was accurate to 1% and the temperatures were reliable to within 0.01°K .

3. RESULTS

3.1. The Velocity Data

The measurements taken at constant pressure and varying temperature are illustrated in Fig. 2 and smoothed data are collected in Table I. In Fig. 2 the experimental points obtained near the λ -curve have been omitted to avoid confusion.

The velocities at the lowest temperatures are particularly relevant to the properties of the phonons below 1°K . Here measurements were taken at constant temperature and varying pressure, as shown in Fig. 3. The velocity is seen to be almost independent of temperature for temperatures less than 1.6°K . and pressures less than 20 atm. Fig. 3 may therefore be used to obtain values of the velocity extrapolated to 0°K . Fig. 3 also includes values of the velocity deduced from the isothermal compressibility, k_T (6, page 237), assuming γ , the ratio of the specific heats, to be unity at these low temperatures and using the relation $u_1 = (\gamma/\rho k_T)^{1/2}$. The agreement is satisfactory.

Fig. 4 shows how the velocity varies with temperature at constant density. The broken curve was calculated from the data of Fig. 2 and the equation of state (6, page 237). The full curve was obtained experimentally by closing off the bomb so that a constant mass of helium remained in it. The slight discrepancy between the two curves is mainly due to the fact that in the experiment the density was not quite constant because the mass of helium in the monel capillary (N in Fig. 1) varied with temperature. It is interesting to note that, above 3°K . when the λ -point anomaly has been passed, the velocity increases with temperature, whereas the opposite is true at constant pressure.

3.2. The Vicinity of the λ -Curve

At no pressure was there any evidence for a discontinuity in velocity at the λ -point, even when the echo was followed closely as the λ -curve was traversed.

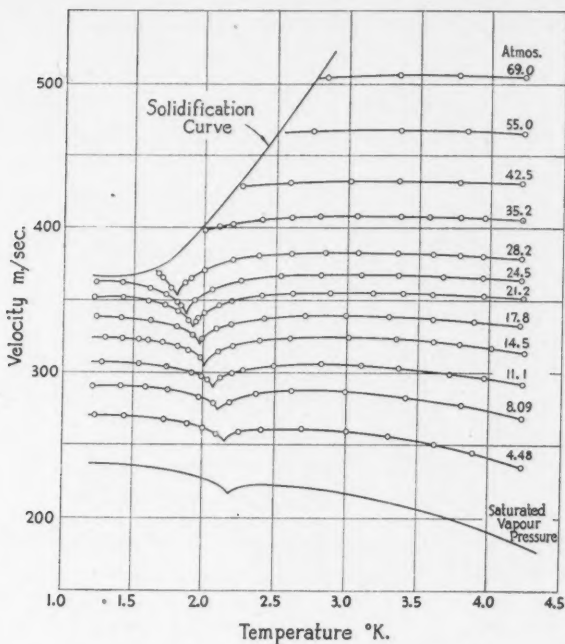


FIG. 2. The velocity at constant pressure.

TABLE I
THE VELOCITY OF FIRST SOUND IN LIQUID HELIUM AT VARIOUS TEMPERATURES AND PRESSURES
(SMOOTHED VALUES)

$T \backslash p$	Vapor pressure	2.5	5.0	10.0	15.0	20.0	25.0	30.0	40.0	50.0	60.0	70.0 atm.
1.25°K.	237	257	273	300	326	346	365					
1.50	235	256	272	299	325	345	362					
1.75	233	252	270	298	323	342	355					
1.80	232	251	269	297	321	339	352					
1.90	229	249	267	295	318	333	348	372				
2.00	227	247	265	292	312	336	358	379				
2.10	222	240	259	288	317	340	361	382				
2.20	219	240	259	293	322	344	366	385	419			
2.25	220	242	261	295	323	345	367	386	420			
2.50	222	244	265	298	326	348	369	388	422	451		
3.00	218	242	264	298	327	349	370	389	423	452	481	510
3.50	206	230	256	296	325	349	370	389	423	452	481	510
4.00	190	216	246	290	321	347	369	388	423	452	481	510
4.20	180	206	241	285	318	345	368	387	422	452	481	510

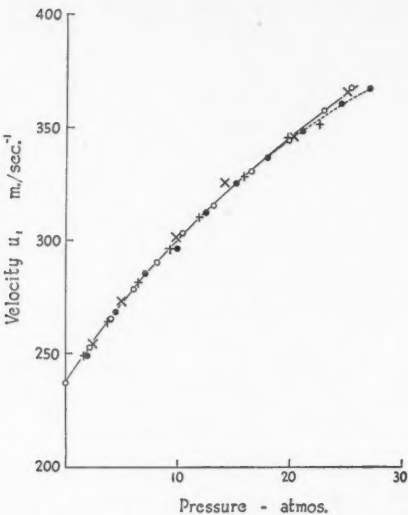


FIG. 3. The velocity as a function of pressure at the lowest temperatures.
 ○ 1.21°K.; + 1.41°K.; ● 1.60°K.
 X Derived from the equation of state (6, p. 237).

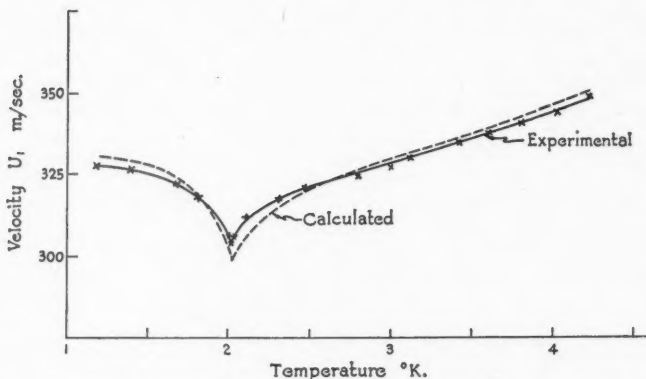


FIG. 4. The velocity at a constant density of 0.165 gm. cm.⁻³

The echo disappeared over a range of a few thousandths of a degree straddling the λ -point because of the high attenuation there, but it reappeared again with a velocity which was the same to within $\frac{1}{2}\%$. The more thorough investigation along the vapor pressure curve (1) demonstrated that the issue can be decided only by plotting a very detailed curve and extrapolating it to the λ -point, if this turns out to be possible. We did not pursue the matter this far because we suspected that the temperature inside the bomb did not correspond to the bath

temperature with sufficient accuracy and the temperature difference probably varied in a complicated and unpredictable manner near the λ -point (8). However, the observations are good enough to exclude the possibility of a large $2\frac{1}{2}\%$ discontinuity such as that found by Findlay, Pitt, Grayson-Smith, and Wilhelm (4), at a frequency of 1.34 Mc.p.s. It remains an open question whether the disagreement provides evidence for dispersion.

3.3. The Attenuation

The behavior of the attenuation was studied qualitatively. Accurate measurements were not possible because the apparatus did not incorporate facilities for varying the path length or lining up the reflector *in situ*. As the pressure was increased the echoes became larger, which is what might be expected on two accounts. Firstly, the attenuation has the form

$$[1] \quad \alpha_1 = \frac{2\pi^2 v^2}{\rho u_1^3} \left(\frac{4}{3} \eta_n + \xi_I \right),$$

in which v is the frequency, ρ the density, u_1 the velocity, and η_n and ξ_I the coefficients of first and second viscosity for the normal component. Both ρ and u_1 increase with pressure, reducing α_1 by a considerable factor. Secondly, the acoustic impedance of the liquid, ρu_1 , increases with pressure so that it becomes easier to feed power from the quartz crystal into the liquid.

At constant pressure the variation of attenuation with temperature was similar to that observed along the vapor pressure curve (1, 7). Starting from a high value near 1°K ., the attenuation fell rapidly as the temperature was raised, passed through a minimum, and rose again at the λ -point. Above the λ -point it fell sharply, passed through a second minimum, and then rose steadily.

4. SOME THEORETICAL CONSEQUENCES

4.1. The Ratio of the Specific Heats

The velocity of first sound can be used to derive the adiabatic compressibility $k_s = 1/\rho u_1^2$. The isothermal compressibility, k_T , can be derived from the equation of state (6, p. 237). The ratio of the specific heat at constant pressure to the specific heat at constant volume may then be deduced from

$$[2] \quad \gamma = C_p/C_v = k_T/k_s.$$

The results are shown in Table II. Because of the experimental errors there is

TABLE II
THE RATIO OF THE SPECIFIC HEATS, γ

$T \backslash p$	5	10	15	20	30 atm.
2.0°K.					
2.5	1.06	1.02	1.08	1.00	1.04
3.0	1.17	1.14	1.10	1.05	1.09
3.5	1.31	1.22	1.17	1.10	1.10
4.0	1.47	1.32	1.27	1.27	1.14

some uncertainty in the important quantity $\gamma - 1$ when deduced in this way. A more direct evaluation can be obtained from

$$[3] \quad \gamma(\gamma - 1) = \frac{T u_1^2}{C_v} \frac{1}{\rho^2} \left(\frac{\partial \rho}{\partial T} \right)_p^2.$$

All the necessary data are available at only one pressure, 19 atm. (6, pp. 218, 237). Fig. 5 gives the derived values of $\gamma - 1$ at this pressure. The rapid rise to

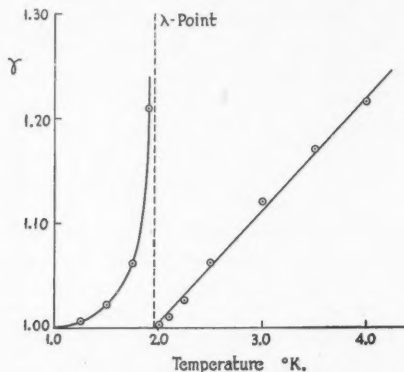


FIG. 5. The ratio of the specific heats at a pressure of 19 atm.

high values just below the λ -point is interesting. It is not so pronounced at the saturated vapor pressure (Atkins and Edwards, to be published shortly). However, it is difficult to estimate to what extent the accuracy is limited by the procedure Keesom and Keesom adopted to smooth out their ρ - T curves to obtain $(\partial \rho / \partial T)_p$.

4.2. The Coefficient of Expansion Below 0.6°K .

If liquid helium below 0.6°K . is similar to a Debye solid and its thermal excitations consist solely of phonons, then its coefficient of thermal expansion should be positive and may be calculated in the following way. The coefficient of expansion is

$$[4] \quad \alpha = \frac{1}{V} \left(\frac{\partial V}{\partial T} \right)_p = - \frac{1}{V} \left(\frac{\partial S}{\partial p} \right)_T.$$

For a Debye solid without transverse modes,

$$[5] \quad S = \frac{1}{3} C_v = \frac{16\pi^5 k^4}{45 h^3 u_1^3} \frac{V}{T^3}.$$

Therefore

$$[6] \quad - \frac{1}{V} \left(\frac{\partial S}{\partial p} \right)_T = \frac{C_v}{V} \left[\frac{1}{u_1} \frac{\partial u_1}{\partial p} - \frac{1}{3} \frac{1}{V} \left(\frac{\partial V}{\partial p} \right)_T \right]$$

$$\text{or} \quad \alpha = \frac{C_v}{V} \left(\frac{1}{u_1} \frac{\partial u_1}{\partial p} + \frac{1}{3} k_T \right).$$

Using the data of Fig. 3 to obtain $(1/u_1) \partial u_1 / \partial p$ directly, C_v from equation 5, and k_T from $k_T = \gamma / \rho u_1^2$, we deduce that, at the saturated vapor pressure,
 $\alpha = + 1.04 \times 10^{-3} T^3 \text{ deg.}^{-1}$

This is large enough to be experimentally observable.

4.3. The Specific Heat at Constant Volume Above 3°K.

From a theoretical point of view the specific heat at constant volume, C_v , is more valuable than at constant pressure or along the vapor pressure curve. Measurements of C_v for helium I along an isopycnal at a constant density of 0.168 gm. cm.⁻³ have been made by Keesom and Keesom (6, p. 218) and are shown as curve 1 in Fig. 6. Assuming that the phonons contribute to the specific

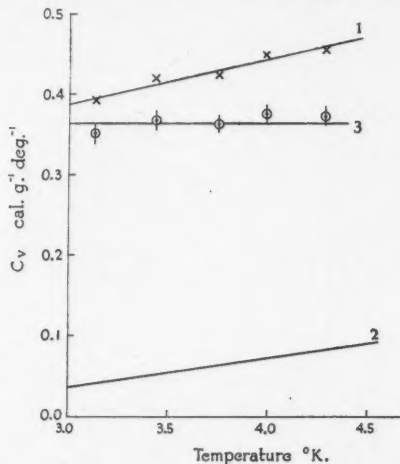


FIG. 6. The specific heat at constant volume above 3°K.
Density = 0.168 gm. cm.⁻³
Curve 1. Experimental data (6, p. 218).
Curve 2. The phonon contribution.
Curve 3. The "excess" specific heat.

heat above 3°K. in the same way that they do below 0.6°K., we have calculated this contribution to obtain curve 2. The Debye temperature was calculated separately at each temperature, using the first sound velocities of Fig. 2 and the equation of state (6, p. 237). The T^3 law no longer holds at these temperatures, so we used exact values of the Debye function. Subtracting curve 2 from curve 1, we get the values shown in curve 3 for the "excess" specific heat. It is remarkable that almost all of the variation with temperature is due to the phonon contribution and that the specific heat due to other effects seems to be independent of temperature.

5. ACKNOWLEDGMENTS

We should like to express our gratitude to Prof. J. M. Anderson and R. W. McKay for their assistance with the electronics. Helpful advice on certain

aspects of the design was obtained from Prof. A. C. H. Hallett and Mr. D. R. Lovejoy. In the later stages of the research Prof. E. W. Guptill gave valuable assistance during the experiments.

REFERENCES

1. ATKINS, K. R. and CHASE, C. E. Proc. Phys. Soc. (London), A, 64: 826. 1951.
2. VAN DIJK, H. and SHOENBERG, D. Nature, 164: 151. 1949.
3. FINDLAY, J. C., PITTS, A., GRAYSON-SMITH, H., and WILHELM, J. O. Phys. Rev. 54: 506. 1938.
4. FINDLAY, J. C., PITTS, A., GRAYSON-SMITH, H., and WILHELM, J. O. Phys. Rev. 56: 122. 1939.
5. KAPITZA, P. L. J. Phys. U.S.S.R. 4: 181. 1941.
6. KEESOM, W. H. Helium. Elsevier Publishing Co. Inc., Amsterdam. 1942.
7. PELLAM, J. R. and SQUIRE, C. F. Phys. Rev. 72: 1245. 1947.
8. WHITE, D., GONZALES, O. D., and JOHNSTON, H. L. Phys. Rev. 89: 593. 1953.

THE SURFACE TENSION OF LIQUID HELIUM¹

By K. R. ATKINS

ABSTRACT

Following a suggestion due to Frenkel, the normal modes of a liquid helium surface are taken to be surface tension waves. The free energy associated with these modes is estimated and is found to give a major contribution to the temperature dependence of the surface tension of liquid helium II. The zero-point energy of the modes is shown to be an appreciable fraction of the total surface energy at 0°K.

1. INTRODUCTION

The surface tension of liquid helium has been measured by van Urk, Keesom, and Kamerlingh Onnes (5) (1925) and by Allen and Misener (1) (1938). Starting from a value of approximately 0.35 erg cm.⁻² at 0°K., it is initially independent of temperature, in accordance with the third law of thermodynamics, but begins to decrease rapidly as the λ -point is approached. Above the λ -point, it decreases almost linearly with temperature, extrapolating to zero at the critical temperature.

The large variation above the λ -point (liquid helium I) is probably partly due to changes in density. Since the surface tension is a measure of the Gibbs free energy associated with the surface, the importance of density may be estimated by seeing how much the free energy of the bulk liquid depends on its density. At constant temperature an increase Δp in the pressure increases the free energy by

$$[1] \quad \Delta G = V\Delta p.$$

The density is 0.146 gm. cm.⁻³ at the λ -point (2.186°K.) and 0.129 gm. cm.⁻³ at 4.2°K. To increase the density to 0.146 gm. cm.⁻³ at 4.2°K. requires a pressure of the order of 8 atm., corresponding to a free energy change of the order of 8×10^6 ergs per unit volume of bulk liquid. The volume of 1 cm.² of the surface layer is approximately δ cm.³, where δ is the average distance between atoms in the liquid, and is therefore approximately 3.6×10^{-8} cm.³. The free energy change in an equal volume of bulk liquid is 0.29 erg. The decrease in surface tension over the same temperature range is 0.18 erg cm.⁻². Of course the behavior of the surface cannot be inferred directly from the properties of the bulk liquid, but the argument is sufficient to convince us that changes in density might play an important role in determining the variation of surface tension with temperature.

In liquid helium II the situation appears to be different. The total change in density is only 0.7% and is in the opposite direction, the coefficient of expansion being negative. Nevertheless, the surface tension continues to increase rapidly with decreasing temperature. We shall therefore examine the possibility that this effect arises from the thermal energy associated with the vibrational modes of the surface. By confining the discussion to liquid helium II, it will be possible to assume that the density is effectively constant.

¹ Manuscript received August 4, 1953.

Contribution from the Department of Physics, University of Toronto, Toronto, Ont.

Frenkel (2, 3) (1940, 1946) has pointed out that the long wave length modes of a liquid surface are similar to surface tension waves. He assumes that the modes of shorter wave length are similar to Rayleigh waves. However, it is by no means certain that Rayleigh waves can exist in liquid helium and so we shall restrict the treatment to surface tension waves, while bearing in mind that they may be an inadequate representation of the high frequency modes.

2. THE SPECTRUM OF THE NORMAL MODES

When discussing the surface tension of liquids at room temperature, Frenkel assumed that all the modes had a frequency much less than kT/h . This assumption is no longer valid in our case and so we proceed differently. Considering a 1 cm. square of surface and applying a procedure similar to that adopted in the Debye theory of solids, it is easy to show that the number of modes with wave lengths between λ and $\lambda + d\lambda$ is

$$[2] \quad g(\lambda) d\lambda = (2\pi/\lambda^3) d\lambda.$$

The velocity of a surface tension wave is

$$[3] \quad c = (2\pi\sigma/\rho\lambda)^{1/2}$$

in which ρ is the density and σ the effective value of the surface tension. The relationship between frequency ν and wave length is

$$[4] \quad \nu^2 = 2\pi\sigma/\rho\lambda^3.$$

The number of modes with frequency between ν and $\nu + d\nu$ is therefore

$$[5] \quad g(\nu) d\nu = \frac{4\pi}{3} \left(\frac{\rho}{2\pi\sigma} \right)^{2/3} \nu^{1/3} d\nu.$$

This equation is rigorous for very long wave lengths but almost certainly breaks down when the wave length is comparable with the average distance

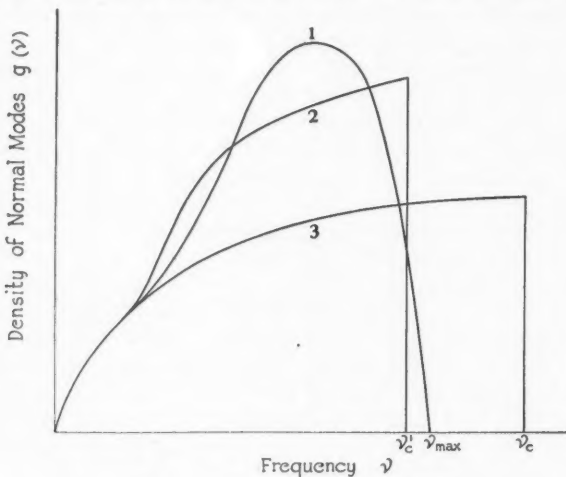


FIG. 1. Approximations to the spectrum of the surface modes.

between atoms, δ . The actual spectrum of the modes may have a form similar to that shown by curve 1 in Fig. 1, extending up to a maximum frequency ν_{\max} corresponding to a minimum wave length equal to δ . Such an exact spectrum is very difficult to calculate: the problem has not yet been completely solved in the case of a solid. We shall therefore first adopt the type of procedure used in the Debye theory, retaining equation 5 at all frequencies but cutting off the spectrum at a frequency ν_c as shown by curve 3. The cutoff frequency will be chosen so that the total number of modes is equal to the total number of atoms in a monomolecular layer at the surface. This gives

$$[6] \quad \nu_c = \frac{1}{\pi^{1/4}} \left(\frac{2\sigma}{\rho} \right)^{1/2} \frac{1}{\delta^{3/2}}.$$

The minimum wave length is then

$$[7] \quad \lambda_c = \sqrt{\pi} \delta = 6.32 \times 10^{-8} \text{ cm.}$$

3. THE ZERO-POINT ENERGY AND THE SURFACE TENSION AT 0°K.

The zero-point energy of the surface modes is

$$[8] \quad Z_0 = \int_0^{\nu_c} \frac{1}{2} h\nu g(\nu) d\nu$$

$$[9] \quad = \frac{2\pi}{7} \left(\frac{\rho}{2\pi\sigma} \right)^{2/3} h\nu_c^{7/3}$$

$$[10] \quad = \frac{2\pi}{7} \left(\frac{2\pi\sigma}{\rho} \right)^{1/2} \frac{h}{\pi^{7/4} \delta_c^{7/2}}.$$

If we put $\sigma = 0.35 \text{ erg cm.}^{-2}$, the experimental value extrapolated to 0°K., Z_0 becomes $0.36 \text{ erg cm.}^{-2}$ which is slightly greater than the total surface energy from all causes. The suggestion that this zero-point energy makes an important contribution to the surface energy raises the fundamental issue of whether this contribution should be included in the value of σ determining the velocity of the surface waves (equation 3). Obviously, for long wave lengths—in the extreme case, those that would be used in a macroscopic experiment—the relevant surface tension is the experimentally determined one, σ_0 . On the other hand, one might expect that the very short waves with a frequency near ν_c would not be influenced greatly by the presence of the other modes and a better description of their behavior would be obtained by using an effective surface tension, σ_e , which does not include the contribution from the zero-point energy. The best approximation to the zero-point energy might therefore be achieved by inserting σ_e in equation 10. The total surface energy would then be

$$[11] \quad \sigma_0 = \sigma_e + \frac{2\pi}{7} \left(\frac{2\pi\sigma_e}{\rho} \right)^{1/2} \frac{h}{\pi^{7/4} \delta_e^{7/2}}.$$

Solving this, σ_e is found to be $0.13 \text{ erg cm.}^{-2}$, leaving $0.22 \text{ erg cm.}^{-2}$ for the contribution from the zero-point energy. Although the approximations which have been made are too crude for these figures to have any great significance, it seems very likely that the zero-point energy of the surface modes represents a considerable part of σ_0 .

The value of the surface tension at 0°K. is now seen to depend on a delicate balance of three factors. Comparing an atom at the surface with one in the interior of the liquid, there is a positive addition to its energy arising from the absence of the negative potential energy of its missing neighbors. But the surface atom is less hemmed in by its neighbors than if it were in the interior and this reduces the zero-point energy arising from the Heisenberg Uncertainty Principle (London (4), 1936), giving a negative contribution to the surface energy. Finally there is the positive zero-point energy of the surface modes which we have just discussed.

The considerations of this section demand a modification of the frequency spectrum. At the long wave length end the spectrum still starts out in accordance with equation 5 and $\sigma = \sigma_0$, but at higher frequencies the curve must rise as the effective value of σ tends towards σ_e (curve 2 in Fig. 1). In equation 6 for the cutoff frequency, the best approximation is to put $\sigma \sim \sigma_e$, which gives

$$[12] \quad \nu_c \sim 1.5 \times 10^{11} \text{ sec.}^{-1}$$

The characteristic temperature is then

$$[13] \quad \theta = h\nu_c/k \sim 7.2^\circ\text{K}.$$

In the absence of a complete knowledge of the spectrum, these figures are correct only in order of magnitude.

4. THE VARIATION OF SURFACE TENSION WITH TEMPERATURE

The energy excited in the surface waves at a temperature T is

$$[14] \quad U = \int_0^{\nu_c} \frac{h\nu}{e^{h\nu/kT} - 1} g(\nu) d\nu.$$

At low temperatures, $T \ll \theta$, only long wave length modes are excited and $g(\nu)$ is therefore obtained by putting $\sigma = \sigma_0$ in equation 5. Then

$$[15] \quad U = \int_0^{\nu_c} \frac{h\nu}{e^{h\nu/kT} - 1} \frac{4\pi}{3} \left(\frac{\rho}{2\pi\sigma_0} \right)^{2/3} \nu^{1/3} d\nu$$

$$[16] \quad = \frac{4\pi}{3} \left(\frac{\rho}{2\pi\sigma_0} \right)^{2/3} h \left(\frac{kT}{h} \right)^{7/3} \int_0^{\theta/T} \frac{x^{4/3}}{e^x - 1} dx.$$

As $\theta/T \rightarrow \infty$ the integral approaches the value 1.68 and

$$[17] \quad U = 9.2 \times 10^{-3} T^{7/3}.$$

The surface tension is determined by the free energy

$$[18] \quad \sigma_0 - \sigma = -(U - TS)$$

$$[19] \quad = +\frac{3}{4}U = 6.9 \times 10^{-3} T^{7/3}$$

from simple thermodynamics (σ_0 and σ are the surface tensions at 0°K. and at the temperature T). Equation 19 is plotted as the full curve in Fig. 2 and is compared with the experimental results of Allen and Misener (1) (1938), σ_0 being assigned the value 0.352 erg cm.⁻² at 0°K. It will be seen that even this simple treatment is able to explain 70% of the variation with temperature up to the λ-point.

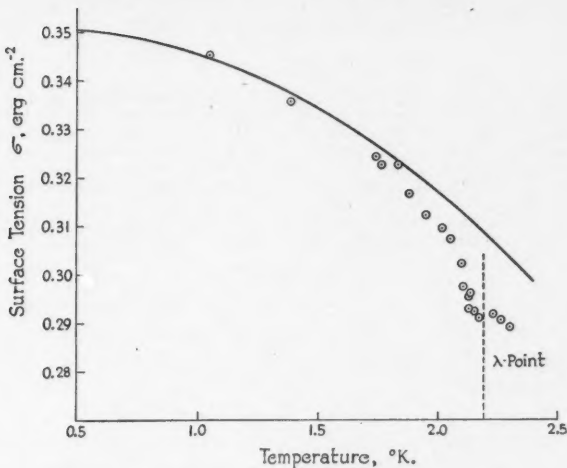


FIG. 2. Variation of surface tension with temperature.
 ○ Experimental results of Allen and Misener.
 — Theoretical.

The characteristic temperature ($\theta \sim 7.2^\circ\text{K}.$) is not really very large compared with $2^\circ\text{K}.$ and so the above treatment is not rigorous. In fact, near the λ -point, it is probable that surface modes are being excited in the region where curves 1 and 2 rise above curve 3 (Fig. 1). This would enhance the contribution from the surface modes and make the surface tension decrease more rapidly, helping to explain the discrepancy between theory and experiment in Fig. 2. There is also a slight suggestion that the surface tension has an anomaly at the λ -point, presumably connected with those effects which produce anomalies in the bulk liquid. There may be other factors, such as the very small change in density, which make their contribution to the exact shape of the curve, but there is good reason to believe that the dominating factor is the behavior of the surface waves. It will be appreciated, however, that their effect cannot be evaluated in detail without solving the very difficult problem of the exact form of the frequency spectrum.

I should like to acknowledge my gratitude to Prof. C. C. Gotlieb and Mr. F. A. H. Parkes of the University of Toronto Computation Centre for their assistance with some of the numerical integrations.

REFERENCES

1. ALLEN, J. F. and MISENER, A. D. Proc. Camb. Phil. Soc. 34: 299. 1938.
2. FRENKEL, J. J. Phys. U.S.S.R. 3: 355. 1940.
3. FRENKEL, J. Kinetic theory of liquids. Oxford University Press, London. 1946. p. 308.
4. LONDON, F. Proc. Roy. Soc. (London), A, 153: 576. 1936.
5. VAN DER WAALS, J., KEEFOM, W. H., and KAMERLINGH ONNES, H. Proc. Roy. Acad. Sci. Amsterdam, 28: 958. 1925.

RAYLEIGH SCATTERING OF CONDENSED MATTER¹

BY O. THEIMER² AND E. LELL³

ABSTRACT

The scattering power $S(\lambda) = I_s/I_d$ (I_s, I_d are the intensities of the scattered and the incident light) for visible light is investigated experimentally for ordinary glass, optical glass, water, and air. It is found that $S(\lambda)$ for glass shows pronounced deviations from Rayleigh's $1/\lambda^4$ law, e.g., a relative maximum of $S(\lambda)$ for $\lambda = 5200 \text{ \AA}$ in the case of ordinary glass. A theory for the Rayleigh scattering of condensed matter is developed and compared with the ideas brought forward by Fürth and Humphreys-Owen in 1951. It is shown that the maxima of $S(\lambda)$ observed by these authors and in the present work can be equally well derived from localized lattice imperfections or from the mosaic blocks considered by Fürth.

1. INTRODUCTION

Since the fundamental work of von Laue (5) and Born (1) on the X-ray scattering and dynamics of ideal lattices, the physics of solid bodies centered for a long time around the investigation of the properties of ideal crystals. Here the scattering of X-rays proved to be one of the most powerful tools. The Rayleigh scattering of visible and ultraviolet light, however, did not contribute much to our knowledge of ideal crystals, this effect being indeed negligibly weak and only loosely related to the most interesting properties of ideal crystals. Hence, the investigation of the Rayleigh scattering has been somewhat neglected throughout the last decades.

This situation has been considerably changed by the growing interest in the "real" state of crystals and other species of condensed matter, e.g., glasses or liquids, deviating from the ideal lattice. Here the Rayleigh scattering can yield useful information. The method of investigation is due to Fürth (2) who showed that in crystals the scattered intensity expressed as a function of the wave length exhibits relative maxima and minima which can be related to a characteristic length, e.g., the mean diameter of the "mosaic blocks" building up the macroscopic crystal.

Fürth, in fact, did not consider any other interpretation of the characteristic length derived from the maxima and minima mentioned above. Although his interpretation is rather convincing in the case of crystals, it is not the only possibility; further, it is not the most satisfactory explanation in the case of glasses and liquids. It is, therefore, the purpose of this work to extend Fürth's investigations to glasses and liquids and to develop other possibilities besides the mosaic structure of interpreting the observed effects in a way more suitable for amorphous matter.

2. EXPERIMENTAL METHOD

(a) Principle of Measurement

The dependence of the scattering power $S(\lambda) = I_s/I_d$ (I_s, I_d are the intensities of the scattered and the incident or direct light) upon the wave length has been determined as follows (see Fig. 1).

¹ Manuscript received July 2, 1953.

Contribution from the Physics Department, Technische Hochschule Graz, Austria (experimental part) and from the Physics Department, University of British Columbia, Vancouver, B.C. (theory).

² Department of Physics, University of British Columbia.

³ Department of Physics, Technische Hochschule Graz, Austria.

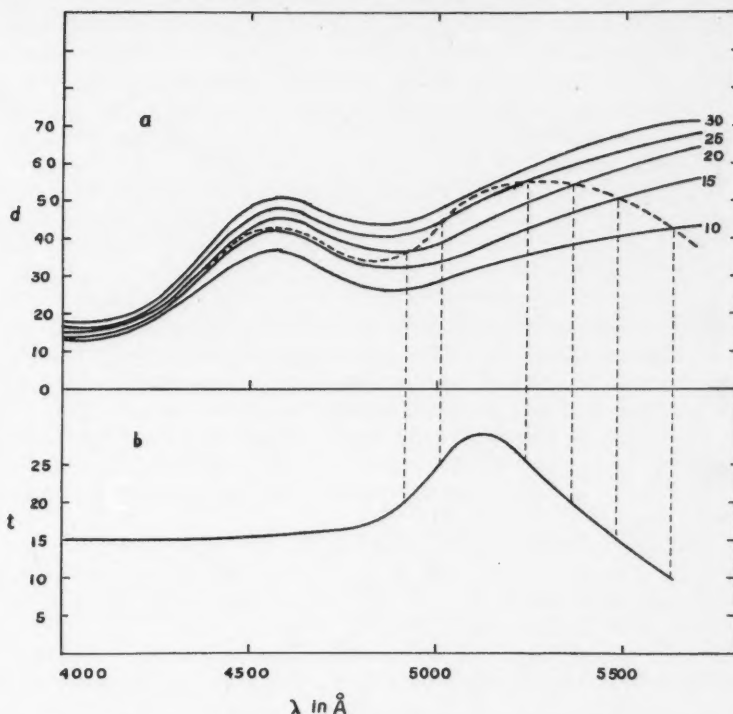


FIG. 1. (a) Typical density distribution and (b) scattering power of solid bodies.

Several spectra of the same continuous light source are photographed with different exposure times t_d on one plate in such a way that the light enters the spectrograph directly, without passing through the scattering body. In addition to these direct spectra, a spectrum of the scattered light of the same source is photographed with such an exposure time t_s that the density of the scattered spectrum lies for all wave lengths between the densities of the strongest and weakest direct spectrum. Typical density distributions $d(\lambda)$ are shown in Fig. 1a (dotted line refers to scattered light).

From Fig. 1a, one can, according to the position of the dotted curve between the full lines, immediately read off the scattering power in the following way.

We consider a point of intersection between the dotted and a full line, corresponding to the exposure time t_d (t_d is indicated on the right-hand side of the lines). Here the densities d_s and d_d produced by the scattered and the direct light are equal and one has, according to Schwarzschild (8),

$$[1] \quad d_s = I_s t_s^p = I_d t_d^p = d_d, \quad p = 1 + \epsilon = \text{Schwarzschild's exponent}, \quad |\epsilon| \ll 1,$$

or

$$[2] \quad \frac{I_s}{I_d} = S(\lambda) = \left(\frac{t_d}{t_s} \right)^p = \frac{t_d}{t_s} \left(\frac{t_d}{t_s} \right)^\epsilon = \frac{t_d}{t_s} f.$$

Now, if ϵ is a small constant independent of λ , f is a factor of the order of magnitude 1 which varies only slowly and *monotonically* with t_d so that its omission cannot shift existing maxima or falsely produce nonexisting maxima of $S(\lambda)$. Since the determination of the existence and position (i.e. wave length) of such maxima is the main subject of the present work, f may easily be neglected,* so that

$$[3] \quad S(\lambda) = t_d/t_s.$$

$S(\lambda)$ is plotted against λ in Fig. 1b, assuming for simplicity that $t_s \approx 1$. It shows a maximum at 5100 Å.

(b) Apparatus and Experimental Details

The experimental arrangement used to obtain (a) scattered and (b) direct spectra can be seen from Fig. 2. The light source S , a Tungsten 36 w. bulb with high brightness, is fixed on an iron rod which can be turned about the vertical axis A , thus permitting one to obtain scattered and direct spectra from the same source. The axis A is the stand of a small table which carries the scattering body B and a black pasteboard housing H provided with stops st_1 and st_2 and the "light trap" T which absorbs completely the direct light passing through the scatterer.

In the case of scattered spectra (Fig. 2a), the light from the source which is concentrated by a converging lens L_1 onto the scatterer B passes through st_2 and B and is absorbed in T . Only the small fraction which is rectangularly scattered passes through st_1 and enters the spectrograph Sp .

For the direct spectra (Fig. 2b) the scatterer B and the housing H are removed from the table, the light source is turned into the optical axis of the spectrograph

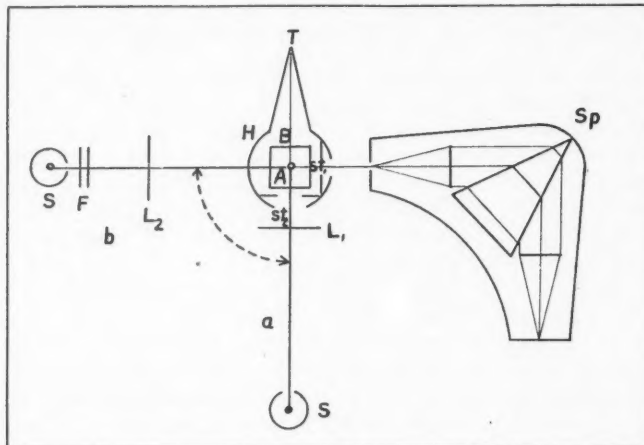


FIG. 2. Experimental arrangement for the measurement of the scattering power.

*The neglect of f is, however, not admissible, if the absolute value of the scattering power or its exact wave-length dependence is to be measured. In this case, the different direct spectra should be photographed with varying width of the collimator slit (instead of varying exposure time) or with a rotating sector, which is generally assumed to reduce $|\epsilon|$ considerably.

and the converging lens L_1 is replaced by the diverging lens L_2 in order to diminish the light entering the spectrograph. For the same reason two panes of frosted glass F are introduced between S and L_2 .^{*} Of course, the density distribution of the spectrum must not be changed by the frosted glass; this has been confirmed experimentally.

We used a Zeiss spectrograph with one glass prism and having a camera lens $f10$. Because of the high f number long exposures of the order of 10 to 100 hr. were necessary, especially in the case of gases.^{**} To reduce the exposure time to a tolerable length we had to use photographic plates of highest sensitivity, the rough grain being harmless, since we were only concerned with the density of continuous spectra. We used "Guilleminot-Superfulgur" for the region between 4000 and 5000 Å and "Ilford H.P.3" for wave lengths from 5000 Å to 6000 Å. The latter plates required about four times the exposure of the former. On each plate several weak mercury-vapor spectra were photographed from which the wave length could be determined with the help of the known dispersion-curve of the spectrograph. The density of the spectra was measured with a recording Moll microphotometer.

3. EXPERIMENTAL RESULTS

The experimental results are contained in Fig. 3 which represents the scattering power $S(\lambda)$ as a function of λ . The logarithmic scale has been chosen so that the wide range of scattering power of four different materials can be plotted on one figure; further, with a logarithmic scale a simple exponential law, e.g., Rayleigh's $1/\lambda^4$ -law (7), is represented by a straight line whose slope immediately gives the exponent. This allows for a quick and simple classification of the experimental curves.

Curve (1) shows the scattering properties of a rectangular block ($16 \times 16 \times 20$ mm.) of ordinary glass† which contained some macroscopic imperfections, i.e., some small bubbles of about 0.1 mm. diameter and small regions containing weak streaks. The glass was, however, perfectly transparent and colorless, even with thickness of 100 mm. The scattering power of this glass is very high and shows a distinct maximum for radiation of $\lambda \sim 5200$ Å. This maximum seems to be superimposed on a simpler scattering function (dotted line) valid in all wave-length regions, which describes an increase of the scattering power with decreasing wave length, roughly in accordance with Rayleigh's law. (Gradient of the dotted line is about -3.5.) The spectrum has been photographed with two different positions of the scattering body (rotation of 90° about optical axis), and in both cases on "Guilleminot" and "Ilford" plates. Thus four spectra were obtained in good agreement with each other, as can be seen from the circles and crosses on curve (1) which represent the experimental results for the two different positions of the scatterer.

Curve (2) represents the scattering power of a rectangular block of optical glass† containing no macroscopic imperfections. The total scattering power of

^{*}It is advantageous to weaken the direct light in order to obtain spectra of a measurable density with exposure times long enough (some minutes) to be controlled easily.

^{**}It would be easy to reduce the exposure times considerably using a spectrograph with larger light gathering power; such an instrument, however, was not at our disposal for this work.

[†]Chemical composition and other characteristics of the glass are unknown.

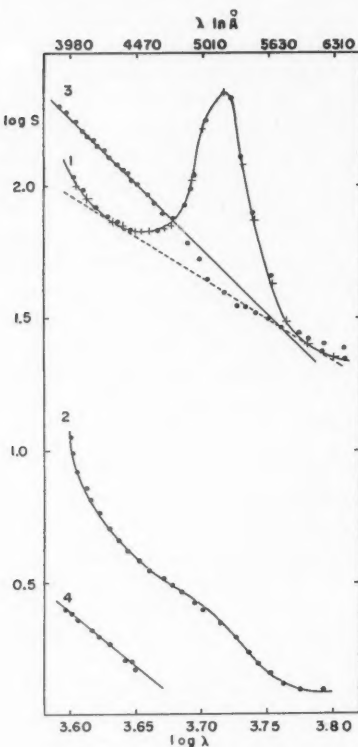


FIG. 3. The scattering power $S(\lambda)$ for ordinary and optical glass, water, and air.

the optical glass is about 1/20 that of ordinary glass. There is no distinct maximum to be seen on curve (2) but the steep rise of this curve, which has a gradient of about -10 on the left-hand side, may be taken as an indication that a maximum exists somewhere in the region of shorter wave lengths.

The scattering power of carefully purified water (curve 3) is of the same order of magnitude as that of ordinary glass but does not exhibit or indicate any relative maximum or minimum. The gradient of the curve, which is nearly a straight line, lies between -4 and -5 , in good agreement with Rayleigh's law.

The scattering power of air (curve 4), for which Rayleigh's law is known to be valid over the whole range of visible and near ultraviolet light, has been investigated to check the accuracy of our measurements. Unfortunately, the scattering power of air is so low that we obtained measurable spectra only in the small region of high sensitivity between 4000 \AA and 4500 \AA . For this region Rayleigh's law was verified within the limit of experimental error.

4. DISCUSSION OF THE EXPERIMENTAL RESULTS

(a) *The Structure of Condensed Matter*

The fundamental molecular model underlying most ideas on the structure of condensed matter is the perturbed lattice. Here the most general type of perturbation can be described as an arrangement of localized lattice imperfections, e.g., unoccupied (holes), displaced, or interchanged lattice points. These imperfections can occur singly or in groups, thus eventually forming large cavities or regions of great disorder. The concept of localized lattice imperfections is especially suitable for the description of real crystals without macroscopic internal strains and for the discussion of liquids which can be considered to be "real crystals" with a very high concentration of lattice imperfections.

For macroscopic perturbations, e.g., plastic deformations, the concept of lattice dislocations has been recently introduced. Here displacements of whole lattice rows and lattice planes are taken into account. Such dislocations can be used to describe a very interesting type of lattice imperfection, the mosaic blocks. These are small crystal blocks of colloidal dimensions (diameter 100-10,000 Å) which build up a macroscopic single crystal in such a way that their crystallographic axes are weakly inclined against each other. Thus all regular geometrical relations between the lattice points of different blocks are destroyed. This model has been introduced in order to explain the observed intensities and angular width of X-ray reflections by single crystals from the assumption that *coherent* X-ray scattering is restricted to only small volume elements of the crystal. To obtain this restriction, the mosaic model is, however, only one among several possibilities and could, for instance, easily be replaced by a model which destroys the long distance order by more continuous changes of the lattice geometry. A decision whether the discontinuous block model is more realistic than a continuous one is very difficult and can not be based on one kind of experiments alone.

In spite of this difficulty the idea of a block structure of solid bodies has been widely accepted and further attempts have been made to confirm it experimentally. One of these experimental tests has been accomplished by Fürth, as indicated in the introduction. Although a new and valuable method for the investigation of condensed matter has been introduced by Fürth's work, his interpretation of the observed facts exclusively in terms of a mosaic structure seems too narrow. It will be shown in the next section that the observed wavelength dependence of the scattering power can be equally well derived from the model of localized lattice imperfections and from the mosaic model. Hence, the Rayleigh scattering of visible and ultraviolet light can not immediately remove the uncertainties inherent in the concept of discontinuous mosaic blocks.

(b) *The Theory of Light Scattering*

It is useful for our purpose to distinguish sharply between the configurational scattering of a rigid assembly of scattering units, e.g. atoms, and the contribution to the scattering by the motions of the atoms, e.g. thermal scattering. Since the theory of thermal scattering is well established and does not account for the complicated wave-length dependence of $S(\lambda)$ which is the object of this investigation, we shall restrict our discussion to the configurational scattering.

We consider a system of scattering units with diameter small compared to the wave length of visible light. The atoms building up the scattering material are, clearly, suitable units of this kind. However, lattice imperfections and special atomic configurations in glass must additionally be taken into account, since it is only the irregular arrangement of such scattering units which can produce relative maxima and minima of $S(\lambda)$. This can be shown in the following way.

The scattering power S of any arbitrary assembly of atoms (denoted by the index k) can be represented by the well-known formula

$$[4] \quad S = \frac{\sigma}{\lambda^4} \sum_k \sum_{k'} \alpha_k \alpha_{k'} e^{-iQ\mathbf{S} \cdot (\mathbf{r}_k - \mathbf{r}_{k'})},$$

with

\mathbf{r}_k = position vector of atom (k),

$Q = 2\pi/\lambda$,

$\mathbf{S} = \mathbf{s} - \mathbf{s}_0 = 2 \sin \Theta$,

2Θ = angle of deflection,

\mathbf{s}, \mathbf{s}_0 = unit vectors in direction of scattered and incident light,

α_k = polarizability of atom (k); more or less dependent on λ and Θ ,

$\sigma = \left(\frac{e^2}{mc^2} \frac{1}{r} \right)^2 \frac{1}{2} (1 + \cos^2 2\Theta) =$ Thomson factor for natural incident light.

According to equation [4] S is generally a complicated function of λ . In some cases, however, e.g. thermal light scattering of gases, the factor $1/\lambda^4$ is dominant (Rayleigh's $1/\lambda^4$ -law). Another limiting case is the scattering of a free electron, where α^2 is proportional to λ^4 and S , consequently, independent of the wave length. But with most scattering systems the exponential, which takes into account the phase relations between the waves scattered by the single atoms, is decisive for the total result.

The double summation in equation [4] can be rigorously carried out only in the case of ideal crystals. For less regular arrangements of the scattering units, statistical methods must be used. To this end we introduce a weighted radial distribution function $\rho_l(r)$ which takes into account the existence of scattering units of different types, e.g. regular atoms, foreign atoms, holes, etc., which are distinguished by the index l . $\rho_l(r)$ is defined by the equation

$$[5] \quad \sum_l \alpha_l N_l(r) dr = 4\pi \bar{\alpha} N(0) r^2 \rho_l(r) dr$$

with

$N_l(r)$ = average number of scattering units of type l with distance between r and $r + dr$ from the center of any arbitrary unit,

$N(0) = \sum_l N_l(0)$ = number of scattering units per cc.

$\rho_l(r)$ = probability of finding the polarizability $\bar{\alpha}N(0) dv$ in a volume element dv with distance r from a unit of type l ,

$\bar{\alpha} = \sum_l (\alpha_l N_l(0)/N(0))$ = mean polarizability of the scattering units.

We assume further that the scattering body is sufficiently large and macroscopically homogeneous, so that $\rho_l(r)$ is the same for all units of type l . This implies that all $\rho_l(r)$ must approach the value 1 for large r but does not exclude strong fluctuations of $\rho_l(r)$ in the vicinity of the central atom l .

Introducing the density function $\rho_l(r)$ and taking into account the above condition of macroscopic homogeneity, equation [4] may be written (β is the angle between \mathbf{S} and \mathbf{r}_k and $2R$ is the mean diameter of the scattering body)

$$[6] \quad S = \frac{2\pi\sigma N(0)\bar{\alpha}}{\lambda^4} \sum_l N_l \alpha_l \int_0^R \int_0^R \rho_l(r) e^{-iq\mathbf{S}\cdot\mathbf{r}} r^2 \sin \beta d\beta dr.$$

The integration with respect to β can be easily carried out and gives, with the substitution

$$[7] \quad Q\mathbf{S}\cdot\mathbf{r} = QSr \cos \beta = \mu r \cos \beta \quad \text{and} \quad \sin \beta d\beta = d \cos \beta,$$

$$[8] \quad S = \frac{4\pi\sigma N(0)\bar{\alpha}}{\lambda^4} \sum_l N_l \alpha_l \int_0^R \rho_l(r) r^2 \frac{\sin \mu r}{\mu r} dr.$$

Since $\rho_l(r)$ is zero for $r > R$ and since the α_l are practically independent of μ for transparent bodies and fixed angle of deflection Θ , equation [8] can be written in the form

$$[9] \quad f(\mu) = \int_0^\infty g(r) \sin \mu r dr$$

which is equivalent to the reciprocal relation

$$[10] \quad g(r) = \frac{2}{\pi} \int_0^\infty f(\mu) \sin \mu r d\mu.$$

With the help of this transformation the unknown density distribution $\rho(r)$ can be represented as a function of the measurable scattering power $S(\mu)$ by the formula

$$[11] \quad \sum_l N_l \alpha_l \rho_l(r) = \frac{\lambda^4}{2\pi^2 \sigma N(0) \bar{\alpha} r} \int_0^\infty S(\mu) \mu \sin \mu r d\mu.$$

Here $S(\mu)$ is identical with $S(\lambda)$ if the angle of deflection is fixed by the method of observation.

Equation [11] gives the maximum possible information on the structure of the scattering body which can be derived from the spectral intensity distribution of the scattered light.

Usually $S(\lambda)$ will be known only within the rather small spectral region of visible, near ultraviolet, or near infrared wave lengths. Such a limited knowledge is not sufficient to determine $\rho(r)$ completely with the help of equation [11]. Methods of a more qualitative character must then be used which are based on the following properties of equations [8] and [11].

(i) If the density distributions $\rho_l(r)$ are constant for all types l of the different scattering units, then $S(\lambda)$ is zero for all angles of deflection Θ with the one exception $\Theta = 0$. This accounts for the rectilinear propagation and the complete absence of configurational scattering of visible light in ideal crystals. In media with atomic structure it can, of course, never be the point density $\rho_l(r)$ itself

which is constant; what is required for a vanishing scattering power is a constant value of the mean density $\overline{\rho_l(r)} = \int_r^{r+\lambda} \rho_l(r)/\lambda dr$, the average being taken over a distance commensurable with λ . This does not exclude a fine structure of $\rho(r)$ with smaller linear dimensions.* Scattering bodies for which the radial density distribution is constant in this sense will be called homogeneous scatterers.

(ii) If the $\overline{\rho_l(r)}$ are variable even for only one or several types l of the scattering units we shall speak of inhomogeneous scatterers. They have a scattering power which is, according to equation [8], a complicated function of the variable density distributions $\rho_l(r)$. If, in particular, the $\rho_l(r)$ have maxima for certain values $r_{l,\max}$ then to each of them corresponds a series of maxima of $S(\lambda)$ with wave lengths

$$[12] \quad \lambda_{l,\max} = \frac{r_{l,\max} \sin \Theta}{0.615}, \frac{r_{l,\max} \sin \Theta}{1.119}, \dots, \frac{4r_{l,\max} \sin \Theta}{\lambda m + \frac{1}{2}}, m = \text{integer}.$$

The properties (i) and (ii) of the scattering power allow for a simple classification of light scattering in condensed matter which will be given in the next section.

(c) Light Scattering in Condensed Matter

(i) Homogeneous Scatterers

With respect to the scattering of visible light homogeneous scatterers are an idealization which is best approximated by ideal crystals and perhaps by pure liquids. Here, neglecting thermal scattering and Raman effect, the only mechanism to deflect the incident light rays is reflection and refraction by the boundaries of the scatterer. The decomposition of the incident radiation into reflected and refracted rays is governed by Fresnel's formulae which show that the intensities of the two rays depend only implicitly on the wave length by way of the index of refraction. This dependence is negligibly small in most cases of transparent bodies. Hence, scattering of transparent bodies as a result of reflections by inner surfaces, e.g. bubbles, macroscopic impurities, or streaks, is practically independent of λ . It seems that this is the type of light deflection which has been called "impurity scattering" by Fürth. Since impurities of molecular or even colloidal dimensions exhibit an entirely different behavior, we prefer the term "surface scattering" for this effect.

(ii) Inhomogeneous Scatterers

Fluctuations of a density distribution $\rho_l(r)$ which produce configurational scattering occur only if there is a most probable distance of the order of magnitude λ between neighboring units. Hence, the atoms building up the bulk of

*For the complete vanishing of the scattering power not only a constant density $\overline{\rho(r)}$ is required but also perfect correlation of the positions of the scattering units, e.g. an ideal crystal lattice. If there is no correlation at all (ideal gases) then the single units produce a scattering power corresponding to the terms of the double sum in formula [4] for which $k = k'$, while only the remaining terms cancel by interference. In most cases of condensed matter the arrangement of the scattering units is intermediate between complete order and randomness. Here the terms with $k = k'$ which are always positive and the terms with $k \neq k'$ whose sum is always \leq zero, provided $\rho(r)$ is constant, partly cancel each other.

crystals or pure liquids can not cause optical inhomogeneity and configurational scattering. The only units which may produce this effect are, therefore, foreign atoms, holes, and other localized lattice imperfections; further mosaic blocks in crystals; and atomic configurations in glasses with suitable linear dimensions. The configurational scattering originating from these inhomogeneities of molecular or at best colloidal dimensions will be called "structure-sensitive" scattering, in analogy to Smekal's (9) distinction between "structure-sensitive" and "structure-insensitive" properties of solids. Here structure refers, of course, not to the ideal lattice structure but to the "real" structure, including the configuration of lattice imperfections of all kinds, mosaic structure, and glasslike structures.

From the wave lengths $\lambda_{i,\max}$ of the maxima of $S(\lambda)$ it can be further concluded that the scattering inhomogeneities are in some way related to characteristic lengths which may be interpreted as the $r_{i,\max}$ of equation [12]. It is, however, hardly possible to determine the physical nature of the characteristic lengths and the kind and exact arrangement of the scattering units from the investigation of the spectral intensity distribution alone.

At first sight, one could expect that the radial density distribution $\rho(r)$, which in principle can be determined experimentally from equation [11], differs considerably for mosaic blocks and localized scattering units; the corresponding differences of $S(\lambda)$ could then be used for a classification of scattering materials. However, the analysis of two typical cases shows that the general behavior of $S(\lambda)$ is rather insensitive against structural differences of the scattering material. Thus, the investigation of the "real" structure of condensed matter must be based on minute details of the spectral intensity distribution of the scattered light which, probably, exceeds the experimental possibilities.

One typical case is the arrangement of localized lattice imperfections in the kind of a strongly distorted lattice so that a most probable distance \bar{a} for first neighbors exists. This case is representative for the configurational scattering by various different scattering units of atomic or molecular dimensions. In order to find $S(\lambda)$ we define three fundamental lattice vectors \mathbf{a}_i in such a way that the mean square displacement $\overline{u_s^2}$ in the direction \mathbf{S} of the scattering points from their positions in the fictitious lattice is a minimum. Then small changes of the \mathbf{a}_i will produce a large change in $\overline{u_s^2}$. The total scattering of the actual assembly has been found (4) to be similar to the scattering of the related ideal lattice, i.e. the scattering spectrum is a line spectrum which fulfills the Bragg condition

$$[13] \quad 2a \sin \Theta = n\lambda, \quad a = \text{spacing of the lattice planes.}$$

The lines are, however, considerably broadened by the factor

$$[14] \quad \beta = (2 \tan \Theta)/v_0, \quad v_0 = \text{fraction of the total scattering volume which is not distorted,}$$

and weakened by the factor e^{-2M} , with

$$[15] \quad M = 8\pi^2 \overline{u_s^2} (\sin^2 \Theta)/\lambda^2.$$

The intensity lost by the lines is partly dissipated into a continuous background.

It remains to mention that the factor $1/\lambda^4$ of the general equation [4] is, of course, not affected by the mechanism of interference which brings about the described result. Because of this factor the total scattering power can be represented as a monotonically decreasing function of the wave length on which the interference maxima are superimposed. Thus, all the characteristic features of the experiment (see Fig. 3, curve 1) can be obtained from the model of localized scattering units.

The second typical case is the mosaic crystal which is representative for scattering by colloidal units. This case has been investigated by Fürth. He assumed that the scattering power of a mosaic crystal should be analogous to the scattering of a system of nonconducting spherical particles with radius r , irregularly distributed in a homogeneous medium. This system has been studied by Mie (6) who gives the following formula for the scattering power:

$$[16] \quad S = Nr^2 P(\gamma, \mu_{1,2}),$$

$$\gamma = 2\pi r/\lambda,$$

$\mu_{1,2}$ = relative index of refraction between particles and medium,

P is a function of λ with relative maxima for

$$[17] \quad \lambda_{\max} = 2\pi r/1.8, 2\pi r/3.8, \dots$$

For wave lengths $\lambda > 10r$, S follows Rayleigh's law, provided that $\mu_{1,2}$ is constant. With the same assumption S gradually becomes independent of λ if r increases to values $r \gg \lambda$. In this limiting case the "mosaic scattering" is transformed into "surface scattering".

From the foregoing discussion it follows that the scattering properties of mosaic crystals and of localized lattice imperfections can be essentially similar. Hence it cannot be immediately decided by scattering experiments in any special case which kind of mechanism is responsible. It would, however, be interesting to investigate whether X-ray and Rayleigh scattering yield the same result for the mosaic block diameter of a given crystal. Agreement between the two different methods could be a strong argument for the mosaic structure. The argument would, of course, not be conclusive since a interpreted as the mean distance of neighboring lattice imperfections could also, by chance, be equal to the diameter of the region of coherence which determines the properties of X-ray reflections. Anyway, a simultaneous investigation of X-ray and Rayleigh scattering under different conditions of temperature, pressure, and plastic deformation could probably yield interesting information on the real structure of solids.

Summarizing one can say that there are three different types of light scattering active in condensed matter.

(i) Thermal scattering which approximately obeys Rayleigh's $1/\lambda^4$ law for most transparent bodies. It is always present and is strong in liquids and weak in solids.

(ii) Surface scattering which is nearly independent of λ for most transparent bodies. It is zero for pure liquids and strong in solids with macroscopic defects.

(iii) Structure-sensitive scattering including mosaic scattering, which exhibits relative maxima of scattering power for wave lengths which are commensurable with characteristic lengths within the scatterer, e.g., diameter of mosaic blocks or most probable distance of neighboring localized lattice imperfections. Structure-sensitive scattering has been observed with crystals, glasses, and colloidal systems.

Concerning the relative share of the single scattering mechanisms toward the total scattering one can obtain some hints by comparing the scattering power of solids and pure liquids. Since pure liquids cause only thermal scattering of visible light and since thermal scattering is considerably weaker in solids than in liquids,* one can deduce the following qualitative conclusions.

If the total measured scattering power of solids is considerably larger than about 10% of the scattering power of pure liquids, then structure-sensitive or surface scattering must be present. The surface scattering can be found by extrapolating the curve for $S(\lambda)$ to very long wave lengths.

From these theoretical expectations one can derive some knowledge of the scattering mechanism in glass. For optical glass (Fig. 3, curve 2) there is almost no surface scattering but probably some structure-sensitive scattering which corresponds in the present case to a characteristic length $\bar{a} < 3000 \text{ \AA}$. In the ordinary glass investigated here, there is considerable surface scattering of the same order of magnitude as the thermal scattering in water; in addition there is structure-sensitive scattering of about the same intensity in the region between 4000 and 6000 \AA . This corresponds to a characteristic length $\bar{a} \approx 3000\text{--}4000 \text{ \AA}$, if the observed maximum is assumed to be of the first order.

REFERENCES

1. BORN, M. Atomtheorie des festen Zustandes. Teubner, Leipzig. 1923.
2. FÜRTH, R. and HUMPHREYS-OWEN, S. P. F. Nature, 167: 715. 1951.
3. GANS, R. Ann. Physik, 77: 317. 1925.
4. JAMES, R. W. The optical principles of the diffraction of X-rays. George Bell and Sons, Ltd., London. 1948.
5. VON LAUE, M. Ann. Physik, 41: 971. 1913.
6. MIE, G. Ann. Physik, 33: 1275. 1910.
7. RALEIGH, LORD. Phil. Mag. 47: 375. 1899.
8. SCHWARZSCHILD, K. Jahrb. Phot. 14: 161. 1900.
9. SMEKAL, A. Handbuch der Physik. Vol. 24. Verlag von Julius Springer, Berlin. 1933. p. 795.

*Gans (3) finds from theoretical considerations that $S(\lambda)$ for pure water is about forty times stronger than for glass.

UN OBJECTIF SPECIAL A GRANDE OUVERTURE NUMERIQUE¹

PAR JEAN LEFAIVRE²

ABSTRACT

A dry objective of numerical aperture 0.84 has been computed for special purposes. It is a catadioptric objective of the centered type, after the terminology of Bouwers. It is not achromatic.

Au cours d'un travail de recherche en optique diffractionnelle, il s'est présenté la nécessité d'un objectif aux qualités un peu exceptionnelles: il devait être très bien corrigé des aberrations de sphéricité et de coma et être d'une ouverture numérique égale ou supérieure à 0.75, sans être à immersion de préférence. Comme dans la plupart des travaux en diffraction, la lumière pratiquement monochromatique est de rigueur, il n'aurait pas besoin d'être achromatique.

Au moment où les calculs de cet objectif ont été entrepris, la région spectrale de travail n'était pas encore définie et pouvait se trouver n'importe où, de l'infra-rouge moyen à l'ultra-violet. Le choix de la région spectrale sera dicté par des considérations autres que la facilité d'obtention de l'objectif. La littérature peut-être fragmentaire que nous avions en mains ne nous indiquait que des objectifs, ou trop peu ouverts, ou accompagnés de trop peu de renseignements sur leurs qualités optiques ou leurs caractéristiques de construction. Ces dernières remarques s'appliquent surtout aux objectifs corrigés pour le rouge, l'infra-rouge proche ou moyen; ces régions spectrales nous semblaient prometteuses pour notre travail.

Comme le problème de l'objectif ne devait occuper qu'une part secondaire dans notre travail, force nous a été de ne considérer qu'un type d'objectif de calcul rapide, même au prix de certaines inélégances de construction, d'autant plus que, une fois la région spectrale déterminée, il nous faudrait de toute façon le recalculer pour cette région particulière (c'est-à-dire pour un autre indice de réfraction des pièces transparentes).

A la suggestion du professeur Albéric Boivin de l'Université Laval, nous avons considéré le travail de Bouwers (1). Les objectifs de ce dernier nous ont servi de point de départ. Nous avons accordé plus d'attention aux objectifs dits "centrés", suivant la terminologie de Bouwers, premièrement à cause de leur absence de coma, deuxièmement à cause de la plus grande rapidité de calcul à laquelle ils se prêtent. En effet, le passage d'une surface à la suivante, dans le tracé trigonométrique des rayons, se fait avec un minimum de transformations dans le cas des surfaces concentriques.

Nous croyons être le premier à présenter les caractéristiques optiques d'un objectif catadioptrique à deux ménisques dont les cinq surfaces sont concéntriques.

La présence d'une grande obstruction centrale, comme c'est le cas dans notre objectif, s'accompagne d'une détérioration du pouvoir de résolution. Cette

¹ *Manuscrit reçu pour la première fois le 6 mars 1953, et sous forme revisée le 18 juin 1953.*
Contribution du Département de Physique, Université Laval, Boulevard de l'Entente,
Québec.

² *Boursier de l'Office des Recherches Scientifiques de la Province de Québec.*

circonstance est évidemment une objection dans les objectifs destinés à former des images étendues, mais heureusement pas dans notre étude de certaines particularités des figures de diffraction.

Le nouvel objectif possède un miroir M (voir Fig. 1) et deux ménisques transparents M_1 et M_2 . Les cinq surfaces sont sphériques et ont comme centre

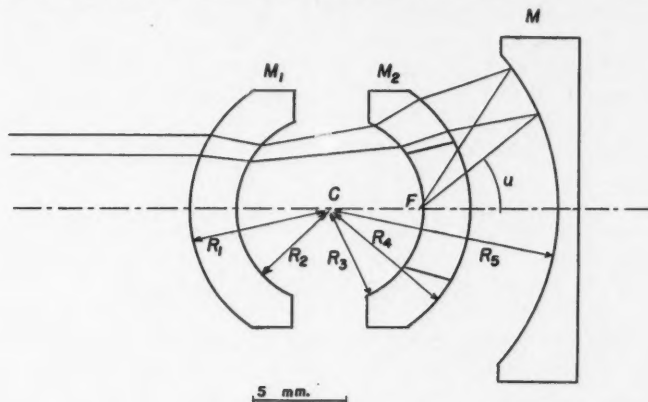


FIG. 1. Coupe de l'objectif.

commun le point C . Il est à noter que le ménisque M_2 est percé afin de ne pas gêner les rayons réfléchis par le miroir.

Les rayons de courbure des cinq surfaces sont les suivants:

$$\begin{array}{lll} R_1: 7.50 \text{ mm.} & R_3: -5.00 & R_5: -12.14 \\ R_2: 5.00 & R_4: -7.50 & \end{array}$$

L'indice de réfraction du verre des ménisques est de 1.5163.

La longueur focale équivalente de l'objectif est de 4.76 mm.

L'un des foyers conjugués pour lesquels la correction a été calculée est à 250 mm. à gauche du centre C et l'autre est au point F , à 7.46 mm. à gauche du miroir. Remarquons que, contrairement à l'objectif de microscope, les rayons lumineux arriveront en F .

L'ouverture numérique est de 0.84. Le centre du système est masqué et la perte de lumière qui en résulte est de 50% environ. Comme les objets lumineux seront toujours de très faible étendue (dans nos conditions d'utilisation), la position du diaphragme délimitant la zone corrigée pourra être l'une des faces du ménisque M_1 . Définissant la condition des sinus par la constance du rapport $\sin u / \sin u_0$ (où u et u_0 sont les angles d'inclinaison sur l'axe du rayon émergeant du miroir et du rayon incident), le système obéit à la condition des sinus à 0.01%.

Fig. 2 montre les traces sur l'axe des rayons émergents. Nous avons indiqué en abscisse la distance x de ces traces au miroir. Figs. 2a et 2b ne diffèrent que par l'échelle des abscisses. En ordonnée est l'angle u . L'angle u est indiqué sur Fig. 1.

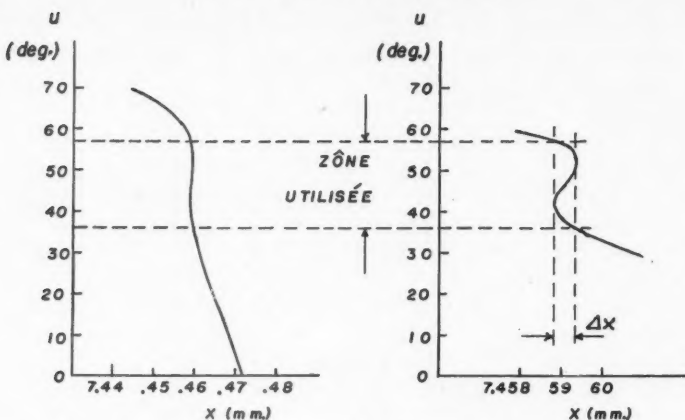


FIG. 2. Position du point F en fonction de l'angle u .

La grandeur Δx est l'aberration longitudinale de sphéricité. Elle est numériquement égale à 0.57 micron. Les lignes horizontales pointillées indiquent les limites de la zone corrigée. Fig. 1 illustre la marche des rayons en bordure de cette zone.

L'information fournie par Fig. 2b nous a permis de calculer, par intégration graphique, le chemin optique aberrant (Ab). Pour ce, nous avons utilisé l'intégrale définissant le chemin optique aberrant cité par le *Handbuch der Physik* (2). Par exemple, si $\lambda = 0.55$ micron,

$$(Ab) = \lambda/9,$$

alors que la tolérance permise est de $\lambda/4$.

La symétrie du système élimine l'aberration de coma. Par comparaison avec les objectifs existants, notre objectif possède deux défauts: il n'est pas achromatique et il a une courbure de champ prononcée. Ces défauts ne nous gênent guère étant donné les conditions particulières de son usage.

Tous les calculs ont été effectués au moyen du tracé trigonométrique des rayons à l'aide des logarithmes à cinq décimales. La solution finale a été vérifiée à l'aide des logarithmes à sept décimales.

BIBLIOGRAPHIE

1. BOUWERS, A. Achievements in optics. Elsevier Publishing Co., Inc., Amsterdam. 1946.
2. Handbuch der Physik, Vol. XVIII. Verlag von Julius Springer, Berlin. 1927. pp. 274, 275.

NOTE

A NOTE ON THE RATIO OF THE QUADRUPOLE MOMENTS OF Li⁶ AND Li⁷*

By N. G. CRANNA**

Schuster and Pake (2) reported a value for the ratio of the magnitudes of the quadrupole moments of Li⁶ and Li⁷ calculated from the quadrupole splitting of the Li⁶ and Li⁷ magnetic resonances obtained from a single crystal of LiAl(SiO₃)₂ (spodumene). Their crystal was mounted so as to rotate about its *c* axis.

The Li⁷ quadrupole interaction in spodumene has been examined in detail in this laboratory by Volkoff, Petch, and Smellie and has been reported in this journal (3). This investigation yielded complete information on the orientation of the principal axes and the degree of axial asymmetry of the field gradient tensor at the sites of the Li nuclei. The results show that maximum splitting of the Li lines is obtained when the crystal is mounted to rotate about its *b* axis. This exceeds by 11.5% the largest splitting obtained by a rotation about the *c* axis.

With a crystal so mounted, and oriented to give the maximum splitting of the Li⁷ lines, the splitting of the Li⁶ lines was observed. The apparatus used is that described in Reference (3) and the measurements were made at room temperature in a field of about 8900 gauss. The resolution obtained is shown in Fig. 1, and represents an improvement over that reported by Schuster and Pake. It is felt that the improvement is sufficient to warrant a recalculation of the quadrupole moment ratio. The improvement is due partly to the increase in the $\Delta\nu$ being measured and partly to a better signal-to-noise ratio which allowed the use of a smaller modulation amplitude. The measured traces were recorded with a modulation amplitude equal to approximately one-sixth of the line width at half maximum. A reduction of this modulation amplitude by a factor of 10 produced no appreciable further improvement in resolution.

From Reference (2) we have

$$[1] \quad |Q_6/Q_7| = \Delta\nu_6 I_6 / \Delta\nu_7 I_7,$$

where $\Delta\nu$ is the frequency difference between the outer components and *I* is the spin,

$$[2] \quad \text{or } |Q_6/Q_7| = \frac{3}{2} \Delta\nu_6 / \Delta\nu_7.$$

Using $\Delta\nu_{\max}$ in each case, $\Delta\nu_7$ was measured to be 75.7 ± 0.5 kc./sec. in agreement with the quadrupole coupling constant $eQ\phi_{zz}/\hbar$ for Li⁷ reported in Reference (3). $\Delta\nu_6$ was then obtained without moving the crystal by measuring the frequency difference between the positions of zero derivative of the two Li⁶ lines. The lines in Fig. 1 and other similar tracings seem to be well

* Work supported by a grant from the National Research Council of Canada.

** Holder of a National Research Council of Canada Fellowship.

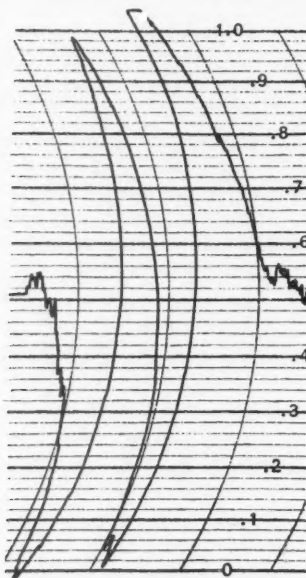


FIG. 1. Li^6 absorption derivative curve in a single crystal of $\text{LiAl}(\text{SiO}_4)_2$ showing the maximum quadrupole splitting obtainable with the crystal b axis perpendicular to the external magnetic field.

Frequency scale approximately 1 div. = 2.6 kc./sec.

enough resolved so that the tail of one does not contribute to the peak of the other. The value of $\Delta\nu_6$ obtained from 30 such measurements is $2.18 \pm .05$ kc./sec. The quoted error is the statistical probable error.

This gives

$$|Q_6/Q_7| = (1.9 \pm 0.1) \times 10^{-2}$$

which is significantly lower than the value $(2.3 \pm 0.2) \times 10^{-2}$ reported by Schuster and Pake. The quoted uncertainty is slightly greater than twice the statistical error. The values of neither Q_6 nor Q_7 separately appear to be known at present (1).

1. HARRIS, E. G. and MELKANOFF, M. A. Phys. Rev. 90: 585. 1953.
2. SCHUSTER, N. A. and PAKE, G. E. Phys. Rev. 81: 157. 1951.
3. VOLKOFF, G. M., PETCH, H. E., and SMELLIE, D. W. L. Can. J. Phys. 30: 270. 1952.

RECEIVED JULY 14, 1953.

PHYSICS DEPARTMENT,
UNIVERSITY OF BRITISH COLUMBIA,
VANCOUVER, B.C.

LETTERS TO THE EDITOR

Under this heading brief reports of important discoveries in physics may be published. These reports should not exceed 600 words and, for any issue, should be submitted not later than six weeks previous to the first day of the month of issue. No proof will be sent to the authors.

Penetration of Radiation through a Thick Slab of Isotropically Scattering Material

The above problem has been solved by Halpern *et al.* (3), and, by a different method, by Ambarzumian (1) and Chandrasekhar (2). Another method will be presented here, which starts from the solutions of the semi-infinite medium case, and uses their asymptotic properties (9). Formulae for these solutions, which have been taken from Chandrasekhar (2), Halpern *et al.* (3), LeCaine (5), and Placzek *et al.* (4, 6, 7, 8), will be reviewed first, in LeCaine's notation.

If a parallel beam of unit density and an angle of incidence $\arccos \mu_0$ illuminates the semi-infinite medium, the radiation density $f_1(z)$ satisfies the equation

$$[1] \quad f_1(z) = e^{-z/\mu_0} + \frac{1}{2}(1-\alpha) \int_0^{\infty} E_1(|z-z'|) f_1(z') dz',$$

where α is the ratio of the absorption to the total cross section, and the mean free path has been taken as unit of length. The asymptotic expression for the bounded solution of [1] is

$$[2] \quad f_1(z) = \frac{\nu(1-\nu^2)\mu_0 H(\mu_0)}{(\nu^2 - \alpha)H(1/\nu)(1-\nu\mu_0)} e^{-\nu z} + O(e^{-z}),$$

where ν is the positive root of $(1-\alpha)\nu^{-1} \operatorname{arth} \nu = 1$. In [2] Chandrasekhar's H -function appears, which is identical with the function P^{-1} of Halpern *et al.* The intensity of the emerging radiation is

$$[3] \quad \psi_1(0, -\mu) = \frac{(1-\alpha)\mu_0 H(\mu_0)H(\mu)}{2(\mu_0 + \mu)},$$

which gives the radiation density at the surface

$$[4] \quad f_1(0) = 2(1-\alpha)^{-1}\psi_1(0, 0) = H(\mu_0),$$

and the density of the ingoing net flux

$$[5] \quad j_1(0) = \int_{-1}^0 \psi_1(0, \mu) \mu d\mu + \mu_0 = \sqrt{\alpha}\mu_0 H(\mu_0).$$

Similar formulae are valid for Milne's case, where the radiation density $f_0(z)$ satisfies the homogeneous equation corresponding to [1]. The asymptotic approximation is

$$[6] \quad f_0(z) = \sqrt{\frac{2\nu^2(1-\nu^2)}{\alpha(\nu^2 - \alpha)}} \sinh \nu(z + z_0) + O(e^{-z}),$$

if the solution is so normalized that $j_0(0) = -1$. On the other hand $j_0(0)$ can be calculated from an expression for $\psi_0(0, -\mu)$ given by Chandrasekhar (2). This leads to an equation for the extrapolation length z_0 ,

$$[7] \quad e^{\nu z_0} = H(1/\nu) \sqrt{\frac{2(\nu^2 - \alpha)}{1 - \nu^2}},$$

and then to

$$[8] \quad \psi_0(0, -\mu) = \frac{(1-\alpha)\nu H(\mu)}{2\sqrt{\alpha}(1-\nu\mu)}$$

and

$$[9] \quad f_0(0) = \nu/\sqrt{\alpha}.$$

For $\alpha \rightarrow 0$ we have $\nu^2 = 3\alpha - 12\alpha^2/5 + \dots$ and $\nu H(1/\nu) = \frac{1}{2}\sqrt{3} + \frac{3}{8}m_2\nu + \dots$, where

$m_2 = \int_0^1 [H(\mu)]_{\alpha=0} \mu^2 d\mu = 0.82035$. For $\alpha = 0$ some of the above expressions reduce as follows:

$$f_1(z) = \sqrt{3}\mu_0 H(\mu_0) + O(e^{-z}), \quad j_1 = 0, \quad f_0(z) = 3(z + z_0) + O(e^{-z}), \quad z_0 = \frac{1}{2}\sqrt{3}m_2 = 0.71045,$$

$$\psi_0(0, -\mu) = \frac{1}{2}\sqrt{3}H(\mu), \quad f_0(0) = \sqrt{3}.$$

Tables for the functions $\nu(\alpha)$, $z_0(\alpha)$, and $H(\mu)$ are available (2, 3, 4, 5, 6, 7, 8). The tables for $H(\mu)$, however, do not include the values $H(1/\nu)$, which therefore are given by the table

below. The table has been checked by calculating from equation [7] the values of $(1 - \alpha)z_0(\alpha)$, which have been found to agree with LeCaine's values (5) to within ± 0.0001 .

α	$H(1/\nu)$	α	$H(1/\nu)$
0	∞	0.4	1.3479
0.025	3.7656	0.5	1.25517
0.05	2.8340	0.6	1.18426
0.075	2.4193	0.7	1.12698
0.1	2.1710	0.8	1.07864
0.15	1.8743	0.9	1.03682
0.2	1.6955	1	1.00000
0.3	1.4799		

The radiation density $f(z)$ in a plane parallel slab satisfies an equation of the same form as [1], but with finite limits $(0, h)$ of the integral. It is known (9) for a thick slab, where $e^{-h} \gg e^{-\nu z}$, that $f(z)$ in the interior asymptotically approaches some solution of the infinite medium case, which has the form $Ae^{\nu z} + Be^{-\nu z}$. Similarly, near each face of the slab the solution equals a solution of the semi-infinite medium case, i.e.

$$[10] \quad f(z) = f_1(z) - Af_0(z) + O(e^{-(h-z)}) = Bf_0(h-z) + O(e^{-z}).$$

Analogous relations with the same coefficients are valid for $\psi(z, \mu)$ and $j(z)$. The coefficients A and B are determined by inserting the asymptotic expressions for f_1 and f_0 , and by comparing the corresponding terms. The result

$$[11] \quad B = Ae^{\nu(h+2z_0)} = \frac{\sqrt{\alpha\mu_0}H(\mu_0)}{(1 - \nu\mu_0)\sinh\nu(h+2z_0)},$$

combined with former equations, solves the problem.

In the case with no absorption ($\alpha = 0$) the net flux is constant throughout the slab,

$$[12] \quad j = B = A = \frac{\mu_0 H(z_0)}{\sqrt{3}(h+2z_0)}.$$

For perpendicular incidence this is equal to $j = 1.6788/(h+1.4209)$, in agreement with Halpern's result (3): $j = 1.68/(h+1.43)$.

The above method can be extended to cases with reflections at the surfaces of the slab, and also to cases with two or more adjoining thick slabs with different values of α . An extension to anisotropic scattering seems to be feasible.

1. AMBARZUMIAN, V. A. Compt. rend. acad. sci. U.R.S.S. 38: 229. 1943.
2. CHANDRASEKHAR, S. Radiative transfer. The Clarendon Press, Oxford. 1950.
3. HALPERN, O., LUENEBURG, R. K., and CLARK, O. Phys. Rev. 53: 173. 1938; 76: 1811. 1949; 88: 232. 1952.
4. LECAINE, J. Phys. Rev. 72: 564. 1947.
5. LECAINE, J. Can. J. Research, A, 28: 242. 1950.
6. MARK, C. Phys. Rev. 72: 558. 1947.
7. PLACZEK, G. Phys. Rev. 72: 556. 1947.
8. PLACZEK, G. and SEIDEL, W. Phys. Rev. 72: 550. 1947.
9. WALLACE, P. R. Can. J. Research, A, 26: 99. 1948.

RECEIVED AUGUST 17, 1953.
INSTITUTE OF PHYSICS,
UNIVERSITY OF LJUBLJANA,
LJUBLJANA, YUGOSLAVIA.

I. KUSCER

Some Characteristics of Secondary Emission from BeCu

An investigation of the properties of the secondary electrons emitted from nonsensitized and from sensitized surfaces of metals under bombardment by electrons has been made by a radial field retardation method in which the target is placed at the center of a sphere to which a variable bias is applied. To carry out the work it has been necessary to overcome the effects, usually serious, of the condensation of oil on the target from the diffusion pump.

Fig. 1 shows the integrated energy distribution as sphere bias vs. per cent of total secondary current, for nonsensitized 2% beryllium bronze (*a*) at the primary energy of maximum yield, (*b*) at primary energy greater than that for maximum yield, and (*c*) at primary energy lower than that for maximum yield. Thus for a series of runs at different primary energies, it is found that the primary energy of maximum yield invariably has the highest proportion of low-energy secondary electrons. This holds for all clean targets investigated including copper, beryllium, and gold.

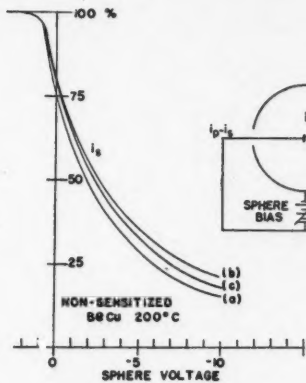


FIG. 1.

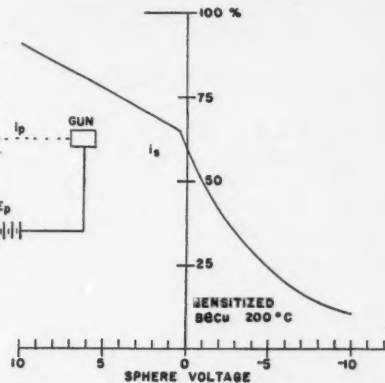


FIG. 2.

Fig. 2 shows the similar curve for beryllium bronze sensitized by a heat treatment in argon (2). As has been observed previously (1), a considerable positive voltage is necessary to collect all the secondary electrons produced; in some experiments as much as 100 volts was required in which case the yield was more than 10. The value of the positive saturation voltage required is approximately a linear function of the yield.

The curve of the sensitized material shows a discontinuity near zero volts sphere bias. The discontinuity may be used as a basis for calculation of ' R ', which is the contribution to the yield of the secondary electrons that escape at zero bias. R plotted against primary energy gives a curve that approximates both in maximum and shape the yield vs. primary energy curve of the nonsensitized surface. This indicates that the sensitization, presumably producing a surface of beryllium oxide, is responsible for the positive bias side of the curve, whereas the beryllium, copper, and copper oxides determine the negative side of the curve.

Bombardment by the primary beam of an oil film on the target tends to decompose the oil and to reduce the yield. The target becomes discolored at the point of impact of the beam. A similar effect has been noted in the reduced yield of a multiplier on the Laval mass spectrometer when operated with high currents. By using a diffusion pump oil of high volatility and maintaining the target at or above 200°C., the oil contamination can be effectively reduced, and the yield stabilized.

Measurements made while the target cooled from 300°C. to 200°C. show no variation of the yield, but the shape of the energy curves varies systematically with temperature.

A description of the apparatus and further results will be communicated at a later date.

1. BRUINING, H. and DE BOER, J. H. *Physica*, 6: 823. 1939.
2. OSBORNE, F. J. F. *Can. J. Phys.* 30: 658. 1952.

RECEIVED SEPTEMBER 15, 1953.
LAVAL UNIVERSITY,
QUEBEC, QUEBEC.

F. J. FITZ OSBORNE



CONTENTS OF VOLUME 31

ALLEN, J. R.—The ultraviolet absorption of silver bromide, 218.

ALLIN, E. J.—See Noakes, G. E.

ATKINS, K. R.—The surface tension of liquid helium, 1165.

ATKINS, K. R., FINDLAY, J. C., LOVEJOY, D. R., and WATSON, W. H.—A method of concentrating $\text{He}^4\text{-He}^4$ mixtures, 679(L).

ATKINS, K. R. and STASIOR, R. A.—First sound in liquid helium at high pressures, 1156.

BAKER, R. G.—See Katz, L.

BARTHOLOMEW, G. A.—See Kinsey, B. B.

BARTHOLOMEW, G. A. and KINSEY, B. B.—Further measurements on the γ rays produced by neutron capture in beryllium and carbon, 49. The neutron capture γ -rays from potassium, 927. Neutron capture γ -rays from heavy odd-charge nuclei, 1025.

BARTHOLOMEW, R. M., BROWN, F., HOWELL, W. D., SHOREY, W. R. J., and YAFFE, L.—The design of an automatic recording electroscope and its use to determine half-lives in radioactive decay, 714.

BAYLY, J. G.—An experimental study of a divergent nuclear reactor, 182.

BELL, R. E.—See Graham, R. L.

BENSON, G. C.—See van der Hoff, B. M. E.

BIGHAM, C. B.—See Dawson, W. K.

BLACKWELL, J. H.—Radial-axial heat flow in regions bounded internally by circular cylinders, 472.

BROCKHOUSE, B. N.—The initial magnetization of nickel under tension, 339. Resonant scattering of slow neutrons, 432.

BROWN, F.—See Bartholomew, R. M.

BROWN, F., WOLFSON, J. L., and YAFFE, L.—Pile neutron capture cross sections of Co^{60} * (10.5 min.) and Co^{60} (5.25 yr.), 903.

BUCKTHOUGHT, K.—A quantum-statistical theory of liquid helium, 932.

CAMERON, A. G. W.—See Haslam, R. N. H.; Millar, C. H.

CAMPBELL, L. L.—See Wait, J. R.

CHALMERS, B.—The preparation of single crystals and bicrystals by the controlled solidification of molten metals, 132. See Jackson, K. A.; Rutter, J. W.

CHAPMAN, J. H.—A study of winds in the ionosphere by radio methods, 120.

CLARKE, R. L.—See Paul, E. B.

COLLINS, C. B., RUSSELL, R. D., and FARQUHAR, R. M.—The maximum age of the elements and the age of the earth's crust, 402.

COX, C. D.—See Johns, M. W.

CRANNA, N. G.—A note on the ratio of the quadrupole moments of Li^6 and Li^7 , 1185. See Petch, H. E.

CRAWFORD, M. F.—See Stansbury, E. J.

CROSBY, E. H.—See Haslam, R. N. H.

CROUCH, M. F. and HAYNAM, G. E.—Counting rate measurement by interval sampling, 356.

DAUPHINEE, T. M.—An isolating potential comparator, 577.

DAWSON, W. K. and BIGHAM, C. B.—Some reactions produced in Ilford emulsions, 167(L).

DEMERS, P.—Energy loss of highly charged particles produced by fission and by cosmic rays. Section I. Observations of fission fragments, 78. Plafonnement des aerostats à grande altitude, 366. See Mathieu, R.

DEMERS, P., LAPALME, J., et THOUVENIN, J.—La régression de l'image latente due aux particules chargées, 295.

DEMERS, P. and LECHNO-WASIUTYNKA, Z.—Energy loss of highly charged particles produced by fission and by cosmic rays. III. The linear density of delta rays. Experiments. *With an appendix by Lechno-Wasiutynka, Z.*—IV. The linear density of delta rays. Theoretical, 480.

DUCKWORTH, H. E.—See Hogg, B. G.

DYNE, P. J.—The absorption spectra of free radicals formed in an electric discharge, 453.

ECKL, D. J.—The decay of the populations of neon atoms in the $2p3s$ levels, 804. The delayed cathode glow produced in a neon discharge tube at low pressure, 1015.

EICHHOLZ, G. G., HILBORN, J. W., and McMAHON, C.—The determination of uranium and thorium in ores, 613.

ENGLISH, W. N. and HANNA, G. C.—Grid ionization chamber measurements of electron drift velocities in gas mixtures, 768.

FARQUHAR, R. M.—See Collins, C. B.

FINLAY, J. C.—See Atkins, K. R.

FOSTER, J. S.—See Johnson, F. A.

FRASER, P. A.—See Nicholls, R. W.

GARDNER, J. W.—Energy selection of charged particles by a magnetic field, 459.

GOVE, H. E. and WALL, N. S.—The angular distribution of gamma rays in the $Cd(p,p'\gamma)$ reaction, 189.

GOWAN, E. H. and LEPPARD, R. E.—Meteorological variations in the quantity of atmospheric ozone over Edmonton (lat. 53°34' N. long. 113°31' W.), 702.

GRAHAM, R. L. and BELL, R. E.—A determination of the half lives of some magnetic dipole γ -ray transitions, 377.

GRAY, A. P.—See Sargent, B. W.

GREENBERG, J. S.—See Westcott, C. H.

GREENBERG, L. H. and HASLAM, R. N. H.—On the shrinkage factor of nuclear emulsions, 1115.

GRIFFITHS, H. D.—Wave guide arrays with symmetrical conductance functions, 520.

GRUENBERG, H.—Second-order beams of slotted wave guide arrays, 55.

GUPTILL, E. W.—The sound field of a piston source, 393.

HANNA, G. C.—See English, W. N.

HARVEY, J. A.—Energy levels in lead and bismuth and nuclear shell structure, 278.

HASLAM, R. N. H.—See Greenberg, L. H.; Summers-Gill, R. G.

HASLAM, R. N. H., HORSLEY, R. J., JOHNS, H. E., and ROBINSON, L. B.—Measurement of nuclear gamma-ray absorption in carbon, 636.

HASLAM, R. N. H., KATZ, L., CROSBY, E. H., SUMMERS-GILL, R. G., and CAMERON, A. G. W.—Cross section for the reaction $B^{3\alpha}(\gamma,p)Li^3$, 210.

HAYNAN, G. E.—See Crouch, M. F.

HERZBERG, G.—Forbidden transitions in diatomic molecules. III. New ${}^1\Sigma_u \leftarrow {}^3\Sigma_g^-$ and ${}^3\Delta_u \leftarrow {}^3\Sigma_g^-$ absorption bands of the oxygen molecule, 657.

HERZBERG, L.—See Locke, J. L.

HILBORN, J. W.—See Eichholz, G. G.

HITSCHFELD, W.—See Marshall, J. S.

HOGG, B. G. and DUCKWORTH, H. E.—An atomic mass study of nuclear shell structure in the region $28 \leq n \leq 50$ and $28 \leq Z \leq 40$, 942.

HORSLEY, R.—See Wiles, D. R.

HORSLEY, R. J.—See Haslam, R. N. H.

HOWELL, W. D.—See Bartholomew, R. M.

HUGO, T. J.—See Naudé, S. M.

HUNTER, D. M.—A rapid-scanning auroral spectrometer, 681.

JACKSON, K. A. and CHALMERS, B.—Influence of striations on the plastic deformation of single crystals of tin, 1017.

JACOBS, J. A.—Temperature-pressure hypothesis and the earth's interior, 370.

JARMAIN, W. R.—See Nicholls, R. W.

JOHNS, H. E.—See Haslam, R. N. H.

JOHNS, M. W., WATERMAN, H., MACASKILL, D., and COX, C. D.—A description of a large double-focusing beta spectrometer and its application to a study of the decay of In^{114} , 225.

JOHNSON, F. A.—The decay of Cd^{108} , 1136.

JOHNSON, F. A. and FOSTER, J. S.—Auger transitions in silver, 469.

KAEMPFER, F. A.—Note on the concept of vacuum in quantum electrodynamics, 165. Theory of the electromagnetic vacuum (preliminary report), 497. The physical meaning of auxiliary conditions in the theory of gravitational waves, 501. Theory of the electromagnetic vacuum. I, 629.

KASTNER, J.—The half-life of europium-152, 154, 169(L).

KATZ, L.—See Haslam, R. N. H.; Montalbetti, R.; Summers-Gill, R. G.

KATZ, L., BAKER, R. G., and MONTALBETTI, R.—The photoneutron cross sections of Rb^{87} , Zr^{90} , and Mo^{98} , 250.

KELLY, F. M. and MACDONALD, D. K. C.—On θ values in metals, 147.

KINSEY, B. B.—See Bartholomew, G. A.

KINSEY, B. B. and BARTHOLOMEW, G. A.—The measurement of energies and intensities of γ -rays with a pair spectrometer, 537. Note on some neutron capture γ -rays from magnesium, 901(L). Neutron capture γ -rays from heavy even-charge nuclei, 1051.

KIRKALDY, J. S.—See Westcott, C. H.

KROTKOV, R. V. and SCHEIDECKER, A. E.—Thermodynamics of some special fields, 329.

KUSCER, I.—Penetration of radiation through a thick slab of isotropically scattering material, 1187(L).

LAMARCHE, G. and VOLKOFF, G. M.—A theoretical investigation of the nuclear resonance absorption spectrum of Al²⁷ in spodumene, 1010.

LAPALME, J.—See Demers, P.

LECHNO-WASIUTYNKA, Z.—See Demers, P.

LEE, P. A.—"Phosphorescent" effect in lead selenide, 1023(L).

LEFAIVRE, J.—Un objectif spécial à grande ouverture numérique, 1182.

LELL, E.—See Theimer, O.

LEPPARD, R. E.—See Gowan, E. H.

LOCKE, J. L. and HERZBERG, L.—The absorption due to carbon monoxide in the infrared solar spectrum, 504.

LOVEJOY, D. R.—See Atkins, K. R.

MACASKILL, D.—See Johns, M. W.

MCDIARMID, I. B.—Angular separation of electron pairs, 337.

MACDONALD, D. K. C.—See Kelly, F. M.

MCKINLEY, D. W. R.—Effect of radar sensitivity on meteor echo durations, 758. Meteor echo duration and radio wave length, 1121.

MCKINLEY, D. W. R. and MILLMAN, P. M.—Long duration echoes from aurora, meteors, and ionospheric back-scatter, 171.

MCMAHON, C.—See Eichholz, G. G.

MANN, K. C.—See Pearce, R. M.

MARSHALL, J. S.—Frontal precipitation and lightning observed by radar, 194.

MARSHALL, J. S. and HITSCHFELD, W.—Interpretation of the fluctuating echo from randomly distributed scatterers. Part I, 962.

MATHIEU, R. and DEMERS, P.—Energy loss of highly charged particles produced by fission and by cosmic rays. Section II. Photometric measurements on fission fragments, 97.

MILLAR, C. H.—Photo-alpha particles from silver and bromine irradiated with 70 Mev. bremsstrahlung, 262.

MILLAR, C. H. and CAMERON, A. G. W.—Photo-alpha reactions in nuclear emulsions, 723.

MILLMAN, P. M.—See McKinley, D. W. R.

MONTALBETTI, R.—See Katz, L.

MONTALBETTI, R. and KATZ, L.—The O¹⁶(γ, n)O¹⁸ and O¹⁸(γ, p)N¹⁷ reactions, 798.

MORGAN, E. R.—See Piercy, G. R.

NAUDÉ, S. M. and HUGO, T. J.—The emission spectrum of aluminum monofluoride, 1106.

NICHOLLS, R. W., JARMAIN, W. R., and FRASER, P. A.—The calculation of vibrational transition probabilities of diatomic molecules, 1019.

NIVEN, C. D.—The effect of thermal radiation on the electrical resistance of hydrophilic organic films, 1095.

NOAKES, G. E. and ALLIN, E. J.—Interference effects in the small angle scattering of X rays by small particles, 40.

OSBORNE, F. J. F.—A simplified ionization gauge circuit, 11. Some characteristics of secondary emission from BeCu, 1189 (L).

PAUL, E. B. and CLARKE, R. L.—Cross-section measurements of reactions induced by neutrons of 14.5 Mev. energy, 267.

PEARCE, R. M. and MANN, K. C.—Compton electron suppression in the gamma-ray spectra of Ra (B + C), Co⁶⁰, and Ta¹⁸¹, 592.

PETCH, H. E., CRANNA, N. G., and VOLKOFF, G. M.—Second order nuclear quadrupole effects in single crystals. Part II. Experimental results for spodumene, 837.

PETRIE, W. and SMALL, R.—The intensities of atomic and molecular features in the auroral spectrum, 911.

PICKUP, E.—Grain size in Ilford G5 emulsions, 898.

PIERCY, G. R. and MORGAN, E. R.—Ferromagnetism and order in nickel manganese alloys, 529.

Post, E. J.—On the characteristic temperatures of single crystals and the dispersion of the "Debye heat waves", 112.

ROBINSON, L. B.—See Haslam, R. N. H.

RUSSELL, R. D.—See Collins, C. B.

RUTTER, J. W. and CHALMERS, B.—A prismatic substructure formed during solidification of metals, 15.

SARGENT, B. W., YAFFE, L., and GRAY, A. P.—Measurement of the half-lives of Ac^{22} , Cu^{66} , Mg^{27} , Ti^{41} , Th^{230} , and V^{51} , 235.

SCHEIDEGGER, A. E.—On some physical aspects of the theory of the origin of mountain belts and island arcs, 1148. See Krotkov, R. V.

SHANNUGADHASAN, S.—The quantization of classical spin theory, 1.

SHOREY, W. R. J.—See Bartholomew, R. M.

SMALL, R.—See Petrie, W.

SMITH, B. W.—See Wiles, D. R.

STANSBURY, E. J., CRAWFORD, M. F., and WELSH, H. L.—Determination of rates of change of polarizability from Raman and Rayleigh intensities, 954.

STASIOR, R. A.—See Atkins, K. R.

STEENBERG, N. R.—The detection of polarized γ radiation by the Compton process, 204.

SUMMERS-GILL, R. G.—See Haslam, R. N. H.

SUMMERS-GILL, R. G., HASLAM, R. N. H., and KATZ, L.—Photoneutron cross sections in silicon and calcium, 70.

THEIMER, O. and LELL, E.—Rayleigh scattering of condensed matter, 1170.

THODE, H. G.—See Wanless, R. K.; Wiles, D. R.

THOUVENIN, J.—See Demers, P.

VAN DER HOFF, B. M. E. and BENSON, G. C.—A method for the evaluation of some lattice sums occurring in calculations of physical properties of crystals, 1087.

VOLKOFF, G. M.—Second order nuclear quadrupole effects in single crystals. Part I. Theoretical, 820. See Lamarche, G.; Petch, H. E.

WAIT, J. R.—A conducting permeable sphere in the presence of a coil carrying an oscillating current, 670.

WAIT, J. R. and CAMPBELL, L. L.—Effect of a large dielectric constant on ground-wave propagation, 456.

WALL, N. S.—See Gove, H. E.

WALLACE, P. R.—Interpretation of the fluctuating echo from randomly distributed scatterers, II, 995.

WANLESS, R. K. and THODE, H. G.—The mass spectrometer determination of the half-life of Kr^{86} , 517.

WATERMAN, H.—See Jones, M. W.

WATSON, W. H.—See Atkins, K. R.

WELSH, H. L.—See Stansbury, E. J.

WEST, D. C.—The photoelectric constants of iodine, 691.

WESTCOTT, C. H., GREENBERG, J. S., and KIRKALDY, J. S.—An experimental study of counting losses due to dead-time effects, 859.

WILES, D. R., SMITH, B. W., HORSLEY, R., and THODE, H. G.—Fission yields of the stable and long-lived isotopes of cesium, rubidium, and strontium and nuclear shell structure, 419.

WOLFSON, J. L.—See Brown, F.

WOOLLEY, H. W.—Note on the resonance method of measuring the ratio of the specific heats of a gas, C_p/C_v , 604.

YAFFE, L.—See Bartholomew, R. M.; Brown, F.; Sargent, B. W.





CANADIAN JOURNAL OF PHYSICS

Notice to Contributors

GENERAL: Manuscripts should be typewritten, double spaced, and the **original and one extra copy** submitted. Style, arrangement, spelling, and abbreviations should conform to the usage of this Journal. Names of all simple compounds, rather than their formulas, should be used in the text. Greek letters or unusual signs should be written plainly or explained by marginal notes. Superscripts and subscripts must be legible and carefully placed. Manuscripts should be carefully checked before being submitted, to reduce the need for changes after the type has been set. If authors require changes to be made after the type is set, they will be charged for changes that are considered to be excessive. **All pages, whether text, figures, or tables, should be numbered.**

ABSTRACT: An abstract of not more than about 200 words, indicating the scope of the work and the principal findings, is required.

ILLUSTRATIONS:

(i) **Line Drawings:** All lines should be of sufficient thickness to reproduce well. Drawings should be carefully made with India ink on white drawing paper, blue tracing linen, or co-ordinate paper ruled in blue only; any co-ordinate lines that are to appear in the reproduction should be ruled in black ink. Paper ruled in green, yellow, or red should not be used unless it is desired to have all the co-ordinate lines show. Lettering and numerals should be neatly done in India ink preferably with a stencil (do not use typewriting) and be of such size that they will be legible and not less than one millimeter in height when reproduced in a cut three inches wide. All experimental points should be carefully drawn with instruments. Illustrations need not be more than two or three times the size of the desired reproduction, but the ratio of height to width should conform with that of the type page. **The original drawings and one set of small but clear photographic copies are to be submitted.**

(ii) **Photographs:** Prints should be made on glossy paper, with strong contrasts; they should be trimmed to remove all extraneous material so that essential features only are shown. Photographs should be submitted in **duplicate**; if they are to be reproduced in groups, one set should be so arranged and mounted on cardboard with rubber cement; the duplicate set should be unmounted.

(iii) **General:** The author's name, title of paper, and figure number should be written in the lower left hand corner (outside the illustration proper) of the sheets on which the illustrations appear. Captions should not be written on the illustrations, but typed together at the end of the manuscript. All figures (including each figure of the plates) should be numbered consecutively from 1 up (arabic numerals). **Each figure should be referred to in the text.** If authors desire to alter a cut, they will be charged for the new cut.

TABLES: Each table should be typed on a separate sheet. Titles should be given for all tables, which should be numbered in roman numerals. Column heads should be brief and textual matter in tables confined to a minimum. **Each table should be referred to in the text.**

REFERENCES: These should be listed alphabetically by authors' names, numbered in that order, and placed at the end of the paper. The form of literature citation should be that used in this Journal. **Titles of papers should not be given.** The first page only of the references cited should be given. **All citations should be checked with the original articles.** Each citation should be referred to in the text by means of the key number.

REPRINTS: A total of 50 reprints of each paper, without covers, are supplied free to the authors. Additional reprints will be supplied according to a prescribed schedule of charges. On request, covers can be supplied at cost.

Approximate charges for reprints may be calculated from the number of printed pages, obtained by multiplying by 0.6 the number of manuscript pages (double-spaced typewritten sheets, 8½ in. by 11 in.) and making allowance for space occupied by line drawings and half-tones (not inserts). The cost per page is tabulated at the back of the reprint request form sent with the galley.

Contents

	Page
Neutron Capture γ -Rays from Heavy Odd-charge Nuclei— <i>G. A. Bartholomew and B. B. Kinsey</i>	1025
Neutron Capture γ -Rays from Heavy Even-charge Nuclei— <i>B. B. Kinsey and G. A. Bartholomew</i>	1051
A Method for the Evaluation of Some Lattice Sums Occurring in Calculations of Physical Properties of Crystals— <i>B. M. E. van der Hoff and G. C. Benson</i>	1087
The Effect of Thermal Radiation on the Electrical Resistance of Hydrophilic Organic Films— <i>C. D. Niven</i>	1095
The Emission Spectrum of Aluminum Monofluoride I— <i>S. M. Naudé and T. J. Hugo</i>	1106
On the Shrinkage Factor of Nuclear Emulsions— <i>L. H. Greenberg and R. N. H. Haslam</i>	1115
Meteor Echo Duration and Radio Wave Length— <i>D. W. R. McKinley</i>	1121
The Decay of Cd ¹⁰⁵ — <i>F. A. Johnson</i>	1136
On Some Physical Aspects of the Theory of the Origin of Mountain Belts and Island Arcs— <i>Adrian E. Scheidegger</i>	1148
First Sound in Liquid Helium at High Pressures— <i>K. R. Atkins and R. A. Stasior</i>	1156
The Surface Tension of Liquid Helium— <i>K. R. Atkins</i>	1165
Rayleigh Scattering of Condensed Matter— <i>O. Theimer and E. Lell</i>	1170
Un Objectif Spécial à Grande Ouverture Numérique— <i>Jean Lefaire</i>	1182
A Note on the Ratio of the Quadrupole Moments of Li ⁶ and Li ⁷ — <i>N. G. Cranna</i>	1185
Letters to the Editor:	
Penetration of Radiation through a Thick Slab of Isotropically Scattering Material— <i>I. Kuscer</i>	1187
Some Characteristics of Secondary Emission from BeCu— <i>F. J. Fitz Osborne</i>	1189
Contents of Volume 31	1190

